

WestminsterResearch

<http://www.westminster.ac.uk/westminsterresearch>

Integrated Filter Antennas for Wireless Transceivers

Ahmad, W.

This is an electronic version of a PhD thesis awarded by the University of Westminster.
© Mr Waqas Ahmad, 2017.

The WestminsterResearch online digital archive at the University of Westminster aims to make the research output of the University available to a wider audience. Copyright and Moral Rights remain with the authors and/or copyright owners.

Whilst further distribution of specific materials from within this archive is forbidden, you may freely distribute the URL of WestminsterResearch: (<http://westminsterresearch.wmin.ac.uk/>).

In case of abuse or copyright appearing without permission, e-mail repository@westminster.ac.uk

INTEGRATED FILTER ANTENNAS FOR WIRELESS TRANSCEIVERS

WAQAS AHMAD



A thesis submitted in partial fulfilment of the requirements of the University of Westminster for the degree of Doctor of Philosophy

September 2017

Abstract

This thesis presents the research carried out on the integration of filters and antennas for wireless transceivers. Filters and antennas are parts of wireless transceivers of all wireless communication systems. Filters and antennas, albeit connected, are separate circuits which take up their own individual space in wireless transceivers. Moreover, since they are individual circuits, the cost to manufacture them is also separate. Hence, to effectively combine them together in the form of a single component has a number of advantages. The overall size of the wireless transceivers with such a single component will reduce. There will be a decrease in the manufacturing cost as well. In addition, the single component will use a single feed network and may also utilise a common ground plane.

The research is driven by the goal of achieving a successful and efficient integration of filters and antennas for wireless transceivers of various wireless communication systems. The research further aims to show that the integration of filters and antennas can address issues pertaining to broadband and narrowband antennas and achieve their solutions. These include the integration of bandstop filters with ultra-wideband bandpass filters and within broadband antennas in order to reject some specific interfering frequency bands and the integration of bandpass filters with narrowband antennas in order to suppress frequency harmonics and noise.

In order to achieve the goal of the research, a methodical approach was adopted. Initially, individual components were designed and electromagnetically simulated. These included bandstop and bandpass filters and broadband and narrowband antennas. After that, bandstop filters were integrated with broadband antennas — forming “broadband filtennas” — and bandpass filters were integrated with narrowband antennas — forming “narrowband filtennas”. Furthermore, the ability to switch off or switch on the bandstop filters in broadband filtennas was incorporated by making the broadband filtennas reconfigurable using standard PIN diodes and novel Graphene based switches. Both sets of filtennas were designed, electromagnetically simulated and their prototypes fabricated. The prototypes were fabricated using the conventional printed circuit board technology and the newly emerging inkjet-printing technology. Hence, both rigid and flexible filtennas were constructed. The fabricated prototypes were then measured.

The simulated and the measured results include S-parameters, current density, distribution of surface currents, radiation patterns, gain and efficiency. Satisfactory and desired results have been obtained for all the developed filtennas; with a reasonable agreement between the simulated and the measured results.

With such results, it can be concluded that the research presented in this thesis reached the intended target and made a significant contribution to knowledge.

Table of Contents

Title Page.....	i
Abstract.....	ii
Acknowledgements.....	viii
Author’s Declarations	ix
List of Abbreviations	x
List of Figures	xii
List of Tables	xvii
Chapter 1: Introduction	1
1.1: Filtennas for Wireless Transceivers	2
1.2: Overview of Past Research Work.....	7
1.3: Aims and Objectives of the Research	9
1.4: Outline of the Thesis	11
1.5: References	14
Chapter 2: Background	18
2.1: Microstrip Transmission Line Theory.....	19
2.1.1: Introduction	19
2.1.2: Microstrip Transmission Lines	19
2.1.3: Analysis Formulas for Microstrip Transmission Lines	20
2.1.4: Synthesis Formulas for Microstrip Transmission Lines.....	23
2.1.5: Discontinuities in Microstrip Transmission Lines.....	27
2.1.6: Coupled Microstrip Transmission Lines	32
2.1.7: Skin Effect in Microstrip Transmission Lines.....	36
2.2: Antenna Theory	38
2.2.1: Introduction	38
2.2.2: Main Parameters of Antennas.....	40
2.3: References	46
Chapter 3: Development of Reconfigurable Bandpass Filters	47
3.1: Introduction	48
3.2: Reconfigurable Elements	52
3.2.1: Overview of Reconfigurable Elements.....	52
3.2.2: Graphene based Switches.....	53

3.2.3: PIN Diodes.....	56
3.3: Design of Bandpass Filters for UWB Applications.....	58
3.3.1: Geometry of the Bandpass Filter	58
3.3.2: Analysis of the Geometry of the Bandpass Filter.....	59
3.3.3: Results of the Bandpass Filter.....	62
3.4: Design of a Frequency Reconfigurable Filter with a Single Notchband for UWB Applications.....	64
3.4.1: Specifications and Initial Parameters.....	64
3.4.2: Realised Structure and Final Parameters.....	65
3.4.3: Results.....	68
3.4.4: Summary of Presented Results	74
3.5: Design of a Frequency Reconfigurable Filter with High Linearity and Independently Controlled Dual Notchband for UWB Applications.....	76
3.5.1: Specifications and Initial Parameters.....	76
3.5.2: Realised Structure and Final Parameters.....	77
3.5.3: Results.....	82
3.5.4: Summary of Presented Results	93
3.6: References	96
Chapter 4: Development of Broadband Single-Element Planar Monopole Filtennas	99
4.1: Introduction	100
4.2: Design of Broadband Planar Monopole Antennas	104
4.2.1: Geometry of the Broadband Planar Monopole Antenna	104
4.2.2: Operating Mechanism of Broadband Planar Monopole Antennas	105
4.2.3: Analysis of the Geometry of the Broadband Planar Monopole Antenna.....	105
4.2.4 Realised Structure of the Broadband Planar Monopole Antenna	107
4.2.5 Results of the Broadband Planar Monopole Antenna	109
4.3: Design of a Frequency Reconfigurable Filtenna with Sharp Dual Notchband for UWB Applications.....	118
4.3.1: Specifications	118
4.3.2: Realised Structure and Final Parameters.....	119
4.3.3: Results.....	124
4.3.4: Summary of Presented Results	134
4.4: Design of a Frequency Reconfigurable Filtenna with Dual Notchband for UWB Applications.....	135
4.4.1: Specifications	135
4.4.2: Realised Structure and Final Parameters.....	136
4.4.3: Results.....	139

4.4.4: Summary of Presented Results	152
4.5: Design of a Compact Inkjet-Printed Flexible Filtenna with Triple Notchband for S-band, ISM Band and UWB Applications	153
4.5.1: Specifications	153
4.5.2: Realised Structures and Final Parameters	154
4.5.3: Results	159
4.5.4: Summary of Presented Results	171
4.6: References	172
Chapter 5: Development of Broadband MIMO-Element Planar Monopole Filtennas	174
5.1: Introduction	175
5.2: Design of a Compact MIMO Filtenna with Dual Notchband, High Isolation and High Diversity for UWB Applications	178
5.2.1: Specifications	178
5.2.2: Realised Structures and Final Parameters	179
5.2.3: Results	183
5.2.4: Summary of Presented Results	198
5.3: References	199
Chapter 6: Development of Narrowband Planar Microstrip Filtennas	202
6.1: Introduction	203
6.2: Design of Narrowband Planar Microstrip Antennas	207
6.2.1: Geometry of the Narrowband Planar Microstrip Antenna	207
6.2.2: Operating Mechanism of Narrowband Planar Microstrip Antennas	208
6.2.3: Analysis of the Geometry of the Narrowband Planar Microstrip Antenna	208
6.2.4 Realised Structure of the Narrowband Planar Microstrip Antenna	211
6.2.5 Results of the Narrowband Planar Microstrip Antenna	213
6.3: Design of a Filtenna Array for Dual-band WLAN Applications	222
6.3.1: Specifications	222
6.3.2: Realised Structure and Final Parameters	222
6.3.3: Results	229
6.4: Design of an Inkjet-Printed Filtenna for WLAN Applications	237
6.4.1: Specifications	237
6.4.2: Realised Structure and Final Parameters	237
6.4.3: Results	242
6.5: Design of an Inkjet-Printed Antenna for 5G Applications	247
6.5.1: Specifications	247
6.5.2: Realised Structure and Final Parameters	247

6.5.3: Results.....	250
6.6: References	257
Chapter 7: Conclusion	259
7.1: Concluding Statements.....	260
7.2: Contributions of the Research.....	263
7.3: Suggestions for Future Work	266
Appendices.....	268
Appendix A: Datasheets.....	269
A.1: NXP™ PIN Diode BAP65-02 SOD523	269
A.2: Fujifilm™ Dimatix™ Materials Printer DMP-3000 for Inkjet-Printing	278
A.3: DuPont™ Kapton® Flexible Polyimide Substrate for Inkjet-Printing	280
A.4: NovaCentrix® Metalon® Silver Nanoparticle Ink JS-B80HV for Inkjet-Printing.....	285
Appendix B: Programming Codes	287
B.1: SonnetLab and MATLAB Code for Graphene based Switches	287
Appendix C: List of Publications.....	291
C.1: Journals	291
C.2: Conferences	291
C.3: Seminars	292

Acknowledgements

First and foremost, thank the Lord Almighty, without whose Will this research would neither have commenced nor have finished.

Secondly, I would like to thank my Director of Studies, Dr Djuradj Budimir, for offering me a doctorate research opportunity under him at the University of Westminster, for his constant guidance, perpetual support and knowledge during the PhD and for allowing me to pursue the research in my own way.

I would also like to thank my second supervisor, Dr Andrzej Tarczynski, and my colleagues in the Wireless Communications Research Group for their advice.

I would like to express my gratitude to the Scholarships Office at the University of Westminster for the award of the full-fee waiver research scholarship.

I would like to appreciate the painstakingly hard work done by my external examiner, Professor John Batchelor, in going through the thesis and providing me with valuable feedback. The discussions during the viva and the comments given were very helpful.

I am extremely grateful to my managers at the University of Westminster's Outreach Office, Rosie Reynolds and Paul Hampson, for employing me throughout the period of the research work. This is also extended to my manager at the University's Volunteering Office, Berekhet Berakhy, and to the Faculty of Science and Technology Registry and the Faculty of Social Sciences and Humanities Registry.

Last but not least, I am forever indebted to my parents, Muhammad Ahmad and Humera Naseem, my siblings, Ayesha, Fahad and Rooshan, for their unconditional love, constant support and inspiration. Furthermore, my friends Mr Saleem Sabir, for his ever-present support, advice and understanding, Mrs Ammara Ali Malik, for the best-cooked foods and interesting discussions, Dr Neha Kapoor, for making the five years of PhD seem little and worthwhile, Dr Amrutha Chillumuri, for always being there for me and being my sports-buddy, and Miss Farah Ali, for her love and funny conversations. You all have always had such tremendous faith and belief in me!

Author's Declarations

I declare that all the material contained in this thesis is my own work.

I declare that no material contained in the thesis has been used in any other submission for an academic award.

I declare that while registered as a candidate for the University's research degree, I have not been a registered candidate or an enrolled student for another award of the University or other academic or professional institution.

I confirm that I have undertaken the programme of related studies in connection with the programme of research in accordance with the requirements of my research degree registration.

Waqas Ahmad

30/09/2017

List of Abbreviations

μm	Micrometre
2D	Two-dimensional
3D	Three-dimensional
5G	5 th Generation mobile networks/wireless systems
ABCD	Transfer Matrix
ABW	Absolute Bandwidth
ADC	Analogue-to-Digital Converter
C-band	Portion of the electromagnetic spectrum covering the microwave range of frequencies from 4 GHz to 8 GHz; as set by the IEEE
CPW	Coplanar Waveguide
CSRR	Complementary Split Ring Resonator
CST	Computer Simulation Technology
DAC	Digital-to-Analogue Converter
DC	Direct Current
dB	Decibel
DSP	Digital Signal Processing
ECC	Electronic Communications Committee
ECC	Envelope Correlation Coefficient
ECM	Equivalent Circuit Model
FBW	Fractional Bandwidth
FCC	Federal Communications Commission
GbS	Graphene based Switches
GHz	Gigahertz
IEEE	Institute of Electrical and Electronics Engineers
ISM	Industrial, Scientific and Medical
ITU	International Telecommunications Union
MEMS	Microelectromechanical Systems
MHz	Megahertz
mm	Millimetre
MIC	Microwave Integrated Circuits

MIMO	Multiple Input Multiple Output
MMIC	Monolithic Microwave Integrated Circuits
n/a	Not Applicable
n/p	Not Presented
PCB	Printed Circuit Board
PEC	Perfect Electric Conductor
PIN	Positive-Intrinsic-Negative
QPSK	Quadrature Phase Shift Keying
RF	Radio Frequency
RFID	Radio-frequency Identification
RLC	Resistor-Inductor-Capacitor
RLC	Resistance-Inductance-Capacitance
S-band	Portion of the electromagnetic spectrum covering the microwave range of frequencies from 2 GHz to 4 GHz; as set by the IEEE
S-parameters	Scattering Parameters
SIR	Stepped Impedance Resonator
SMA	Sub-Miniature version A
SRR	Split Ring Resonator
TE	Transverse Electric Propagation Mode
TEM	Transverse Electromagnetic Propagation Mode
THz	Terahertz
TM	Transverse Magnetic Propagation Mode
UWB	Ultra-wideband
VSWR	Voltage Standing Wave Ratio
WBAN	Wireless Body Area Network
WiMAX	Worldwide Interoperability for Microwave Access
WLAN	Wireless Local Area Network

List of Figures

Figure 1.1–1: Block diagram of the architecture of a full-duplex super-heterodyne transceiver.	3
Figure 1.1–2: Advantages of inkjet-printing technology.	4
Figure 1.1–3: Typical set-up and process of inkjet-printing technology.....	5
Figure 2.1–1: Cross-sectional view of microstrip transmission lines with their corresponding electric field (solid lines) and magnetic field (dashed lines).	19
Figure 2.1–2: Cross-sectional view of CPW-fed structures.....	22
Figure 2.1–3: Characteristic impedance as a function of the width to height ratio for various values of the relative dielectric constant.....	24
Figure 2.1–4: Effective dielectric constant as a function of the width to height ratio for various values of the relative dielectric constant.	24
Figure 2.1–5: Diagrams and equivalent circuit models of various microstrip discontinuities: (a) step, (b) open-end, (c) gap and (d) bend.	32
Figure 2.1–6: Cross-sectional views of coupled microstrip transmission lines with their corresponding electromagnetic field distributions during the (a) even mode and (b) odd mode excitations.....	32
Figure 2.1–7: Equivalent lumped element circuit model of coupled microstrip transmission lines.	34
Figure 2.2–1: Antenna as a transition device [2-7].	39
Figure 2.2–2: Equivalent circuit model of antennas [2-7].	39
Figure 2.2–3: Reflection, conduction and dielectric losses in antennas.....	45
Figure 3.1–1: Example of (a) fixed single-band multiservice communication systems and (b) reconfigurable multi-band multiservice communication systems.	49
Figure 3.2–1: Surface resistance of Graphene at the chemical potentials of 0.0eV and 1.0eV when (a) $\tau = 3$ ps, (b) $\tau = 5$ ps, (c) $\tau = 10$ ps and (d) $\tau = 125$ ps.	55
Figure 3.2–2: Equivalent lumped element circuit models of PIN diodes in the (a) switch OFF and (b) switch ON states.	57
Figure 3.3–1: Equivalent transmission line circuit model of the filter.....	58
Figure 3.3–2: Equivalent lumped element circuit model of (a) quarter-wavelength transmission lines and (b) half-wavelength transmission lines.	59
Figure 3.3–3: Equivalent lumped element circuit model of the filter.	60
Figure 3.3–4: S-parameters of the filter.	63
Figure 3.4–1: Geometry of the filter.	66
Figure 3.4–2: Breakdown of the notchband structure.	67
Figure 3.4–3: Photograph of the fabricated PCB filter.	68
Figure 3.4–4: S-parameters of the equivalent lumped element circuit model of the filter. .	69
Figure 3.4–5: S-parameters of the filter using PEC based switches in the (a) switch OFF and (b) switch ON states.....	70
Figure 3.4–6: S-parameters of the filter using Graphene based switches in the (a) switch OFF and (b) switch ON states.....	72

Figure 3.4–7: S-parameters of the filter using PIN diodes in the (a) switch OFF and (b) switch ON states.....	74
Figure 3.5–1: Geometry of the filter.....	78
Figure 3.5–2: Equivalent transmission line circuit model of the filter.....	79
Figure 3.5–3: Photograph of the fabricated PCB filter.	82
Figure 3.5–4: S-parameters of the equivalent lumped element circuit model of the filter. .	83
Figure 3.5–5: S-parameters of the filter using PEC based switches in (a) state 1, (b) state 2, (c) state 3 and (d) state 4.	86
Figure 3.5–6: S-parameters of the filter using Graphene based switches in (a) state 1, (b) state 2, (c) state 3 and (d) state 4.....	89
Figure 3.5–7: S-parameters of the filter using PIN diodes in (a) state 1, (b) state 2, (c) state 3 and (d) state 4.	92
Figure 3.5–8: Linearity performance of the filter using PIN diodes in state 1 and state 2....	93
Figure 4.2–1: Geometry of the antenna.	104
Figure 4.2–2: Multiple overlapping resonant modes of broadband planar monopole antennas.	105
Figure 4.2–3: Photographs of (a) the top side and (b) the bottom side of the fabricated antenna.	109
Figure 4.2–4: Return loss of the antenna.	110
Figure 4.2–5: Parametric study of the effects on the return loss of the antenna by varying (a) the ground width and (b) the gap width.	112
Figure 4.2–6: E-field of the antenna at the three resonant modes of (a) 3.72 GHz, (b) 6.5 GHz and (c) 9.65 GHz.	115
Figure 4.2–7: Radiation patterns of the antenna at (a) 3 GHz, (b) 4.5 GHz and (c) 7.5 GHz.	116
Figure 4.2–8: Gain of the antenna.	117
Figure 4.2–9: Efficiency of the antenna.	117
Figure 4.3–1: Geometry of the filtenna.	119
Figure 4.3–2: Geometry of the filter.	121
Figure 4.3–3: Equivalent lumped element circuit model of the filter.	122
Figure 4.3–4: Photograph of the fabricated PCB filter.	123
Figure 4.3–5: Photograph of the top side of the fabricated PCB filtenna.	123
Figure 4.3–6: S-parameters of the equivalent lumped element circuit model of the filter.	124
Figure 4.3–7: S-parameters of the filter in the (a) switch OFF and (b) switch ON states. ...	126
Figure 4.3–8: Return loss of the filtenna in the (a) switch OFF and (b) switch ON states. ...	129
Figure 4.3–9: Radiation patterns of the filtenna at (a) 3.1 GHz, (b) 4.5 GHz and (c) 6.5 GHz.	130
Figure 4.3–10: Gain of the filtenna in the (a) switch OFF and (b) switch ON states.....	132
Figure 4.3–11: Efficiency of the filtenna in the (a) switch OFF and (b) switch ON states....	133
Figure 4.4–1: Geometry of the filtenna.	137
Figure 4.4–2: Photographs of (a) the top side and (b) the bottom side of the fabricated PCB filtenna.	139
Figure 4.4–3: Return loss of the filtenna in the (a) switch OFF and (b) switch ON states. ...	142
Figure 4.4–4: Parametric study of the effects on the VSWR of the filtenna by varying the position of (a) the 3.5 GHz resonator and (b) the 5.8 GHz resonators.	144
Figure 4.4–5: Current density of the filtenna at 3.45 GHz in the (a) switch OFF and (b) switch ON states.....	145

Figure 4.4–6: Current density of the filtenna at 6.03 GHz in the (a) switch OFF and (b) switch ON states.....	146
Figure 4.4–7: Current density of the filtenna at 9.55 GHz in the (a) switch OFF and (b) switch ON states.....	146
Figure 4.4–8: Photograph of the inside of an anechoic chamber showing the filtenna under test.	147
Figure 4.4–9: Radiation patterns of the filtenna at (a) 3.1 GHz, (b) 4.5 GHz and (c) 6.5 GHz.	148
Figure 4.4–10: Gain of the filtenna in the (a) switch OFF and (b) switch ON states.....	150
Figure 4.4–11: Efficiency of the filtenna in the (a) switch OFF and (b) switch ON states....	151
Figure 4.5–1: Geometry of the filtenna.	156
Figure 4.5–2: Photograph of the fabricated inkjet-printed antenna.	158
Figure 4.5–3: Photograph of the fabricated inkjet-printed filtenna.	159
Figure 4.5–4: Photograph of a probe station having the filtenna under test.....	160
Figure 4.5–5: Return loss of the antenna.	161
Figure 4.5–6: Return loss at the various design steps/stages of the filtenna.....	161
Figure 4.5–7: Return loss of the filtenna.	162
Figure 4.5–8: Parametric study of the effects on the VSWR of the filtenna by varying the position of (a) the 3.5 GHz R1 resonators and (b) the 5.8 GHz R2 resonators.	164
Figure 4.5–9: Distribution of the surface currents in the filtenna at (a) 3.55 GHz, (b) 4 GHz, (c) 5.65 GHz and (d) 8.16 GHz.	166
Figure 4.5–10: Photograph of the inside of an anechoic chamber showing (a) the horn antenna and (b) the filtenna under test.	167
Figure 4.5–11: Radiation patterns of the filtenna at (a) 3.1 GHz, (b) 4 GHz and (c) 5.78 GHz.	168
Figure 4.5–12: Gain of the antenna and the filtenna.	169
Figure 4.5–13: Efficiency of the antenna and the filtenna.	170
Figure 4.5–14: Measured return loss of the filtenna when bent/curved at various radii. ...	171
Figure 5.2–1: Geometry of the antenna.	180
Figure 5.2–2: Geometry of the filtenna.	181
Figure 5.2–3: Photographs of (a) the top side and (b) the bottom side of the fabricated PCB antenna.	182
Figure 5.2–4: Photographs of (a) the top side and (b) the bottom side of the fabricated PCB filtenna.	182
Figure 5.2–5: Return loss of the antenna.	183
Figure 5.2–6: Return loss of the filtenna.	184
Figure 5.2–7: Isolations between (a) the adjacent elements and (b) the opposite elements of the antenna.	186
Figure 5.2–8: Isolations between (a) the adjacent elements and (b) the opposite elements of the filtenna.	187
Figure 5.2–9: Current density of the filtenna at the dual notchband frequencies of (a) 3.45 GHz and (b) 6.04 GHz.	188
Figure 5.2–10: Current density of the filtenna at the frequencies of (a) 7.32 GHz and (b) 4.36 GHz.	190
Figure 5.2–11: Radiation patterns of the filtenna at (a) 3.1 GHz, (b) 4.5 GHz and (c) 6.5 GHz.	191
Figure 5.2–12: Gain of the antenna and the filtenna.	192
Figure 5.2–13: Efficiency of the antenna and the filtenna.	193

Figure 5.2–14: Envelope correlation coefficient of the adjacent elements of the antenna: (a) full view and (b) zoomed-in view.....	194
Figure 5.2–15: Envelope correlation coefficient of the opposite elements of the antenna: (a) full view and (b) zoomed-in view.....	195
Figure 5.2–16: Envelope correlation coefficient of the adjacent elements of the filtenna: (a) full view and (b) zoomed-in view.....	196
Figure 5.2–17: Envelope correlation coefficient of the opposite elements of the filtenna: (a) full view and (b) zoomed-in view.....	197
Figure 6.2–1: Geometry of the antenna.	207
Figure 6.2–2: Single resonant mode of narrowband planar microstrip antennas.....	208
Figure 6.2–3: Photographs of (a) the top side and (b) the bottom side of the fabricated antenna.	213
Figure 6.2–4: Return loss of the antenna.	214
Figure 6.2–5: Parametric study of the effects on the return loss of the antenna by varying (a) the width of the radiating element, (b) the length of the radiating element and (c) the width of the quarter-wavelength transmission line.	218
Figure 6.2–6: Current density of the antenna at 5.79 GHz.	219
Figure 6.2–7: Radiation patterns of the antenna at 5.8 GHz.	220
Figure 6.2–8: Gain of the antenna.	220
Figure 6.2–9: Efficiency of the antenna.	221
Figure 6.3–1: Geometry of the antenna array.	224
Figure 6.3–2: Equivalent transmission line circuit model of the antenna array.....	225
Figure 6.3–3: Geometry of the filters.	226
Figure 6.3–4: Geometry of the filtenna array.....	228
Figure 6.3–5: Photograph of the fabricated PCB filtenna array.	229
Figure 6.3–6: Return loss of the antenna array.	230
Figure 6.3–7: S-parameters of (a) the 2.4 GHz filter and (b) the 5.8 GHz filter.	231
Figure 6.3–8: Return loss of the filtenna array.	232
Figure 6.3–9: Current density of the filtenna array at (a) 2.4 GHz and (b) 5.8 GHz.	233
Figure 6.3–10: Radiation patterns of the filtenna array at (a) 2.4 GHz and (b) 5.8 GHz.....	235
Figure 6.3–11: Gain of the antenna array and the filtenna array.....	236
Figure 6.3–12: Efficiency of the antenna array and the filtenna array.....	236
Figure 6.4–1: Geometry of the antenna.	238
Figure 6.4–2: Geometry of the filter.	240
Figure 6.4–3: Geometry of the filtenna.	241
Figure 6.4–4: Return loss of the antenna.	243
Figure 6.4–5: S-parameters of the filter.	244
Figure 6.4–6: Parametric study of the effects on the S-parameters of the filter by varying (a) the conductivity of the ink and (b) the thickness of the ink metallisation.	245
Figure 6.4–7: Return loss of the filtenna.	246
Figure 6.5–1: Geometry of the antenna.	248
Figure 6.5–2: Return loss of the antenna.	250
Figure 6.5–3: Distribution of surface currents in the antenna at 27.66 GHz.....	251
Figure 6.5–4: Radiation patterns of the antenna at 27.66 GHz.	251
Figure 6.5–5: Gain of the antenna.	252
Figure 6.5–6: Efficiency of the antenna.	252
Figure 6.5–7: Parametric study of the effects on the (a) return loss, (b) gain and (c) efficiency of the antenna by varying the conductivity of the ink.	255

Figure 6.5–8: Parametric study of the effects on the return loss of the antenna by varying the thickness of the ink metallisation. 256

List of Tables

Table 3.2–1: Average values of the surface resistance and the surface reactance of Graphene at the chemical potentials of 0.0eV and 1.0eV at various relaxation times.	56
Table 3.3–1: Element values for third-order Chebyshev lowpass prototype filters for a passband ripple level of 0.1 dB and normalised to an angular cut-off frequency, ω_c , of 1 rad/s and a characteristic system impedance, Z_0 , of 1 Ω	61
Table 3.4–1: Required specifications of the filter.....	64
Table 3.4–2: Values of the lumped elements of the filter.....	65
Table 3.4–3: Values of the dimension parameters of the filter.....	66
Table 3.4–4: Summary of the resulting S-parameters of the filter in the switch OFF and switch ON states using the equivalent circuit model, PEC based switches, Graphene based switches and PIN diodes.	75
Table 3.5–1: Required specifications of the filter.....	76
Table 3.5–2: Values of the lumped elements of the filter.....	77
Table 3.5–3: Values of the dimension parameters of the filter.....	79
Table 3.5–4: Values of the transmission line parameters of the filter.	80
Table 3.5–5: Possible reconfigurable states of the filter.	81
Table 3.5–6: Summary of the resulting S-parameters of the filter in the four reconfigurable states using the equivalent circuit model, PEC based switches, Graphene based switches and PIN diodes.	95
Table 4.2–1: Values of the dimension parameters of the antenna.....	108
Table 4.3–1: Required specifications of the filtenna.	118
Table 4.3–2: Values of the dimension parameters of the filtenna.	120
Table 4.3–3: Values of the dimension parameters of the filter.....	121
Table 4.3–4: Values of the lumped elements in the equivalent circuit model of the filter.	122
Table 4.3–5: Summary of the results of the filtenna in the switch OFF and switch ON states using PEC based switches, Graphene based switches and PIN diodes.....	134
Table 4.4–1: Required specifications of the filtenna.	135
Table 4.4–2: Values of the dimension parameters of the filtenna.	137
Table 4.4–3: Summary of the results of the filtenna in the switch OFF and switch ON states using PEC based switches, Graphene based switches and PIN diodes.....	152
Table 4.5–1: Required specifications of the filtenna.	153
Table 4.5–2: Values of the dimension parameters of the filtenna.	156
Table 4.5–3: Summary of the results of the antenna and the filtenna.	171
Table 5.2–1: Required specifications of the filtenna.	178
Table 5.2–2: Values of the dimension parameters of the antenna.....	180
Table 5.2–3: Values of the dimension parameters of the filtenna.	181
Table 5.2–4: Summary of the results of the antenna and the filtenna.	198
Table 6.2–1: Initial values of the dimension parameters of the antenna.....	212
Table 6.2–2: Final values of the dimension parameters of the antenna.	212
Table 6.2–3: Summary of the resulting return loss of the antenna using the initial/calculated values and the final/optimised values.	215

Table 6.3–1: Required specifications of the filtenna array.....	222
Table 6.3–2: Values of the dimension parameters of the antenna array.....	224
Table 6.3–3: Values of the transmission line parameters of the antenna array.	225
Table 6.3–4: Values of the dimension parameters of the 2.4 GHz filter.	226
Table 6.3–5: Values of the dimension parameters of the 5.8 GHz filter.	227
Table 6.3–6: Values of the dimension parameters of the filtenna array.....	228
Table 6.4–1: Required specifications of the filtenna.	237
Table 6.4–2: Values of the dimension parameters of the antenna.	239
Table 6.4–3: Values of the dimension parameters of the filter.....	240
Table 6.5–1: Required specifications of the antenna.	247
Table 6.5–2: Values of the dimension parameters of the antenna.	249

Chapter 1:

Introduction

1.1: Filtennas for Wireless Transceivers

The telecommunications industry is constantly going through significant technological evolutions and advancements. Newer systems are considerably better than the previous ones in terms of being capable of multi-band operation, having higher data throughput and data rates and being lesser in size and costs. This has led to an increased demand in the number of wireless services being offered.

The increase in demand for offered wireless services has led an increased concern about interference. Furthermore, since the electromagnetic spectrum is continuously being populated, it is necessary that these devices provide an efficient utilisation of the allocated spectrum.

Filters and antennas are the most common and integral parts of all wireless communication systems, such as radars, satellites, computers, mobile phones, etc. Wireless transmitters and receivers in such communication systems are fitted with antennas. The antennas in the transmitter modules perform the task of the conversion of electrical signals to electromagnetic field and the antennas in the receiver modules perform the task of the conversion of electromagnetic field to electrical signals. Almost always, the information carried by frequencies needs to be curtailed. In other words, some frequencies need to be removed or altered for various reasons, such as to reduce interference and/or noise. These functions, generally known as signal processing, are performed by filters. Filters are the specific circuits that perform such signal processing i.e. blocking particular frequencies while allowing others to pass.

While various architectures of transceivers exist depending on the wireless communication systems, generally the architectures are the same as the one depicted in Figure 1.1–1 of a full-duplex super-heterodyne transceiver with a single conversion stage [1-1].

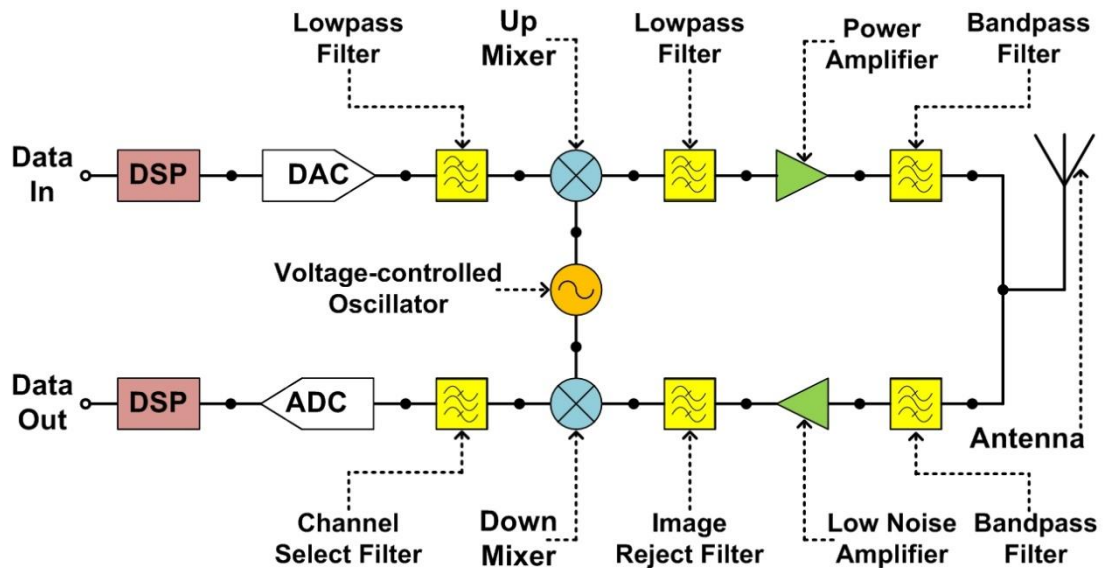


Figure 1.1–1: Block diagram of the architecture of a full-duplex super-heterodyne transceiver.

The architecture in Figure 1.1–1 consists of two parallel branches: the top one for transmitting data and the bottom one for receiving data. The last two components in both branches are a filter and an antenna. These usually appear as two separate components in transceivers. While the two are requisite components, they are a part of the same chain and, hence, can be combined and replaced by a single component.

Integrated filter antennas — or “filtennas” — perform the combined task of filters and antennas. Filtennas are employed in wireless transceivers’ front-ends to relieve the necessity of two standalone components.

Furthermore in many applications, particularly the receiver modules, due to the low power of the received signals, the out-of-band noise and the adjacent channel interferences have an adverse effect on the signal to noise ratio. This, in turn, reduces the total bit error rate of the system. Therefore, highly selective bandpass filter integrated with antennas can be used to alleviate the influence of these spurious signals and the inter-stages loss as well.

The integrated filters can be used either for the rejection of some frequency bands within the wide passband(s) of broadband antennas or for the suppression of any frequency fluctuations, harmonics or noise near the narrow passband(s) of narrowband antennas. Furthermore, because of such integration, filtennas are smaller in size and cost less to manufacture. In addition, they have a single feed network and share the ground plane. Thereby, addressing the concern and demand for a reduction in the overall size and cost of wireless transceivers.

The electronics industry has seen a swift growth and has had considerable commercial success. This, in turn, has enthused the development of new technologies for the fabrication of modern electronic devices, including filter antennas for wireless transceivers. Inkjet-printing technology is one such emerging technology. The filter antennas in the presented research work will be developed using standard PCB technology and, as well as, the new inkjet-printing technology.

As given in Figure 1.1–2, inkjet-printing technology has a range of advantages over PCB technology. Inkjet-printing is a fast, an additive and a non-vacuum technique, reducing material usage and waste content without compromising the quality. Manufacturing using traditional PCB technology requires expensive set-up for fabrication as well as sourcing costly spare and/or replacement parts. Whereas, inkjet-printing has a one-off high-cost initially only. Moreover, the actual process of printing of circuits using inkjet-printing technology is similar to that of a text document being printed using a typical inkjet printer — albeit the set-up and settings for inkjet-printing are complex. Furthermore, inkjet-printing technology allows flexible substrates to be used, which lowers production costs even further and allows the fabrication of mechanically conformal circuits. While inkjet-printing typically uses rigid substrates, such as silicon and glass, large-scale production almost exclusively employs flexible substrates. However, the main attraction of inkjet-printing technology for the fabrication of electronics is roll-to-roll (or reel-to-reel) production. Roll-to-roll production is extremely fast, supports flexible substrates, permits large circuits to be fabricated easily, ensures efficient usage of materials and allows high-volume production.

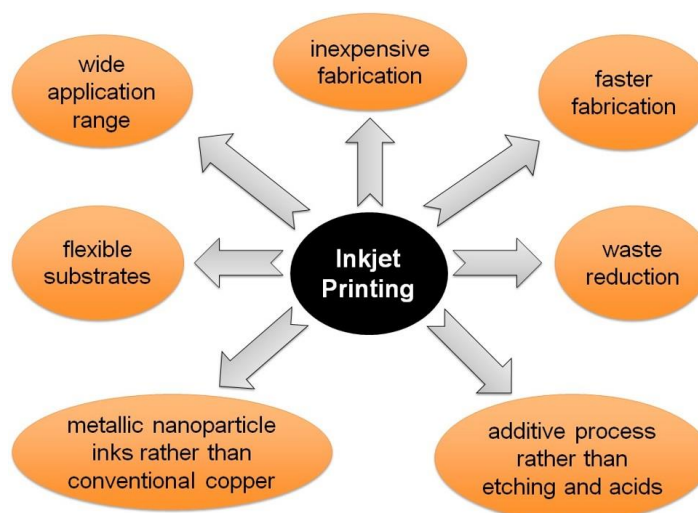


Figure 1.1–2: Advantages of inkjet-printing technology.

Inkjet-printing can be a continuous process or a drop-on-demand process. The drop-on-demand process is further divided into two processes: thermal drop-on-demand and piezoelectric drop-on-demand. Most of the commercial and industrial markets follow the piezoelectric drop-on-demand route. The primary reasons for adopting this route are low operating costs, long service lives, high speeds and a considerable gap between the printers' printheads and the substrates.

A typical set-up for large-scale fabrication using inkjet-printing technology, by a piezoelectric drop-on-demand process, with ink as metallisation on a flexible substrate and a roll-to-roll production line is shown in Figure 1.1–3 [1-2]. A roll/reel has a sheet of flexible substrate laid over it. The roll rotates and the substrate passes and moves under the printhead. The printhead consists of an ink supply and a piezoelectric motor. As and when required, a voltage is applied to drive the motor. This allows the ink to be released from its supply and be printed on the substrate below the printhead. The printhead and the piezoelectric motor have additional settings which allow the control of the speed, the amount of the ink released and the control of the time interval between the successive drops of ink.

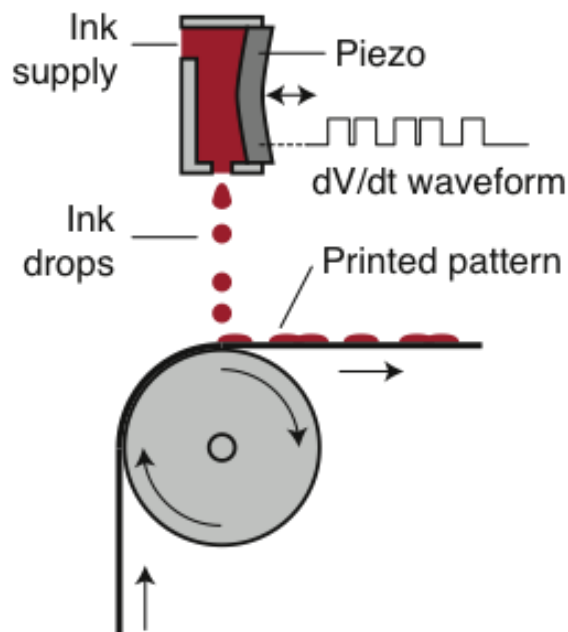


Figure 1.1–3: Typical set-up and process of inkjet-printing technology.

Within the next ten years, the printed flexible electronics market is expected to more than double in growth [1-3]. The market is predicted to increase from the current value of £20.27 billion in 2016 to £52.73 billion in 2026 [1-3]. Following this trend, filter antennas for wireless transceivers can be fabricated using the new inkjet-printing

technology as well. For the undertaken research, the filter antennas will be fabricated using piezoelectric drop-on-demand inkjet-printing technology, with conductive silver nanoparticle ink as the metallisation on flexible Kapton substrate. The inkjet printer used for all the inkjet fabrications is Fujifilm Dimatix Materials Inkjet Printer DMP-3000. A photograph of the inkjet printer is shown in Appendix A.2.

Some of the filter antennas developed and presented in this research work will be reconfigurable. Reconfigurability is a very attractive additional property in wireless transceivers. Its significance will be explained later in the chapter. This property of the filter antennas is achieved by the inclusion of reconfigurable elements. The reconfigurable elements used in the presented work are conventional PIN diodes and novel Graphene based switches (which will be developed in the next chapter). Graphene was first reported in 2004 [1-4]. In recent times, it has caught the attention of the entire research community and the industrial and commercial markets. The reasons are the unique chemical, thermal, mechanical, electrical and optical properties that it possesses [1-5]. Graphene is a monolayer of graphite, which is arranged in a honeycomb lattice structure [1-5]. Being the first 2D material, it has a thickness of only 0.34 nm [1-5]. Graphene presents a very promising future for the replacement of conventional materials and its implementation in future electronics [1-5]. As compared to conventional materials, Graphene has been realised in a wide range of applications over the last few years due to its unique properties. The published work [1-6]–[1-9] reports a plethora of applications in the microwave and the mm-wave range. For example, from Graphene based patch antennas reported in [1-6] and [1-7], to Graphene based filters in [1-8] and to phase shifters in [1-9]. However, Graphene has never been used as a switch for use in reconfigurable devices. The undertaken research addresses this and develops novel Graphene based switches for use in reconfigurable filter antennas. These kinds of reconfigurable filter antennas would be directed at supporting multiple wireless services and frequency bands.

1.2: Overview of Past Research Work

In this section, a brief overview of the past research works, which are relevant to the stated aims and objectives of the undertaken research, is given. These will include some of the recent developments in bandpass filters, in broadband planar monopole filtennas and antennas and in narrowband planar microstrip filtennas and antennas.

A) Bandpass Filters

In recent times, electronically reconfigurable devices such as bandpass filters have been in great demand for wireless transceivers. Reconfigurability would have two states, where the characteristics of the passband of the filters can be varied at a specific frequency. This can be used to accept or reject any interfering wireless services in a wide passband. For this purpose various techniques can be employed; such as applying a slot resonator [1-10] or a terminated cross-shaped resonator [1-11] or by using PIN diodes [1-12] and [1-13].

Moreover, other filter configurations have also been employed; such as applying coupled stubs [1-14], terminated resonators [1-15], stubs [1-16], embedded notchband [1-17] and short-circuited quarter-wavelength transmission lines [1-18]. In [1-14], the filter has high losses and is capable of only a single notchband. The structure in [1-15] has a fixed notchband and not enough rejection. Comparatively high losses and signal distortion are experienced in [1-16]. In [1-17], the reconfigurability is not good and does not provide full rejection characteristics. Even though the reconfigurability and rejection characteristics are good in [1-18], the bandstop structure which originates the notchband is cascaded with the rest of the filter; resulting in a larger area taken by the final circuit.

B) Broadband Planar Monopole Filtennas and Antennas

Since the broadband planar monopole filtennas that are developed in the presented research work are intended for various applications and employ different fabrication techniques, a broad range of literature was reviewed.

As stated earlier, filters must be combined with broadband planar monopole antennas in order to improve the selectivity of antenna and to reject any interfering wireless services present within the passband bandwidth. To achieve this, numerous approaches are used; such as using stubs [1-19] and [1-20], slits/slots [1-

21], capacitively-loaded resonators [1-21] or by SRRs [1-22]. Yet, in these works, the notchband are either not at a good measured rejection value or are not sharp enough for their intended band [1-21]–[1-22] or the filters are cascaded with the antenna [1-19]–[1-20], rather than being integrated within; so increasing size, cost and complexity of circuits.

The combination of MIMO technology for UWB applications is an interesting research orientation [1-23]. Various MIMO filtennas for UWB applications have been proposed [1-24]–[1-28]. However, these do not satisfy the main challenges in MIMO filtenna design; such as placing multiple elements closely while maintaining a high isolation, a wide operation band and a rejection of the interfering bands.

In [1-29]–[1-33], broadband planar monopole antennas using inkjet-printing technology have been developed. But these works still do not satisfy all challenges, such as being compact in size and the rejection of interfering frequency bands. Furthermore, in wireless transceivers having inkjet-printed filtennas, the efficiency of the system depends on the integrated filtennas which should be conformal, lightweight, compact, low profile and mechanically robust. Yet, [1-29]–[1-31] have been printed on paper substrates. Although cheap and flexible, paper has a low tensile strength of 17 MPa and introduces discontinuities where high levels of bending are needed. Moreover, it has a high dielectric loss tangent of 0.07, which compromises the filtennas' efficiency [1-32]. In [1-33], the chosen substrate for inkjet-printing is too thick, not flexible and has high dielectric losses.

C) Narrowband Planar Microstrip Filtennas and Antennas

Amongst others, one of the developed narrowband planar microstrip filtennas for the undertaken research work is a narrowband filtenna array for dual-band WLAN applications. Generally, it is difficult to achieve a planar antenna array with stable directional radiation patterns from 2.0–6.0 GHz, as gain is proportional to the radiation aperture [1-34]. Hence, a dual-band array structure is preferred due to its simple system configuration and cost minimisation. Although similar work has been proposed in [1-34] and [1-35], it is disadvantageous with respect to quite a number of factors. These include larger 2×2 array structures, single-band operation, final response not being sufficiently sharp and, most importantly, noise and spurious harmonics not being fully rejected. Similarly, [1-36] and [1-37] are unfavourable as well since the filters employed are of 3rd and 4th orders and, again, noise and spurious harmonics have not been fully rejected.

1.3: Aims and Objectives of the Research

The main aims of the undertaken research work presented in this thesis are as follows:

- [A-1] The optimal integration of filters and antennas with each other for the formation of filtennas for wireless transceivers of various applications.
- [A-2] The integration of filters within antennas for the purpose of rejecting specific frequency bands within the passband of the antennas.
- [A-3] The integration of filters with antennas for the purpose of suppressing any frequency harmonics, noise and fluctuations present near the passband of the antennas.
- [A-4] The implementation of reconfigurability, using existing and new reconfigurable elements, within the filtennas for the purpose of switching off or switching on the integrated filters.
- [A-5] The use of various fabrication technologies for the development of the filtennas.

In order to achieve the desired aims listed above, the undertaken research follows a list of steps and objectives:

- [O-1] A thorough literature review in the investigation of and in the most recent developments of filtennas, both with and without reconfigurable characteristics, for wireless transceivers of various applications.
- [O-2] Theoretical knowledge of the working of antennas and filters.
- [O-3] The development of Graphene based switches, by the aid of software programs, as a new reconfigurable element for use in reconfigurable filtennas.
- [O-4] The integration of Graphene based switches within filtennas for reconfigurability.
- [O-5] The integration of PIN diodes as an existing reconfigurable element for reconfigurability in filtennas and to provide a comparison and validation of the newly developed Graphene based switches.
- [O-6] The development of bandpass filters for UWB applications.
- [O-7] The implementation of reconfigurability in the developed UWB bandpass filters for the purpose of switching off or switching on any rejected frequency bands.

- [O-8] The development of broadband planar monopole antennas for S-band, ISM band and UWB applications.
- [O-9] The integration of resonators having filtering effects within the broadband planar monopole antennas for the purpose of rejecting any interfering and unwanted frequency bands within the wide passband of the antennas.
- [O-10] The implementation of reconfigurability in the broadband planar monopole filterennas for the purpose of switching off or switching on any rejected frequency bands.
- [O-11] The development of narrowband planar microstrip antennas for WLAN and 5G applications.
- [O-12] The use of pseudo-interdigital bandpass filters for integration with the narrowband planar microstrip antennas for the purpose of allowing the desired operating frequency of application and suppressing any additional frequency harmonics, noise and fluctuations near the operating frequency of the antennas.
- [O-13] The use of conventional PCB technology for the fabrication of the developed broadband planar monopole filterennas and the developed narrowband planar microstrip filterennas.
- [O-14] The use of circuit designer software programs and PCB prototyping machines for the conventional PCB fabrication technology.
- [O-15] The use of the newly developed inkjet-printing technology for the fabrication of the developed broadband planar monopole filterennas and the developed narrowband planar microstrip filterennas.
- [O-16] The use of flexible substrates, conductive metallic inks and inkjet printers for the filterennas fabricated using inkjet-printing technology.
- [O-17] The use of full-wave electromagnetic analysis and solvers for the development of the filterennas.
- [O-18] The use of network analysers for the measurement of the S-parameters of all the developed filterennas.
- [O-19] The use of anechoic chambers for the measurement of the radiation patterns, gain and efficiency of the developed filterennas.
- [O-20] The presentation and the comparison of the simulations and measurements of all the developed filterennas.
- [O-21] The in-depth study of the results obtained, including the return loss, distribution of surface currents, current density, radiation patterns, gain and efficiency, of all the developed filterennas.

1.4: Outline of the Thesis

This section summarises the contents and the organisation of this thesis which presents the research work carried out over a period of four years, from 2012 to 2016.

The work has been organised into seven main chapters. Each chapter is further divided into sections; which are further broken-down into subsections. Each main section is numbered “x.y”; where x and y denote the chapter number and the section number respectively. Each subsection is numbered “x.y.z”; where x and y mean the same thing as above and z represents the subsection number. For example, 1.2.3 means chapter 1, section 2, subsection 3.

All figures and tables in the thesis are captioned “Figure x.y–z” and “Table x.y–z” respectively; where x denotes the chapter number, y the section number and z the figure number (in the case of a figure) or the table number (in the case of a table). For example, Figure 1.2–3 or Table 1.2–3 means chapter 1, section 2, figure or table 3.

All equations and references in the thesis are numbered “(x.y)” and “[x-y]” respectively; where x represents the chapter number and y represents either the equation number (in the case of an equation) or the reference number (in the case of a reference). For example, (1.2) denotes chapter 1, equation 2 and [1-2] denotes chapter 1, reference 2.

Unless otherwise stated, all equations, constants, variables, numbers and quantities use SI units.

The outline of the seven main chapters — and each’s sections — is given below. For a quick navigation of each chapter and its sections and subsections in the thesis, the Table of Contents has been linked to the tree-like expandable/collapsible bookmarks of the electronic *pdf* file. If using the software program Adobe Reader™, these bookmarks can be accessed in the navigation pane by going to *View > Show/Hide > Navigations Panes > Bookmarks*.

Chapter 1 is an introductory chapter which is divided into five sections. The first section introduces the main topic of the thesis, i.e. filtennas. Alongside, the key elements adopted for the research work, i.e. inkjet-printing and Graphene, are also introduced. Additionally, within this section, several advantages of inkjet-printing technology and Graphene, which make them very attractive for wireless devices, are also provided. The second section lists the aims and objectives of the

undertaken research. The third section presents a thorough literature review of the previously published research work.

Chapter 2 presents the background theory relevant to the undertaken research work. The chapter is divided into three sections. The first section introduces basic microstrip transmission line theory. This includes the discontinuities present in microstrip transmission lines and the working of coupled microstrip transmission lines. The section also presents the design methods and the main design equations for each of these transmission lines. The second section presents the basic antenna theory. It also gives a brief description of the main parameters and properties of antennas. The design equation of these parameters are also provided.

Chapter 3 presents the development of reconfigurable bandpass filters for UWB applications. The chapter is divided into five sections and begins with an introduction of the UWB and the importance of UWB filters. It also highlights the interferences within the commercial UWB frequency range. Reconfigurability in wireless devices is then discussed: its importance and its usage. In the second section, a number of reconfigurable elements are reviewed, alongside their advantages and disadvantages. The undertaken research work uses two reconfigurable elements, i.e. Graphene based switches and PIN diodes. Hence, their behaviour and theoretical working have been discussed in deeper detail within the section. In the next two sections, two frequency reconfigurable bandpass filters for UWB applications are demonstrated. The first filter is implemented with a single notchband, for the WLAN band, which can be switched off or switched on as required. The second is a high linearity filter with the capability of an independently controlled dual notchband for the WiMAX and the C-band satellite communications system bands.

Chapter 4 presents the development of broadband single-element planar monopole filtennas. The chapter is divided into six sections. The first section introduces the topic, including the significance and use of broadband filtennas. The second section details the working mechanism and the design method of broadband planar monopole antennas. In addition, a single-element broadband planar monopole antenna is designed as an example. Parametric studies of the various parameters of the designed antenna have also been presented in the section. Following this, the third section presents a frequency reconfigurable filtenna for UWB applications with sharp dual notchband for the two WLAN bands and the fourth section presents a frequency reconfigurable filtenna for UWB applications with dual notchband for the WiMAX and WLAN bands. Expanding on this, a novel and compact filtenna, made using inkjet-printing technology on flexible substrate, with triple notchband for the

WiMAX, WLAN and satellite communications system bands is presented in the fifth section. Within this section, the justification for the choice of substrate employed for inkjet-printing technology is also provided.

Chapter 5 presents the development of broadband MIMO-element planar monopole filtennas. The chapter comprises three sections. It starts with a brief discussion of broadband planar microstrip filtennas with MIMO technology. In the second section, a compact MIMO filtenna for UWB applications with dual notchband for the WiMAX and WLAN bands is developed.

Chapter 6 presents the development of narrowband planar microstrip filtennas for wireless transceivers. The chapter is separated into six sections. It starts with a brief discussion of narrowband planar microstrip filtennas. The second section details the working mechanism, the design method and the equations required for narrowband planar microstrip antennas. A sample antenna is designed and studied thoroughly. The ensuing three sections demonstrate various types of narrowband planar microstrip filtennas. These include the design of a 1×2 filtenna array for dual-band 2.4 GHz and 5.8 GHz WLAN applications in the first, a single-band inkjet-printed filtenna for 5.8 GHz WLAN applications in the second and the last design is an inkjet-printed antenna operating at 28 GHz for 5G applications.

The last section of Chapters 1–6 lists the relevant references of its entire respective chapter.

Chapter 7 is split into three sections. The main conclusions of the undertaken research work are summarised in the first section. The second lists the contributions of this research work. Moreover, the potentials and suggestions for future work are identified in the last section.

Lastly, the thesis contains three appendices. In the first, all the datasheets of the devices relevant to the undertaken research work, i.e. NXP PIN diode BAP65-02, Fujifilm Dimatix Materials Inkjet Printer DMP-3000, DuPont Kapton flexible dielectric substrate and NovaCentrix Metalon silver nanoparticle ink JS-B80HV, are given. The second appendix presents the MATLAB code which was written and used for simulating and implementing reconfigurability using Graphene based switches. The last appendix lists the important and relevant publications authored during the course of the undertaken research work.

1.5: References

- [1-1] F. Ellinger, "Transceiver architectures," in *Radio Frequency Integrated Circuits and Technologies*, 2nd ed. Berlin, Germany: Springer, 2008, ch. 2, pp. 55.
- [1-2] M. Hösel, "Large-scale roll-to-roll fabrication of organic solar cells for energy production," PhD thesis, Department of Energy Conversion and Storage, Technical University of Denmark, Kongens Lyngby, Denmark, December 2013.
- [1-3] R. Das and P. Harrop, "Printed, Organic & Flexible Electronics Forecasts, Players & Opportunities 2016-2026," IDTechEx, Cambridge, United Kingdom, Report, May 2016.
- [1-4] K. S. Novoselov, A. K. Geim, S. V. Morozov, D. Jiang, Y. Zhang, S. V. Dubonos, I. V. Grigorieva, and A. A. Frisov, "Electric field effect in atomically thin carbon films," *Science*, vol. 306, no. 5696, pp. 666–669, October 2004.
- [1-5] A. K. Geim and K. S. Novoselov, "The rise of Graphene," *Nature Materials*, vol. 6, pp. 183–191, March 2007.
- [1-6] D. Mencarelli, M. Dragoman, L. Pierantoni, T. Rozzi, and F. Coccetti, "Design of a coplanar Graphene-based nano-patch antenna for microwave application," *IEEE MTT-S International Microwave Symposium Digest*, pp. 1–4, June 2013.
- [1-7] M. Dragoman, A. A. Muller, D. Dragoman, F. Coccetti, and R. Plana, "Terahertz antenna based on Graphene," *Journal of Applied Physics*, vol. 107, no. 10, pp. 104313–104313-3, May 2010.
- [1-8] M. Danaeifar, N. Granpayeh, A. Mohammadi, and A. Setayesh, "Graphene-based tunable terahertz and infrared band-pass filter," *Applied Optics Letters*, vol. 52, no. 22, pp. E68–E72, June 2013.
- [1-9] P-Y. Chen, C. Argyropoulos, and A. Alu, "Terahertz antenna phase shifters using integrally-gated transmission-lines," *IEEE Transactions on Antennas and Propagation*, vol. 61, no. 4, pp. 1528–1537, April 2013.
- [1-10] W. Menzel and P. Feil, "Ultra-wideband (UWB) filter with WLAN notch," *IEEE 36th European Microwave Conference*, pp. 595–598, September 2006.

- [1-11] H. Wang, K-W. Tam, S-K. Ho, W. Kang, and W. Wu “Design of ultra-wideband bandpass filters with fixed and reconfigurable notch bands using terminated cross-shaped resonators,” *IEEE Transactions on Microwave Theory and Techniques*, pp. 252–265, January 2014.
- [1-12] M. F. Karim, Y-X. Guo, Z. N. Chan, and L. C. Ong, “Miniaturized reconfigurable and switchable filter from UWB to 2.4 GHz WLAN using PIN diodes,” *IEEE MTT-S International Microwave Symposium Digest*, pp. 509–512, June 2009.
- [1-13] Y-H. Chun, H. Shaman, and J-S. Hong, “Switchable embedded notch structure for UWB bandpass filter,” *IEEE Microwave and Wireless Components Letters*, vol. 18, no. 9, pp. 590–592, September 2008.
- [1-14] W. Ahmad and D. Budimir, “Reconfigurable WLAN notch for UWB filters,” *IEEE 44th European Microwave Conference*, pp. 1536–1539, October 2014.
- [1-15] H. Wang, K-W. Tam, S-K. Ho, W. Kang, and W. Wu, “Design of ultra-wideband bandpass filters with fixed and reconfigurable notch bands using terminated cross-shaped resonators,” *IEEE Transactions on Microwave Theory and Techniques*, pp. 252–265, January 2014.
- [1-16] M. F. Karim, Y-X. Guo, Z. N. Chan, and L. C. Ong, “Miniaturized reconfigurable and switchable filter from UWB to 2.4 GHz WLAN using PIN diodes,” *IEEE MTT-S International Microwave Symposium Digest*, pp. 509–512, June 2009.
- [1-17] Y-H. Chun, H. Shaman, and J-S. Hong, “Switchable embedded notch structure for UWB bandpass filter,” *IEEE Microwave and Wireless Components Letters*, vol. 18, no. 9, pp. 590–592, September 2008.
- [1-18] K. Rabbi, L. Athukorala, C. Panagamuwa, J. C. Vardaxoglou, and D. Budimir, “Compact UWB bandpass filter with reconfigurable notched band,” *IET Electronics Letters*, vol. 49, no. 11, pp. 709–711, May 2013.
- [1-19] J. R. Kelly, P. S. Hall, and P. Gardner, “Band-notch UWB antenna incorporating a microstrip open-loop resonator,” *IEEE Transactions on Antennas and Propagation*, vol. 59, no. 8, pp. 3045–3048, August 2011.
- [1-20] Y. Sung, “Triple band-notched UWB planar monopole antenna using a modified H-shaped resonator,” *IEEE Transactions on Antennas and Propagation*, vol. 61, no. 2, pp. 278–280, February 2013.
- [1-21] C. Lin, P. Jin, and R. Ziolkowski, “Single, dual and tri-band-notched UWB antennas using CLL resonators,” *IEEE Transactions on Antennas and Propagation*, vol. 60, no. 1, pp. 102–109, January 2012.

- [1-22] J. Y. Siddiqui, C. Saha, and Y. Antar, "Compact SRR loaded UWB circular monopole antenna with frequency notch characteristics," *IEEE Transactions on Antennas and Propagation*, vol. 62, no. 8, pp. 4015–4020, August 2014.
- [1-23] T. Kaiser, F. Zheng, and E. Dimitrov, "An overview of UWB systems with MIMO," *Proceedings of the IEEE*, vol. 97, no. 2, pp. 285–312, February 2009.
- [1-24] J-F. Li, Q-X. Chu, Z-H. Li, and X-X. Xia, "Compact dual band-notched UWB MIMO antenna with high isolation," *IEEE Transactions on Antennas and Propagation*, vol. 61, no. 9, pp. 4759–4766, September 2013.
- [1-25] X-L. Liu, Z-D. Wang, Y-Z. Yin, J. Ren, and J-J. Wu, "A compact UWB MIMO antenna using QSCA for high isolation," *IEEE Antennas and Wireless Propagation Letters*, vol. 13, pp. 1497–1500, 2014.
- [1-26] J. Ren, W. Hu, Y. Yin, and R. Fan, "Compact printed MIMO antenna for UWB applications," *IEEE Antennas and Wireless Propagation Letters*, vol. 13, pp. 1517–1520, 2014.
- [1-27] N. K. Kiem, H. N. B. Phuong, Q. N. Hieu, and D. N. Chien, "A compact printed 4x4 MIMO-UWB antenna with WLAN band rejection," *IEEE International Symposium on Antennas and Propagation and North American Radio Science Meeting*, pp. 2245–2246, July 2013.
- [1-28] Y. Li, W. Li, C. Liu, and T. Jiang, "Two UWB-MIMO antennas with high isolation using sleeve coupled stepped impedance resonators," *IEEE Asia-Pacific Conference on Antennas and Propagation*, pp. 21–22, August 2012.
- [1-29] B. S. Cook and A. Shamim, "Inkjet printing of novel wideband and high gain antennas on low-cost paper substrate," *IEEE Transactions on Antennas and Propagation*, vol. 60, no. 9, pp. 4148–4156, September 2012.
- [1-30] A. R. Maza, B. Cook, G. Jabbour, and A. Shamim, "Paper-based inkjet-printed ultra-wideband fractal antennas," *IET Microwaves, Antennas & Propagation*, vol. 6, no. 12, p. 1366–1373, April 2012.
- [1-31] G. Shaker, S. Safavi-Naeini, N. Sangary, and M. M. Tentzeris, "Inkjet printing of ultrawideband antennas on paper-based substrates," *IEEE Antennas and Wireless Propagation Letters*, vol. 10, pp. 111–114, 2011.
- [1-32] H. R. Khaleel, "Design and fabrication of compact inkjet printed antennas for integration within flexible and wearable electronics," *IEEE Transactions*

- on Components, Packaging and Manufacturing Technology*, vol. 4, no. 10, pp. 1722–1728, October 2014.
- [1-33] D. Unnikrishnan, D. Kaddour, S. Tedjini, E. Bihar, and M. Saadaoui, “CPW-fed inkjet printed UWB antenna on ABS-PC for integration in molded interconnect devices technology,” *IEEE Antennas and Wireless Propagation Letters*, vol. 14, pp. 1125–1128, 2015.
- [1-34] W. K. Toh, X. Qing, and Z. Chen, “A planar dualband antenna array,” *IEEE Transactions on Antennas and Propagation*, vol. 59, no. 3, pp. 833–838, March 2011.
- [1-35] C. Lin and S. Chung, “A filtering microstrip antenna array,” *IEEE Transactions on Microwave Theory and Techniques*, vol. 59, no. 11, pp. 2856–2863, November 2011.
- [1-36] M. Rivera, J. Costantine, Y. Tawk, and C. Christodoulou, “Failure detection and correction in switch reconfigurable antenna arrays,” *IEEE International Symposium on Antennas and Propagation and North American Radio Science Meeting*, pp. 976–979, 2011.
- [1-37] S. Dasgupta, B. Gupta, and H. Saha, “Development of circular microstrip patch antenna array for rectenna application,” *IEEE Annual India Conference INDICON*, pp. 1–6, December 2010.

Chapter 2:

Background

2.1: Microstrip Transmission Line Theory

2.1.1: Introduction

The microstrip transmission line is one of the most popular types of planar transmission lines. This is principally for the reasons that it can be easily integrated with other active and passive microwave devices and that it can be fabricated using photolithographic processes.

Furthermore, the characterisation of discontinuity reactance is necessary in the case of microstrip transmission lines. Discontinuities in microstrip transmission lines involve a sudden transformation in the dimensions of the conductor; which results in alterations of the electric field distributions and the magnetic field distributions. Most of the discontinuities present in microstrip transmission lines contribute to parasitic reactance.

Therefore, this chapter presents the procedure and the equations required for the design of microstrip transmission lines and their discontinuities.

2.1.2: Microstrip Transmission Lines

Microstrip transmission lines comprise a conductor printed atop a grounded dielectric substrate. The cross-sectional view of the geometry of a microstrip transmission line is illustrated in Figure 2.1–1. The properties of the conductor in conjunction with the dielectric substrate define the signal transmission characteristics of the transmission line.

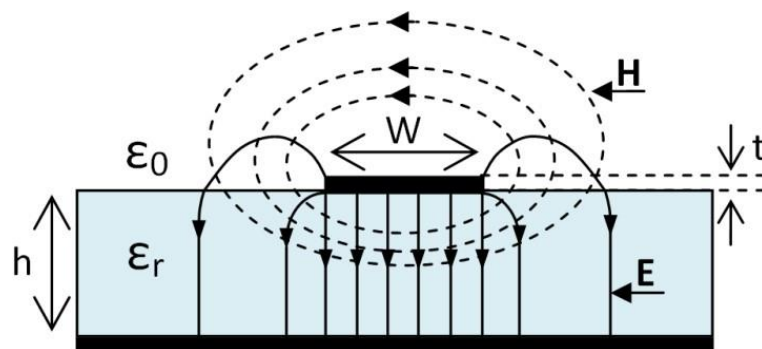


Figure 2.1–1: Cross-sectional view of microstrip transmission lines with their corresponding electric field (solid lines) and magnetic field (dashed lines).

Due to the nature of microstrip transmission lines, the electromagnetic fields exist not only within the dielectric substrate, but they also propagate into the air above. The relative dielectric permittivity of the dielectric substrate, ϵ_r , is almost always greater than unity. This causes the fields in the air to propagate faster than the fields within the dielectric substrate. Therefore, microstrip transmission lines are unable to support a pure transverse electromagnetic wave.

The comparably weak longitudinal field elements allow a quasi-static approximation to be applied in characterising the microstrip transmission lines up to a few GHz [2-1]. This technique takes into account the propagation of a pure transverse electromagnetic mode which, in turn, greatly simplifies the related calculations.

Once the capacitance per unit length with and without the dielectric — C_d and C_0 respectively — are known, the effective dielectric constant, ϵ_{eff} , the characteristic impedance in free space, Z_0 , the phase constant, β , the angular frequency, ω , and the phase velocity, v_p , can be calculated using (2.1)–(2.4) given below. In these equations, “ c ” is the speed of light.

$$\epsilon_{eff} = \frac{C_d}{C_0} \quad (2.1)$$

$$Z_0 = \frac{1}{c\sqrt{C_d C_0}} \quad (2.2)$$

$$\beta = \frac{\omega}{c} \left(\frac{C_d}{C_0} \right) \quad (2.3)$$

$$v_p = c \sqrt{\frac{C_0}{C_d}} \quad (2.4)$$

2.1.3: Analysis Formulas for Microstrip Transmission Lines

A) Microstrip Line-fed Structures

For microstrip line-fed structures, such as the one shown in Figure 2.1–1, the closed form expressions for the effective dielectric constant, ϵ_{eff} , and the characteristic impedance, Z_0 , are given in (2.5)–(2.8) below. These expressions provide an accuracy of more than 1 %. In these equations, “ W ” is the width of the microstrip

transmission line, “ h ” is the height of the dielectric substrate and “ η ” is the wave impedance in free space and has a value of $120\pi \Omega$.

for narrow microstrip transmission lines, i.e. when $\frac{W}{h} < 1$, use (2.5) and (2.6):

$$\epsilon_{eff} = \left(\frac{\epsilon_r + 1}{2} \right) + \left[\left(\frac{\epsilon_r - 1}{2} \right) \times \left\{ \left(1 + \frac{12h}{W} \right)^{-\frac{1}{2}} + 0.04 \left(1 - \frac{W}{h} \right)^2 \right\} \right] \quad (2.5)$$

$$Z_0 = \left(\frac{\eta}{2\pi\sqrt{\epsilon_{eff}}} \right) \times \left[\ln \left(\frac{8h}{W} + \frac{W}{4h} \right) \right] \quad (2.6)$$

for wide microstrip transmission lines, i.e. when $\frac{W}{h} > 1$, use (2.7) and (2.8):

$$\epsilon_{eff} = \left(\frac{\epsilon_r + 1}{2} \right) + \left[\left(\frac{\epsilon_r - 1}{2} \right) \times \left\{ \left(1 + \frac{12h}{W} \right)^{-\frac{1}{2}} \right\} \right] \quad (2.7)$$

$$Z_0 = \left(\frac{\eta}{\sqrt{\epsilon_{eff}}} \right) \times \left[\frac{W}{h} + 1.393 + 0.677 \ln \left(\frac{W}{h} + 1.444 \right) \right]^{-1} \quad (2.8)$$

B) CPW-fed Structures

A CPW feed comprises a conductor printed atop an ungrounded dielectric substrate. The conductor is also called the signal transmission line or the signal trace in some literature. On both sides of the signal transmission line, at a fixed and equal gap, there are other transmission lines which act as the ground planes for the structure. The cross-sectional view of the geometry of a CPW-fed structure is illustrated in Figure 2.1–2.

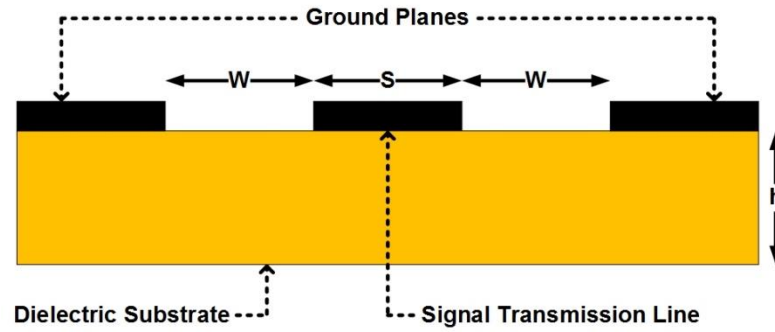


Figure 2.1-2: Cross-sectional view of CPW-fed structures.

The effective dielectric constant, ϵ_{eff} , and the characteristic impedance, Z_0 , of the CPW-fed structures, such as the one shown above, can be calculated using (2.9) and (2.10) respectively. The detailed explanation and derivation of these equations can be found in [2-2].

$$\epsilon_{eff} = 1 + \left[\frac{\epsilon_r - 1}{2} \times \frac{K(k_1)}{K(k'_1)} \times \frac{K(k'_0)}{K(k_0)} \right] \quad (2.9)$$

$$Z_0 = \frac{30\pi}{\sqrt{\epsilon_{eff}}} \times \frac{K(k'_0)}{K(k_0)} \quad (2.10)$$

where ϵ_r is the relative dielectric constant and k_1 , k'_1 , k_0 and k'_0 can be calculated using (2.11)–(2.14).

$$k_1 = \frac{\sinh\left(\frac{\pi S}{4h}\right)}{\sinh\left(\frac{\pi S + 2\pi W}{4h}\right)} \quad (2.11)$$

$$k'_1 = \sqrt{1 - (k_1)^2} \quad (2.12)$$

$$k_0 = \frac{S}{S + 2W} \quad (2.13)$$

$$k'_0 = \sqrt{1 - (k_0)^2} \quad (2.14)$$

where h is the height of the dielectric substrate, S is the width of the signal transmission line and W is the width of each gap between the signal transmission line and the two ground planes.

2.1.4: Synthesis Formulas for Microstrip Transmission Lines

The approximate expressions for the ratio of the microstrip transmission line width to the dielectric substrate height, W/h , in terms of the characteristic impedance, Z_0 , and the relative dielectric permittivity, ϵ_r , were derived in [2-3] and are given by (2.15)–(2.18) below.

when $\frac{W}{h} < 2$, use (2.15) and (2.16):

$$\frac{W}{h} = \frac{8e^A}{e^{2A} - 2} \quad (2.15)$$

$$A = \left[\left(\frac{Z_0}{60} \right) \times \left(\sqrt{\frac{\epsilon_r + 1}{2}} \right) \right] + \left[\left(\frac{\epsilon_r - 1}{\epsilon_r + 1} \right) \times \left(0.23 + \frac{0.11}{\epsilon_r} \right) \right] \quad (2.16)$$

when $\frac{W}{h} > 2$, use (2.17) and (2.18):

$$\frac{W}{h} = \frac{2}{\pi} \left[(B - 1) - \ln(2B - 1) + \left\{ \left(\frac{\epsilon_r - 1}{2\epsilon_r} \right) \left(\ln(B - 1) + 0.39 - \frac{0.61}{\epsilon_r} \right) \right\} \right] \quad (2.17)$$

$$B = \frac{60\pi^2}{Z_0\sqrt{\epsilon_r}} \quad (2.18)$$

Using the equations given above, the characteristic impedance, Z_0 , was plotted as a function of the ratio of the microstrip transmission line width to the dielectric substrate height, W/h , for various sample values of the relative dielectric constant, ϵ_r , [2-4] and is given in Figure 2.1–3. Similarly, the effective dielectric constant, ϵ_{eff} , was plotted as a function of the ratio of the microstrip transmission line width to the

dielectric substrate height, W/h , for various sample values of the relative dielectric constant, ϵ_r , [2-4] and is given in Figure 2.1–4.

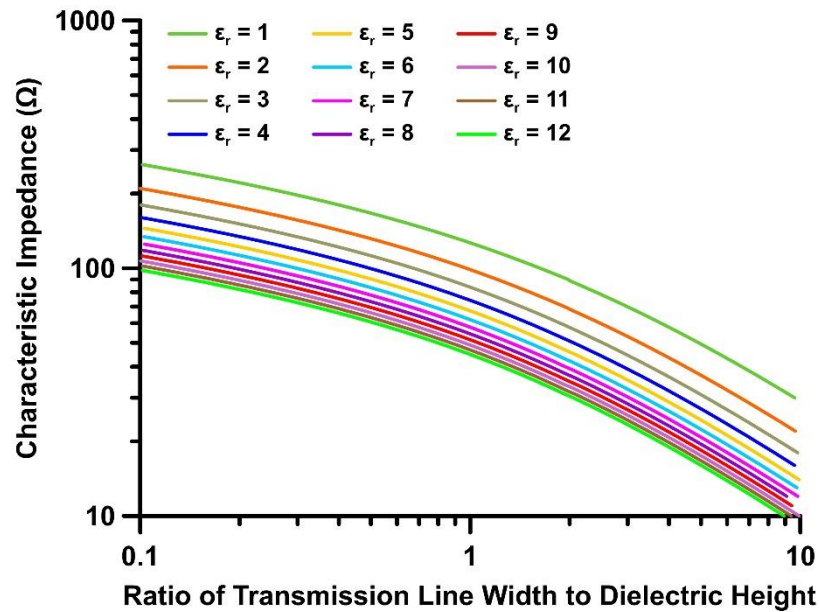


Figure 2.1–3: Characteristic impedance as a function of the width to height ratio for various values of the relative dielectric constant.

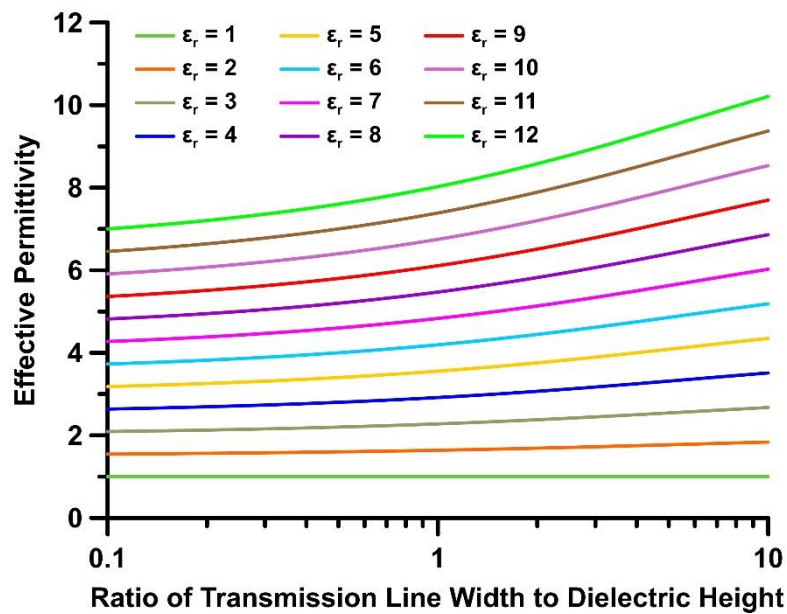


Figure 2.1–4: Effective dielectric constant as a function of the width to height ratio for various values of the relative dielectric constant.

Although filtennas can be analysed manually using the electromagnetic theory, practically manual analysis is a very complex and tedious task. This is because the

theory is the mathematical formulation of the propagation of electromagnetic waves and it is concerned with interrelated electric and magnetic fields as well as the time-varying effects between two fields. In modern times, the advancement of technology and the prevalent availability of powerful computing resources and abundant memory resources has led to an extensive use of full-wave electromagnetic analysis software programs which employ various numerical methods in their programming code. These numerical methods solve Maxwell's equations for the respective parameters of microstrip transmission lines by making use of the specified boundary conditions. The calculations within these numerical methods are usually performed for several frequency points and also take into account all the field components at each point. Therefore, these full-wave electromagnetic analysis software programs and their respective methods are able to account for even the minute dispersive effects of microstrip transmission lines and provide extremely accurate results.

Microstrip transmission lines comparatively have a high loss overall. The individual components of the overall high loss are the conductor loss, the dielectric loss and the radiation loss. Because of the finite conductance of the trace metallisation, conductors dissipate power as heat. Due to the applied field distributions, the vibration of the atoms within the dielectric substrate is such that it gives rise to heat. The dielectric loss is caused by this heat. Additionally, since the microstrip transmission line is a semi-open structure, any radiation is unrestricted to propagate away or to induce currents in the metallic vicinity. This causes the radiation loss (also named housing loss). Of the aforementioned three types of losses, the major ones are the conductor loss and the dielectric loss.

Generally, conductor loss is the main contributor to the overall loss experienced by microstrip transmission lines. Moreover, it is worsened at high frequencies owing to the skin effect [2-5]. In the radio and microwave frequency range, the current is no longer evenly distributed across the cross-section of the signal trace. Owing to the eddy currents induced within the signal trace, the signal current is concentrated near the edges of the signal trace and ceases to exist in the centre of the conductor. This, in turn, reduces the cross-sectional area of the signal trace at high frequencies and increases the resistance of the signal trace. This results in an increase in the attenuation constant of the transmission line. An accurate result of the attenuation constant can be attained if the full characteristics of the geometry of the signal trace and the field distributions are known [2-6]. However, these calculations are long and complex. Alternatively, other procedures, such as the perturbation method [2-1] and the Wheel's incremental inductance formula [2-6] as given by (2.19), can be used to

attain an approximate value of the conductor attenuation constant, α_c , in dB per unit length.

$$\alpha_c = \frac{R_s}{2Z_0} \sqrt{\frac{\mu_0}{\epsilon}} \frac{dZ_0}{dx} \quad (2.19)$$

where R_s is the surface resistance (skin resistance) and is given by (2.20), Z_0 is the characteristic impedance, W is the width of the signal trace, μ_0 is the permeability of free space and has a value of $4\pi \times 10^{-7}$ H/m and x is the distance into the signal trace.

$$R_s = \sqrt{\frac{\omega\mu_0}{2\sigma}} \quad (2.20)$$

where ω is the angular frequency, μ_0 is the permeability of free space and has a value of $4\pi \times 10^{-7}$ H/m and σ is the conductivity of the material used as the conductor.

Due to the widespread accessibility and use of full-wave electromagnetic analysis software programs, it is possible to obtain the attenuation constants from a matched microstrip transmission line, one by one, from simulations using (2.21).

For instance, when the conductor attenuation constant is to be calculated, the condition that the loss factor of the dielectric substrate is zero, i.e. $\tan \delta = 0$, is assumed. Similarly, so as to calculate the dielectric attenuation constant, the conductivity of the metallisation is assumed to be infinite, i.e. $\sigma = \infty$.

The total attenuation constant can be obtained by the summation of these individual attenuation constants. The obtained net attenuation is required to determine the unloaded quality factors of resonators; which, in turn, is inversely proportional to the power dissipation within resonators.

$$\alpha_{c/d} = \frac{-\ln|S_{21}|}{z} \quad (2.21)$$

2.1.5: Discontinuities in Microstrip Transmission Lines

Discontinuities in microstrip transmission lines are generally experienced during the design of practical filtennas. The typical discontinuities include changes/steps in the widths, open-ends, gaps, bends and junctions. These, alongside their respective equivalent circuits, are illustrated in Figure 2.1–5. Discontinuities in microstrip transmission lines generate parasitic reactances which effect the field distributions of the transmission lines. The transformed electric field distribution can be characterised by an equivalent capacitance and the transformed magnetic field distribution can be characterised by an equivalent inductance.

The equivalent circuit model of the region containing the discontinuity can be modelled accurately by deducing the effective dimensions and these, in turn, being taken into account during the filtenna design with full-wave electromagnetic simulations.

A) Steps in Width

The discontinuity named “steps in width” is formed on the junction of two transmission lines which have different widths.

The equivalent circuit model of this discontinuity consists of a shunt capacitance, C , in the plane of the junction and two series inductances, L_1 and L_2 , representing the two transmission lines on either side of the shunt capacitance. This is shown in Figure 2.1–5 (a) [2-5].

For a symmetrical step, approximate values for the capacitance, C , in pF and the inductances, L_1 and L_2 , in nH can be by calculated using the formulas from [2-3] as given in (2.22)–(2.26) below.

$$C = (0.00137h) \left(\frac{\sqrt{\epsilon_{eff1}}}{Z_{01}} \right) \left(1 - \frac{W_2}{W_1} \right) \left(\frac{\epsilon_{eff1} + 0.3}{\epsilon_{eff1} - 0.258} \right) \left(\frac{\frac{W_1}{h} + 0.264}{\frac{W_1}{h} + 0.8} \right) \quad (2.22)$$

$$L_1 = L \left(\frac{L_{w1}}{L_{w1} + L_{w2}} \right) \quad (2.23)$$

$$L_2 = L \left(\frac{L_{w2}}{L_{w1} + L_{w2}} \right) \quad (2.24)$$

$$L = (0.000987h) \times \left[1 - \left(\frac{Z_{01}}{Z_{02}} \sqrt{\frac{\epsilon_{eff1}}{\epsilon_{eff2}}} \right) \right]^2 \quad (2.25)$$

$$L_{wi} = \frac{Z_{0i} \sqrt{\epsilon_{effi}}}{c} \quad (2.26)$$

where h is the height of the dielectric substrate in μm , W_i for $i = 1$ and 2 are the widths of the first and the second transmission lines having widths W_1 and W_2 respectively, ϵ_{effi} for $i = 1$ and 2 are the effective dielectric constants corresponding to the width W_i , Z_{0i} for $i = 1$ and 2 are the characteristic impedances corresponding to the width W_i , L_{wi} for $i = 1$ and 2 are the inductances per unit length of the transmission lines corresponding to the width W_i and c is the speed of light.

B) Open-ends

The discontinuity named “open-ends” is formed when a transmission line ends in an open-circuit.

The equivalent circuit model of this discontinuity consists of an open-circuit capacitance, C_p . This is shown in Figure 2.1–5 (b) [2-5]. The open-circuit capacitance causes fringing effects [2-7] and, hence, there is an apparent increase by a margin of Δl in the length of the transmission line.

The approximate values for the open-circuit capacitance, C_p , and the increase in the length, Δl , can be calculated using the formulas from [2-3] as given in (2.27) and (2.28) respectively. For $W/h \geq 0.2$ and $2 \leq \epsilon_r \leq 50$, these equations give results which are within 4% of the numerical results.

$$\Delta l = (0.412h) \times \left(\frac{\epsilon_{eff} + 0.3}{\epsilon_{eff} - 0.258} \right) \times \left(\frac{\frac{W}{h} + 0.264}{\frac{W}{h} + 0.8} \right) \quad (2.27)$$

$$C_p = \Delta l \times \frac{\sqrt{\epsilon_{eff}}}{cZ_0} \quad (2.28)$$

where ϵ_r is the relative dielectric constant of the dielectric substrate, h is the height of the dielectric substrate, ϵ_{eff} is the effective dielectric constant, W is the width of the transmission line, c is the speed of light and Z_0 is the characteristic impedance.

C) Gaps

The discontinuity named “gaps” is formed when there is gap between two transmission lines.

The equivalent circuit model of this discontinuity can be denoted by a pi-network consisting of two capacitances, C_p , and a capacitance, C_g . This is shown in Figure 2.1–5 (c) [2-5].

The corresponding susceptances can be obtained from these three equivalent capacitances. If the two microstrip transmission lines are identical, then a plane of circuit symmetry exists and it can be analysed using even and odd mode analysis. In the even mode, the incident waves along the transmission lines are symmetrical and equal, i.e. equal in magnitude and phase, and in the odd mode, they are anti-symmetrical and opposite, i.e. equal in magnitude, but 180° out of phase. The even and odd mode is expressed by C_e and C_o respectively. The capacitances of the equivalent circuit model, C_p and C_g , can be then determined once the values for the C_e and C_o are known. These can be calculated using the formulas from [2-3] as given in (2.29)–(2.38).

$$C_p = 0.5C_e \quad (2.29)$$

$$C_g = 0.5C_o - 0.25C_e \quad (2.30)$$

where C_e and C_o can be calculated using (2.31) and (2.32) respectively.

$$C_e = (12W) \times \left(\frac{\epsilon_r}{9.6}\right)^{0.9} \times \left(\frac{S}{W}\right)^{m_e} \times (e^{k_e}) \quad (2.31)$$

$$C_o = (W) \times \left(\frac{\epsilon_r}{9.6}\right)^{0.8} \times \left(\frac{S}{W}\right)^{m_o} \times (e^{k_o}) \quad (2.32)$$

where m_o and k_o can be calculated using (2.33)–(2.34) for various values of S/W and m_e and k_e can be calculated using (2.35)–(2.38) for various values of S/W .

when $0.1 \leq s/W \leq 1.0$, use (2.33) and (2.34):

$$m_o = \frac{W}{h} \times \left[\left\{ 0.619 \log \left(\frac{W}{h} \right) \right\} - 0.3853 \right] \quad (2.33)$$

$$k_o = 4.26 - \left[1.453 \log \left(\frac{W}{h} \right) \right] \quad (2.34)$$

when $0.1 \leq s/W \leq 0.3$, use (2.35) and (2.36):

$$m_e = 0.8675 \quad (2.35)$$

$$k_e = 2.043 \times \left(\frac{W}{h} \right)^{0.12} \quad (2.36)$$

when $0.3 \leq s/W \leq 1.0$, use (2.37) and (2.38):

$$m_e = \frac{1.565}{\left(\frac{W}{h} \right)^{0.16}} - 1 \quad (2.37)$$

$$k_e = 1.97 - \frac{0.03h}{W} \quad (2.38)$$

D) Bends

The discontinuity named “bends” is formed when a transmission line changes direction by a margin of 90° .

The equivalent circuit model of this discontinuity can be denoted by a T-network consisting of a shunt capacitance, C , and two series inductances, L , on either side of the shunt capacitance. This is shown in Figure 2.1–5 (d) [2-5].

The approximate values for the shunt capacitance, C , in pF and the series inductances, L , in nH can be by calculated using the formulas from [2-5] as given in (2.39)–(2.40) and (2.41) respectively.

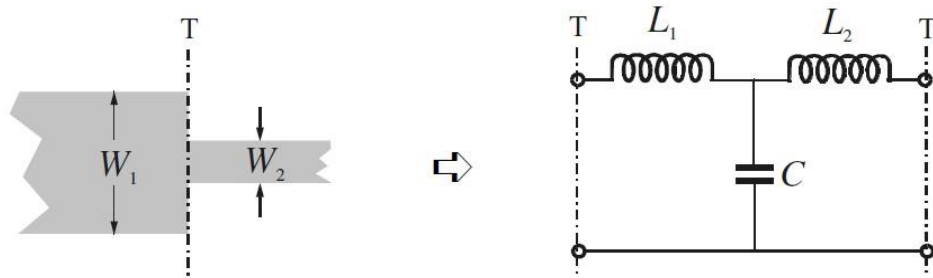
when $\frac{W}{h} < 1$, use (2.39):

$$C = \frac{\left\{ \frac{W}{h} (14\epsilon_r + 12.5) \right\} - 18\epsilon_r + 2.25}{\sqrt{\frac{W}{h}}} + \frac{0.02\epsilon_r}{\frac{W}{h}} \quad (2.39)$$

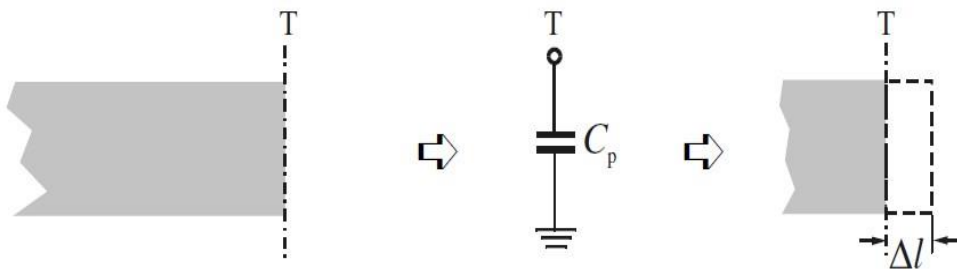
when $\frac{W}{h} \geq 1$, use (2.40):

$$C = W \left[\left\{ \frac{W}{h} (9.5\epsilon_r + 1.25) \right\} + 5.2\epsilon_r + 7 \right] \quad (2.40)$$

$$L = 100h \times \left[\left(4 \sqrt{\frac{W}{h}} \right) - 4.21 \right] \quad (2.41)$$



(a)



(b)

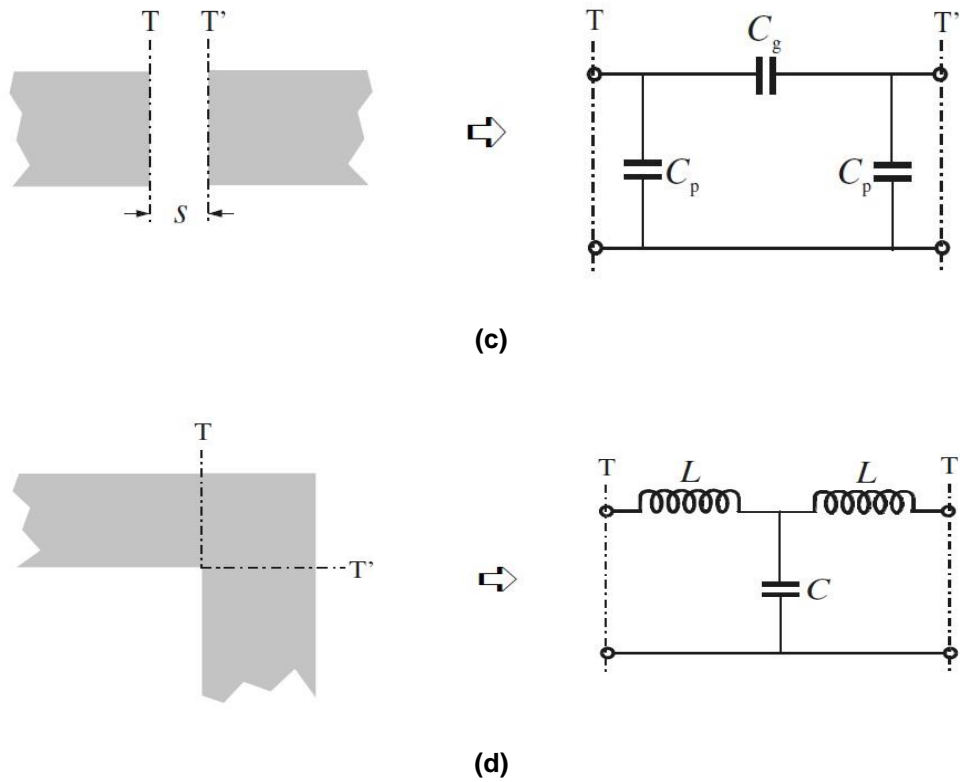


Figure 2.1–5: Diagrams and equivalent circuit models of various microstrip discontinuities: (a) step, (b) open-end, (c) gap and (d) bend.

2.1.6: Coupled Microstrip Transmission Lines

When a pair microstrip transmission lines are placed parallel to each other and are close enough, the signals from one transmission line are coupled to the other. The cross-sectional views of a pair of transmission lines which are coupled with each other, alongside their corresponding electromagnetic fields in the even mode and odd mode excitations, are shown in Figure 2.1–6.

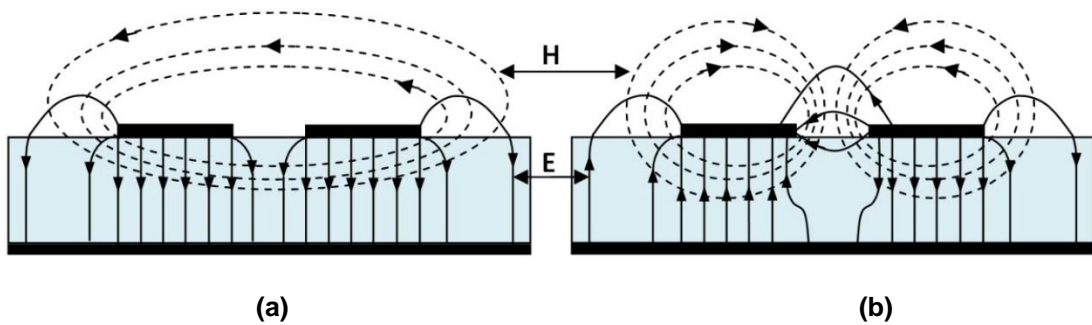


Figure 2.1–6: Cross-sectional views of coupled microstrip transmission lines with their corresponding electromagnetic field distributions during the (a) even mode and (b) odd mode excitations.

Generally, any voltage or current excitation on the transmission lines can be broken down into its even and odd components. In the even mode, the coupling of the signals happens through the magnetic field and in the odd mode, it happens through the electric field.

Although both types of fields contribute towards the coupling of the signals, depending on the excitation of the transmission lines, they could combine in either a constructive way or a destructive way [2-5]. Therefore, the coupling strength observed is because of the interaction and the merging of these two effects.

In coupled microstrip transmission lines, there is a difference in the phase velocities of the propagation of the even mode and the odd mode. The reason for the difference is the different field distributions exhibited by each mode.

An equivalent lumped element circuit model of a pair of coupled microstrip transmission lines is shown in Figure 2.1–7. In the model, I_1 , V_1 , L_1 and C_1 , are the current, voltage, self-inductance per unit length and shunt-capacitance per unit length respectively of the first (top) transmission line. I_2 , V_2 , L_2 and C_2 , are the current, voltage, self-inductance per unit length and shunt-capacitance per unit length respectively of the second (bottom) transmission line. L_m and C_m are the mutual inductance per unit length and mutual capacitance per unit length respectively between the two transmission lines. The terminal voltages and the currents in general of the transmission lines can be defined by the differential equations (2.42)–(2.45).

$$\frac{dV_1}{dz} = L_1 \frac{dI_1}{dt} + L_m \frac{dI_2}{dt} \quad (2.42)$$

$$\frac{dV_2}{dz} = L_2 \frac{dI_2}{dt} + L_m \frac{dI_1}{dt} \quad (2.43)$$

$$\frac{dI_1}{dz} = C_{1g} \frac{dV_1}{dt} + C_m \frac{d(V_1 - V_2)}{dt} \quad (2.44)$$

$$\frac{dI_2}{dz} = C_{2g} \frac{dV_2}{dt} + C_m \frac{d(V_2 - V_1)}{dt} \quad (2.45)$$

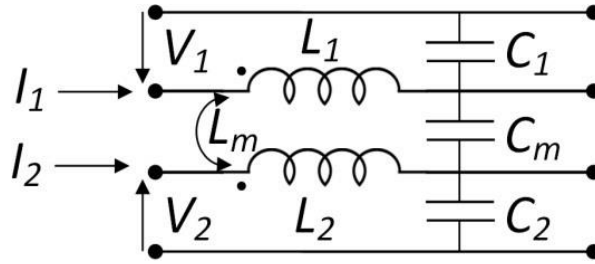


Figure 2.1-7: Equivalent lumped element circuit model of coupled microstrip transmission lines.

For an even mode excitation, the conditions that the terminal voltage $V_1 = V_2 = V$ and that the currents $I_1 = I_2 = I$ are assumed. When these two conditions are applied to (2.42)–(2.45) above, they give rise to (2.46)–(2.49).

$$\frac{dV}{dz} = L_1 \frac{dI}{dt} + L_m \frac{dI}{dt} = (L_1 + L_m) \frac{dI}{dt} \quad (2.46)$$

$$\frac{dV}{dz} = L_2 \frac{dI}{dt} + L_m \frac{dI}{dt} = (L_2 + L_m) \frac{dI}{dt} \quad (2.47)$$

$$\frac{dI}{dz} = C_{1g} \frac{dV}{dt} = (C_1 - C_m) \frac{dV}{dt} \quad (2.48)$$

$$\frac{dI}{dz} = C_{2g} \frac{dV}{dt} = (C_2 - C_m) \frac{dV}{dt} \quad (2.49)$$

where $C_1 = C_{1g} + C_m$ is the self-capacitance per unit length of the first transmission line and $C_2 = C_{2g} + C_m$ is the self-capacitances per unit length of the second transmission line.

The equivalent inductance and the equivalent capacitance in the even mode is $L_1 + L_m$ and $C_1 - C_m$ respectively for the first transmission line. Similarly, the equivalent inductance and the equivalent capacitance in the even mode is $L_2 + L_m$ and $C_2 - C_m$ respectively for the second transmission line.

Following this, the even mode characteristic impedance, Z_{e1} , of the first transmission line can be calculated by (2.50) and of the second transmission line, Z_{e2} , can be calculated by (2.51).

$$Z_{e1} = \sqrt{\frac{L_1 + L_m}{C_1 - C_m}} \quad (2.50)$$

$$Z_{e2} = \sqrt{\frac{L_2 + L_m}{C_2 - C_m}} \quad (2.51)$$

Similar to the conditions applied for an even mode excitation, for an odd excitation, the conditions that the terminal voltage $V_1 = -V_2 = V$ and that the currents $I_1 = -I_2 = I$ are assumed. When these conditions are applied to (2.42)–(2.45), they result in (2.52)–(2.55).

$$\frac{dV}{dz} = L_1 \frac{dI}{dt} - L_m \frac{dI}{dt} = (L_1 - L_m) \frac{dI}{dt} \quad (2.52)$$

$$\frac{dV}{dz} = L_2 \frac{dI}{dt} - L_m \frac{dI}{dt} = (L_2 - L_m) \frac{dI}{dt} \quad (2.53)$$

$$\frac{dI}{dz} = C_{1g} \frac{dV}{dt} + C_m \frac{dV}{dt} + C_m \frac{dV}{dt} = (C_1 + C_m) \frac{dV}{dt} \quad (2.54)$$

$$\frac{dI}{dz} = C_{2g} \frac{dV}{dt} + C_m \frac{dV}{dt} + C_m \frac{dV}{dt} = (C_2 + C_m) \frac{dV}{dt} \quad (2.55)$$

where $C_1 = C_{1g} + C_m$ is the self-capacitance per unit length of the first transmission line and $C_2 = C_{2g} + C_m$ is the self-capacitances per unit length of the second transmission line.

From these expressions, i.e. (2.52)–(2.55), the equivalent inductance and the equivalent capacitance in the odd mode are obtained. The equivalent inductance and the equivalent capacitance in the odd mode is $L_1 - L_m$ and $C_1 + C_m$ respectively for the first transmission line. Likewise, the equivalent inductance and the equivalent capacitance in the odd mode is $L_2 - L_m$ and $C_2 + C_m$ respectively for the second transmission line.

Following this, the odd mode characteristic impedance, Z_{o1} , of the first transmission line can be calculated by (2.56) and of the second transmission line, Z_{o2} , can be calculated by (2.57).

$$Z_{o1} = \sqrt{\frac{L_1 - L_m}{C_1 + C_m}} \quad (2.56)$$

$$Z_{o2} = \sqrt{\frac{L_2 - L_m}{C_2 + C_m}} \quad (2.57)$$

Another main parameter involved in the design of coupled microstrip transmission lines is the coupling coefficient. The coupling coefficient describes the interaction of two transmission lines and is expressed by the ratio of the coupled energy to the stored energy.

The normalised electric coupling coefficient is a function of the mutual capacitance per unit length between the two transmission lines and the self-capacitance per unit length of both transmission lines. Whereas, the normalised magnetic coupling coefficient is a function of the mutual inductance per unit length between the two transmission lines and the self-inductance per unit length of both transmission lines. Therefore, these functions of the normalised electric coupling coefficient, K_E , and the normalised magnetic coupling coefficient, K_M , can be given by (2.58) and (2.59) respectively.

$$K_E = \frac{C_m}{\sqrt{C_1 C_2}} \quad (2.58)$$

$$K_M = \frac{L_m}{\sqrt{L_1 L_2}} \quad (2.59)$$

2.1.7: Skin Effect in Microstrip Transmission Lines

Skin effect is a phenomena where an alternating current flows mostly near the outer surface of an electrical conductor. Consequently, the current density is largest near the surface of the electric conductor — and decreases with greater depths in the conductor. The level at which this flow takes place — i.e. where the skin effect is valid — is called the skin depth. Most — almost 98 % — of the current will flow within a layer 2–3 times the skin depth from the surface. This tendency is distinct from that of a direct current; which will be distributed evenly across the cross-

section of the conductor. In other words, skin depth is also a measure of the amount of penetration of a plane electromagnetic wave into a material.

Skin effect becomes more and more apparent as the frequency increases. The effect causes the effective resistance of the electric conductor to increase at higher frequencies where the skin depth is smaller; thus reducing the effective cross-section of the conductor [2-8].

Skin effect occurs in all wires, cables and any metal object that conducts a signal; including metallisations used for microstrip transmission lines. For this reason, the thicknesses of microstrip transmission lines need to be kept in check before simulation and fabrication of circuits. The depth at which the skin effect is valid can be calculated using (2.60).

$$\delta = \sqrt{\frac{2\rho}{\omega\mu_r\mu_0}} \quad (2.60)$$

where δ is the skin depth, ρ is the resistivity of the material used for metallisation, ω is the angular frequency, μ_r is the relative magnetic permeability of the material used for metallisation and μ_0 is the permeability of free space and has a value of $4\pi \times 10^{-7}$ H/m.

In the presented research work, copper metallisation was used for all the circuits fabricated via printed circuit board technology. All the frequency/frequencies used in these circuits fell within the range of 1 GHz to 12.5 GHz. Using (2.60), the skin depth for this frequency range and copper metallisation comes to be about 2.06–0.58 μm . All the copper metallisations used in these circuits had a pre-set thickness of 17.5 μm ; which is almost 8.5 times more than the maximum required skin depth of 2.06 μm . Therefore, skin depth will not be individually calculated and/or discussed for any of the developed PCB circuits.

On the other hand, silver ink metallisation was used for all the circuits fabricated via inkjet-printing technology. Since silver ink metallisation was self-printed in all cases, its thickness was not pre-set at a standard value. Therefore, for each developed inkjet-printed circuit, the skin depth will be individually calculated and discussed within its respective section.

2.2: Antenna Theory

2.2.1: Introduction

The main goal of the undertaken research work is the development of filter antennas for wireless transceivers. Before the development of these filter antennas, it is necessary to familiarise with the fundamental antenna theory. Furthermore, it is also essential to define and understand the main parameters which characterise the performance of antennas and have to be considered during their design.

Antennas are an important and an essential part of any wireless transceiver. According to the IEEE standards [2-9], an antenna is defined as “that part of a transmitting or receiving system that is designed to radiate or to receive electromagnetic waves”. In other words, without antennas there would be no wireless communication.

The above definition signifies that there are two types of antennas: transmitting antennas and receiving antennas. Transmitting antennas are the antennas which take the signals from a transmission line, convert them into electromagnetic waves and then broadcast them into free space. Whereas receiving antennas operate in reverse, i.e. they collect the electromagnetic waves from free space, convert them into signals and then put them back in the transmission line.

The definition and the two types of antennas imply that antennas are essentially a transition device. An example of an antenna as a transition device is shown in Figure 2.2–1 [2-7]. The equivalent circuit model of antennas consists of a voltage source, a current, an impedance and an RLC network. An illustration of the equivalent circuit model is provided in Figure 2.2–2 [2-7].

Additionally, in wireless transceivers, antennas are usually also required to optimise or enhance the radiation energy in some directions and suppress it in others at certain frequencies. This infers that antennas also act as a directional device on top of being a transition device.

So as to meet the specific requirements of being a directional and a transition device, antennas take various forms. These forms can include pieces of conducting wires, patches, collections of multiple elements (arrays), lens, reflectors, apertures, etc. An efficient design of antennas can relax the requirements and improve the overall performance of the wireless communication systems.

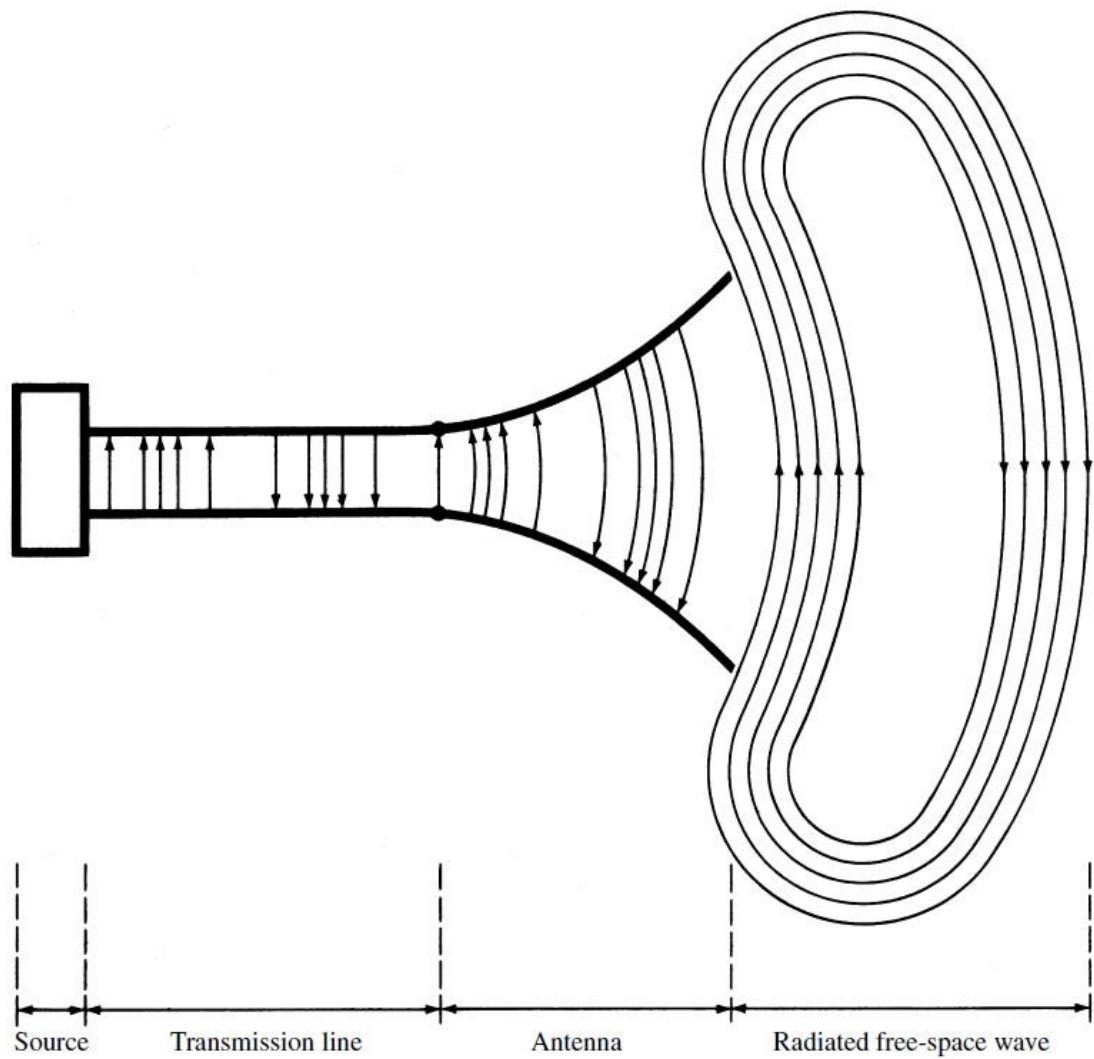


Figure 2.2-1: Antenna as a transition device [2-7].

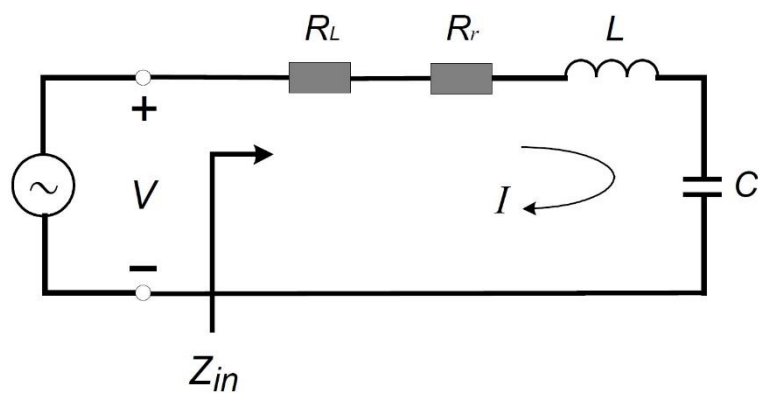


Figure 2.2-2: Equivalent circuit model of antennas [2-7].

2.2.2: Main Parameters of Antennas

In order to describe the performance of antennas, definitions and meanings of various parameters and terms are necessary. In reality, there are a number of important parameters which describe antennas. But the importance of these parameters changes according to the practical and intended applications of the antennas.

For the undertaken research work, the parameters of the antennas that will be looked at include the return loss, frequency bandwidth, radiation patterns, directivity, gain and efficiency.

A) Return Loss

In wireless communications, return loss is defined as the loss of power in the signal which is reflected/received by a discontinuity within a transmission line. This discontinuity can be either a mismatch with a device inserted in the transmission line or with the terminating load. The return loss, RL , is a function of the incident power and the reflected power and it can be given by (2.61).

$$RL = 10 \log_{10} \left(\frac{P_i}{P_r} \right) \quad (2.61)$$

where RL is the return loss in dB, P_i is the incident power and P_r is the reflected power.

In the case of wireless transceivers, this device is the antenna. In antennas, the return loss is a characterisation of how well the antennas are matched with the rest of the device. A match is considered good if the return loss is high.

For antennas, the return loss is the difference in decibels between the incident (transmitted) power sent to the antennas and the power reflected (received) from them.

Once the incident power and the reflected power are known, the return loss can be calculated using (2.62).

$$RL = P_i - P_r \quad (2.62)$$

where RL is the return loss in dB, P_i is the incident power in dBm and P_r is the reflected power in dBm.

For a signal travelling in an antenna, the ratio of the amplitude of the reflected wave, V_r , to the amplitude of the incident wave, V_i , is called the reflection coefficient, Γ . Hence, the reflection coefficient can be given by (2.63) below.

$$\Gamma = \frac{V_r}{V_i} \quad (2.63)$$

This reflection coefficient can also be expressed in terms of the source impedance and the load impedance or in terms of the voltage standing wave ratio. These are given by (2.64) and (2.65) respectively.

$$\Gamma = \frac{Z_L - Z_S}{Z_L + Z_S} \quad (2.64)$$

where Z_L is the impedance towards the load and Z_S is the impedance towards the source.

$$\Gamma = \frac{VSWR - 1}{VSWR + 1} \quad (2.65)$$

The return loss of antennas is the negative function of the magnitude of the aforementioned reflection coefficient in dB. This relation is given below in (2.66).

$$RL = -20 \log_{10} |\Gamma| \quad (2.66)$$

where the vertical brackets indicate magnitude.

Therefore, a large positive return loss indicates that the reflected power is small compared to the incident power. This indicates a good impedance match from the source to the load.

Moreover, from the above equations, it can be seen that the return loss is related to both the voltage standing wave ratio and the reflection coefficient. An increase in the return loss corresponds to a decrease in the voltage standing wave ratio.

At the same time, though related, the return loss is generally preferred over the voltage standing wave ratio because it has a better resolution for small values of the reflected wave.

B) Frequency Bandwidth

In antennas, the frequency bandwidth can be taken as the specific range of frequencies on either side of the centre/resonant frequency, within which an antenna performance characteristic is within an acceptable value of those at the centre/resonant frequency. From antennas standards, this characteristic is the return loss and the acceptable value is at least 10 dB [2-7] and [2-9].

The frequency bandwidth of antennas can be given in terms of either the absolute bandwidth or the fractional bandwidth.

The absolute bandwidth, ABW , is expressed as a difference between the upper limit and the lower limit of the bandwidth. It is given by (2.67).

$$ABW = f_H - f_L \quad (2.67)$$

where f_H and f_L are the upper limit and the lower limit respectively of the frequency range at a return loss of 10 dB.

Whereas, the fractional bandwidth is a percentage function of the upper limit of the bandwidth, the lower limit of the bandwidth and the centre frequency of an antenna. This relation is given in (2.68) below.

$$FBW = \frac{f_H - f_L}{\sqrt{f_H f_L}} \times 100 \quad (2.68)$$

where f_H and f_L are the upper limit and the lower limit respectively of the frequency range at a return loss of 10 dB.

C) Radiation Patterns

The radiation patterns represent the radiation properties of the antenna as a function of space coordinates. Generally, radiation patterns are checked in the far-field region where the spatial (angular) distribution of the radiated power does not depend on the distance. The radiation patterns typically describe the normalised field (power) values with respect to the maximum values.

The important radiation properties are the 2D or the 3D spatial distributions of the radiated energy as a function of an observer's position along a path or surface of constant radius. Generally, the 3D radiation patterns are required and can be constructed in a series of 2D radiation patterns. Practically, and for most applications, a few plots of the radiation patterns as a function of ϕ for some

particular values of the frequency and a few plots of the radiation patterns as a function of θ for some particular values of the frequency are enough to provide the useful and required information; where ϕ and θ are the two axes in a spherical coordinate system.

For antennas which are linearly polarised, their performance is usually described with respect to their radiation patterns in the E-plane and the H-plane. The E-plane is the plane containing the electric-field vector and the direction of maximum radiation. Whereas, the H-plane is the plane containing the magnetic-field vector and the direction of maximum radiation [2-7].

The radiation patterns which are commonly used to describe the radiation properties of antennas are the respective radiation patterns of three different types of antenna.

These types are:

- i. Isotropic antenna: An ideal, theoretical and lossless antenna which radiates equally in all directions. The radiation patterns from this antenna are used as a reference for expressing the radiation properties of actual antennas.
- ii. Directional antenna: An antenna which radiates more efficiently in some directions than in others. This is usually valid for an antenna where its maximum directivity is considerably more than that of a half-wave dipole.
- iii. Omnidirectional: An antenna which has an essentially non-directional radiation pattern in a given plane and a directional radiation pattern in any orthogonal plane.

D) Directivity and Gain

In order to describe the directional properties of the radiation patterns of antennas, the directivity is used. The directivity, D , is defined as the ratio of the radiation intensity, U , in a given direction from an antenna over that of an isotropic source, U_0 . Moreover, since the radiation intensity for an isotropic source is known, the directivity can be computed further. The final expression and the intermediate step is given in (2.69).

$$D = \frac{U}{U_0} = \frac{4\pi U}{P_{rad}} \quad (2.69)$$

where U is the radiation intensity of the antenna, U_0 is the radiation intensity of the isotropic source and P_{rad} is the radiated power of the isotropic source.

If a value is not specified, the directivity of an antenna implies its maximum value, D_0 . This is given by (2.70).

$$D_0 = \frac{U|_{max}}{U_0} = \frac{U_{max}}{U_0} = \frac{4\pi U_{max}}{P_{rad}} \quad (2.70)$$

Although the gain of antennas is related to the directivity of antenna, it takes into account the radiation efficiency of the antennas as well. This relation is given by (2.71).

$$G = e_{rad}D \quad (2.71)$$

where e_{rad} is the radiation efficiency of the antenna and D is the directivity of the antenna.

As was shown in the equivalent circuit model of antennas in Figure 2.2–2, the components included a voltage source, V , a current, I , an input impedance, Z_{in} , a loss resistance, R_L , a radiation resistance, R_r , an inductance, L , and a capacitance, C . Of these components, the current, the loss resistance and the radiation resistance can be used to determine the radiation efficiency. The radiation efficiency is function of the power delivered to the radiation resistance and the sum of power delivered to radiation resistance and loss resistance. This can be transformed into (2.72) below.

$$e_{rad} = \frac{0.5|I|^2R_r}{(0.5|I|^2R_r) + (0.5|I|^2R_L)} = \frac{R_r}{R_r + R_L} \quad (2.72)$$

where I is the current in the antenna, R_r is the radiation resistance and R_L is the loss resistance.

Similarly to (2.71), the maximum gain of antennas, G_0 , is related to the maximum directivity, D_0 ; as given by (2.73).

$$G_0 = e_{rad}D_0 \quad (2.73)$$

E) Efficiency

The total antenna efficiency of antennas is used to take into consideration the losses at the input terminals and, as well as, the losses within the structures of the

antennas. As shown in Figure 2.2–3 [2-7], these losses can be due to the reflections — because of the mismatch between the transmission line and the antenna — and the conduction and the dielectric losses.

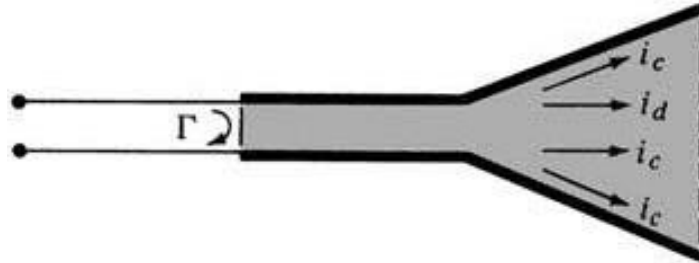


Figure 2.2–3: Reflection, conduction and dielectric losses in antennas.

Generally, the overall efficiency of antennas, e_0 , can be expressed by (2.74).

$$e_0 = e_r e_c e_d \quad (2.74)$$

where e_r is the reflection/mismatch efficiency, e_c is the conduction efficiency and e_d is the dielectric efficiency.

Generally, e_c and e_d are extremely complex to calculate. Nevertheless, they can be determined by measurements. At the same time, even by measurements, they cannot be separated. Thus, it is usually more suitable to write them together as “ e_{cd} ”. Additionally, this e_{cd} is the antenna radiation efficiency, i.e. e_{rad} , which was calculated previously from (2.72). These expressions are given in (2.75).

$$e_c e_d = e_{cd} = e_{rad} \quad (2.75)$$

Moreover, the reflection efficiency, e_r , can be expressed in terms of the reflection coefficient; as shown by (2.76).

$$e_r = 1 - |\Gamma|^2 \quad (2.76)$$

Therefore, using (2.75)–(2.76), (2.74) can now be written in the form of (2.77).

$$e_0 = e_{cd}(1 - |\Gamma|^2) \quad (2.77)$$

2.3: References

- [2-1] D. M. Pozar, *Microwave Engineering*. 3rd edition, New York, United States of America: John Wiley & Sons, 2004.
- [2-2] Rainee N. Simons, *Coplanar Waveguide Circuits, Components, and Systems*. John Wiley & Sons, Inc., 2001.
- [2-3] T. C. Edward and M. B. Steer, *Foundation of Interconnect and Microstrip Design*. 3rd edition, New York: Wiley, 2000.
- [2-4] K. Chang, I. Bahl, and V. Nair, *RF and Microwave Circuit and Component Design for Wireless Systems*. John Wiley and Sons, 2002.
- [2-5] J-S. Hong and M. J. Lancaster, *Microstrip Filters for RF/microwave Applications*. New York, United States of America: John Wiley & Sons, 2001.
- [2-6] S. B. Cohn, "Dissipation loss in multiple-coupled-resonator filters," *Proceedings of the IRE*, vol. 47, no. 8, pp. 1342–1348, August 1959.
- [2-7] C. A. Balanis, *Antenna Theory: Analysis and Design*. Hoboken, New Jersey, United States of America: John Wiley & Sons, Inc., 2005.
- [2-8] Wikipedia, "Skin effect". [Online]. Available: https://en.wikipedia.org/wiki/Skin_effect
- [2-9] *IEEE Standard for Definitions of Terms for Antennas*, IEEE Std 145™-2013, 2013.

Chapter 3:

**Development of
Reconfigurable Bandpass Filters**

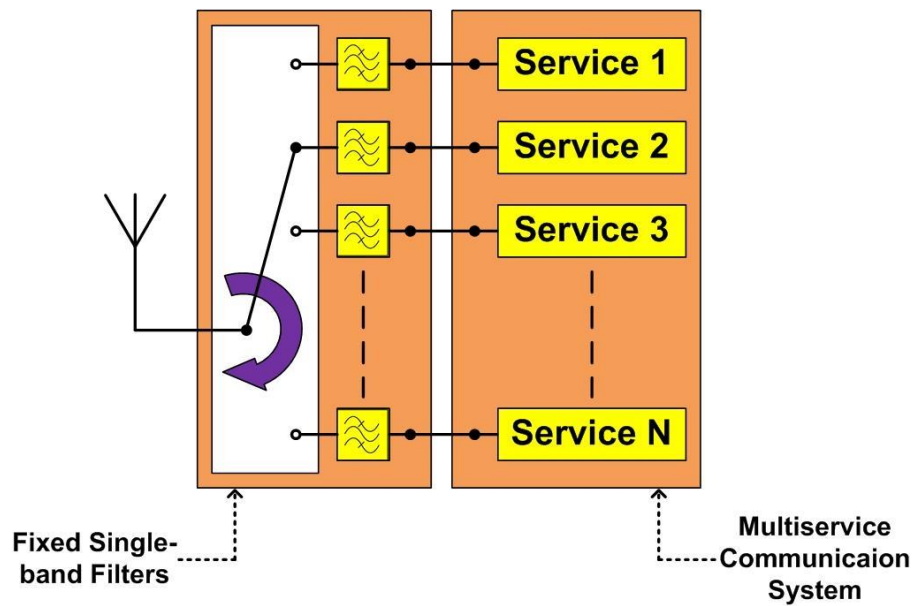
3.1: Introduction

Ever since the frequency range of 3.1 GHz to 10.6 GHz was released for commercial UWB communications [3-1]–[3-2], wireless UWB technology has been in constant demand; predominantly amongst the research community. This is primarily due to the short-distance communications, short broadcast times and the high data rates that UWB technology can support because of the short duration of the UWB pulses. This has resulted in a continuous increase in the number of wireless UWB applications. These applications [3-3] include indoor and home systems, such as wireless storages, wireless monitors, wireless printing and wireless data transfers between mobile phones and other handheld devices such as portable media players and laptops. Moreover, the applications also include outdoor, commercial and military systems, such as real-time position/location tracking systems, see-through-the-wall radar and imaging systems, WBANs, sensor networks and environments sensitive to radio frequencies, for instance hospitals.

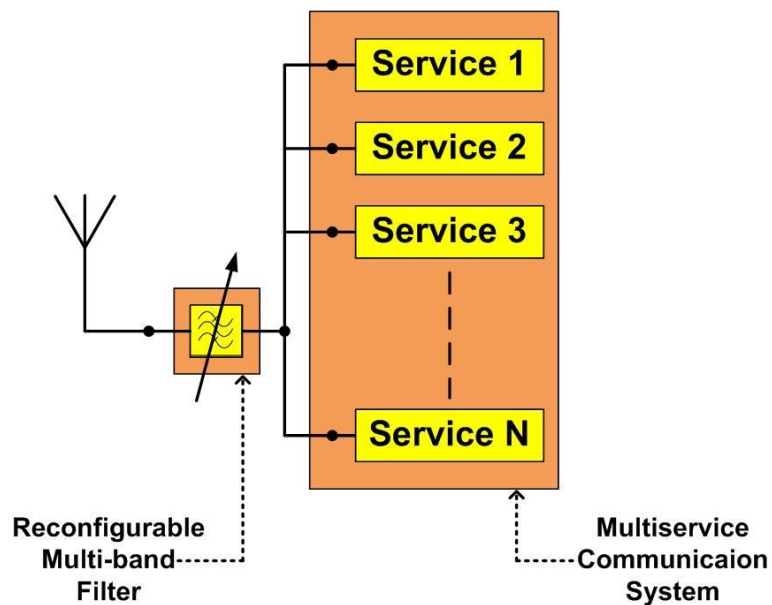
Since the commercial UWB covers a wide frequency range of 3.1–10.6 GHz, a number of other wireless services overlap it; such as the IEEE 802.16 WiMAX 3.4–3.6 GHz band, the IEEE 802.11 WLAN 5.725–5.825 GHz band and the IEEE C-band satellite communication system 3.7–4.2 GHz band. Since the power level of these overlapping wireless services is about 70 dB more than the limited maximum power spectral density of -41.3 dBm/MHz within 3.1–10.6 GHz [3-1]–[3-2], they interfere with the UWB signals. This causes signal distortion and loss of sensitivity. Hence, filtering within the passband is necessary for the best usage of the UWB. A possible and effective solution is to realise notchband at the interfering frequency bands.

The rapid rise in the number of wireless communication systems and services and the demand to access these multiple services by means of a single technology has led to an increase in the interest, research and development of reconfigurable devices. These include reconfigurable multi-band filters, antennas and filtennas. One such application for these reconfigurable devices are multiservice communication systems; where transceivers are able to operate on multiple frequency bands. As compared with devices having a fixed single-band operation, reconfigurable multi-band devices are able to provide more functionality, compactness and lower costs for these multiservice communication systems. An

example of a reconfigurable multi-band filter replacing fixed single-band filters for a multiservice communication system is illustrated in Figure 3.1–1.



(a)



(b)

Figure 3.1–1: Example of (a) fixed single-band multiservice communication systems and (b) reconfigurable multi-band multiservice communication systems.

UWB filters are one of the components in the wireless transceivers of UWB applications. Due to the increased demand for wireless UWB technology, UWB filters too have experienced research, development and growth. This has generally

been with regards to their size, cost, reconfigurability and high-linearity while maintaining a wide operating bandwidth and a low insertion loss in their passbands. For the development of such filters, planar microstrip filter structures have become popular due to their compactness, ease of designing, inclusion of reconfigurability and inexpensive manufacturing.

For this purpose, several filter configurations have been employed; such as applying slot resonators [3-4], terminated resonators [3-5], stubs [3-6], embedded notchband [3-7] and short-circuited quarter-wavelength transmission lines [3-8]. However, the structure in [3-5] has a fixed notchband and not enough rejection. Comparatively high losses and signal distortion are experienced in [3-6]. In [3-7], the reconfigurability is not good and does not provide full rejection characteristics. Even though the reconfigurability and rejection characteristics are good in [3-8], the notchband structure is cascaded with the filter; resulting in a larger area taken by the final circuit. Furthermore, in all the aforementioned works, high linearity has not been a priority in the design. Moreover, UWB bandpass filters consisting of quarter-wavelength and/or half-wavelength stubs are quite appealing owing to the advantages of obtaining a relatively wide operational bandwidth and a lower insertion loss in their passbands. For example, quarter-wavelength resonators have been used to realise the interdigital and combline filters in [3-9]–[3-11].

Although, as discussed above, there is extensive literature on reconfigurable bandpass filters for wireless transceivers of UWB applications, keeping in view the limitations of these filters, some important points which need to be addressed are as follows:

- Development of filter structures which are capable of integration with UWB antennas to form UWB filter antennas.
- Development of an equivalent circuit model which could and would be used as the basis for the design of the UWB bandpass filters.
- Small-sized structures to suit modern UWB applications.
- Complete rejection of any interfering frequency bands present within the passband of the filters.
- Incorporation of reconfigurable elements so as to make the filters reconfigurable.
- Using different reconfigurable elements without affecting the performance of the filters.
- Independent control of frequency reconfigurable states within the same operational bandwidth without affecting other characteristics of the filters.

The purpose of the overall chapter is to introduce a filter topology which addresses the points listed above, alongside its theory and design equations. These equations can be used for acquiring the physical parameters of the resonators from the values of the prototype networks. Later on, in this chapter, two reconfigurable bandpass filters for wireless transceivers of UWB applications have been developed.

Section 3.2 gives an overview of various reconfigurable elements. A new reconfigurable element based on Graphene has been developed and presented; alongside its working, design equations and results. In addition, a deeper detail of the working of PIN diodes is given. These two elements will be used later in this chapter and all subsequent chapters, i.e. throughout the entire research work.

Section 3.3 introduces the topology of a bandpass filter whose variants will be used in this chapter. Alongside an analysis of its geometry, the section also details its theoretical working, design method and design equations. Additionally, the results based on the design method and design equations are also presented.

Section 3.4 presents the first bandpass for UWB applications. While having a wide 3.1–10.6 GHz passband, the filter is capable of a single sharp notchband for the rejection of the IEEE 802.11 WLAN 5.8 GHz band. The section presents an analysis of the equivalent circuit model of the filter and describes its working. Furthermore, reconfigurability is introduced in the filter using two different reconfigurable elements. Thus, it is possible to switch off or switch on the single notchband.

Section 3.5 presents the second bandpass filter for UWB applications. The filter operates in the lower UWB range of 3.1–5.25 GHz, as defined in [3-2]. The bandpass filter structure is coupled with two resonators — which have stopband effects — separately. Therefore, within its passband, the filter exhibits dual notchband and is able to reject the IEEE 802.16 WiMAX 3.5 GHz and the IEEE C-band satellite communication system 4.2 GHz bands. Furthermore, the filter is made reconfigurable by the inclusion of two different reconfigurable elements. Because of the specific design of the presented filter structure, it is possible to control the two notchband separately. As a result, the bandpass filter is able to operate in four different states: with both notchband switched off, with any one notchband switched off and the other switched on, or with both notchband switched on.

Because of the particular topology of the developed filters and the concept of the independent control of multiple notchband, the filters' responses can be modified and/or controlled over a wider frequency range. These features, thus, provide filter designers an additional level of freedom to redesign the bandpass filters for any other frequency bands of need and interest.

3.2: Reconfigurable Elements

3.2.1: Overview of Reconfigurable Elements

Frequency reconfigurable filters, antennas and filtennas are formed by the presence of synchronously tuned resonators which have reconfigurable elements in their circuits at a point where the behaviour of the required frequencies can be affected. These elements can be employed for controlling the frequency transformation between a bandpass and a bandstop response for the entire operational frequency range or for a few selected frequency points. They can also be used for altering the centre frequency or the bandwidth of a device. Generally, reconfigurability in filters and antennas can be introduced by attaching reconfigurable elements with the resonators forming the filters and with the transmission lines forming the antennas. Filtennas can be made reconfigurable by either cascading reconfigurable filters with antennas or by integrating reconfigurable resonators within the antennas.

These reconfigurable elements include MEMS switches, optical switches, varactor diodes, Graphene based switches, PIN diodes, etc. Each reconfigurable element has its own set of advantages and disadvantages over the other one depending on the application and the usage.

MEMS switches largely behave like voltage-controlled actuators. They can be used either as variable capacitors or switches. MEMS switches have a low transmission loss and power consumption, are highly linear and have high quality factors [3-12]. Furthermore, they provide a good isolation and are very adaptable since they can be used with various substrates. However, they have poor switching speeds, require a high degree of design complexity and have a low reliability [3-12].

Optical switches, such as the silicon dice, were first proposed in 1975 [3-13]. Optical switches work by exploiting the photoconductive effect of silicon to achieve a switching effect. They are advantageous due to their high switching speeds, high power-handling capabilities, high linearity and ability to provide an excellent isolation [3-14]. Moreover, they do not require an internal biasing circuitry [3-14]. At the same time, they are disadvantaged by their extremely low conductivity when in a switched on state and their fabrication complexities.

Varactor diodes are widely used because of their low-costs, high reliability, high switching speeds, component robustness and versatility for circuit integration. On the other hand, they suffer from a low linearity because of the signal distortion from

their voltage-controlled capacitance, require biasing circuitry and exhibit a high transmission loss. Moreover, their high power consumption in the switched on state and their poor quality factor makes them unsuitable for high-frequency applications. Graphene based switches are a novel concept. They will be presented, alongside their working and significant advantages, later in the chapter. Their main disadvantage is that they yet have to fully make the move from the research stages to the industrial and commercial markets. Furthermore, most of the fabrication of their integration within printed circuits is still in testing stages as well.

PIN diodes are attractive reconfigurable elements due to a number of reasons. They have a low-cost production and a precise manufacturing process leading to high reliability and high quality end-products. Moreover, PIN diodes offer ruggedness and are versatile and robust for circuit integration [3-15]. Furthermore, they have high switching speeds, high power-handling capabilities and a small physical size. They can control large radio frequency signals while using smaller levels of DC excitation. Although they require biasing circuitry to operate, it can be included during the process of designing the devices. Their drawbacks include a high power consumption and a low linearity because of their voltage-controlled capacitance.

This thesis will use Graphene based switches (simulations only) and PIN diodes (simulations and measurements) as the elements to introduce reconfigurability in the developed devices.

3.2.2: Graphene based Switches

As stated earlier, Graphene has been implemented in a variety of applications, but has reportedly never been used as a reconfigurable element, such as a switch for use in reconfigurable filters, antennas or filterennas. Since Graphene is a 2D material, its surface conductivity is expressed as a tensor in the most general form [3-16]. Variables, such as the gate voltage and the substrate thickness, define the chemical potential of Graphene. The chemical potential can be controlled by doping and/or by applying an electrostatic bias field. Upon varying the chemical potential, a frequency shift of the real and imaginary parts of the conductivity is observed. When there is no magnetic bias field present and no doping present in operational frequencies below the THz range, the surface conductivity of Graphene is a scalar. It is expressed by the formula [3-16] given in (3.1).

$$\sigma = -j \frac{q_e^2 k_B T}{\pi \hbar^2 (\omega - j2\Gamma)} \left[\frac{\mu_c}{k_B T} + 2 \ln \left(e^{\frac{\mu_c}{k_B T}} + 1 \right) \right] \quad (3.1)$$

where σ is the surface intraband conductivity, j is the imaginary constant, q_e is the charge of an electron, k_B is the Boltzmann's constant, T is the temperature in Kelvin, \hbar is the reduced Planck's constant, ω is the angular frequency in radians, Γ is the scattering rate calculated using (3.2) and μ_c is the chemical potential.

$$\Gamma = \frac{1}{2\tau} \quad (3.2)$$

where τ is the average relaxation time.

Relaxation times can be made to vary between 0.05 ps and 100 ns [3-17]–[3-18].

The change in the surface conductivity causes the surface resistance and the surface reactance to change as well. These relationships, i.e. surface resistance and surface reactance, are given in (3.3) and (3.4) respectively.

$$\text{surface resistance} = \text{Re} \left(\frac{1}{\sigma} \right) \quad (3.3)$$

$$\text{surface reactance} = \text{Im} \left(\frac{1}{\sigma} \right) \quad (3.4)$$

Graphene based switches can be implemented by modelling the surface resistance and surface reactance of Graphene. As compared with traditional bulk modelling, surface impedance modelling is much faster and takes up considerably less computing and memory resources.

The combination of changeable relaxation times and changeable chemical potential can create a switching effect. For a fixed value of relaxation time, a change in the chemical potential between 0.0eV and 1.0eV, will cause a corresponding change in the conductivity. For a relaxation time of another fixed value, the same working will follow. Following this theory, Graphene can be configured to behave as a reconfigurable element, i.e. a switch.

In each graph of Figure 3.2–1, a different value of the relaxation time parameter has been used to demonstrate how the surface resistance changes with respect to the change in values of the chemical potential [3-16]–[3-18]. Surface reactance has not been shown and will not be discussed further in detail since in the microwave range,

i.e. the GHz frequencies, it has an insignificant effect on the conductivity. In all the four examples, the value of the temperature parameter, T , is set to 300 K.

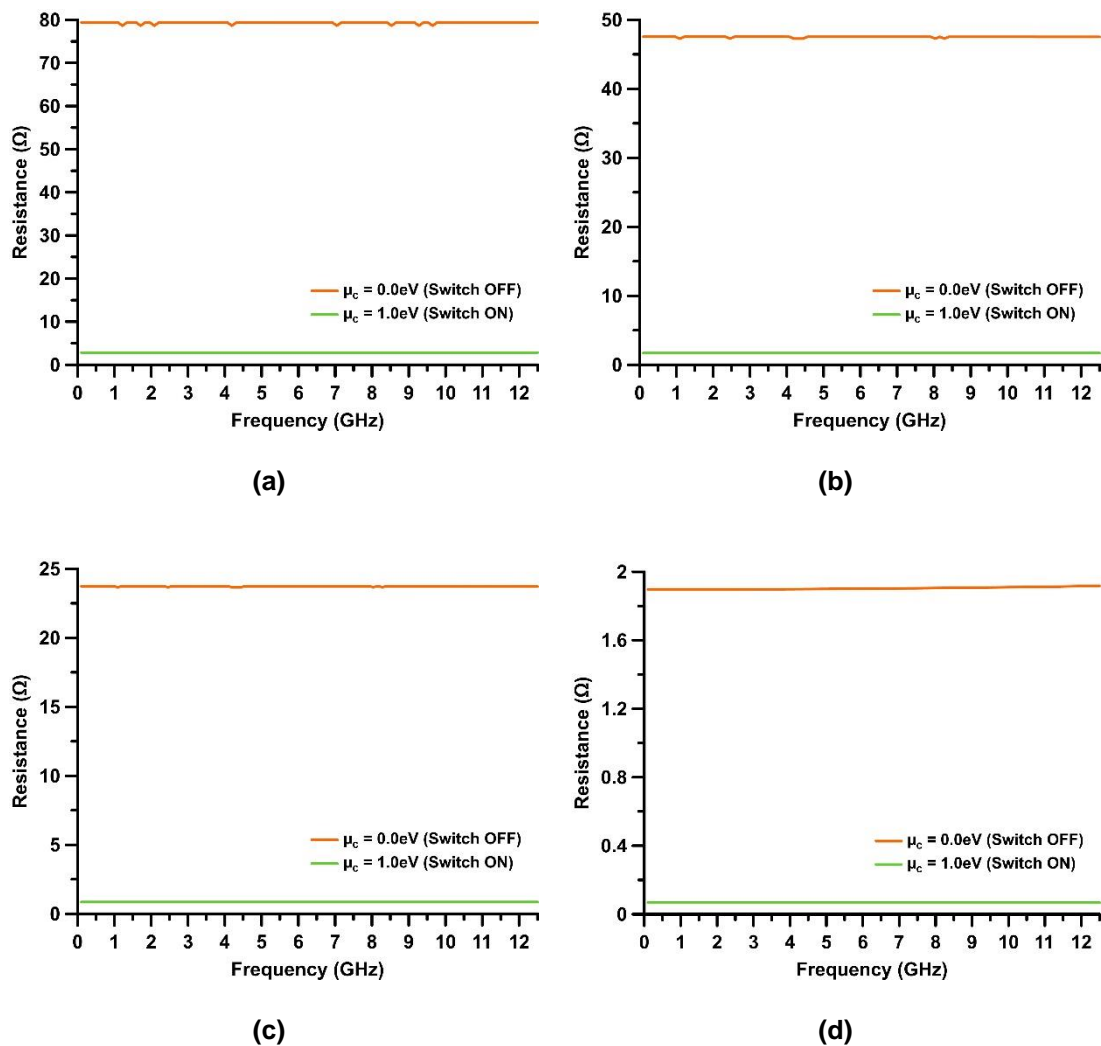


Figure 3.2–1: Surface resistance of Graphene at the chemical potentials of 0.0eV and 1.0eV when (a) $\tau = 3$ ps, (b) $\tau = 5$ ps, (c) $\tau = 10$ ps and (d) $\tau = 125$ ps.

These four demonstrated relaxation times of 3 ps, 5 ps, 10 ps and 125 ps will be used for the undertaken research. For these relaxation times, the corresponding values of the surface resistance and the surface reactance at the chemical potentials of 0.0eV and 1.0eV are summarised in Table 3.2–1.

Table 3.2–1: Average values of the surface resistance and the surface reactance of Graphene at the chemical potentials of 0.0eV and 1.0eV at various relaxation times.

τ (ps)	3		5		10		125	
μ_c (eV)	0.0	1.0	0.0	1.0	0.0	1.0	0.0	1.0
Surface Resistance (Ω)	79.33	2.83	47.52	1.70	23.73	0.85	1.90	0.07
Surface Reactance (Ω)	9.46	0.34	9.43	0.34	9.41	0.34	9.38	0.34

These examples show that by applying the correct values for the variables in (3.1)–(3.4), the required reconfigurable characteristics of Graphene can be obtained and, thus, culminating in Graphene based switches. Furthermore, these examples show that when the chemical potential is 0.0eV, the resistance is more than what it is at a chemical potential of 1.0eV. Hence, a chemical potential of 0.0eV can be equated to a switch OFF state and a chemical potential of 1.0eV can be equated to a switch ON state for the Graphene based switches.

3.2.3: PIN Diodes

PIN diodes are semiconductor devices which are popular switching elements, especially in MIC designs. Their advantages have been already discussed earlier. In radio frequency circuits, PIN diodes are essentially current-controlled variable resistors. Their resistance is described in [3-19] and is given by (3.5).

$$R_s = \frac{k}{\tau \times I_f} \quad (3.5)$$

where k is a device constant, τ is the minority carrier lifetime and I_f is the forward bias DC current.

For example, if there are two transmission lines joined to each other with a PIN diode, a current can be provided to the PIN diode to turn it off or on. In a reverse-bias condition or a switch OFF state, there is no connection between the two transmission lines. This is because, as illustrated in the equivalent circuit model in Figure 3.2–2 (a) of the switch OFF state, the PIN diode appears as a parallel plate capacitor, C_p , essentially independent of reverse voltage [3-20]. Associated with the

diode capacitance is a parallel resistance, R_p , which represents the net dissipative resistance in the reverse-biased diode [3-20] and also degrades the high frequency isolation of the device.

In contrast, when a current is provided to turn on a PIN diode, it is in a forward-bias condition or a switch ON state. The equivalent circuit model of this state is shown in Figure 3.2–2 (b). In this state, the PIN diode behaves like a small resistance. So if the two transmission lines from the previous example are connected to each other by means of a PIN diode in a switch ON state, a short circuit is created between them and they act like a single, longer transmission line.

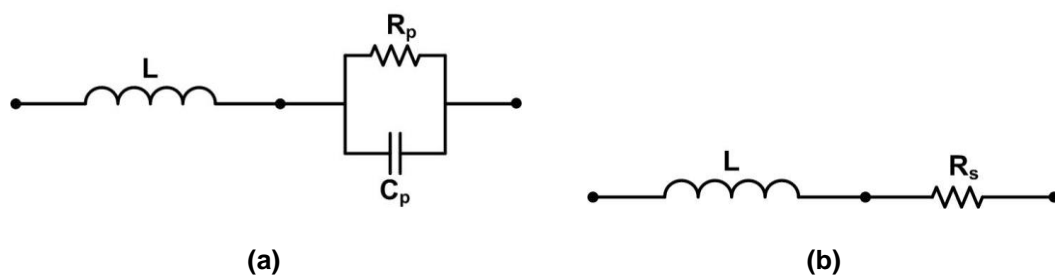


Figure 3.2–2: Equivalent lumped element circuit models of PIN diodes in the (a) switch OFF and (b) switch ON states.

Non-linearity in PIN diodes arises due to the time-varying forward resistance [3-20]; which is varied because of the modulation of the stored charge in the PIN diodes by the radio frequency signals [3-21]. The effects of non-linearity decrease with an increase in the bias voltage. High non-linearity can affect the performance of radio frequency devices. Due to this inherent negative characteristic, the linearity performance of some radio frequency devices may need to be evaluated.

3.3: Design of Bandpass Filters for UWB Applications

3.3.1: Geometry of the Bandpass Filter

The equivalent transmission line circuit model of the bandpass filter is shown in Figure 3.3–1. This topology will be heavily used throughout this chapter. For this reason, in this section, the structure will be discussed in greater detail. The discussion will also include its theory, equivalent circuit models, design equations and calculations.

The proposed filter is a third-order bandpass filter. The structure comprises one half-wavelength resonator, of a length of L_{HW} and an impedance of Z_{HW} , and two quarter-wavelength resonators, each of a length of L_{QW} and an impedance of Z_{QW} . The half-wavelength resonator is placed in the middle. While one end of each quarter-wavelength resonator is connected to either end of the half-wavelength resonator, the other end is short-circuited to ground. The electrical lengths of all three resonators have been calculated at the centre frequency of the bandpass filter.

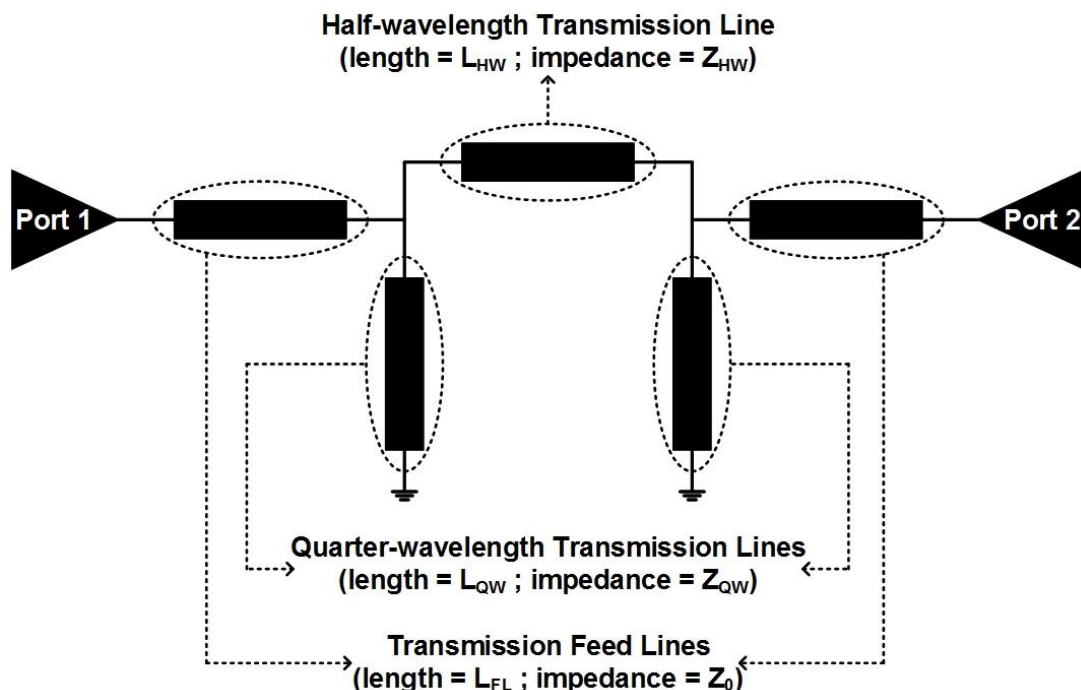


Figure 3.3–1: Equivalent transmission line circuit model of the filter.

3.3.2: Analysis of the Geometry of the Bandpass Filter

The centre frequency and the absolute bandwidth of the filter can be calculated using (3.6) and (3.7) respectively; where f_H and f_L are the upper limit and the lower limit respectively of the frequency range at an insertion loss of 3 dB.

$$\omega_C = \sqrt{\omega_H \omega_L} \quad (3.6)$$

$$\Delta\omega = \omega_H - \omega_L \quad (3.7)$$

For a given degree of filter, the characteristics of a bandpass filter will depend on the characteristic admittances of the stub transmission lines and the characteristic impedance of the connecting transmission line. In the circuit model of the bandpass filter presented above, since the quarter-wavelength short circuited stubs look like parallel resonant circuits [3-22]–[3-23], they can be used as the shunt parallel LC resonators for bandpass filters. Whereas, since the half-wavelength transmission line, in the circuit model, behaves like a series resonant circuit, it can be used as a series LC resonator for bandpass filters. These are depicted in Figure 3.3–2.

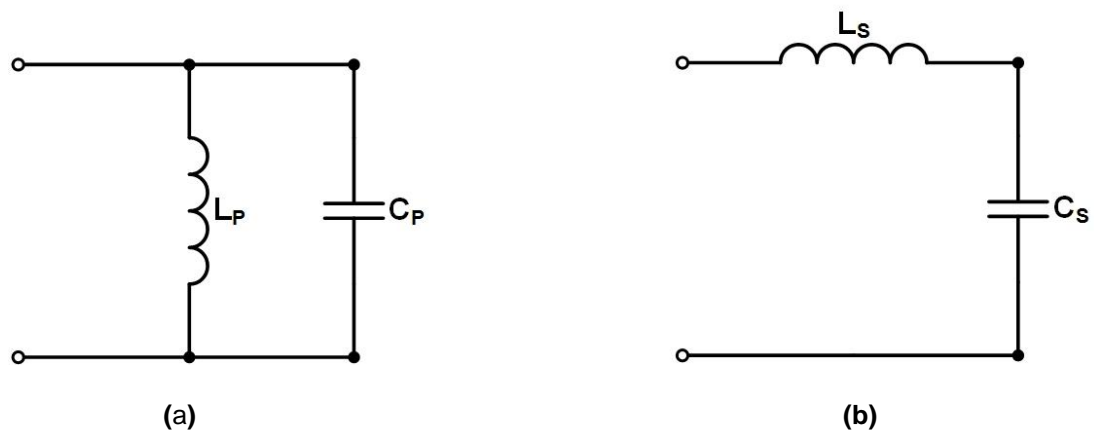


Figure 3.3–2: Equivalent lumped element circuit model of (a) quarter-wavelength transmission lines and (b) half-wavelength transmission lines.

The characteristic admittance of the stub transmission lines (quarter-wavelength transmission lines), Y_{QW} , and the characteristic impedance of the connecting transmission line (half-wavelength transmission line), Z_{HW} , are given in (3.8) and (3.9) respectively.

$$Y_{QW} = \frac{1}{Z_{QW}} = \frac{4\omega_c C}{\pi} \quad (3.8)$$

$$Z_{HW} = \frac{2\omega_c L}{\pi} \quad (3.9)$$

Following the equivalent lumped element circuits of the quarter-wavelength and the half-wavelength transmission lines, the overall equivalent lumped element circuit model of the bandpass filters is given in Figure 3.3–3.

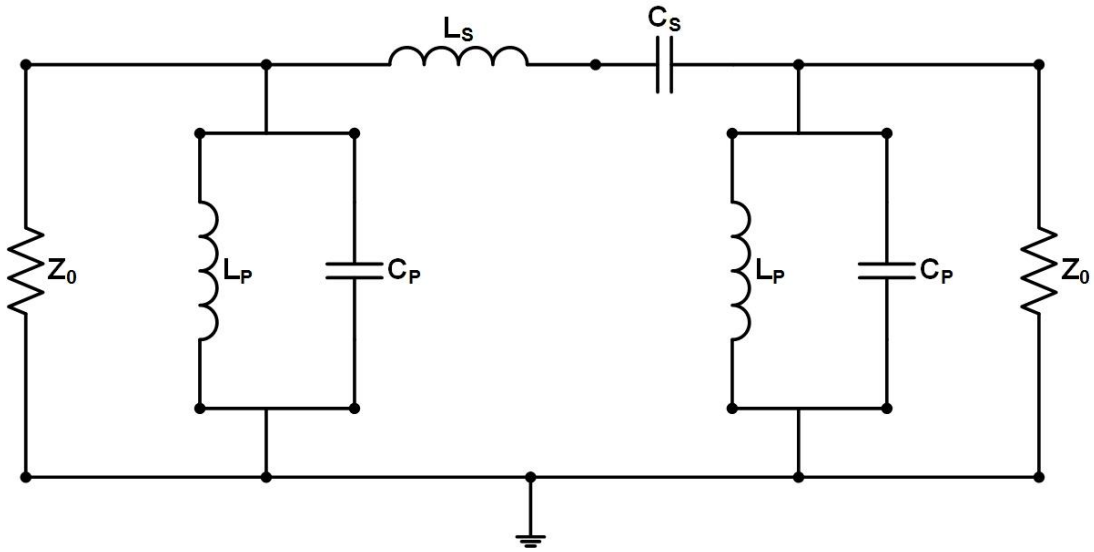


Figure 3.3–3: Equivalent lumped element circuit model of the filter.

For parallel-tuned elements in a parallel/shunt configuration, the inductance, L_P , and the capacitance, C_P , can be calculated from (3.10) and (3.11) respectively.

$$L_P = \frac{Z_0 \Delta\omega}{g_i \omega_c^2} \quad (3.10)$$

$$C_P = \frac{g_i}{Z_0 \Delta\omega} \quad (3.11)$$

where Z_0 is the characteristic impedance of the system in Ω and g_i is the lowpass prototype element value.

For series-tuned elements in a series configuration, the inductance, L_S , and the capacitance, C_S , can be calculated from (3.12) and (3.13) respectively.

$$L_S = \frac{g_i Z_0}{\Delta\omega} \quad (3.12)$$

$$C_S = \frac{\Delta\omega}{g_i Z_0 \omega_c^2} \quad (3.13)$$

where g_i is the lowpass prototype element value and Z_0 is the characteristic impedance in Ω .

Once the final values of all the lumped elements are obtained, their corresponding dimensions of microstrip transmission lines can be calculated using (2.15)–(2.18) and the equations in chapter 5 of [3-24].

Table 3.3–1: Element values for third-order Chebyshev lowpass prototype filters for a passband ripple level of 0.1 dB and normalised to an angular cut-off frequency, ω_c , of 1 rad/s and a characteristic system impedance, Z_0 , of 1 Ω .

g_0	g_1	g_2	g_3	g_4
1.0000	1.0316	1.1474	1.0316	1.0000

In order to calculate the response of the proposed bandpass filter, the scattering matrix of the overall circuit of the filter has to be determined. This involves determining the individual scattering matrices of the transmission lines comprising the filter. The scattering matrix of the quarter-wavelength lines and the scattering matrix of the half-wavelength line is given in (3.14) and (3.15) respectively.

$$\begin{bmatrix} A_{QW} & B_{QW} \\ C_{QW} & D_{QW} \end{bmatrix} = \begin{bmatrix} 1 & 0 \\ Y_{QW} & 1 \end{bmatrix} \quad (3.14)$$

where Y_{QW} is the admittance of the quarter-wavelength transmission line.

$$\begin{bmatrix} A_{HW} & B_{HW} \\ C_{HW} & D_{HW} \end{bmatrix} = \begin{bmatrix} \cos \theta & jZ_{HW} \sin \theta \\ j \frac{\sin \theta}{Z_{HW}} & \cos \theta \end{bmatrix} \quad (3.15)$$

where Z_{HW} is the impedance of the half-wavelength transmission line.

The scattering matrix of the overall circuit of the bandpass filter can be determined using (3.16). The resultant scattering matrix is given in (3.17). The intermediate calculation is as follows:

overall scattering matrix of filter = scattering matrix of the first quarter-wavelength line \times scattering matrix of the half-wavelength line \times scattering matrix of the second quarter-wavelength line

$$\begin{bmatrix} A & B \\ C & D \end{bmatrix} = \begin{bmatrix} A_{QW} & B_{QW} \\ C_{QW} & D_{QW} \end{bmatrix} \times \begin{bmatrix} A_{HW} & B_{HW} \\ C_{HW} & D_{HW} \end{bmatrix} \times \begin{bmatrix} A_{QW} & B_{QW} \\ C_{QW} & D_{QW} \end{bmatrix} \quad (3.16)$$

$$\begin{bmatrix} A & B \\ C & D \end{bmatrix} = \begin{bmatrix} 1 & 0 \\ Y_{QW} & 1 \end{bmatrix} \times \begin{bmatrix} \cos \theta & jZ_{HW} \sin \theta \\ j \frac{\sin \theta}{Z_{HW}} & \cos \theta \end{bmatrix} \times \begin{bmatrix} 1 & 0 \\ Y_{QW} & 1 \end{bmatrix}$$

$$\begin{bmatrix} A & B \\ C & D \end{bmatrix} = \begin{bmatrix} \cos \theta + jZ_{HW}Y_{QW} \sin \theta & jZ_{HW} \sin \theta \\ 2Y_{QW} \cos \theta + j \frac{\sin \theta}{Z_{HW}} + jZ_{HW}Y_{QW}^2 \sin \theta & \cos \theta + jZ_{HW}Y_{QW} \sin \theta \end{bmatrix} \quad (3.17)$$

3.3.3: Results of the Bandpass Filter

The elements within the obtained scattering matrix of the bandpass filter can be used to derive the expressions for the S-parameters of the bandpass filter. The expressions for the return/reflection loss, S_{11} , and the insertion loss, S_{21} , are given by (3.18) and (3.19) respectively.

$$S_{11} = \frac{A + \frac{B}{Z_0} + CZ_0 + D}{A + \frac{B}{Z_0} + CZ_0 - D} \quad (3.18)$$

$$S_{21} = \frac{2}{A + \frac{B}{Z_0} + CZ_0 + D} \quad (3.19)$$

where A , B , C and D are the elements of the scattering matrix from (3.17) and Z_0 is the characteristic impedance of the system.

The S-parameters of the proposed bandpass filter were calculated using (3.18) and (3.19). The results have been presented in Figure 3.3–4.

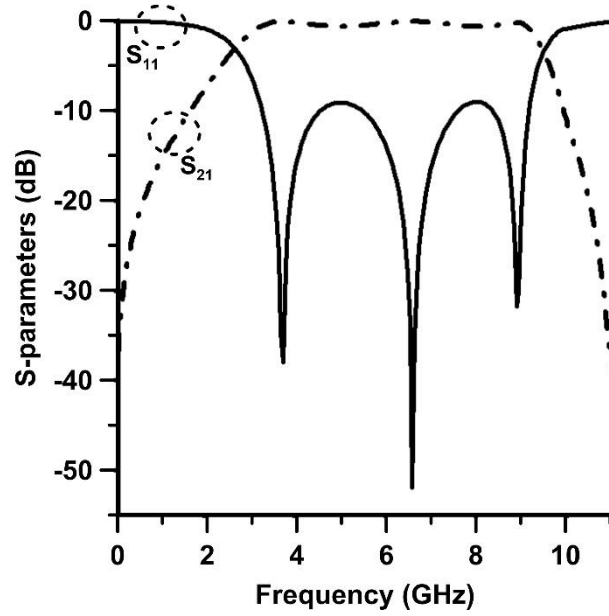


Figure 3.3-4: S-parameters of the filter.

As seen from the presented graph of the S-parameters, the return loss has three reflection zeros within it. These appear at the three frequencies of f_{P1} , f_{P2} and f_C . f_C is the centre frequency of the filter. f_{P1} and f_{P2} can be numerically calculated using (3.20) and (3.21) respectively.

$$f_{P1} = \frac{1}{\pi} \left(\tan^{-1} \sqrt{\frac{\left(1 + \frac{Z_{HW}}{Z_{QW}}\right) \times \left(\frac{Z_{HW}}{Z_{QW}}\right)}{\left(1 + \frac{Z_{HW}}{Z_{QW}}\right) - Z_{HW}^2}} \right) \quad (3.20)$$

$$f_{P2} = \frac{1}{\pi} \left[\pi - \left(\tan^{-1} \sqrt{\frac{\left(1 + \frac{Z_{HW}}{Z_{QW}}\right) \times \left(\frac{Z_{HW}}{Z_{QW}}\right)}{\left(1 + \frac{Z_{HW}}{Z_{QW}}\right) - Z_{HW}^2}} \right) \right] \quad (3.21)$$

where Z_{HW} is the impedance of the half-wavelength transmission line and Z_{QW} is the impedance of the quarter-wavelength transmission line.

3.4: Design of a Frequency Reconfigurable Filter with a Single Notchband for UWB Applications

3.4.1: Specifications and Initial Parameters

This section introduces a reconfigurable bandpass filter based on the specifications given in Table 3.4–1. The required specifications ask for a third-order filter, having a ripple level of 0.1 dB and operating at the full UWB range of 3.1–10.6 GHz. Furthermore, the filter ought to have a microstrip-based feeding method; where the characteristic impedance should be 50 Ω . Moreover, the filter should be fabricated via PCB technology. The specifications further state that there should be a single notchband present for the rejection of the interfering IEEE 802.11 WLAN band operating at 5.8 GHz. Based on these specifications, the lowpass prototype element values are determined using Table 3.3–1. The three lowpass prototype element values are $g_1 = 1.0316$, $g_2 = 1.1474$ and $g_3 = 1.0316$.

Table 3.4–1: Required specifications of the filter.

Parameter	Description of Parameter	Value
Filter	Type of filter	Chebyshev
Technology	Fabrication technology	PCB
Feed	Feeding method	Microstrip
Z_0	Characteristic impedance of system	50 Ω
n	Order of filter	3
L_R	Maximum ripple level within passband	0.1 dB
f_L	Lower passband frequency	3.1 GHz
f_H	Upper passband frequency	10.6 GHz
f_C	Centre frequency	5.73 GHz
FBW	Fractional bandwidth	≥ 130.84 %
n_{NB}	Number of notchband	Single
f_{NB}	Notchband frequency	5.8 GHz

3.4.2: Realised Structure and Final Parameters

A) Final Layout

The equivalent lumped element circuit model of the bandpass filter without its notchband structure is the same one as shown in Figure 3.3–3. The final values of the lumped elements, i.e. after converting the lowpass prototype element values to bandpass values, were calculated using (3.10)–(3.13) and are given in Table 3.4–2; where $Lg_1 = L_P$, $Cg_1 = C_P$, $Lg_2 = L_S$, $Cg_2 = C_S$, $Lg_3 = L_P$ and $Cg_3 = C_P$.

Table 3.4–2: Values of the lumped elements of the filter.

Element	Value (nH)	Element	Value (pF)
Lg_1	1.7607	Cg_1	0.4378
Lg_2	1.2174	Cg_2	0.6332
Lg_3	1.7607	Cg_3	0.4378

The geometry of the final bandpass filter is illustrated in Figure 3.4–1; with the values of its dimension parameters given in Table 3.4–3. The filter is designed with a centre frequency of 5.73 GHz. It is inductively coupled to the source and the load and is excited via ports 1 and 2; where the characteristic impedance, Z_0 , of the transmission feed lines is 50Ω . It is a third-order filter: consisting of a half-wavelength, $\lambda_g/2$, resonator placed between a pair of short-circuited quarter-wavelength, $\lambda_g/4$, resonators; where λ_g is the guided wavelength at the centre frequency of 5.73 GHz. The three resonators have an impedance of 54.3Ω , which translates to a transmission line width of 0.5 mm. The two short-circuited resonators are folded so as to utilise a common ground via. This arrangement also allows to shrink the size of the filter.

The notchband is inserted within the passband of the filter by the coupling of an identical, but inverted, pair of three-section resonators. The first section comprises stepped impedance resonators, with rectangular open-circuited stubs in the stepped impedance resonators' symmetry plane as the third section and transmission lines connecting the stepped impedance resonators and the open-circuited stubs as the second section. The stubs introduce sharp rejection at the desired frequency band. The bandwidth of the notchband is determined by the width of the transmission lines connecting the stepped impedance resonators and the stubs.

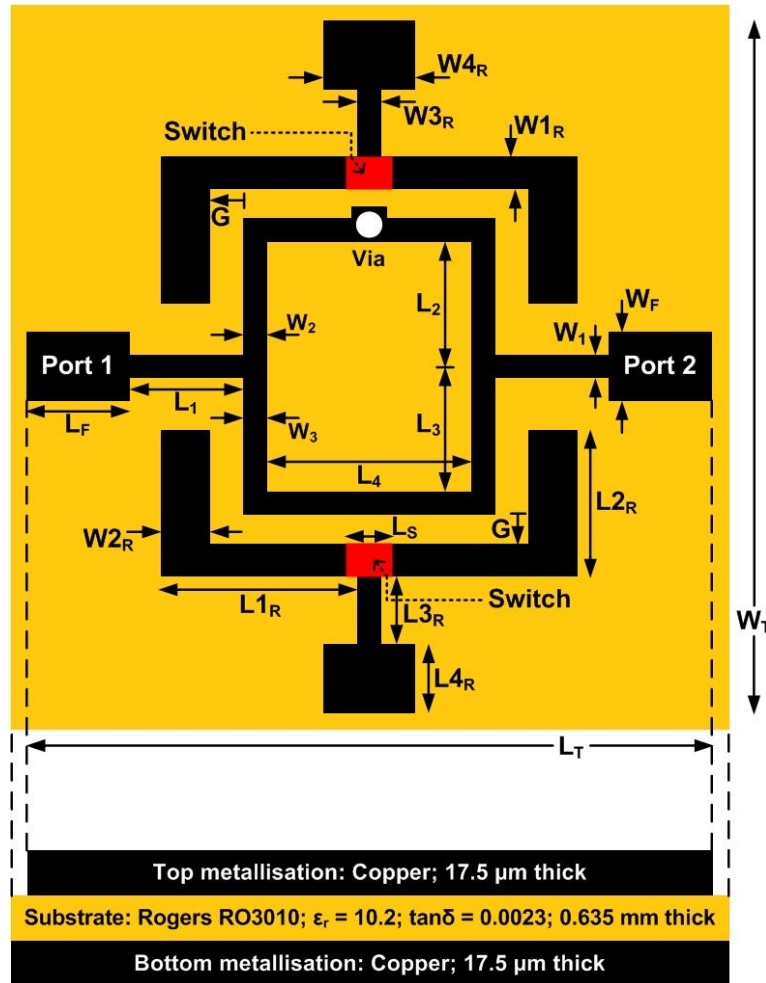


Figure 3.4-1: Geometry of the filter.

Table 3.4-3: Values of the dimension parameters of the filter.

Parameter	Value (mm)	Parameter	Value (mm)
W_T	13.4	W_{1R}	0.5
L_T	16	L_{1R}	2.75
W_F	0.7	W_{2R}	0.6
L_F	5	L_{2R}	2.6
W_1	0.4	W_{3R}	0.5
L_1	0.9	L_{3R}	1.3
W_2	0.5	W_{4R}	2.3
L_2	2.4	L_{4R}	1.8
L_3	2.3	G	0.3
L_4	3.2	L_S	0.52
Diameter _{Via}	0.6		

B) Attainment of Reconfigurability

The filter can be made reconfigurable in order to control the behaviour of the notchband. This can be done by placing switching elements at the two points indicated in red in the geometry of the filter given in Figure 3.4–1. These two points are where the stepped impedance resonators meet the connecting transmission line. The length of the switching points should be at least 0.02 mm larger than the width of the connecting transmission line so as to cover the width of the connecting transmission line in its entirety.

Switching elements placed at the two points would effectively be dividing each three-section resonator into three subsections: with two of the subsections being the two arms of the stepped impedance resonator and the third subsection being the connecting transmission line and the open-circuited stub. This breakdown is shown in Figure 3.4–2. In the switch OFF state of the switching elements, there would be no connection between the three subsections and, thus, there would be no flow of current. This should result in a passband without any notchband present within. On the other hand, in the switch ON state of the switching elements, the three subsections would all be connected. Current will flow in the three-section resonator. Consequently, resulting in a notchband.

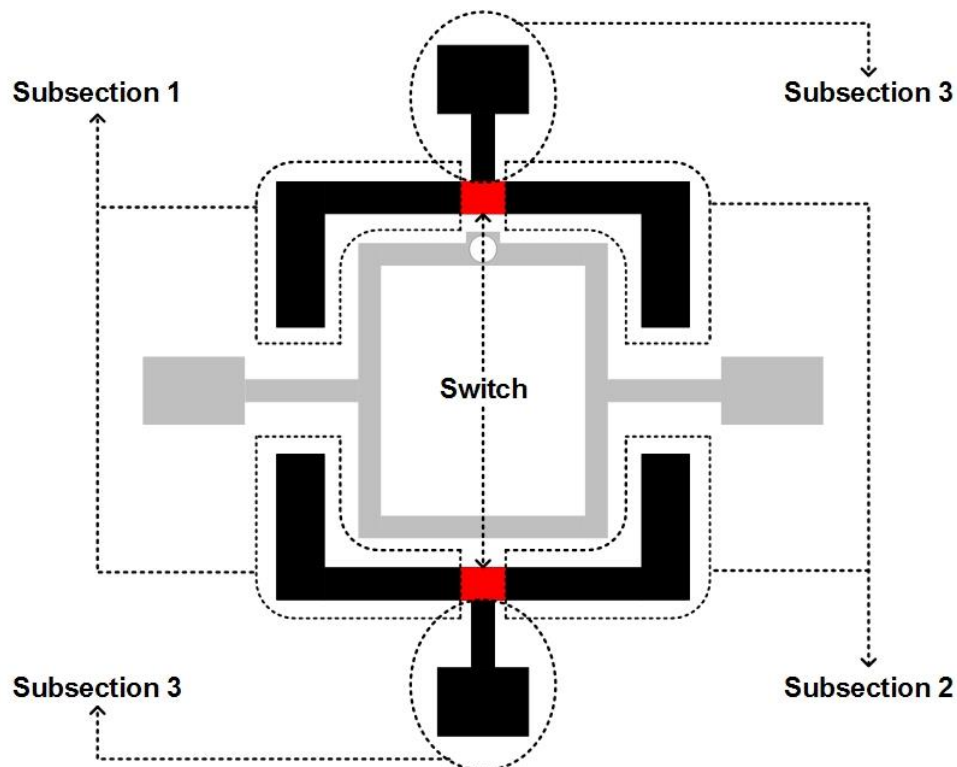


Figure 3.4–2: Breakdown of the notchband structure.

C) Fabrication of Final Layout

The proposed bandpass filter structure is designed on a Rogers RO3010 substrate of a thickness of 0.635 mm, having a dielectric permittivity of $\epsilon_r = 10.2$ and a dielectric loss factor of $\tan \delta = 0.0023$. It is modelled and simulated using the commercial full-wave electromagnetic simulation software program Sonnet. A photograph of the fabricated PCB filter is shown in Figure 3.4–3.



Figure 3.4–3: Photograph of the fabricated PCB filter.

3.4.3: Results

A) S-parameters using Equivalent Circuit Model

The equivalent lumped element circuit model of the bandpass filter given in Figure 3.3–3 was simulated using the final values from Table 3.4–2. The plots of the obtained S-parameters are shown in Figure 3.4–4. The S-parameters show a 3 dB passband of the filter from 2.54 GHz to 12.95 GHz. The insertion loss of the filter at the centre frequency of 5.74 GHz is negligible. The exceptionally low insertion loss is due to the results being a simulation of ideal lumped elements which do not include the actual metallisation losses, substrate losses, or tolerances of the materials used which would be present in fabricated prototypes of the bandpass filter. The return loss of the filter is more than 16.4 dB in the passband region. There are three poles present at 3.34 GHz, 5.73 GHz and 9.84 GHz.

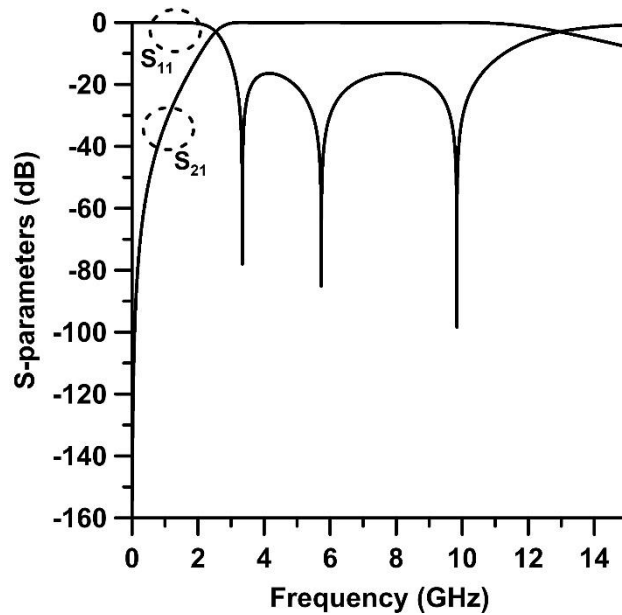


Figure 3.4–4: S-parameters of the equivalent lumped element circuit model of the filter.

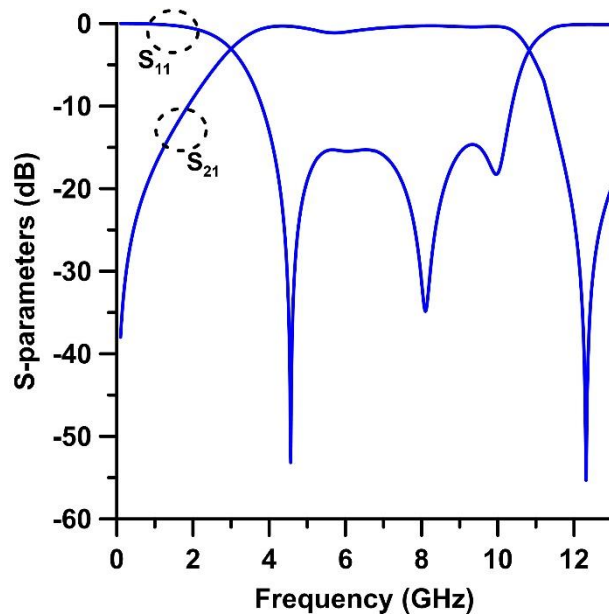
B) S-parameters using PEC based Switches

The bandpass filter from Figure 3.4–1, with its dimensions given in Table 3.4–2, was electromagnetically simulated in Sonnet. In order to determine the results of the filter in switch OFF state and switch ON state without the use of lossy switching elements, the simulations for the two states were carried out using gaps and PEC based switches. The switch OFF state was simulated by leaving gaps at the two points wherein the actual switches would be placed. Whereas, the filter in the switch ON state was simulated by placing PEC metallic patches at the two points.

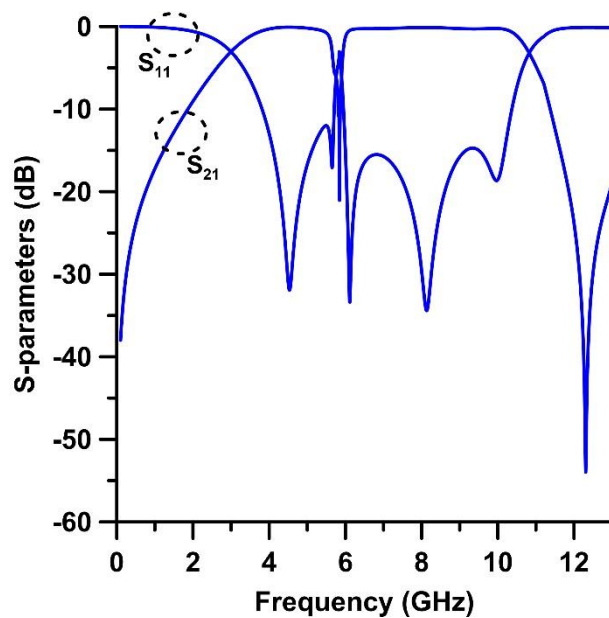
The obtained S-parameters from the simulation of the bandpass filter in the switch OFF state are shown in Figure 3.4–5 (a). The 3 dB passband of the filter is about 3.01 GHz to 10.79 GHz; which covers the required UWB frequency range. The passband region exists within the entire aforementioned range. The centre frequency of the filter is at 5.7 GHz. The insertion loss at this point is 0.1 dB. The return loss of the filter within the passband is more than 14.7 dB. The three poles of the filter can be seen at 4.57 GHz, 8.1 GHz and 9.96 GHz.

The results of the simulation of the bandpass filter in the switch ON state are shown in Figure 3.4–5 (b). The results show the 3 dB passband of the filter remains almost unchanged; being at 3.01 GHz to 10.8 GHz. However, the insertion loss in the passband has increased to 0.3 dB. This is due to the extra notchband metallisation. The notchband metallisation is in work because of the PEC metallic patches. The three subsections of the three-section resonator are connected to each other and,

hence, the resonator is coupled with the rest of the filter structure. Therefore, within the passband, a single notchband is introduced. The notchband is present at 5.8 GHz and is attained at an insertion loss of 21.1 dB. This infers that the bandpass filter in switch ON state is able to reject the interfering WLAN band.



(a)



(b)

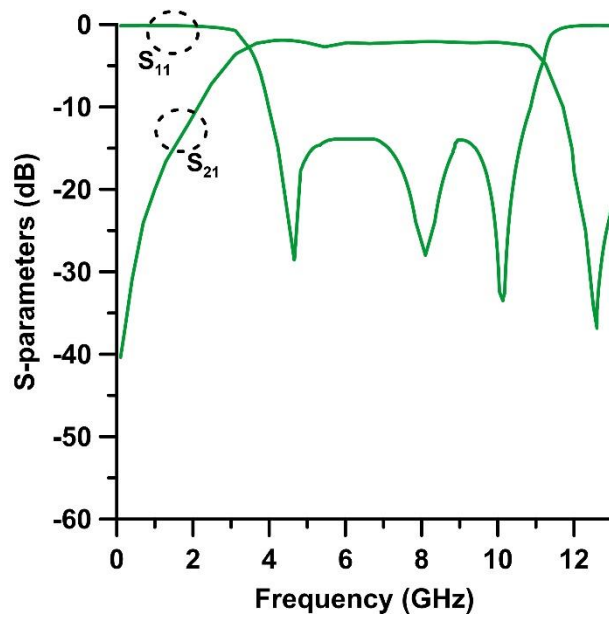
Figure 3.4–5: S-parameters of the filter using PEC based switches in the (a) switch OFF and (b) switch ON states.

C) S-parameters using Graphene based Switches

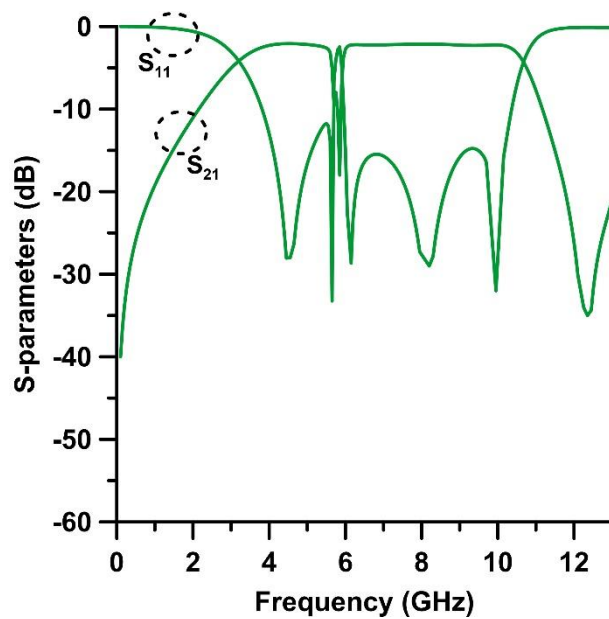
The values of the varying surface resistance and the varying surface reactance of Graphene based switches were calculated using (3.1)–(3.4) in MATLAB; where the relaxation time, τ , was 5 ps. The Graphene based switches are implemented in Sonnet as a “General” metal type and are placed in the filter structure at the two points marked for switching elements in Figure 3.4–1. The programming software programs SonnetLab and MATLAB are used to electromagnetically simulate the filter in Sonnet using the programming code given in Appendix B. The filter is simulated twice: first with the Graphene based switches in switch OFF state and then with the Graphene based switches in switch ON state.

The resulting S-parameters of the bandpass filter in switch OFF state are shown in Figure 3.4–6 (a). The 3 dB passband of the filter appears to be from 3.35 GHz to 10.96 GHz. The calculated centre frequency is at 6.06 GHz and the insertion loss of the filter in the passband is 0.9 dB. In switch OFF state, the Graphene based switches act like insulators and, thus, current does not flow in the coupled three-section resonator. Hence, there is no notchband present within the passband region. This allows the filter to cover the 5.8 GHz WLAN band. The return loss of the filter is more than 13.9 dB in the passband region. The three poles are present at 4.67 GHz, 8.1 GHz and 10.13 GHz.

The S-parameters of the bandpass filter in switch ON state are shown in Figure 3.4–6 (b). The 3 dB passband of the filter is about 3.25 GHz to 10.65 GHz. The insertion loss at the calculated centre frequency of 5.88 GHz is about 1.1 dB. The Graphene based switches behave like conductors in switch ON state. This allows the flow of current in the coupled three-section resonator. Therefore, a notchband is introduced in the passband of the filter. The single notchband is present at 5.85 GHz — rejecting the WLAN band — at an insertion loss of about 18 dB.



(a)



(b)

Figure 3.4–6: S-parameters of the filter using Graphene based switches in the (a) switch OFF and (b) switch ON states.

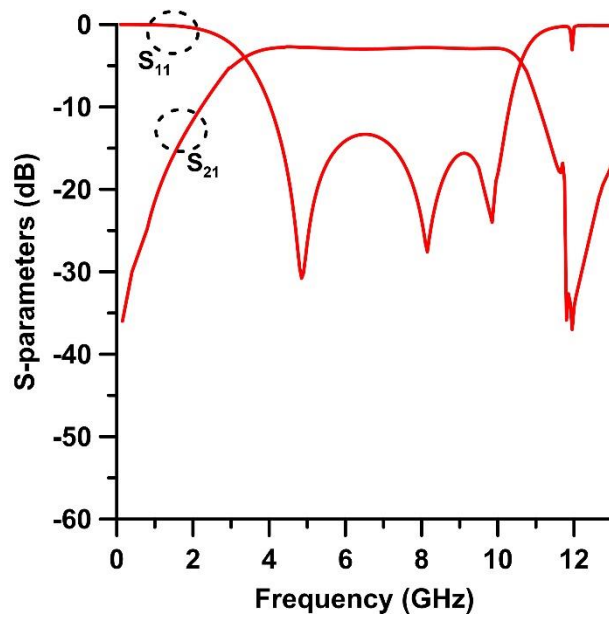
D) S-parameters using PIN Diodes

For a comparison with the PEC based switches and the Graphene based switches, and for the verification of actual results, a prototype of the bandpass filter from Figure 3.4–1 is fabricated. PIN diodes are used as the switching elements for the fabricated prototype. The PIN diodes used are NXP BAP65–02. This type has been

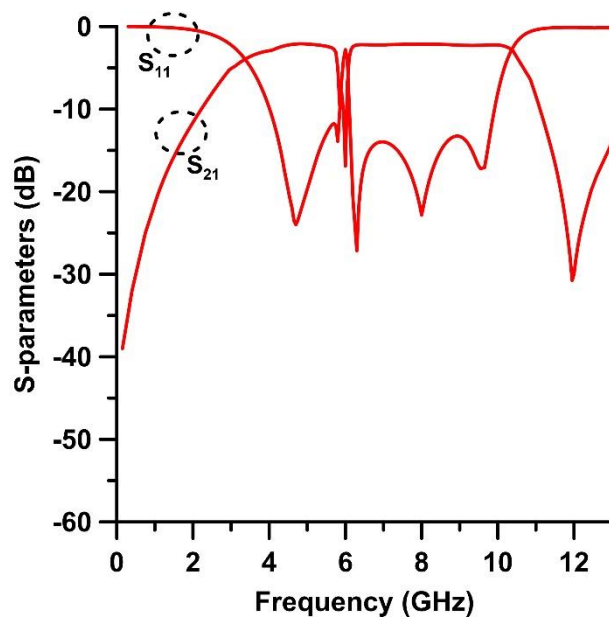
used since its specifications — a resistance of 0.9Ω , an inductance of 0.6 nH and a capacitance of 0.8 pF [3-19] — correspond with the switching circuit parameters of the Graphene based switches used. The PIN diodes are powered on by supplying an external DC voltage of 3 V and a current of 1 mA . The DC blocking capacitance is 33 pF and a resistor of $1 \text{ k}\Omega$ is used for biasing. The S-parameters of the fabricated prototype of the bandpass filter with the PIN diodes are measured using an Agilent E8361A PNA Network Analyser.

The results of the bandpass filter in switch OFF state obtained from the network analyser are shown in Figure 3.4–7 (a). The measured passband region exists within 3.3 GHz to 10.75 GHz . The calculated centre frequency of the filter is shifted to 5.81 GHz and the passband is measured at an insertion loss of 1.1 dB . Since the filter is in the switch OFF state because of the reverse-biasing of the PIN diodes, the three-section resonator is disconnected. Hence, there is no notchband present within the passband of the filter. The return loss of the filter within the passband is decreased as compared with the other switches, but is more than 13.3 dB . Similarly, the three poles, present at 4.85 GHz , 8.15 GHz and 9.85 GHz , are decreased in their values as well.

The results of the bandpass filter in switch ON state are given in Figure 3.4–7 (b). The passband has been measured from 3.25 GHz to 10.4 GHz . The insertion loss of the filter in the passband is increased to 1.7 dB . In this switch ON state, since the PIN diodes are forward-biased, the three-section resonators are coupled with the rest of the filter structure. Therefore, a notchband is introduced within the passband of the filter. The notchband is present at 6 GHz and its achieved insertion loss rejection is 16.9 dB .



(a)



(b)

Figure 3.4–7: S-parameters of the filter using PIN diodes in the (a) switch OFF and (b) switch ON states.

3.4.4: Summary of Presented Results

The results of the bandpass filter are summarised in Table 3.4–4.

It can be seen from the table that although the fractional bandwidth obtained using each of the switches meets the required specification of the filter, the passband

region using some of the switches does not meet the required specification. This implies that the lengths of the resonators need to be optimised further in order to achieve the best possible match.

Similarly, in switch ON state, the notchband is present at 5.8 GHz using PEC based switches, at 5.85 GHz using Graphene based switches and at 6 GHz using PIN diodes. While the frequency of the notchband obtained using PEC based switches is ideal, the frequencies of the notchband attained using Graphene based switches and PIN diodes are not and are slightly shifted. While they are acceptable keeping in view the size limitations within the plotting cells (mesh size) of the electromagnetic software programs and due to the fabrication tolerances and discrepancies, the lengths of the coupled three-section resonators can be adjusted further so as to obtain the precise or the near-precise frequency.

The summary table states that the insertion loss rejection achieved by the filter at the notchband frequency in the switch ON state is at 21.1 dB using PEC based switches, 18 dB using Graphene based switches and 16.9 dB using PIN diodes. PEC based switches give a higher rejection due to them being a simulation and lossless. The rejections using Graphene based switches and PIN diodes are nearer to each other because Graphene based switches include most losses and the rejection obtained using PIN diodes is a measured value.

Table 3.4–4: Summary of the resulting S-parameters of the filter in the switch OFF and switch ON states using the equivalent circuit model, PEC based switches, Graphene based switches and PIN diodes.

Switch Type	Switch State	Passband (GHz)	FBW (%)	Notchband Frequency (GHz)	Notchband Rejection (dB)
ECM	n/a	2.54–12.95	181.51	n/a	n/a
PEC	OFF	3.01–10.79	136.52	None present	n/a
	ON	3.01–10.80	136.63	5.8	21.1
GbS	OFF	3.35–10.96	125.60	None present	n/a
	ON	3.25–10.65	125.78	5.85	18
PIN	OFF	3.30–10.75	125.10	None present	n/a
	ON	3.25–10.40	123.00	6	16.9

3.5: Design of a Frequency Reconfigurable Filter with High Linearity and Independently Controlled Dual Notchband for UWB Applications

3.5.1: Specifications and Initial Parameters

This section presents a reconfigurable bandpass filter based on the specifications given in Table 3.5–1. The specifications require a third-order filter, having a ripple level of 0.1 dB and operating at the lower UWB range of 3.1–5.2 GHz. Additionally, the filter has to have a microstrip-based feeding method; where the characteristic impedance of the feed network and the system should be 50 Ω . Furthermore, the filter should be fabricated via PCB technology. The specifications further ask that there should be dual notchband present for the rejection of the interfering IEEE 802.16 WiMAX band operating at 3.5 GHz and the IEEE C-band satellite communication system band operating at 4.2 GHz. Based on the specifications, the lowpass prototype element values are determined using Table 3.3–1. The three lowpass prototype element values are $g_1 = 1.0316$, $g_2 = 1.1474$ and $g_3 = 1.0316$.

Table 3.5–1: Required specifications of the filter.

Parameter	Description of Parameter	Value
Filter	Type of filter	Chebyshev
Technology	Fabrication technology	PCB
Feed	Feeding method	Microstrip
Z_0	Characteristic impedance of system	50 Ω
n	Order of filter	3
L_R	Maximum ripple level within passband	0.1 dB
f_L	Lower passband frequency	3.1 GHz
f_H	Upper passband frequency	5.2 GHz
f_C	Centre frequency	4.02 GHz
FBW	Fractional bandwidth	$\geq 52.3\%$
n_{NB}	Number of notchband	Dual
f_{NB1} and f_{NB2}	Notchband frequencies	3.5 and 4.2 GHz

3.5.2: Realised Structure and Final Parameters

A) Final Layout

The equivalent lumped element circuit model of the bandpass filter without its notchband structures is the same one as shown in Figure 3.3–3. Equations (3.10)–(3.13) are used to convert the lowpass prototype element values to the bandpass values. The final values of the lumped elements are given in Table 3.5–2; where $Lg_1 = L_P$, $Cg_1 = C_P$, $Lg_2 = L_S$, $Cg_2 = C_S$, $Lg_3 = L_P$ and $Cg_3 = C_P$.

Table 3.5–2: Values of the lumped elements of the filter.

Element	Value (nH)	Element	Value (pF)
Lg_1	1.0049	Cg_1	1.5637
Lg_2	4.3480	Cg_2	0.3614
Lg_3	1.0049	Cg_3	1.5637

The geometry of the final bandpass filter is given in Figure 3.5–1; with the values of its dimension parameters given in Table 3.5–3. Moreover, the equivalent transmission line circuit model of the final layout of the filter is presented in Figure 3.5–4; with the impedances and the electrical lengths of the respective transmission lines given in Table 3.5–3. Before optimisation, transmission lines $A = B = E = F = H = I$. The filter is designed with a centre frequency of 4.02 GHz. It is inductively coupled to the source and the load and is stimulated via ports 1 and 2; where the characteristic impedance, Z_0 , of the transmission feed lines is 50Ω . It is a third-order filter: comprising a half-wavelength, $\lambda_g/2$, resonator (a combination of transmission lines H and I) placed between a pair of short-circuited quarter-wavelength, $\lambda_g/4$, resonators (transmission lines A and B); where λ_g is the guided wavelength at the centre frequency of 4.02 GHz. The three resonators have the same impedance of 109.7Ω , translating to a transmission line width of 1.2 mm. In order to shrink the size of the filter and utilise a common ground via, the two quarter-wavelength resonators are folded in such a way that one end of each is connected to the same single via. A shunt quarter-wavelength long line (transmission line G), of an impedance 77.8Ω , is connected with the middle of the half-wavelength resonator. The other end of the shunt line leads to the middle of an open-circuited half-wavelength line (a combination of transmission lines E and F), which lies inside the filter. In all the above instances, λ_g is the guided wavelength at the centre frequency of 4.02 GHz. Since the widths — and thus the impedances —

of the feed ports/transmission feed lines and the filter resonators are different, for the efficient power transfer between them, impedance transformation is required. For this purpose, stepped impedance matching is employed to transform the impedance between the transmission feed lines and the filter resonators. This can be seen in Figure 3.5–1.

The dual notchband are introduced within the passband of the filter by the coupling of an identical, but inverted, pair of U-shaped resonators. The resonator for the notchband at 3.5 GHz is coupled from outside with the outer half-wavelength filter resonator. This notchband resonator is represented by a combination of transmission lines *J* and *K* in Figure 3.5–2. Whereas the resonator for the notchband at 4.2 GHz is placed inside the filter structure; to be coupled with the inner half-wavelength line. This notchband resonator is represented by a combination of transmission lines *C* and *D* in Figure 3.5–2. The two notchband resonators are placed in the symmetry plane of the filter. Both resonators are half-wavelength long at their respective notchband frequency and are coupled with the main filter structure at a gap, *G*, of 0.3 mm. The dashed-crosses represent couplings. The resonators build sharp rejections at the desired frequency bands.

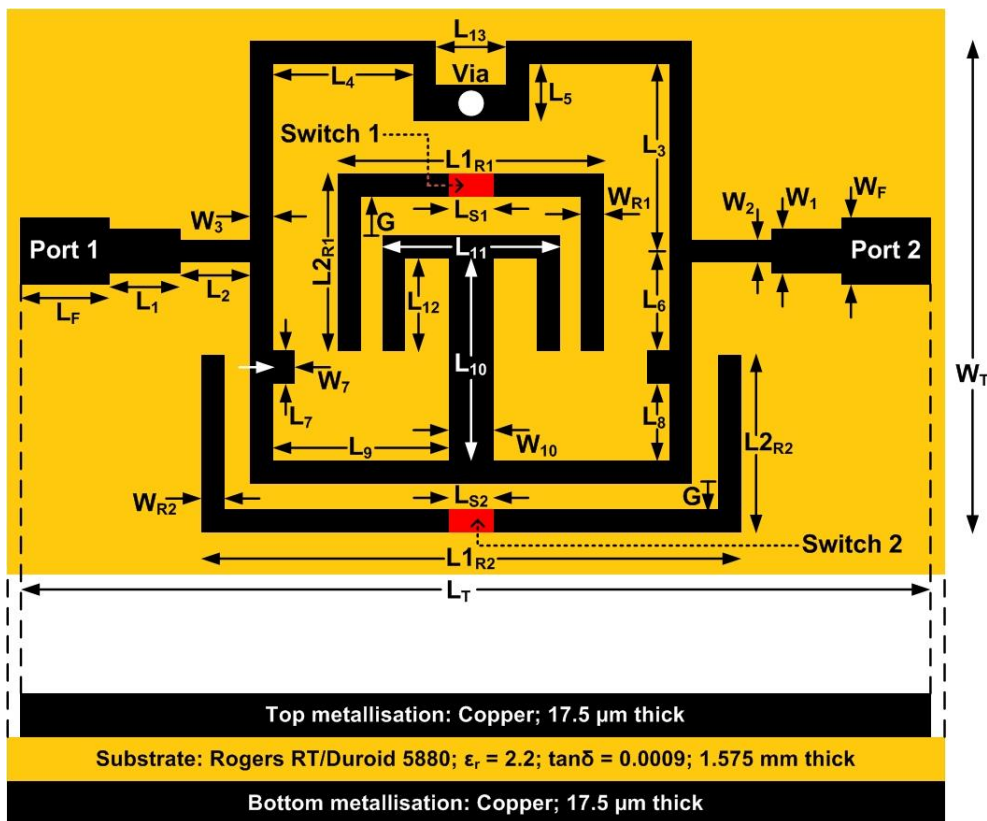


Figure 3.5–1: Geometry of the filter.

Table 3.5–3: Values of the dimension parameters of the filter.

Parameter	Value (mm)	Parameter	Value (mm)
W_T	21.9	L_9	5.7
L_T	31.8	W_{10}	2.4
W_F	5.1	L_{10}	12.6
L_F	2.4	L_{11}	9
W_1	2.7	L_{12}	6
L_1	3.9	L_{13}	1.8
W_2	0.9	Diameter _{Via}	0.6
L_2	1.5	W_{R1}	1.2
W_3	1.2	L_{1R1}	12
L_3	7.95	L_{2R1}	8.7
L_4	4.8	W_{R2}	1.2
L_5	2.1	L_{1R2}	19.8
L_6	4.05	L_{2R2}	8.4
W_7	1.5	G	0.3
L_7	2.7	L_{S1}	0.5
L_8	3.3	L_{S2}	0.5

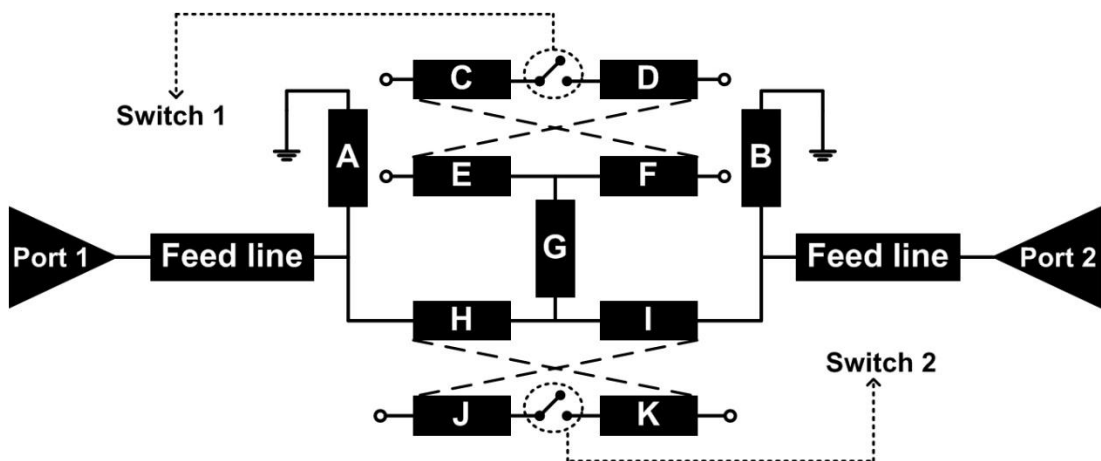


Figure 3.5–2: Equivalent transmission line circuit model of the filter.

Table 3.5–4: Values of the transmission line parameters of the filter.

Transmission Line	Impedance (Ω)	Electric Length (degrees)
A	109.7	$\lambda_g/4$ at 4.02 GHz
B	109.7	$\lambda_g/4$ at 4.02 GHz
C	109.7	$\lambda_g/4$ at 4.20 GHz
D	109.7	$\lambda_g/4$ at 4.20 GHz
E	109.7	$\lambda_g/4$ at 4.02 GHz
F	109.7	$\lambda_g/4$ at 4.02 GHz
G	77.8	$\lambda_g/4$ at 4.02 GHz
H	109.7	$\lambda_g/4$ at 4.02 GHz
I	109.7	$\lambda_g/4$ at 4.02 GHz
J	109.7	$\lambda_g/4$ at 3.50 GHz
K	109.7	$\lambda_g/4$ at 3.50 GHz

B) Attainment of Transmission Zeroes

This section refers to the transmission lines from the equivalent transmission line circuit model in Figure 3.5–2. Transmission line G generated a transmission zero originally at 4.06 GHz. But since the line is connected to transmission lines E and F, the overall length increases; causing the transmission zero, $TZ1$, to move to 2.15 GHz. The first harmonic of $TZ1$ at $3f_0$ produces another transmission zero, $TZ3$, at 6.45 GHz. The combination of transmission lines C and D is essentially for the notchband at 3.5 GHz, but its first harmonic at $2f_0$ produces a transmission zero, $TZ4$, at 7 GHz. Similarly, the first harmonic, at $2f_0$, by the combination of transmission lines J and K gives a transmission zero, $TZ5$, at 8.4 GHz. Together transmission lines E and F generate a transmission zero, $TZ2$, which varies between 5.63 GHz and 5.77 GHz. All the generated transmission zeroes significantly improve attenuation and selectivity in the lower and upper stopbands. They will be shown in the subsequent results section.

C) Attainment of Reconfigurability

The filter can be made reconfigurable in order to control the behaviour of the notchband. In order to achieve reconfigurable characteristics, switching elements are placed at the two points indicated in red in the geometry of the filter given in Figure 3.5–1. These two points are the mid-points of the notchband resonators. The

length of the switching points should be at least equal to the length of the switching elements and the width of the switching points should cover the entire width of the notchband resonators.

Switching elements placed at the two points would effectively be dividing each notchband resonator into two sections of equal lengths. In other words, each resonator would effectively consist of two quarter-wavelength long transmission lines conjoined with a switching element. This is also illustrated in Figure 3.5–2; where the 4.2 GHz notchband resonator is represented by quarter-wavelength long transmission lines *C* and *D* with a switch between them and, likewise, the 3.5 GHz notchband resonator is represented by quarter-wavelength long transmission lines *J* and *K* with a switch between them. In the switch OFF state of the switching elements, there would be no connection between the two sections. Therefore, there would be no flow of current; resulting in an entirely notchband-free passband. Conversely, in the switch ON state of the switching elements, the two sections of both notchband resonators would be connected to each other. As a result of the connection, the subsequent length of the resonators becomes half-wavelength at their respective notchband frequency. Current will then flow in the resonators. Consequently, dual notchband within the passband are produced.

Since the two notchband resonators are coupled independently of each other, each notchband can be controlled separately by just using the switching element of the required notchband. Hence, the filter has four possible reconfigurable states in which it can be operational. These states and the corresponding switch conditions are given in Table 3.5–5.

Table 3.5–5: Possible reconfigurable states of the filter.

Filter State	Switch 1 Position	Switch 2 Position	Resulting Notchband
1	OFF	OFF	None present
2	ON	ON	3.5 GHz and 4.2 GHz
3	ON	OFF	4.2 GHz only
4	OFF	ON	3.5 GHz only

D) Fabrication of Final Layout

The proposed bandpass filter structure from Figure 3.4–1 is designed on a Rogers RT5880 substrate of a thickness of 1.575 mm, having a dielectric permittivity of $\epsilon_r = 2.2$ and a dielectric loss factor of $\tan \delta = 0.0009$. It is modelled and simulated

using the commercial full-wave electromagnetic simulation software program Sonnet. A photograph of the fabricated PCB filter is shown in Figure 3.5–3.

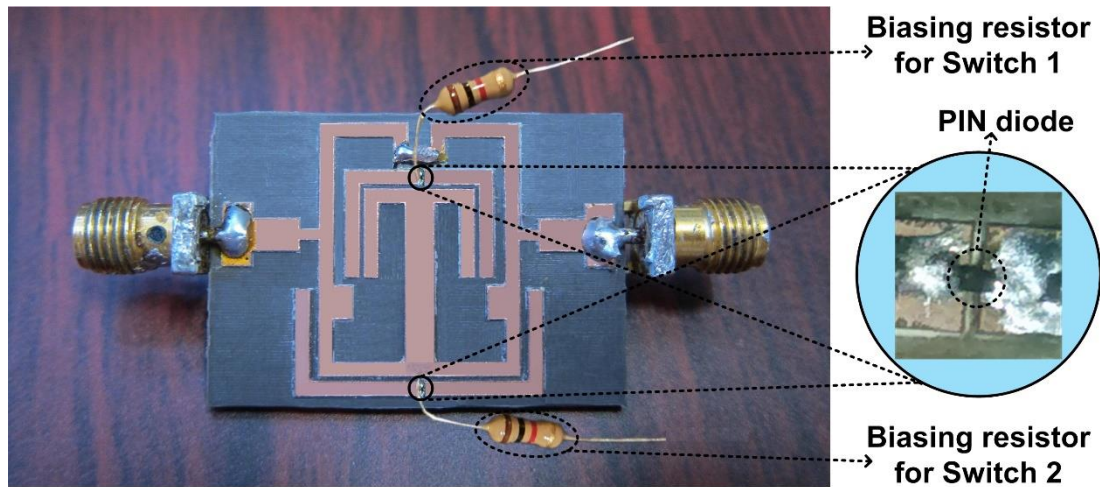


Figure 3.5–3: Photograph of the fabricated PCB filter.

3.5.3: Results

A) S-parameters using Equivalent Circuit Model

The equivalent lumped element circuit model of the bandpass filter given in Figure 3.3–3 was simulated using the final values from Table 3.5–2. The obtained S-parameters are shown in Figure 3.5–4. The plots show a 3 dB passband of the filter from 2.81 GHz to 5.73 GHz. The insertion loss of the filter at the centre frequency of 4.02 GHz is negligible. The extremely low insertion loss is because of the results being a simulation of ideal lumped elements which do not include any actual metallisation losses, substrate losses, or tolerances of the materials used which would be present in fabricated prototypes of the bandpass filter. The return loss of the filter is more than 16.4 dB in the passband region. There are three poles present at 3.21 GHz, 4.02 GHz and 5.03 GHz.

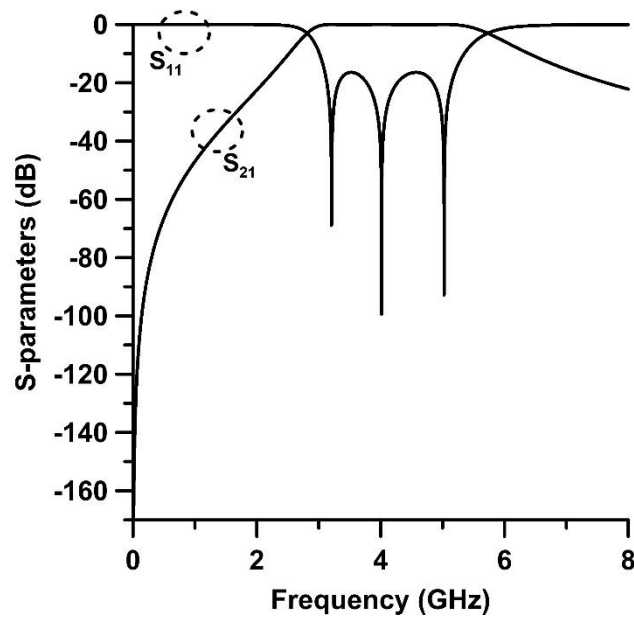


Figure 3.5-4: S-parameters of the equivalent lumped element circuit model of the filter.

B) S-parameters with PEC based Switches

The bandpass filter from Figure 3.5-1, with its dimensions given in Table 3.5-3, was electromagnetically simulated in Sonnet. In order to determine the simulation results of the filter in the four reconfigurable states without the use of lossy switching elements, the switches' positions/conditions were configured using gaps and PEC based switches. The switch OFF position was simulated by leaving gaps at the two points wherein the actual switches would be placed. Whereas, the switch ON position was simulated by placing PEC metallic patches at the two points. The filter was then simulated using the combinations of the switching positions given in Table 3.5-5.

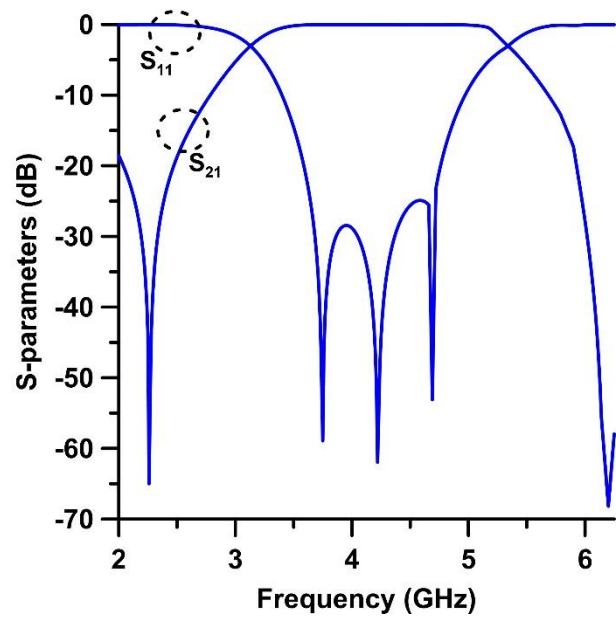
The obtained S-parameters from the simulation of the bandpass filter in state 1 are shown in Figure 3.5-5 (a). The 3 dB passband of the filter is about 3.1 GHz to 5.34 GHz; which corresponds to the lower UWB frequency range. Since both switches are in OFF position, there are no notchband present within the passband. The centre frequency of the filter is at 4.07 GHz. The insertion loss at this point is 0.03 dB. The return loss of the filter within the passband is more than 24.9 dB. The three poles of the filter can be seen at 3.75 GHz, 4.22 GHz and 4.69 GHz.

The results of the simulation of the bandpass filter in state 2 are shown in Figure 3.5-5 (b). The results show the 3 dB passband of the filter to be from 3.1 GHz to 5.23 GHz. The centre frequency is at 4.03 GHz. The insertion loss at the centre frequency is increased. This is due to the extra notchband metallisations which are

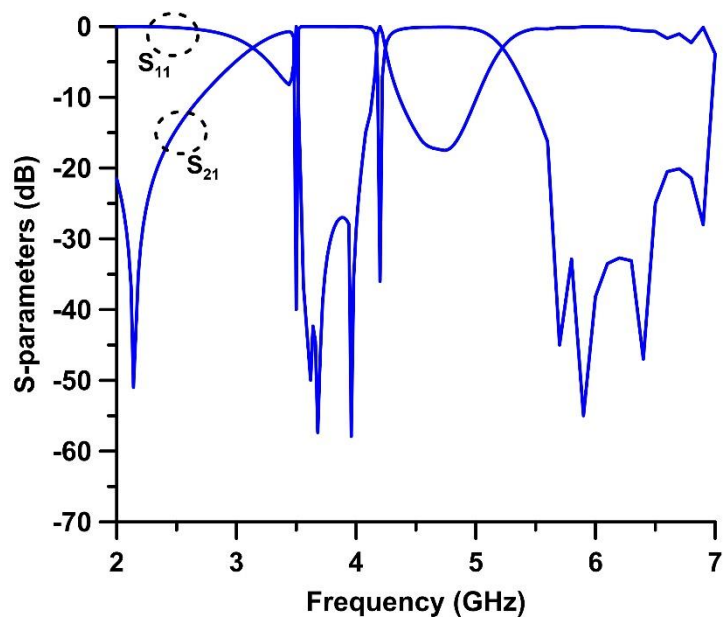
in work. The notchband metallisations are in work because of the PEC metallic patches. The two sections of both notchband resonators are connected to each other and, hence, the resonators are coupled with the rest of the filter structure. Therefore, within the passband, dual notchband are introduced. The dual notchband are present at 3.5 GHz and 4.2 GHz and are attained at an insertion loss of 40 dB and 36 dB respectively. This infers that the bandpass filter in state 2 is able to reject the interfering WiMAX band and the satellite communication system band.

The simulated results of the bandpass filter in state 3 are given in Figure 3.5–5 (c). The 3 dB passband of the filter is about 3.1 GHz to 5.34 GHz. Since only switch 1 is in ON position, only its respective notchband resonator is switched on and fully coupled with the rest of the filter structure. As a result, only one notchband is produced within the passband. The single notchband is present at 4.2 GHz and obtained at an insertion loss of 35 dB. This deduces that the bandpass filter in state 3 is able to reject only the satellite communication system band. Additionally, the attenuation in this state is not as good as state 1, but it is better than state 2. This is because, in this state, only one of the two notchband resonators is switched on.

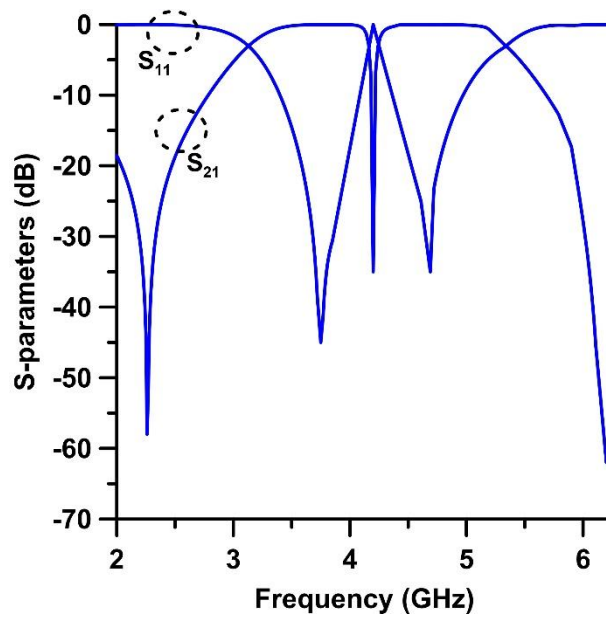
The results of the bandpass filter simulated in state 4 are given in Figure 3.5–5 (d). The 3 dB passband of the filter is from 3.1 GHz to 5.23 GHz. The situation is reversed as compared to state 3: only switch 2 is in ON position and, hence, only its respective notchband resonator is switched on and fully coupled with the rest of the filter structure. This results in only one notchband being produced within the passband. The single notchband is present at 3.5 GHz and obtained at an insertion loss of 45 dB. This indicates that in state 4, the bandpass filter is capable of rejecting only the WiMAX band. Moreover, similar to state 3, the attenuation in this state is not as good as state 1, but it is better than state 2. This is due to only one notchband resonator being switched on.



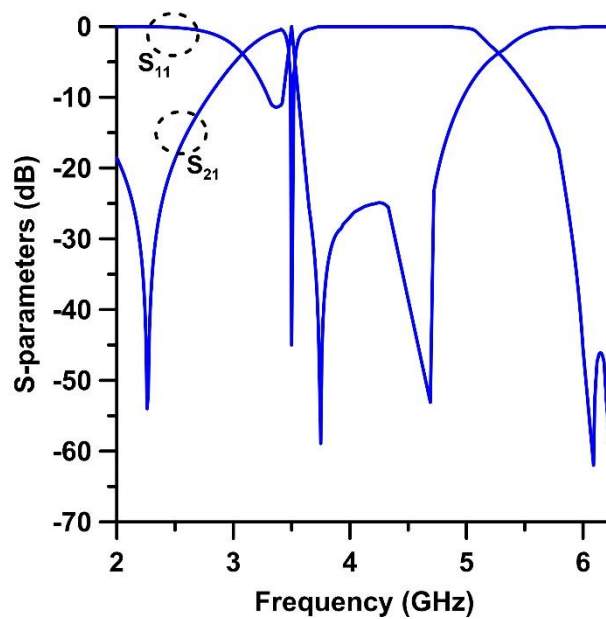
(a)



(b)



(c)



(d)

Figure 3.5-5: S-parameters of the filter using PEC based switches in (a) state 1, (b) state 2, (c) state 3 and (d) state 4.

C) S-parameters with Graphene based Switches

The values of the varying surface resistance and the varying surface reactance of Graphene based switches were calculated using (3.1)–(3.4) in MATLAB; where the relaxation time, τ , was 3 ps. The Graphene based switches are implemented in Sonnet as a “General” metal type and are placed in the filter structure at the two

points marked for switching elements in Figure 3.5–1. For Graphene based switches, the dimension parameters L_{s1} and L_{s2} have a value of 0.6 mm and 0.1 mm respectively. The programming software programs SonnetLab and MATLAB are used to electromagnetically simulate the filter in Sonnet using the programming code given in Appendix B. The filter is simulated four times: each time for one of the each possible reconfigurable states from Table 3.5–5.

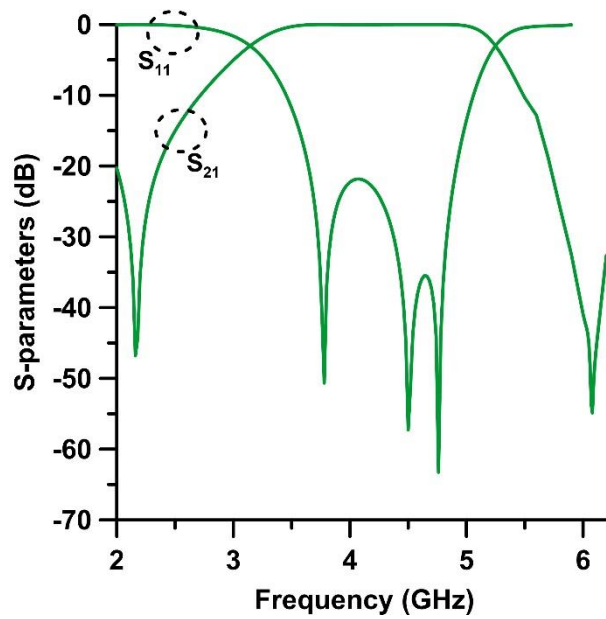
The obtained S-parameters of the bandpass filter in state 1 are shown in Figure 3.5–6 (a). The 3 dB passband of the filter appears to be from 3.15 GHz to 5.33 GHz. The insertion loss of the filter at the centre frequency of 4.1 GHz is 0.08 dB. In switch OFF positions, the Graphene based switches behave like insulators and, thus, current does not flow in the two coupled notchband resonators. Hence, there is no notchband present within the passband region. This allows the filter to cover the 3.5 GHz WLAN band and the 4.2 GHz satellite communication system band. The return loss of the filter is more than 21.8 dB in the passband region. The three poles are present at 3.78 GHz, 4.5 GHz and 4.76 GHz.

The S-parameters of the bandpass filter in state 2 are shown in Figure 3.5–6 (b). The 3 dB passband of the filter is changed, i.e. 3.22 GHz to 5.22 GHz. The insertion loss at the centre frequency of 4.1 GHz is 0.15 dB. In switch ON positions, the Graphene based switches behave like conductors. Since both switches are in ON position, this allows the flow of current in both notchband resonators. Therefore, dual notchband are obtained within the passband of the filter. The two notchband are present at 3.54 GHz, at an insertion loss of 29.2 dB, and at 4.28 GHz, at an insertion loss of 30.2 dB. Because of the notchband resonators, the frequencies of the three poles of the filter are shifted.

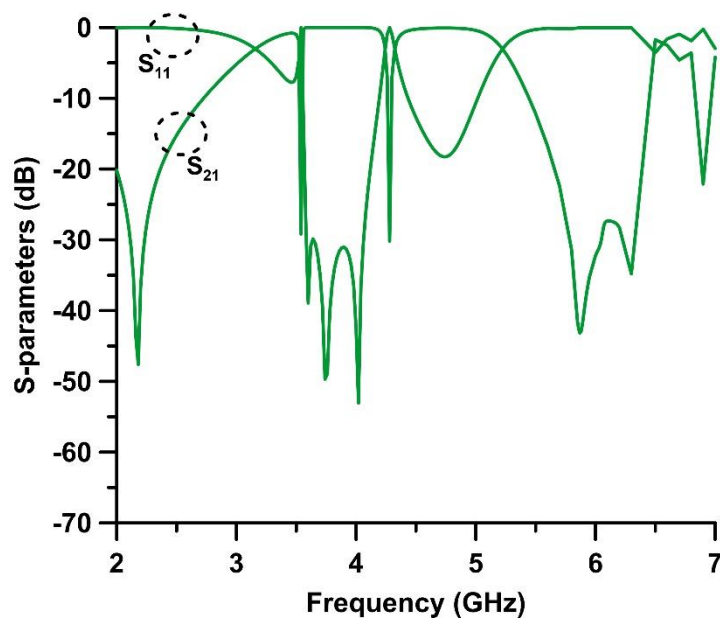
The simulated results of the bandpass filter using Graphene based switches in state 3 are given in Figure 3.5–6 (c). The 3 dB passband of the filter moves to being 3.15 GHz to 5.32 GHz. The insertion loss of the filter is about 0.11 dB. As only switch 1 is in ON position, only its respective notchband resonator is switched on. Accordingly, only one notchband is attained within the passband. The single notchband is present at 4.28 GHz and obtained at an insertion loss of 30 dB. This infers that the bandpass filter operating in state 3 is able to reject only the satellite communication system band.

The results of the bandpass filter simulated in state 4 are given in Figure 3.5–6 (d). The 3 dB passband of the filter shifts once again; becoming 3.2 GHz to 5.25 GHz. The insertion loss of the filter is 0.13 dB. In this state, only switch 2 is in ON position and, therefore, only its respective notchband resonator is switched on. This results in only a single notchband being introduced within the passband: at a frequency of

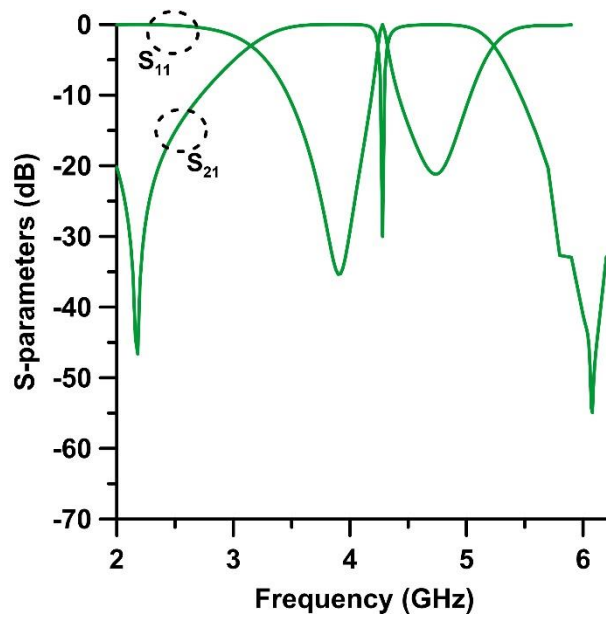
3.54 GHz and at an insertion loss of 37 dB. This denotes that the bandpass filter operating in state 4 is capable of rejecting only the WiMAX band.



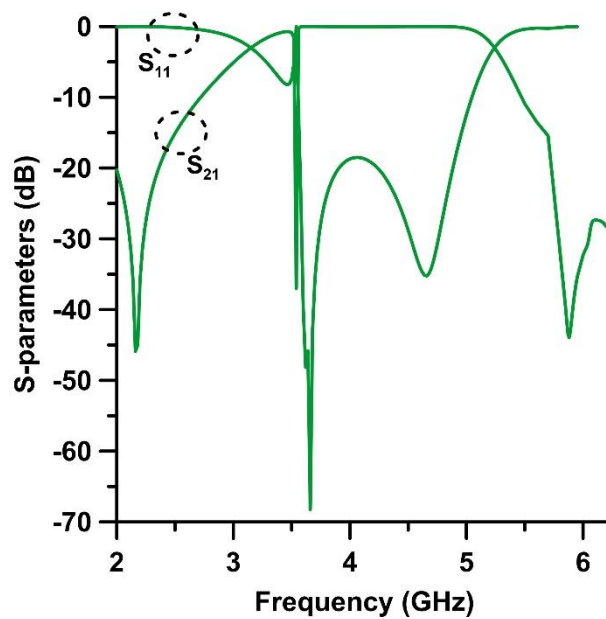
(a)



(b)



(c)



(d)

Figure 3.5–6: S-parameters of the filter using Graphene based switches in (a) state 1, (b) state 2, (c) state 3 and (d) state 4.

D) S-parameters with PIN Diodes

In order to carry out verification of the actual results and also to provide a comparison with the results obtained using the PEC based switches and the Graphene based switches, a prototype of the bandpass filter from Figure 3.5–1 is fabricated. PIN diodes are used as the switching elements for the fabricated

prototype. The PIN diodes used are NXP BAP65–02. This type has been used since its specifications — a resistance of 0.9Ω , an inductance of 0.6 nH and a capacitance of 0.8 pF [3-19] — correspond with the switching circuit parameters of the Graphene based switches used. The PIN diodes are powered on by supplying an external DC voltage of 3 V and a current of 1 mA . The DC blocking capacitance is 33 pF and a resistor of $1 \text{ k}\Omega$ is used for biasing. The S-parameters of the fabricated prototype of the bandpass filter with the PIN diodes are measured in the four reconfigurable states using an Agilent E8361A PNA Network Analyser.

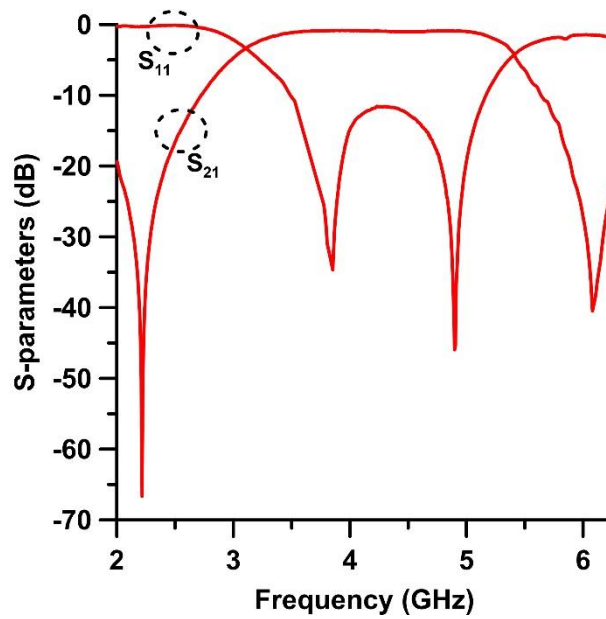
The obtained results of the bandpass filter in state 1 are shown in Figure 3.5–7 (a). The measured passband in the state is about 3.14 GHz to 5.35 GHz . The centre frequency of the filter is shifted to 4.1 GHz and is measured at an insertion loss of 0.7 dB . Since both switches are in OFF position because of the reverse-biasing of the PIN diodes, the two notchband resonators are disconnected. Hence, there is no notchband present within the passband of the filter. The return loss of the filter within the passband is decreased as compared with the PEC based switches and the Graphene based switches, but is more than 11.6 dB . Only two poles can be seen in the measured result. They are present at 3.85 GHz and 4.9 GHz ; and are decreased in their magnitudes as well as compared with the other two switches.

The resulting S-parameters of the bandpass filter in state 2 are given in Figure 3.5–7 (b). The passband has been measured from 3.25 GHz to 5.12 GHz . The insertion loss of the filter at the centre frequency of 4.08 GHz is increased to 1.25 dB . In this state, since both PIN diodes are forward-biased, the two notchband resonators are coupled with the rest of the filter structure. Therefore, dual notchband are introduced within the passband of the filter. The notchband are present at 3.48 GHz and 4.3 GHz and their achieved insertion loss rejection is 19.5 dB and 20.5 dB respectively.

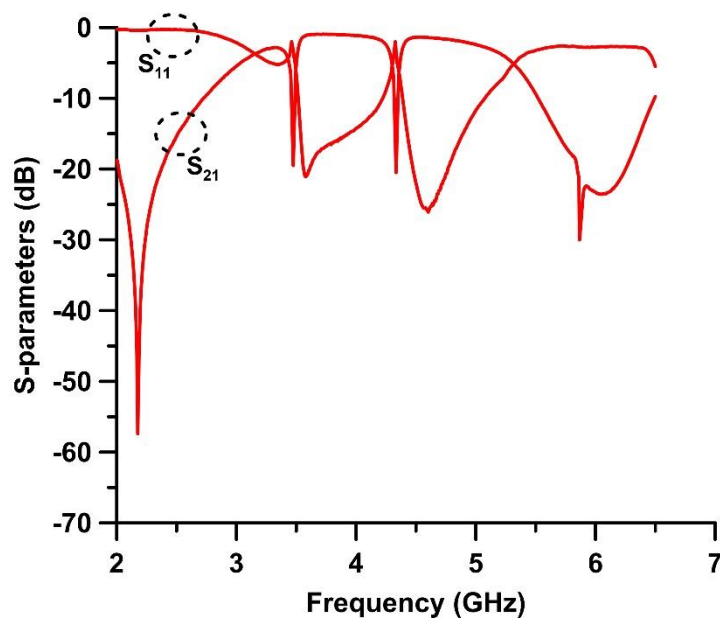
The measured S-parameters of the bandpass filter acquired in state 3 are given in Figure 3.5–7 (c). The passband is present from 3.14 GHz to 5.34 GHz . The insertion loss of the filter in this state is 1.1 dB . Since, of the two PIN diodes, only the one at the switch 1 point is forward-biased, state 3 shows a single notchband at 4.3 GHz which is obtained at an insertion loss of 22 dB .

The measured results of the bandpass filter in state 4 are given in Figure 3.5–7 (d). The passband of the filter exists from $3.24\text{--}5.31 \text{ GHz}$ at an insertion loss of 0.9 dB . In this state, the switching conditions are opposite as compared with state 3: the PIN diode at the switch 2 point is forward-biased and the PIN diode at the switch 1 point is reverse-biased. Therefore, the notchband are also reversed. A passband

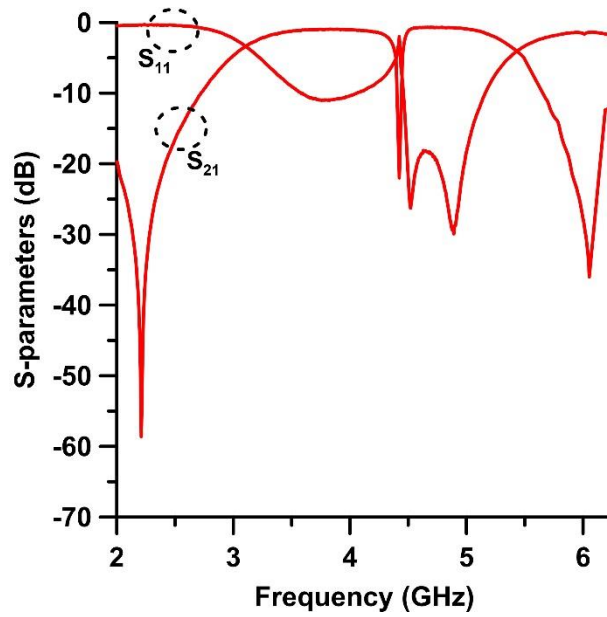
exists at 4.2 GHz and the single notchband is present at 3.49 GHz at an insertion loss of 23 dB.



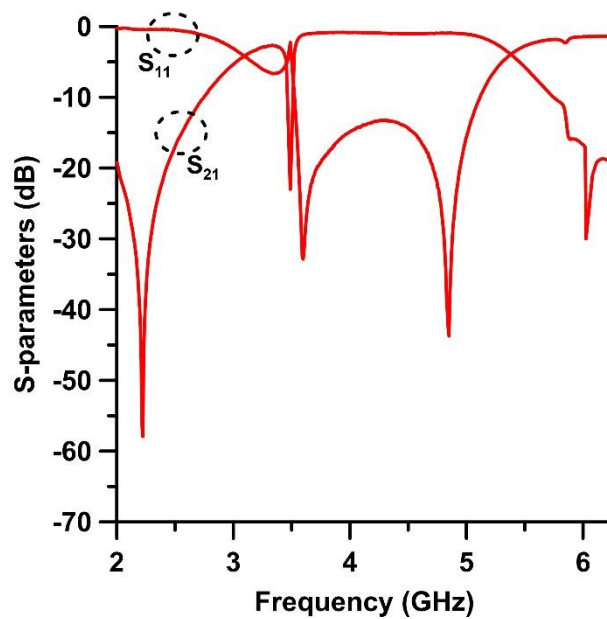
(a)



(b)



(c)



(d)

Figure 3.5–7: S-parameters of the filter using PIN diodes in (a) state 1, (b) state 2, (c) state 3 and (d) state 4.

E) Linearity Performance using PIN Diodes

The non-linearity introduced by PIN diodes is a function from (3.5) of the forward bias current, I_f , and the radio frequency current, i_f , [3-19]. Generally, better linearity may be obtained when the extent of the bias current modulation by the radio

frequency current decreases. This modulation effect can be minimised by deliberately operating at a higher forward bias current [3-19].

For the purpose of validating the high-linearity characteristics of the presented bandpass filter, a 5 MHz QPSK modulation signal was provided to the filter. The filter was evaluated with and without the PIN diodes in state 1 and state 2. The third-order intermodulation performance at various passband frequencies in the two states was measured and has been shown in Figure 3.5–8. Input power between a range of -25 dBm and 10 dBm resulted in very good linearity.

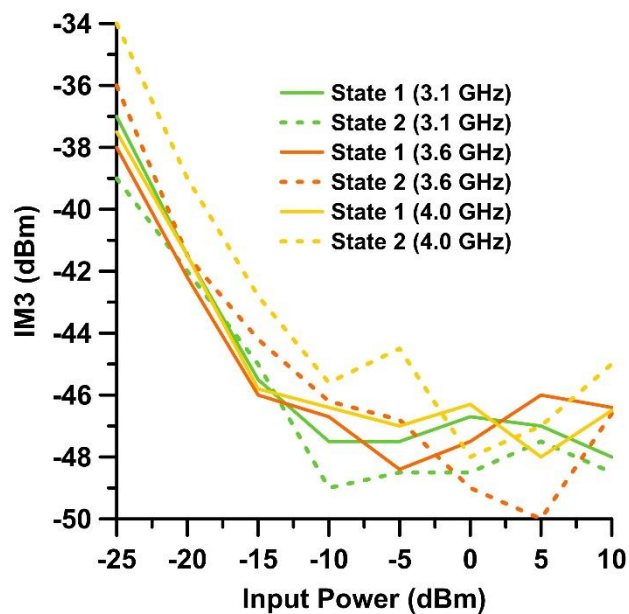


Figure 3.5–8: Linearity performance of the filter using PIN diodes in state 1 and state 2.

3.5.4: Summary of Presented Results

The results of the bandpass filter in the four reconfigurable states are summarised in Table 3.5–6.

It can be seen from the table that while the fractional bandwidths attained using each of the switching elements in most of the reconfigurable states meets the minimum required specification of the filter, the passband frequency range using Graphene based switched and PIN diodes does not fully meet the minimum required specification. This indicates that the lengths of the three resonators of the bandpass filter need to be optimised further in order to achieve the best possible match with the required specifications of the filter.

While the frequencies of the notchband obtained using PEC based switches is ideal, the frequencies of the notchband acquired using Graphene based switches and PIN diodes are not and are slightly shifted. In states 2, 3 and 4, the notchband produced using Graphene based switches and PIN diodes are present at shifted frequency points than the intended frequency points of 3.5 GHz and 4.2 GHz. While these obtained results are acceptable in light of the size limitations within the plotting cells (mesh size) of the electromagnetic software programs and due to the fabrication tolerances and discrepancies, the lengths of the two coupled notchband resonators can to be tuned further with the aim of obtaining the precise or the near-precise notchband frequencies.

It is also observed from the summary table that when using PEC based switches in any state, the insertion loss in the passband is much less than and at the notchband frequencies much high than when using Graphene based switches or PIN diodes. This is due to PEC based switches being a simulation and lossless switches. The insertion losses using Graphene based switches and PIN diodes are closer to each other for the reason that Graphene based switches include most losses and PIN diodes are an actual measurement which include all losses.

Furthermore, the bandpass filter seems to be sensitive at the higher frequencies as seen from the deterioration in the upper stopband of the measured PIN diodes results.

Moreover, as compared with switch 1, switch 2 seems to have a more weakening effect on the filter. This is evident from the results in state 2 and 4; in which when switch 2 is switched on, the upper end of the passband shows more loss, the upper stopband is severely deteriorated and the stopband attenuation is also significantly reduced. Furthermore, switch 2 causes the lower stopband to deteriorate as well; albeit much less than the upper stopband. This can be seen in state 2 and state 4; where the lower end of the passband is pushed forward by 100–110 MHz as compared with state 1 and state 3.

Table 3.5–6: Summary of the resulting S-parameters of the filter in the four reconfigurable states using the equivalent circuit model, PEC based switches, Graphene based switches and PIN diodes.

Switch Type	Filter State	Passband (GHz)	FBW (%)	Notchband Frequency (GHz)	Notchband Rejection (dB)
ECM	n/a	2.81–5.73	72.77	n/a	n/a
PEC	1	3.10–5.34	55.06	None present	n/a
	2	3.10–5.23	52.90	3.5 & 4.2	40 & 36
	3	3.10–5.34	55.06	4.2	35
	4	3.10–5.23	52.90	3.5	45
GbS	1	3.15–5.33	53.20	None present	n/a
	2	3.22–5.22	48.78	3.54 & 4.28	29.2 & 30.2
	3	3.15–5.32	53.01	4.28	30
	4	3.20–5.25	50.02	3.54	37
PIN	1	3.14–5.35	53.92	None present	n/a
	2	3.25–5.12	45.84	3.48 & 4.30	19.5 & 20.5
	3	3.14–5.34	53.73	4.30	22
	4	3.24–5.31	49.91	3.49	23

3.6: References

- [3-1] M. J. Copps, "Revision of part 15 of the commission's rules regarding ultra-wideband transmission systems," Federal Communications Commission, Washington, D.C., United States of America, Report FCC 02-48, pp. 98–153, February 2002.
- [3-2] Electronic Communications Committee, "The protection requirements of radio communications systems below 10.6 GHz from generic UWB applications," European Conference of Postal and Telecommunications Administrations, Helsinki, Finland, Report 64, February 2005.
- [3-3] S. Ullah, M. Ali, M. A. Hussain, and K. S. Kwak, "Applications of UWB Technology," July 2010.
- [3-4] W. Menzel and P. Feil, "Ultra-wideband (UWB) filter with WLAN notch," *IEEE 36th European Microwave Conference*, pp. 595–598, September 2006.
- [3-5] H. Wang, K-W. Tam, S-K. Ho, W. Kang, and W. Wu, "Design of ultra-wideband bandpass filters with fixed and reconfigurable notch bands using terminated cross-shaped resonators," *IEEE Transactions on Microwave Theory and Techniques*, pp. 1–14, January 2014.
- [3-6] M. F. Karim, Y-X. Guo, Z. N. Chan, and L. C. Ong, "Miniaturized reconfigurable and switchable filter from UWB to 2.4 GHz WLAN using PIN diodes," *IEEE MTT-S International Microwave Symposium Digest*, pp. 509–512, June 2009.
- [3-7] Y-H. Chun, H. Shaman, and J-S. Hong, "Switchable embedded notch structure for UWB bandpass filter," *IEEE Microwave and Wireless Components Letters*, vol. 18, no. 9, pp. 590–592, September 2008.
- [3-8] K. Rabbi, L. Athukorala, C. Panagamuwa, J. C. Vardaxoglou, and D. Budimir, "Compact UWB bandpass filter with reconfigurable notched band," *IET Electronics Letters*, vol. 49, no. 11, pp. 709–711, May 2013.
- [3-9] G. L. Matthaei, "Interdigital bandpass filters," *IEEE Transactions on Microwave Theory and Techniques*, vol. 10, no. 6, pp. 479–491, November 1962.
- [3-10] J. S. Wong, "Microstrip tapped-line filter design," *IEEE Transactions on Microwave Theory and Techniques*, vol. 27, no. 1, pp. 44–50, January 1979.

- [3-11] E. G. Cristal, "Tapped-line coupled transmission lines with application to interdigital and combline filters," *IEEE Transactions on Microwave Theory and Techniques*, vol. 23, no. 12, pp. 1007–1012, December 1975.
- [3-12] G. M. Rebeiz and J. B. Muldavin, "RF MEMS switches and switch circuits," *IEEE Microwave Magazine*, vol. 2, no. 4, pp. 59–71, December 2001.
- [3-13] D. H. Auston, "Picosecond optoelectronic switching and gating in silicon," *Applied Physics Letters*, vol. 26, no. 3, pp. 101–103, February 1975.
- [3-14] A. Chauraya, "Photoconductive switching using Silicon and its applications in antennas and reconfigurable metallodielectric EBG structures," PhD thesis, Department of Mechanical, Electrical and Manufacturing Engineering, Loughborough University, Loughborough, United Kingdom, 2006.
- [3-15] S. Gevorgian, "Agile microwave devices," *IEEE Microwave Magazine*, vol. 10, no. 5, pp. 93–98, August 2009.
- [3-16] G. W. Hanson, "Dyadic green's functions for an anisotropic non-local model of biased Graphene," *IEEE Transactions on Antennas and Propagation*, vol. 56, no. 8, pp. 747–757, March 2008.
- [3-17] C. Volk, C. Neumann, S. Kazarski, S. Fringes, S. Engels, F. Haupt, A. Müller, and C. Stampfer, "Probing relaxation times in Graphene quantum dots," *Nature Communications*, vol. 4, pp. 1–6, April 2013.
- [3-18] Y-W. Tan, Y. Zhang, K. Bolotin, Y. Zhao, S. Adam, E. H. Hwang, S. Das Sarma, H. L. Stormer, and P. Kim, "Measurement of Scattering Rate and Minimum Conductivity in Graphene," *Physical Review Letters*, vol. 99, December 2007.
- [3-19] W. E. Doherty, Jr. and R. D. Joos, "PIN diode RF switches," in *The PIN Diode Circuit Designers' Handbook*. Watertown, MA, United States of America: Microsemi Corporation, 1998, ch. 2, pp. 18–20.
- [3-20] B. Doherty, "PIN diode fundamentals," in *PIN Diode Application Notes MicroNote Series*. Aliso Viejo, CA, United States of America: Microsemi Corporation. [Online]. Available: https://www.microsemi.com/document-portal/doc_download/134814-micronote-701-pin-diode-fundamentals/
- [3-21] R. H. Caverly and G. Hiller, "Distortion properties of MESFET and PIN diode microwave switches," *IEEE MTT-S International Microwave Symposium Digest*, pp. 533–536, 1992.
- [3-22] M-Y. Hsieh and S-M. Wang, "Compact and wideband microstrip bandstop filter," *IEEE Microwave and Wireless Components Letters*, vol. 15, no. 7, pp. 472–474, July 2005.

- [3-23] K. M. F. Rabbi, "Miniaturised and reconfigurable planar filters for ultra-wideband applications," PhD thesis, Faculty of Science and Technology, University of Westminster, London, United Kingdom, 2014
- [3-24] J-S. Hong and M. J. Lancaster, *Microstrip Filters for RF/microwave Applications*. New York, United States of America: John Wiley & Sons, 2001.

Chapter 4:

Development of Broadband Single-Element Planar Monopole Filtennas

4.1: Introduction

Broadband systems have a very large operational bandwidth. For the purpose of this research, “broadband” encompasses the UWB frequency range and other frequency bands near the lower or the upper limit of the UWB. This very large bandwidth offers several advantages; such as high data rate, low power consumption, low-cost implementation, high time resolution, resistance to interference, obstacle penetration and covert transmission. Such advantages facilitate a wide range of applications which include indoor, outdoor, commercial and military systems; such as devices communicating wirelessly, positioning, imaging and radar applications.

Arguably, the first experiment involving a wide wireless communication link was on an UWB system conducted by Heinrich Hertz in 1893 [4-1]. In other words, the first wireless communication system was a broadband system.

Broadband antennas have been studied for several decades [4-1]. Typical broadband antennas include spiral antennas, log-periodic antennas and complementary antennas [4-1]. However, most of these existing broadband antennas are non-planar and cannot be directly mounted on metallic platforms [4-1]. Planar monopole antennas have numerous benefits and are a good choice for broadband applications. This is primarily due to their wideband characteristics, simple structure design, small size, low-cost, low-weight and easy fabrication and compatibility with the typical manufacturing processes of planar circuits. Moreover, they exhibit omnidirectional radiation patterns in the H-plane. Because of such patterns, they can transmit or receive wireless signals equally in all directions of the H-plane.

Furthermore, a number of new fabrication technologies have emerged in the recent years. These technologies have different fabrication processes, use different metallisation and dielectric substrates as compared with conventional PCB technology. For such emerging technologies, planar monopole antennas are the preferred solution for realising compact wireless transceivers of broadband applications.

As stated in Chapter 3, the wide frequency range of 3.1–10.6 GHz is overlapped by a number of other interfering wireless services; such as the IEEE 802.16 WiMAX 3.4–3.6 GHz band, the IEEE 802.11 WLAN 5.15–5.35 and 5.725–5.825 GHz bands and the ITU satellite communication system 8.025–8.4 GHz band. Since, these

interferences cause signal distortion and loss of sensitivity, filtering within the wide passband is necessary for the best usage of that wide frequency range. In such instances, a possible and effective solution is to integrate the broadband planar monopole antennas with stopband filters. Such filters have a low insertion loss in their passband and a high attenuation in their stopband. Therefore, they are able to realise notchbands at the frequency bands of the interfering wireless services. This integration results in the formation of broadband filtennas for wireless transceivers.

So as to achieve this, numerous approaches are used; such as using stubs [4-3]–[4-6], slits and slots [4-7]–[4-8], capacitively-loaded resonators [4-7] or by SRRs [4-9]. Yet, in these works, the notchband are either not at a good measured rejection value or are not sharp enough for their respective band [4-7] and [4-9] or the filters are cascaded with the antenna [4-3]–[4-4], rather than being integrated within; so increasing the size, cost and complexity of the circuits. However, in most of the aforementioned works, the notchband are permanent, with no possibility of reverting the resulting responses to a full bandpass response. Moreover, in [4-5] and [4-8], the notchband is a single band from 5–6 GHz; thereby rejecting the spectrum of 5.35–5.725 GHz which is not a part of the WLAN. These issues can be countered by using switching elements to control the responses and by introducing extremely sharp dual or triple notchband when rejecting closely-spaced interference bands.

With regards to broadband filtennas fabricated using inkjet-printing technology, little work has been done; with the exception being [4-10]–[4-15]. But these works still do not satisfy all challenges; such as compact size and the rejection of interfering bands. Furthermore, the efficiency of wireless systems depends on the integrated filtenna which should be conformal, lightweight, compact, low profile and mechanically robust. Yet, [4-10]–[4-12] have been printed on paper substrates. Though cheap and flexible, paper has a low tensile strength of 17 MPa and introduces discontinuities where high levels of bending are needed. Moreover, it has a high dielectric loss tangent of 0.07 which compromises the efficiency of the filtennas [4-13]. In [4-14], the chosen substrate for inkjet printing is thick, not flexible and has high dielectric losses.

While there is a plethora of published research on broadband single-element planar monopole filtennas for wireless transceivers, further research is still needed. Some important points which need to be addressed, especially keeping in view the aforementioned limitations of published broadband planar monopole filtennas, are as follows:

- Development of broadband single-element planar filtennas by the integration of filter structures with broadband single-element planar monopole antennas.
- Development of broadband single-element planar monopole filtennas having different topologies of the integrated filters.
- Complete rejection of any interfering frequency bands present within the passband of the monopole antennas.
- Incorporation of reconfigurable elements so as to make the filtennas reconfigurable.
- Using different reconfigurable elements without affecting performance of the filtennas.
- Using different fabrication technologies for the development of broadband single-element planar monopole filtennas.

The purpose of the overall chapter is to integrate filters with or within planar monopole antennas to form broadband planar monopole filtennas which address the points listed above. Moreover, an additional purpose is to develop a broadband planar monopole filtenna following the same approach, but using a new and emerging fabrication technology. Therefore, four filtennas for wireless transceivers of broadband applications have been developed. Of the three presented in this chapter, the first two are reconfigurable PCB filtennas and the third is a fixed-band inkjet-printed flexible filtenna. The fourth (last) broadband planar monopole filtenna will be discussed in the next chapter.

Section 4.2 introduces the topology of an antenna whose variants will be used in this chapter. Alongside an analysis of its geometry, the section also details its theoretical working, design method and design equations. Additionally, the results based on the design method and design equations are also presented.

Section 4.3 presents the first PCB filtenna for wireless transceivers of UWB applications. The filtenna is formed by the capacitive coupling of four stepped impedance resonators with an UWB antenna. Because of the coupled resonators, the resultant filtenna produces sharp dual notchband which reject the IEEE 802.11 WLAN 5.25 and 5.8 GHz frequency bands. Reconfigurability has been incorporated in the filtenna by the addition of two different reconfigurable elements within the four stepped impedance resonators. Because of these elements, the filtenna is able to switch off or switch on the dual notchband. The filtenna has been fabricated using conventional PCB technology on a rigid substrate with copper as the metallisation.

In section 4.4, the second PCB filtenna for wireless transceivers of UWB applications has been developed. The filtenna is formed by the addition of three split ring bandstop resonators to an UWB antenna. Hence, the filtenna is able to produce a dual notchband which filters out the two interfering IEEE 802.16 WiMAX 3.5 GHz and IEEE 802.11 WLAN 5.8 GHz frequency bands. Furthermore, the filtenna has been made reconfigurable by the insertion of two different reconfigurable elements which are attached to the bandstop resonators. Therefore, the filtenna is able to switch off or switch on the dual notchband. The filtenna has been fabricated using conventional PCB technology on a rigid substrate with copper as the metallisation. Section 4.5 presents a novel compact broadband planar monopole filtenna for wireless transceivers of flexible S-band, ISM band and UWB applications. The filtenna is formed by the integration of three pairs of bandstop resonators in a broadband planar monopole antenna. The ensuing broadband planar monopole filtenna able to reject the three interfering frequency bands of IEEE 802.16 WiMAX 3.5 GHz, IEEE 802.11 WLAN 5.8 GHz and ITU satellite communication system 8.2 GHz which are present within its wide passband. The filtenna has been developed using the new inkjet-printing technology and is the first of its kind. Silver nanoparticle ink is the metallisation and the dielectric substrate is Kapton. Because of this particular fabrication technology and the choice of the printing substrate, the developed filtenna is flexible.

4.2: Design of Broadband Planar Monopole Antennas

4.2.1: Geometry of the Broadband Planar Monopole Antenna

The geometry of a broadband planar monopole antenna is given in Figure 4.2–1. This geometry will be used for the later sections as well. A ground plane, of a finite length, L_G , starting on the bottom edge of the substrate and ending just before the radiating element, can be seen. A gap, of a width G , exists between the end-point of the ground plane and the radiating element.

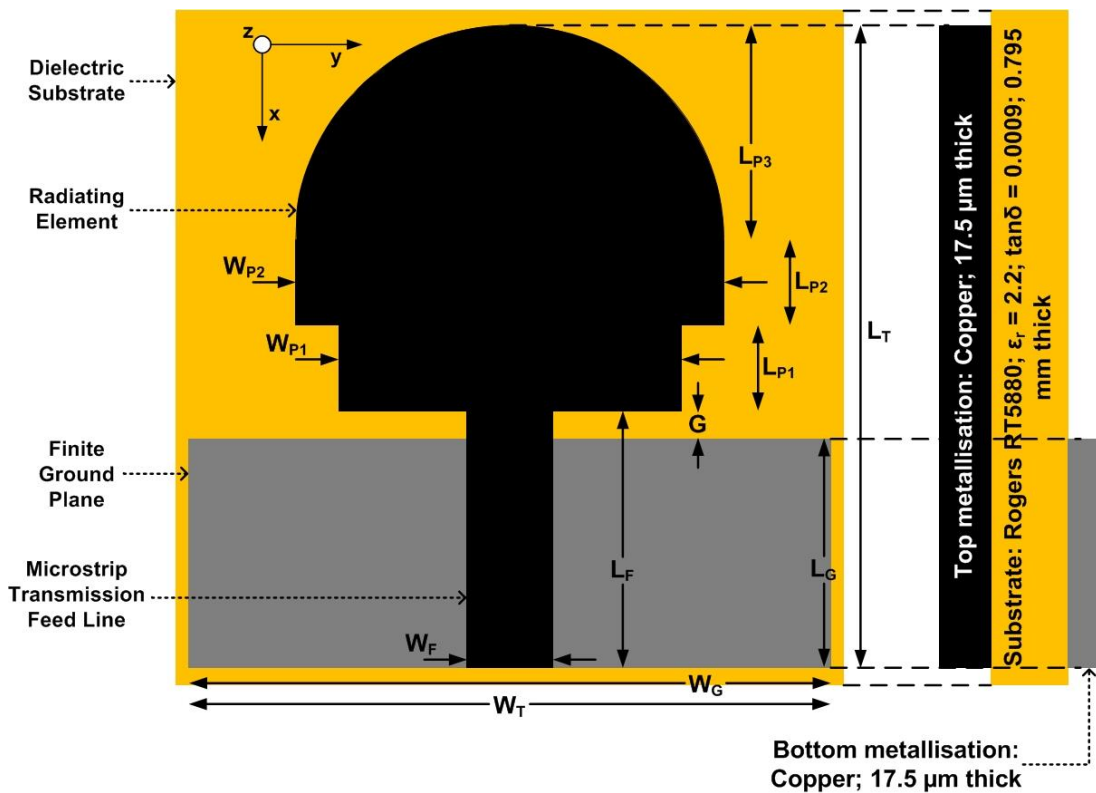


Figure 4.2–1: Geometry of the antenna.

4.2.2: Operating Mechanism of Broadband Planar Monopole Antennas

In order to design and determine the initial parameters of broadband planar monopole antennas, their operating mechanism needs to be understood first.

Broadband planar monopole antennas with a finite ground plane, such as the aforementioned one, are capable of operating at multiple resonant modes instead of at only one resonant mode as in the case of conventional microstrip patch antennas with a complete ground plane. When these multiple closely-spaced resonant modes overlap each other, as shown in Figure 4.2–2, a wide bandwidth is obtained.

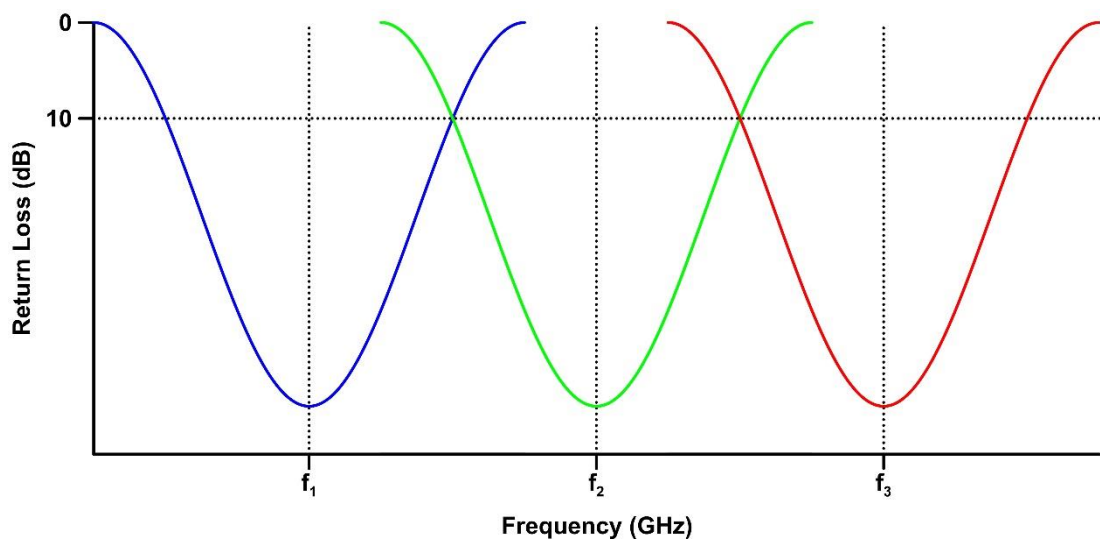


Figure 4.2–2: Multiple overlapping resonant modes of broadband planar monopole antennas.

Such broadband antennas essentially consist of many wire antennas. The presence of numerous possible current modes in each of these wire antennas explains the reason of the obtained wide bandwidth. The current modes which can exist in the radiating elements of the broadband planar monopole antennas are in the form of higher order Bessel functions of the first kind [4-17]–[4-18], where the currents are small at the centre of the elements and mostly concentrated on the boundaries.

4.2.3: Analysis of the Geometry of the Broadband Planar Monopole Antenna

Broadband planar monopole antennas can be fed using various feeding methods; such as microstrip line feed, coplanar waveguide feed, proximity coupling feed or

aperture coupling feed. In this thesis, the two feeding techniques used for the developed broadband antennas are microstrip line feed and coplanar waveguide feed. Since the antennas should have a characteristic impedance corresponding to the given specifications of the system, the width of a microstrip line feed and a CPW feed can be calculated from the equations given in section 2.1.

The frequency of the first resonant mode can be determined by the size of the radiating element. At the first resonance, f_1 , the antenna behaves like a quarter-wavelength monopole antenna. Hence, the length of the entire radiating element is $\lambda/4$ at the first resonant frequency. The higher order modes, i.e. f_2, f_3, \dots, f_N , are harmonics of the first mode. The total length of the radiating element, L_E , is calculated by (4.1) and the frequency of the first resonant mode, f_1 , is calculated by (4.2); in which c is the speed of light.

$$L_E = L_{P1} + L_{P2} + L_{P3} \quad (4.1)$$

$$f_1 = \frac{c}{4L_E} \quad (4.2)$$

After optimisation, the width of the ground plane, W_G , is very close to twice the width of the first patch, W_{P1} , connected to the transmission feed line; as derived in [4-16]–[4-17] and given in (4.3).

$$W_G \approx 2W_{P1} \quad (4.3)$$

The gap between the finite ground plane and the transmission feed line is a very important parameter in the design of broadband planar monopole antennas. The width of the gap affects the impedance matching between the transmission feed line and the radiating element. The width of the gap, G , is directly related to the length of the finite ground plane, L_G . In all designs, the width will be such that the length of the transmission feed line will always be more than the length of the finite ground plane. The length of the ground plane — and, hence, the width of the gap — can be determined using full-wave electromagnetic solvers or numerical electromagnetic modelling methods.

Most of the flow of current in broadband planar monopole antennas is concentrated on the boundary of the antennas; as if a wire antenna is running along the perimeters of the radiating elements of these antennas. For broadband design, the first resonant frequency should be slightly higher than the lower band boundary. The

perimeter of the radiating element should have a length of about one wavelength at the lowest in-band frequency. Practically, this frequency should be lower than the lowest frequency of the impedance bandwidth of the antennas so as to compensate for variations in the environment. The perimeter of the radiating element, P_E , can be calculated by (4.4).

$$P_E = (W_{P1} - W_F) + 2L_{P1} + (W_{P2} - W_{P1}) + 2L_{P2} + \pi L_{P3} \quad (4.4)$$

Since the perimeter of the radiating element is close to one wavelength of the average medium of radiation, this relation can be used to calculate the lowest frequency of the bandwidth of the antennas. The expression was derived in [4-16]–[4-17] from this relation and is given in (4.5).

$$f_L = \frac{300}{P_E \times \sqrt{\epsilon_{eff}}} \quad (4.5)$$

where f_L is the lower limit of the frequency bandwidth in GHz, P_E is the perimeter of the radiating element in mm and ϵ_{eff} is the effective permittivity of the medium of radiation.

The effective permittivity, ϵ_{eff} , is calculated by (4.6).

$$\epsilon_{eff} = \frac{\epsilon_r + 1}{2} \quad (4.6)$$

where ϵ_r is the relative permittivity of the medium of radiation and can be checked from the medium's datasheet.

For a desired lower frequency limit of the bandwidth, the perimeter of a broadband planar monopole antenna can be calculated by reversing (4.5).

4.2.4 Realised Structure of the Broadband Planar Monopole Antenna

A) Final Parameters

By using the design method given above and (4.1)–(4.6), the values of the dimension parameters of the antenna were determined for a sample broadband

impedance bandwidth of 3 GHz to 12 GHz. The optimised values are given in Table 4.2–1.

Table 4.2–1: Values of the dimension parameters of the antenna.

Parameter	Value (mm)	Parameter	Value (mm)
W_T	32	G	0.5
L_T	36.2	W_{P1}	15
W_G	32	L_{P1}	4.3
L_G	13.1	W_{P2}	23.8
W_F	2.4	L_{P2}	6.4
L_F	13.6	L_{P3}	11.9

The calculated value of the frequency of the first resonant mode, f_1 , obtained using (4.1) and (4.2), is 3.32 GHz. The calculated value of the lower limit of the frequency bandwidth, f_L , obtained using (4.4)–(4.6), is 2.96 GHz.

B) Fabrication of Final Layout

The antenna from Figure 4.2–1 using the values from Table 4.2–1 is designed on a Rogers RT5880 substrate of a thickness of 0.795 mm, having a dielectric permittivity of $\epsilon_r = 2.2$ and a dielectric loss factor of $\tan \delta = 0.0009$. It is modelled and simulated using the commercial full-wave electromagnetic simulation software program Sonnet. Photographs of the top side and the bottom side of the fabricated antenna are shown in Figure 4.2–3.

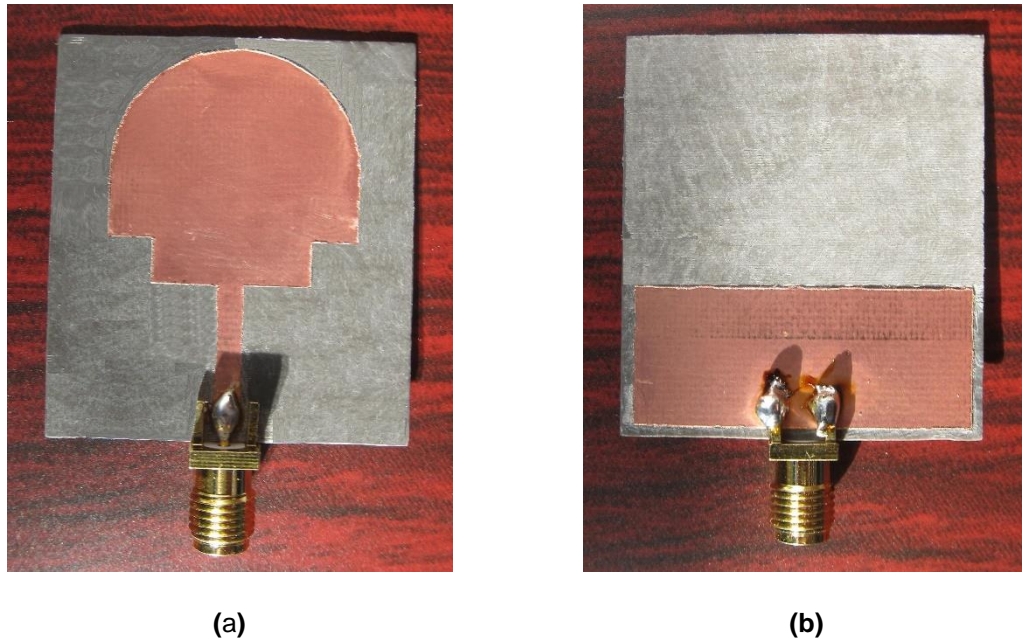


Figure 4.2-3: Photographs of (a) the top side and (b) the bottom side of the fabricated antenna.

4.2.5 Results of the Broadband Planar Monopole Antenna

A) Return Loss

The fabricated prototype of the antenna was measured using an Agilent E8361A PNA Network Analyser. The obtained measured results, alongside the simulated results, are given in Figure 4.2-4. Overall, the antenna exhibits a broadband impedance bandwidth in both the simulated and the measured results.

At a return loss of 10 dB, the simulated absolute bandwidth is 8.98 GHz. The lower limit of the simulated bandwidth is 2.89 GHz and the upper limit is 11.87 GHz. The three resonant modes of the antenna are present at the frequencies of 3.72 GHz, 6.5 GHz and 9.65 GHz. While the magnitudes of the return loss of the first and the third modes are relatively same, the second mode is present at a comparatively higher return loss. Furthermore, all three modes are moderately sharp.

Although the measured result is in a reasonable agreement with the simulated result, there are differences present. At a return loss of 10 dB, the measured absolute bandwidth is 9.17 GHz. The lower limit of the measured bandwidth is 2.8 GHz and the upper limit is 11.97 GHz. The three resonant modes of the antenna are present at the frequencies of 3.59 GHz, 6.66 GHz and 9.5 GHz. The first two resonant modes are sharp and are present at a higher return loss than the third resonant mode. Moreover, the third mode is not sharp but flatter. The shifts in the

frequencies of the three resonant modes between the measured and the simulated results and the lower measured return loss at the higher frequencies could be due to the losses experienced because of the SMA connector which was not modelled in the simulation and/or due to the substrate losses.

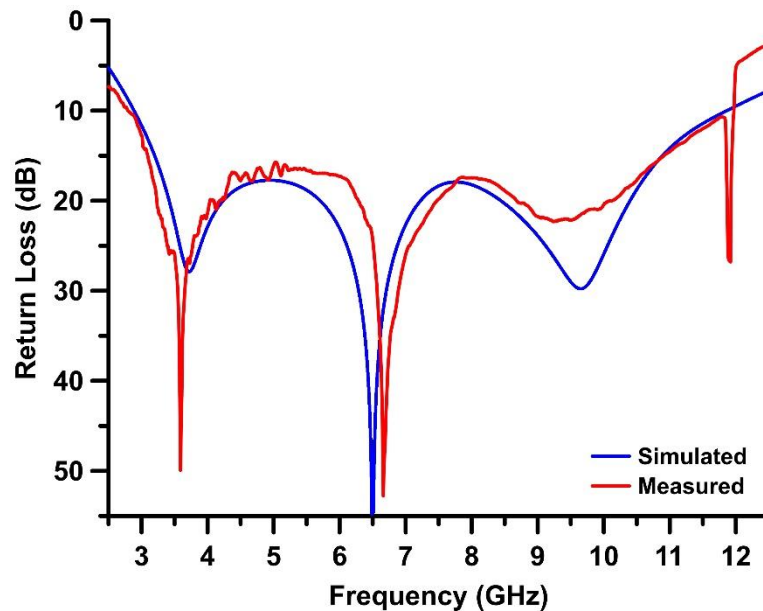


Figure 4.2-4: Return loss of the antenna.

B) Parametric Study of Various Parameters

With the aim of gaining a better understanding of how the various parameters of the broadband planar monopole antenna affect its performance, parametric studies were undertaken.

In the first instance, the width of the ground plane, W_G , was varied. The resulting effects are shown in Figure 4.2-5 (a).

The results indicate that as the width of the finite ground plane decreases, the upper frequency limit of the bandwidth shifts forwards. However, this effect is at the cost of a deterioration in the return loss at the resonant modes. This is evident from the three curves when the width of the ground plane is reduced from the optimal value of 32 mm to 30 mm, 28 mm and 26 mm. As can be seen from these three curves, the response at the resonant modes starts becoming flatter very quickly. At the value of 26 mm, the passband at frequencies below 8 GHz deteriorates completely. On the other hand, as the width of the finite ground plane is increased from the optimal value of 32 mm, the upper frequency limit of the bandwidth is not affected. Nevertheless, at the increased values, the return loss at the resonant modes again starts deteriorating. These effects can be seen at the values of 34 mm, 36 mm and

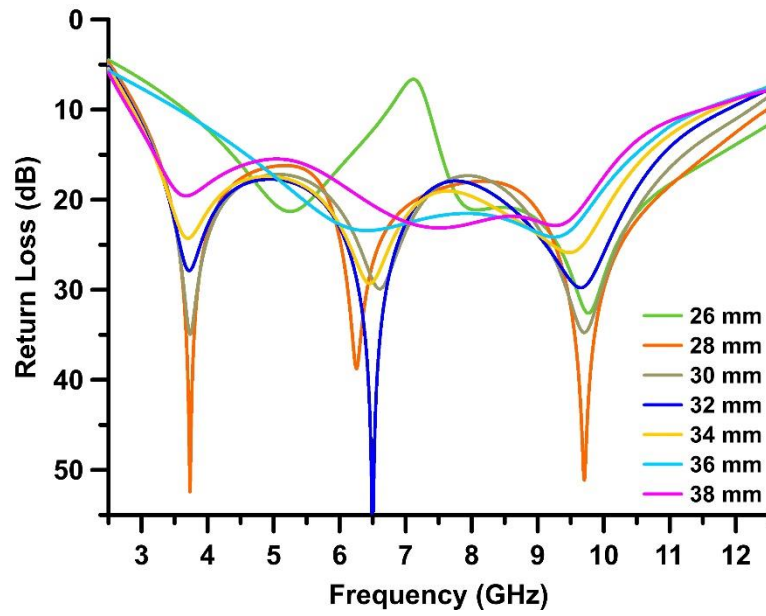
38 mm. At 36 mm and 38 mm, the sharp spikes at the three resonant modes disappear completely.

Amongst the seven curves, the two best values are 28 mm and 32 mm. From (4.3), the width, W_G , of the ground plane should be roughly 30 mm. This calculated approximate value is between the two best values. After further iterations using the software program, 32 mm was found to be the better and the optimal value.

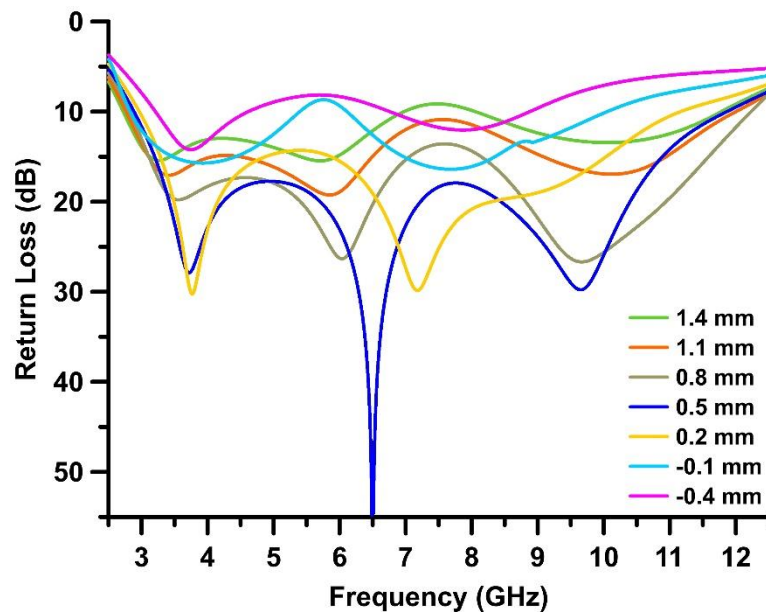
In the second case, the effects of changing the width, G , of the gap were observed; which is, effectively, done by altering the length of the ground plane, L_G . The results are shown in Figure 4.2–5 (b).

The results show that while the lower frequency limit and the upper frequency limit of the bandwidth are not considerably affected because of the width of the gap, the passband matching is significantly affected. Hence, by tuning the width of the gap, it can be used to control the impedance matching between the radiating element and the transmission feed line so as to achieve the best possible passband. The antenna was simulated with seven values for the width of the gap and, as mentioned above, the passband matching was found to be very sensitive to the value of the width. This is evident from the three curves when the width of the gap is reduced from the optimal value of 0.5 mm to 0.2 mm, -0.1 mm and -0.4 mm and when it is increased from the optimal value of 0.5 mm to 0.8 mm, 1.1 mm and 1.4 mm. (Positive values signify the length of the ground plane to be smaller than the length of the transmission feed line and the negative values signify the length of the ground plane to be greater than the length of the transmission feed line.) As can be seen from these six curves, the response at the resonant modes starts becoming flatter very quickly and the passband matching starts deteriorating as well. Furthermore, at the extreme high and low values of the width, G , of the gap, especially when the ground plane starts overlapping the transmission feed line, the return loss across the passband starts becoming less than 10 dB and the antenna stops radiating.

Amongst the seven curves, the best and the optimal value for the width, G , of the gap is 0.5 mm. This value was obtained from multiple iterations using the full-wave electromagnetic software program.



(a)

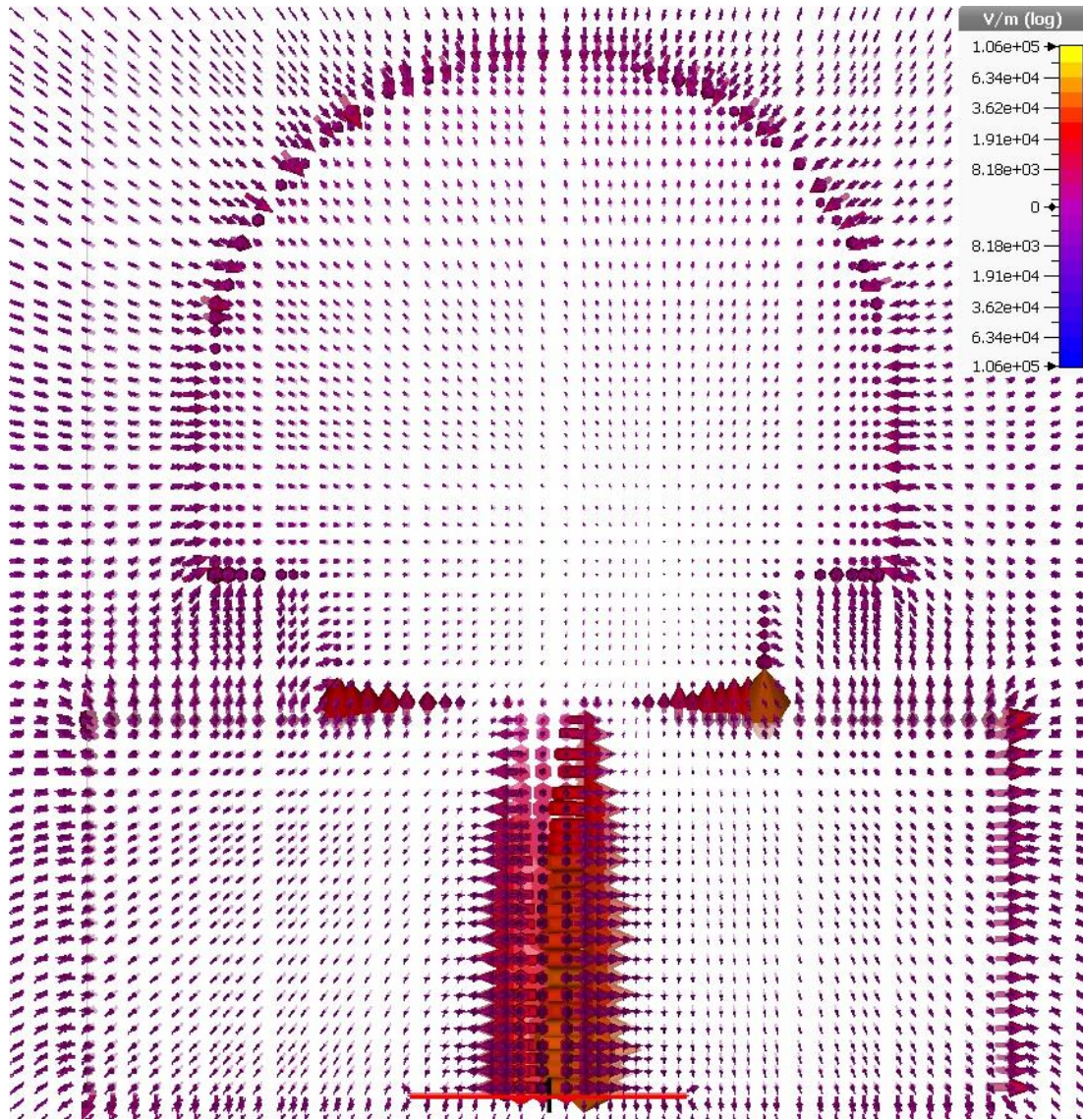


(b)

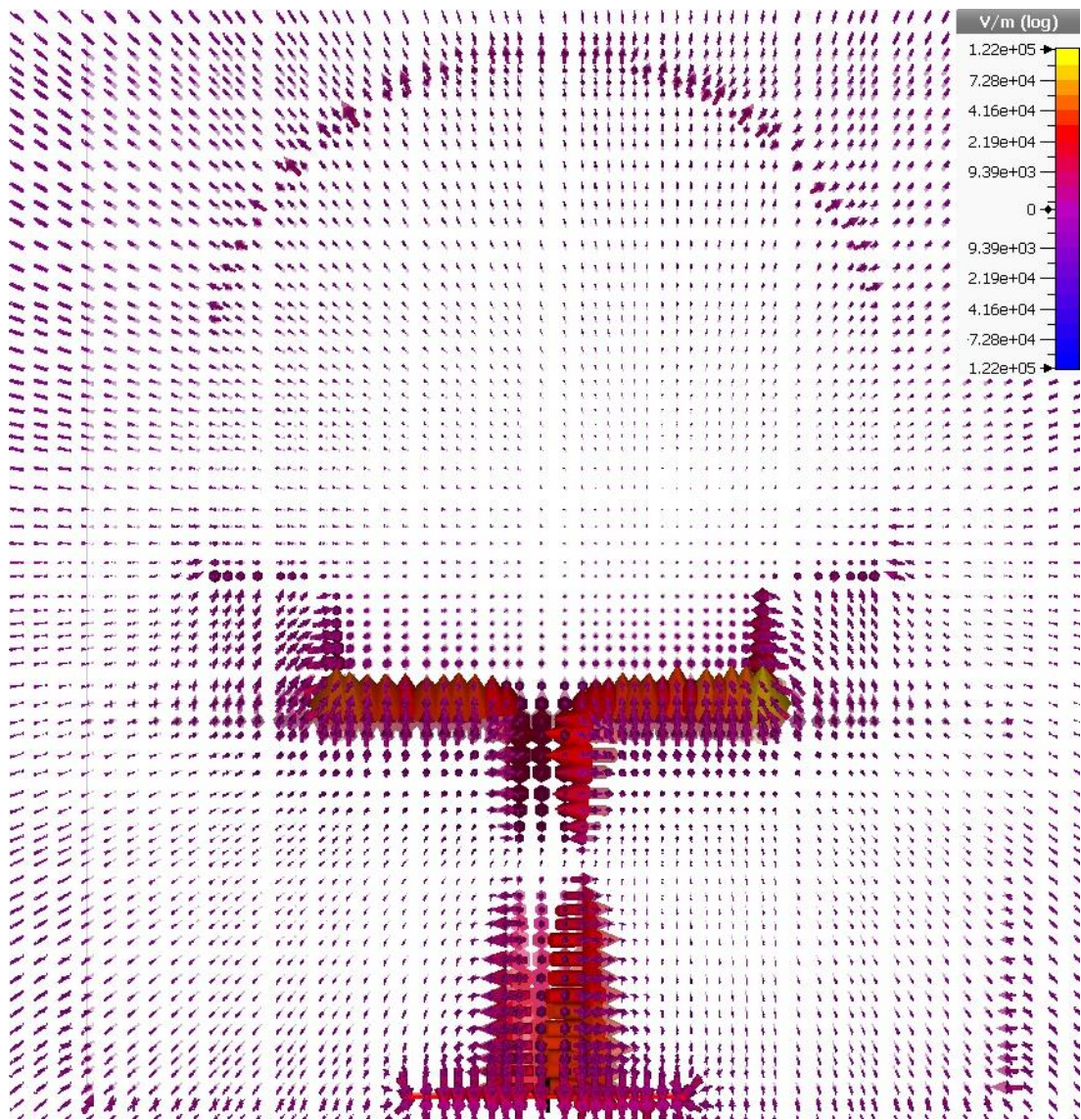
Figure 4.2–5: Parametric study of the effects on the return loss of the antenna by varying (a) the ground width and (b) the gap width.

C) Electric Field

The simulated E-field of the broadband antenna at the frequencies of the three resonant modes, i.e. 3.72 GHz, 6.5 GHz and 9.65 GHz, is shown in Figure 4.2–6.



(a)



(b)

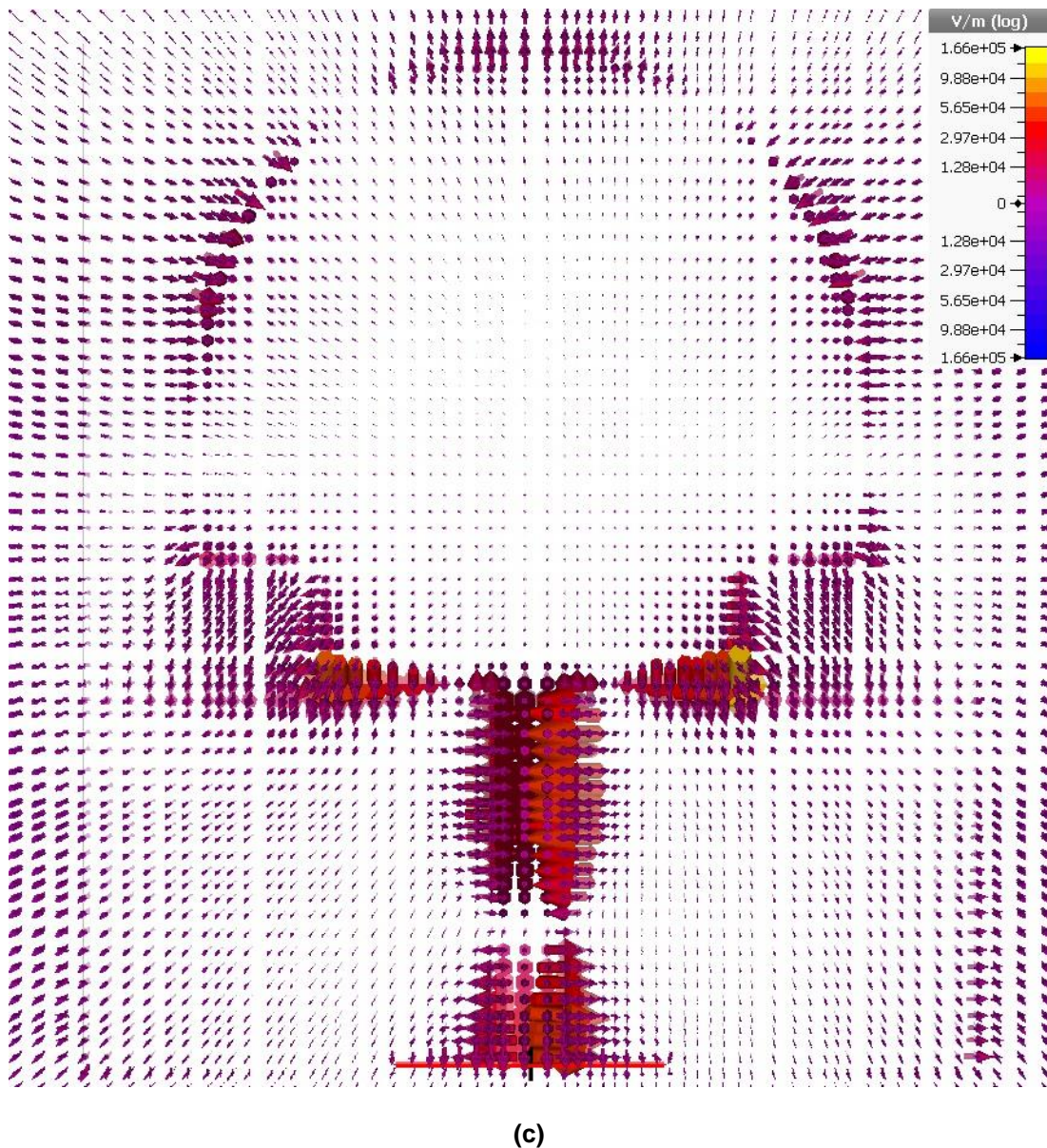


Figure 4.2–6: E-field of the antenna at the three resonant modes of (a) 3.72 GHz, (b) 6.5 GHz and (c) 9.65 GHz.

D) Radiation Patterns

The simulated radiation patterns of the broadband antenna in the E-plane and the H-plane are given in Figure 4.2–7. The results are presented for the frequencies of 3 GHz, 4.5 GHz and 7.5 GHz. The radiation patterns have been calibrated to the gain of the antenna. The antenna exhibits bidirectional radiation patterns in the E-plane. Moreover, at the higher frequency of 7.5 GHz, the pattern is slightly deteriorated. On the other hand, the H-plane displays omnidirectional radiation patterns at the three frequencies; inferring the antenna radiates in all directions in that plane.

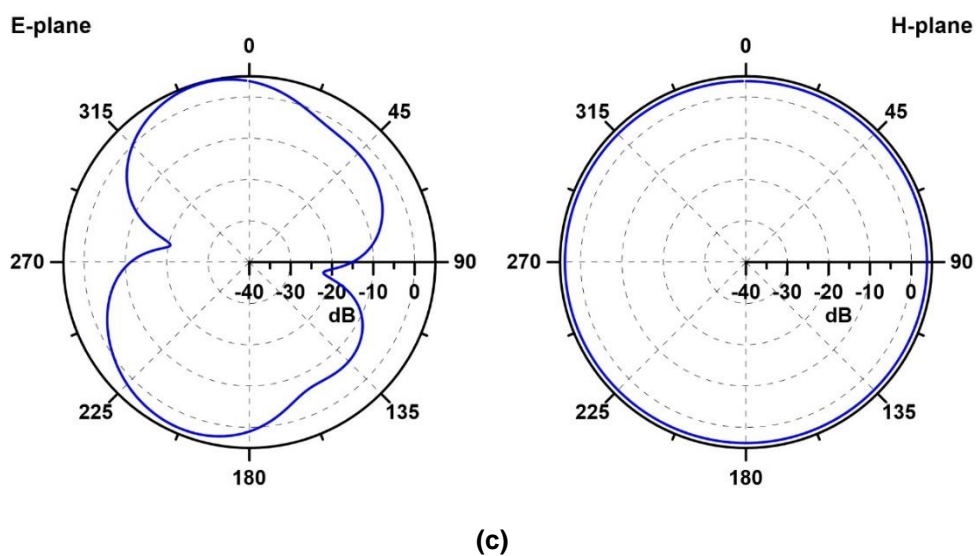
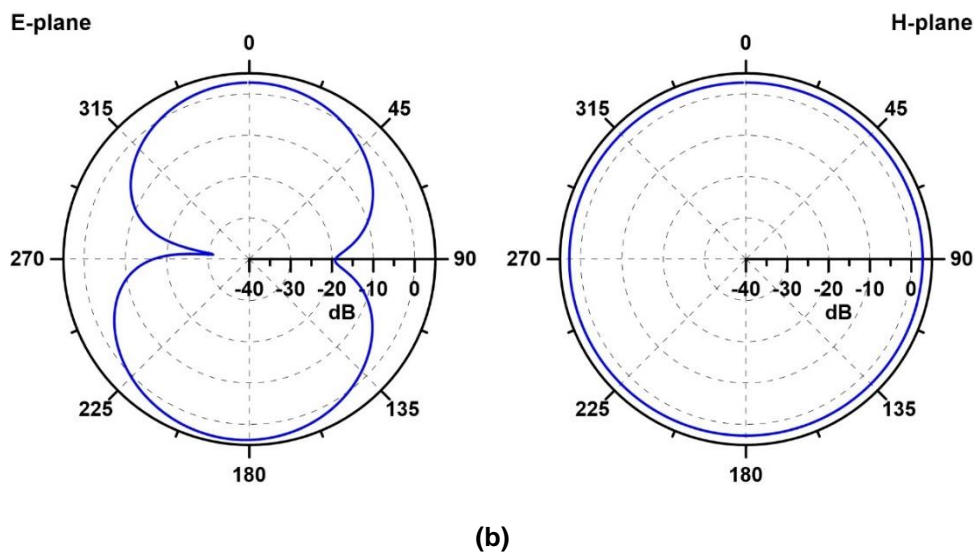
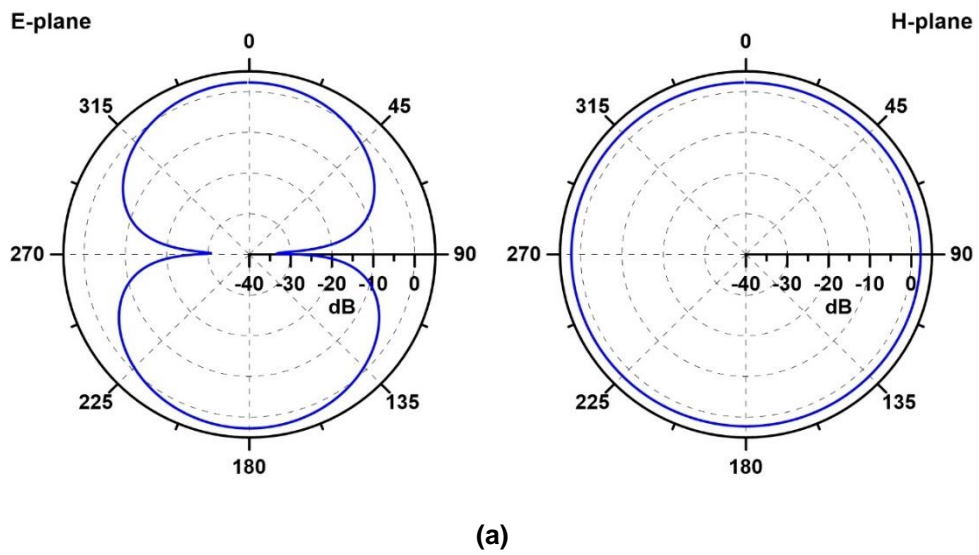


Figure 4.2–7: Radiation patterns of the antenna at (a) 3 GHz, (b) 4.5 GHz and (c) 7.5 GHz.

E) Gain

The gain of the antenna was simulated and the acquired result is given in Figure 4.2–8. Within the passband of 2.89 GHz to 11.87 GHz, the gain varies from a minimum of 2.66 dBi to a maximum of 5.25 dBi. Additionally, the variance in the gain across the passband is within 2.75 dBi.

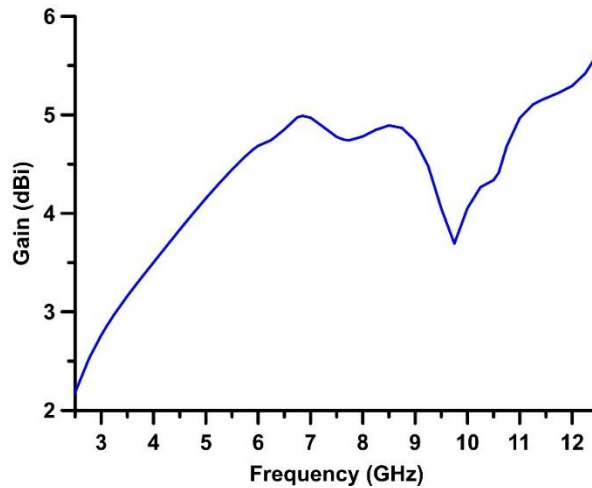


Figure 4.2–8: Gain of the antenna.

F) Efficiency

The efficiency of the antenna was simulated and the obtained result is given in Figure 4.2–9. The average efficiency across the passband of 2.89 GHz to 11.87 GHz is about 96.2 %. The high value is due to the result being a simulation and due to the exclusion of metallisation losses.

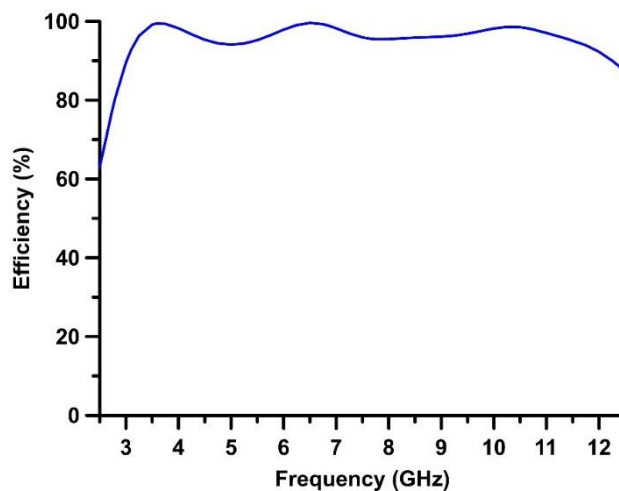


Figure 4.2–9: Efficiency of the antenna.

4.3: Design of a Frequency Reconfigurable Filtenna with Sharp Dual Notchband for UWB Applications

4.3.1: Specifications

This section presents a broadband planar monopole filtenna based on the specifications given in Table 4.3–1. The specifications require a single-element monopole filtenna operating at the full UWB range of 3.1–10.6 GHz. The filtenna ought to have a microstrip-based feeding method. The characteristic impedance of the system is 50 Ω . The filtenna should be fabricated via PCB technology. The specifications further ask that there should be dual notchband present for the rejection of the two interfering IEEE 802.11 WLAN bands operating at 5.25 GHz and 5.8 GHz.

Table 4.3–1: Required specifications of the filtenna.

Parameter	Description of Parameter	Value
Filtenna	Type of filtenna	Single Monopole
Technology	Fabrication technology	PCB
Feed	Feeding method	Microstrip
Z_0	Characteristic impedance of system	50 Ω
f_L	Lower passband frequency	3.1 GHz
f_H	Upper passband frequency	10.6 GHz
f_c	Centre frequency	5.73 GHz
FBW	Fractional bandwidth	$\geq 130.84\%$
n_{NB}	Number of notchband	Dual
f_{NB1} and f_{NB2}	Notchband frequencies	5.25 and 5.8 GHz

4.3.2: Realised Structure and Final Parameters

A) Final Layouts

The proposed filtenna meeting the above specifications is illustrated in Figure 4.3–1; with the values of its dimension parameters given in Table 4.3–2. The constituent antenna within the filtenna is based on the same design as the one given in the previous section. Hence, the same equations and layout can be used.

The proposed filtenna utilises a defected ground structure with a partial ground plane; whose length, L_G , is 12 mm. The filtenna has a microstrip-based feed network. The transmission feed line has a width, W_F , of 2.2 mm. This width corresponds to the required characteristic impedance of 50Ω of the system.

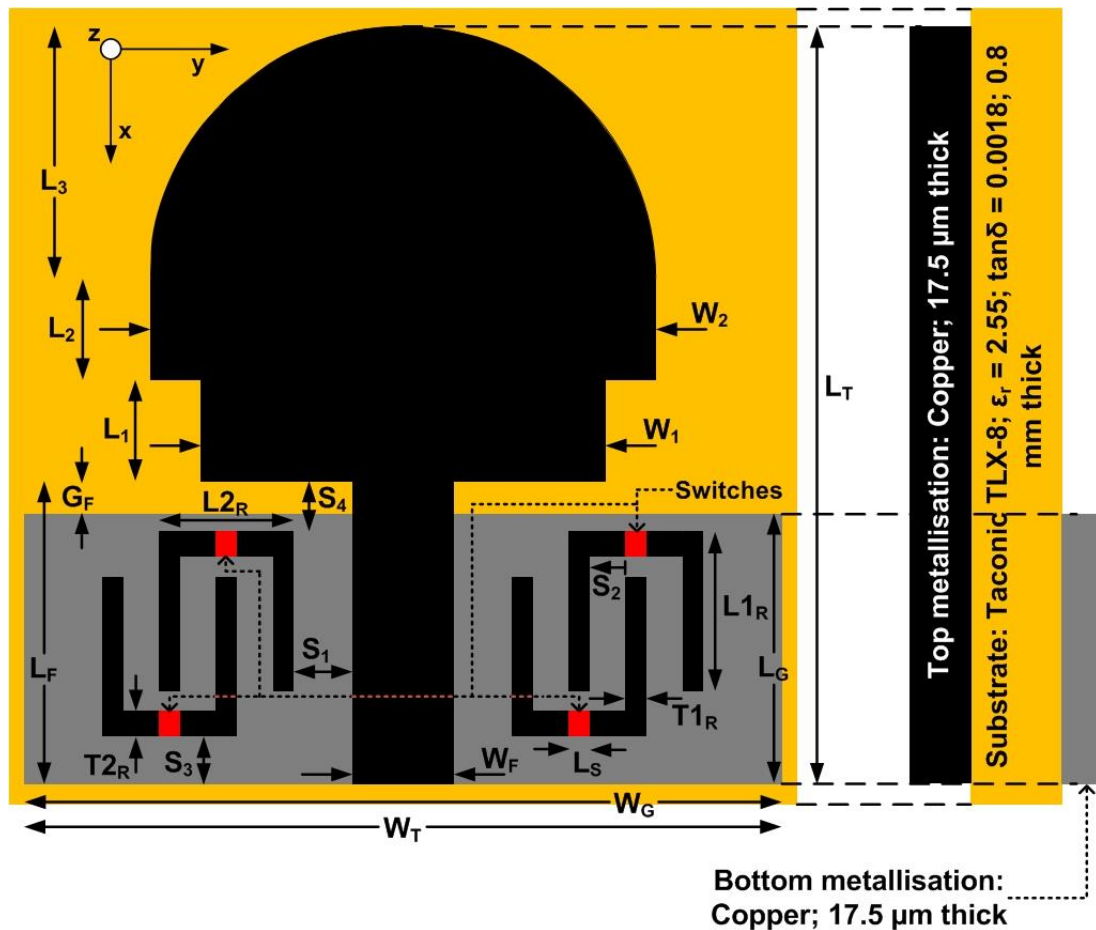


Figure 4.3–1: Geometry of the filtenna.

Table 4.3–2: Values of the dimension parameters of the filtenna.

Parameter	Value (mm)	Parameter	Value (mm)
W_T	30	L_3	11
L_T	33.8	L_{1R}	8.1
W_G	30	L_{2R}	4.5
L_G	12	T_{1R}	1
W_F	2.2	T_{2R}	0.6
L_F	12.8	S_1	0.2
G_F	0.8	S_2	0.75
W_1	14	S_3	2.5
L_1	4	S_4	0.85
W_2	22	L_S	0.5
L_2	6		

The dual notchband are inserted in the passband of the filtenna by the coupling of an integrated bandstop filter. The proposed filter structure is shown in Figure 4.3–2; with the values of its dimension parameters given in Table 4.3–3. As can be seen, the filter is made of multiple stepped impedance resonators. The structure consists of two identical pairs of half-wavelength, $\lambda_g/2$, stepped impedance resonators; where λ_g is the guided wavelength at the mid-frequency between the dual notchband. The two resonators within each pair are set in a complementary shape in order to occupy a smaller area and be compact. Each pair is placed on each side of the feed line. As the first spurious modes of the half-wavelength stepped impedance resonators are at frequencies greater than $2f_0$, the spurious harmonics are out of the required UWB frequency range and do not interfere in the required passband. The bandwidths of the dual notchband are determined by the width of the gap present between the stepped impedance resonators and the transmission feed line. Whereas, the width of the gap present between the two resonators within each pair of resonators determines their insertion loss.

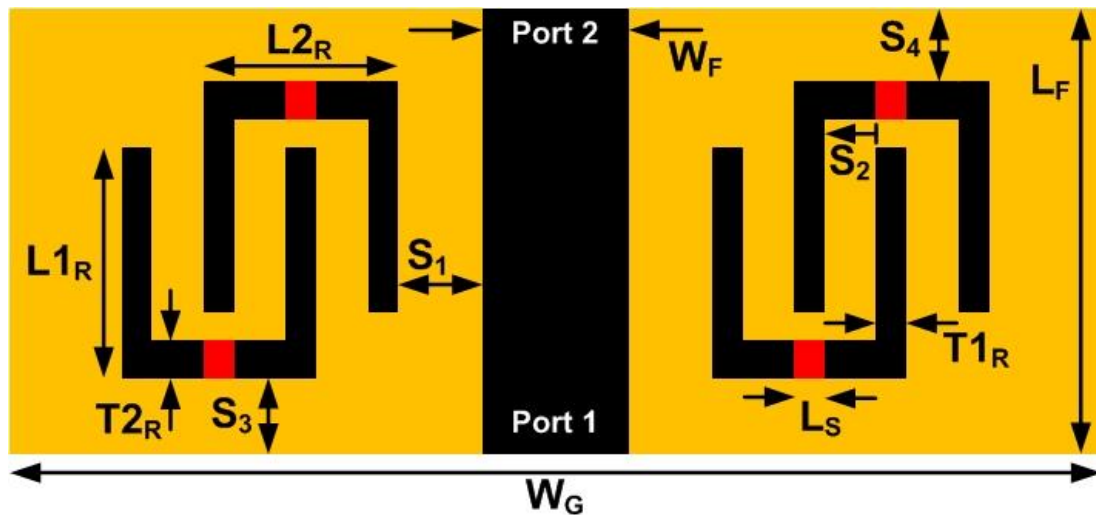


Figure 4.3-2: Geometry of the filter.

Table 4.3-3: Values of the dimension parameters of the filter.

Parameter	Value (mm)	Parameter	Value (mm)
W_G	30	$T2_R$	0.6
W_F	2.2	S_1	0.2
L_F	12.8	S_2	0.75
$L1_R$	8.1	S_3	2.5
$L2_R$	4.5	S_4	0.85
$T1_R$	1	L_S	0.5

The equivalent lumped element circuit model of the bandstop filter is given in Figure 4.3-3.

In the equivalent circuit model, each stepped impedance resonator is represented by an inductor, of an inductance L_R , and a capacitor, of a capacitance C_R ; where L_R is the total inductance and C_R is the total capacitance of the inductances and capacitances respectively of the three transmission lines which make up each stepped impedance resonator.

The gap present between the stepped impedance resonators and the transmission feed line can be denoted by a J-inverter. Therefore, there are two J-inverters, each having a capacitance C_{J1} , to represent the gap on each side.

Since the couplings because of the gaps in the outer fingers of the stepped impedance resonators are opposite to each other, they cancel each other. Therefore, the only remaining gap present between the two resonators of each pair

of stepped impedance resonator is denoted by only one J-inverter, having a capacitance C_{J2} , on each side of the transmission feed line.

The values of the lumped elements and the J-inverters were calculated using the equations from [4-19]–[4-20] and then fine-tuned using the commercial electronic design automation software program Keysight Advanced Design System. After optimisation, the final values obtained are given in Table 4.3–4.

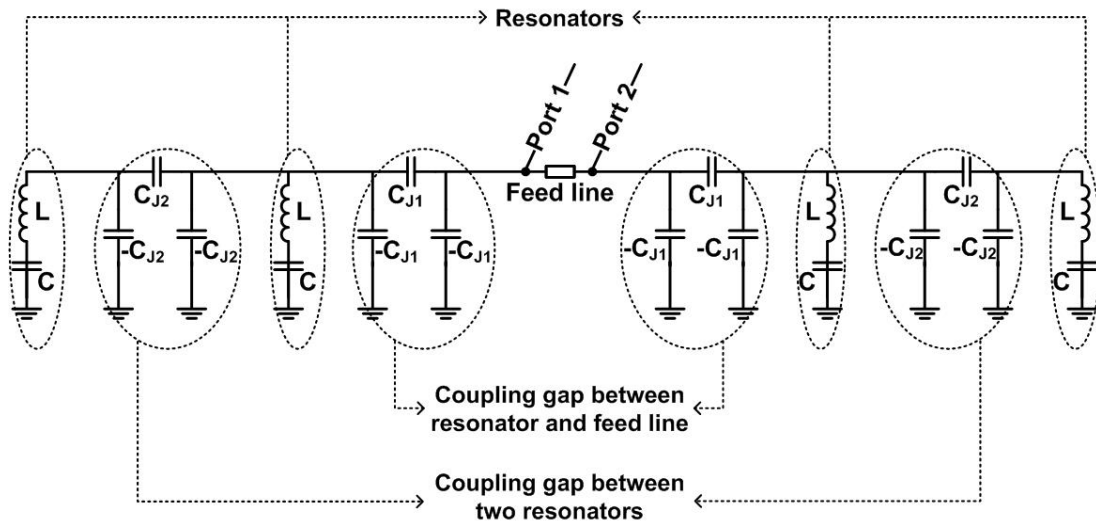


Figure 4.3–3: Equivalent lumped element circuit model of the filter.

Table 4.3–4: Values of the lumped elements in the equivalent circuit model of the filter.

Element	Value	Element	Value
L_R	1.64 nH	C_{J1}	1.43 pF
C_R	0.50 pF	C_{J2}	6.37 pF

B) Attainment of Reconfigurability

So as to attain reconfigurable characteristics in the filter, and thereby control the behaviour of the dual notchband, switching elements are placed at four points in the filter. These four points are the mid-points of each of the four interconnecting transmission lines joining the outer fingers of the resonators and have been indicated in red in the two geometries given in Figure 4.3–1 and Figure 4.3–2. The length, L_s , of these points is 0.5 mm.

Switching elements positioned at the aforementioned four points would effectively be dividing each of the four individual resonators of the bandstop filter into two sections of equal size. In other words, each resonator would effectively consist of

four transmission lines — two low impedance and two high impedance — conjoined with a switching element.

When the switching elements are in their switch OFF state, there would be no connection between the two sections of each resonator. As a result, current will not flow in the resonators; resulting in a passband without a notchband present. On the other hand, when the switching elements are in their switch ON state, the two sections of each resonator will be connected to each other. Current will then flow in each of the resonators to make the structure act as a complete coupled bandstop filter; ensuing a dual notchband within the passband of the filtenna.

C) Fabrication of Final Layouts

The standalone bandstop filter and the final filtenna are designed on a Taconic TLX-8 substrate of a thickness of 0.8 mm, having a dielectric permittivity of $\epsilon_r = 2.55$ and a dielectric loss factor of $\tan \delta = 0.0018$. They are modelled and simulated using the commercial full-wave electromagnetic simulation software program Sonnet. A photograph of the fabricated PCB bandstop filter is shown in Figure 4.3–4 and of the PCB filtenna in Figure 4.3–5.

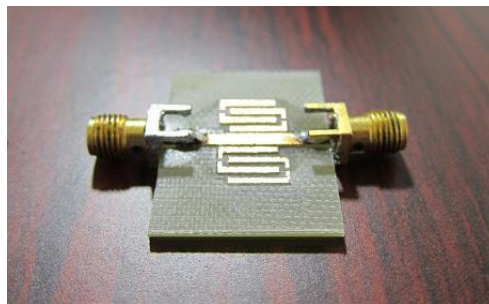


Figure 4.3–4: Photograph of the fabricated PCB filter.

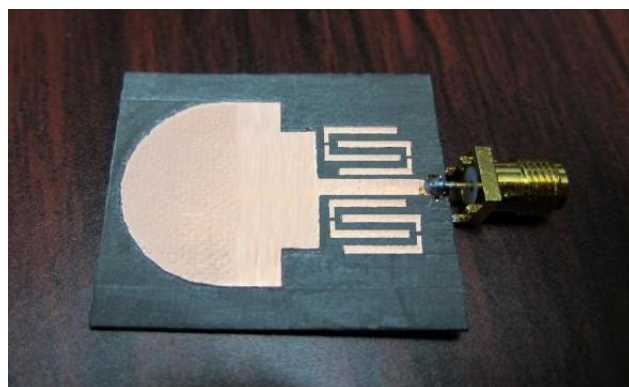


Figure 4.3–5: Photograph of the top side of the fabricated PCB filtenna.

4.3.3: Results

A) S-parameters of Filter

The equivalent lumped element circuit model of the bandstop filter given in Figure 4.3–3 was simulated using the final values from Table 4.3–4. The plots of the obtained S-parameters are shown in Figure 4.3–6. The S-parameters show an all-pass response, except at two frequency points where dual notchband are attained. These two frequency points — at 5.34 GHz and 5.77 GHz — reasonably match the two frequency bands which have to be rejected. The insertion loss rejection obtained at these points is 94.69 dB and 85.88 dB respectively. The insertion loss of the filter is negligible. The exceptionally high rejection at the dual notchband frequencies and the extremely low insertion loss is due to the results being a simulation of ideal lumped elements which do not include the actual metallisation losses, substrate losses, or tolerances of the materials used which would be present in fabricated prototypes of the filter. The return loss of the filter is more than 16.62 dB in the passband region.

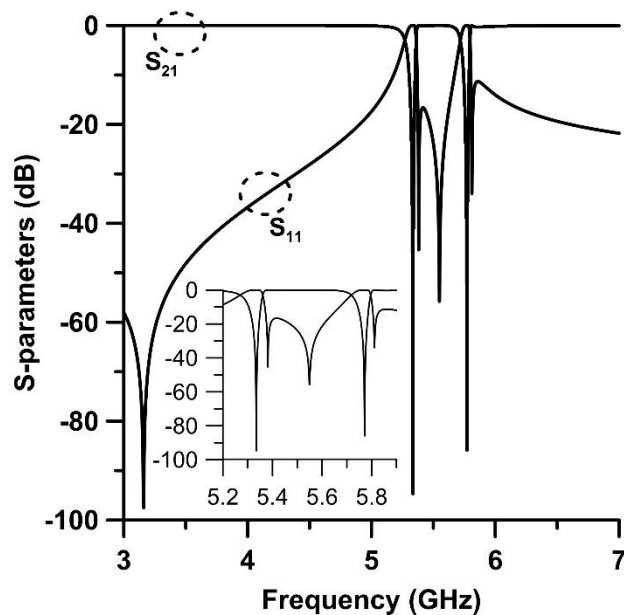


Figure 4.3–6: S-parameters of the equivalent lumped element circuit model of the filter.

The bandstop filter from Figure 4.3–2 was electromagnetically simulated using the vales provided in Table 4.3–3. In order to determine the results of the filter in switch OFF state and switch ON state without the use of lossy switching elements, the simulations for the two states were carried out using gaps and PEC based switches. The switch OFF state was simulated by leaving gaps at the four points wherein the

actual switches would be placed. The switch ON state was simulated by placing PEC metallic patches at the four locations.

The obtained S-parameters from the simulation of the bandstop filter in the switch OFF state are shown in Figure 4.3–7 (a). The result, specifically the negligible insertion loss curve, shows no notchband in the entire simulated frequency range. The filter is considered as exhibiting an all-pass response in this state and, thus, there is no rejection of any frequency band.

The results of the simulation of the bandstop filter in the switch ON state are shown in Figure 4.3–7 (b). The results show the passband of the filter as remaining almost unchanged from switch OFF state except at two frequency points. These two points are at 5.28 GHz and 5.75 GHz; where sharp dual notchband are produced at an insertion loss of 36 dB and 34 dB respectively. The dual notchband are introduced within the passband because in this state, the PEC based switches complete the connections within each of the four stepped impedance resonators of the bandstop filter and, hence, the resonators are able to couple with the rest of the filter structure.

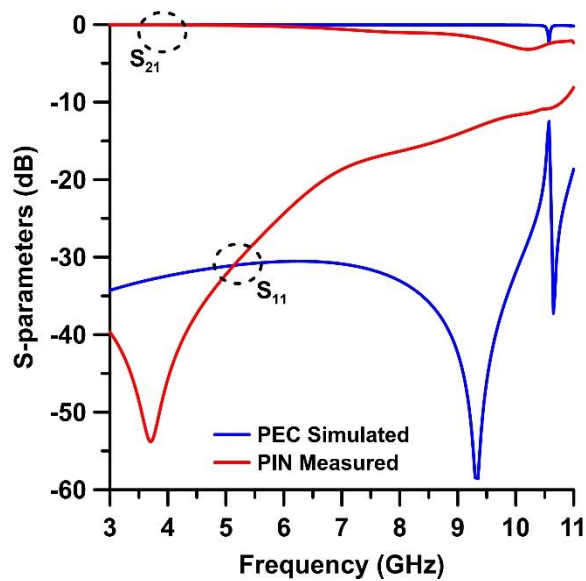
For a comparison with the PEC based switches and for the verification of actual results, the fabricated prototype of the bandstop filter in Figure 4.3–4 is affixed with PIN diodes as the switching elements. The PIN diodes used are NXP BAP65–02. Each PIN diode has a resistance of 0.9Ω , an inductance of 0.6 nH and a capacitance of 0.8 pF [3-19]. The PIN diodes are powered on by supplying an external DC voltage of 3 V and a current of 1 mA . The DC blocking capacitance is 33 pF and a resistor of $1 \text{ k}\Omega$ is used for biasing. The S-parameters of the fabricated prototype of the filter with the PIN diodes are measured using an Agilent E8361A PNA Network Analyser.

The results of the bandstop filter when the PIN diodes are reverse-biased, i.e. in switch OFF state, are obtained from the network analyser and shown in Figure 4.3–7 (a). The results are a good match with the PEC based switches. The four stepped impedance resonators are disconnected because of the reverse-biasing of the PIN diodes. Hence, the passband region, without any notchband, exists within the entire measured frequency range.

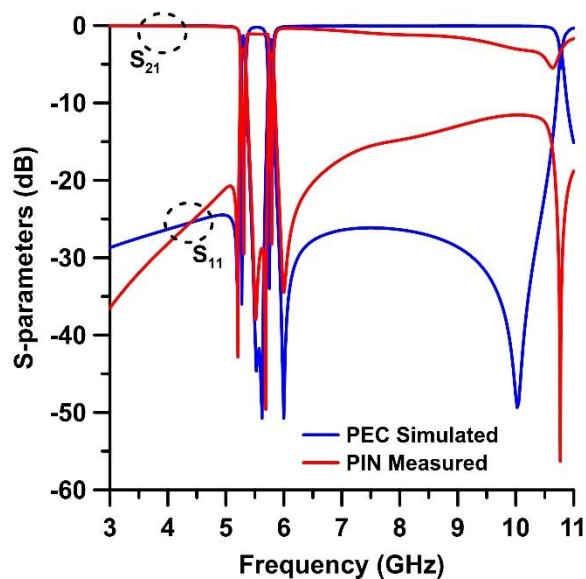
The measured results of the bandstop filter when the PIN diodes are forward-biased, i.e. in switch ON state, are shown in Figure 4.3–7 (b). The results using PIN diodes reasonably agree with the PEC based switches. The insertion loss of the filter in the passband is slightly increased as compared with the PIN diodes in switch OFF state. The result shows sharp dual notchband introduced within the passband of the filter. The dual notchband are present at 5.31 GHz , at an insertion loss of

29.51 dB, and at 5.79 GHz, at an insertion loss of 28.29 dB. This infers that the bandstop filter in switch ON state is able to reject the interfering WLAN bands.

Although the shape and the nature of the response of the filter in the switch ON state using the PEC based switches and the PIN diodes is quite similar to the response from the equivalent lumped element circuit model of the filter, the magnitude of the insertion loss and the return loss is much less. This is because the results attained using the PEC based switches and the PIN diodes take into account more metallisation, substrate and fabrication losses.



(a)



(b)

Figure 4.3–7: S-parameters of the filter in the (a) switch OFF and (b) switch ON states.

B) Return Loss of Filtenna

The filtenna from Figure 4.3–1, with its dimensions given in Table 4.3–2, was electromagnetically simulated using the commercial electromagnetic simulation software Sonnet. For the PEC based switches, the method of implementing the switches in both the switch OFF state and the switch ON state is the same as the one carried out for the PEC based switches in the bandstop filter described above.

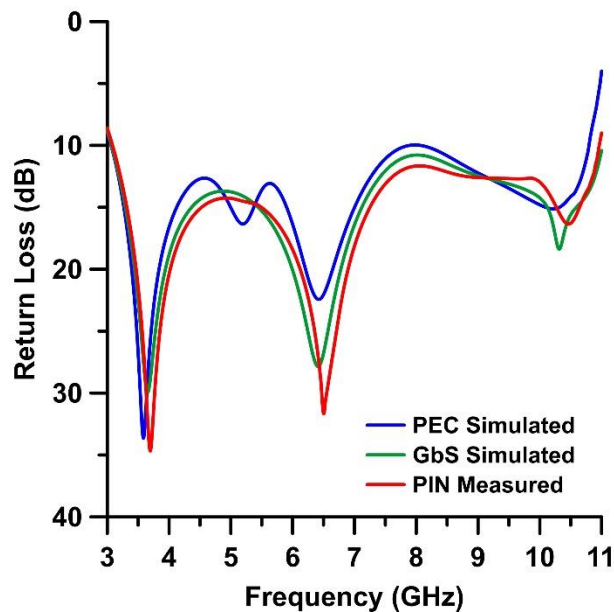
The simulated return loss of the filtenna using the PEC based switches in switch OFF state and switch ON state are given in Figure 4.3–8 (a) and Figure 4.3–8 (b) respectively. The results in both states show the passband of the filtenna to be from about 3.06 GHz to 10.67 GHz at a return loss of more than 10 dB. In the switch OFF state, a complete bandpass response without any notchband is obtained. This allows the filtenna to operate at the 5.25 GHz and 5.8 GHz WLAN bands. In the switch ON state, sharp dual notchband are present at 5.32 GHz and 5.76 GHz at a return loss of 1.97 dB and 1.81 dB respectively. Thus, the two WLAN bands are rejected.

For obtaining the results using Graphene based switches, the values of the varying surface resistance and the varying surface reactance of Graphene based switches were calculated using (3.1)–(3.4) in MATLAB; where the relaxation time, τ , was 10 ps. The Graphene based switches are implemented in Sonnet as a “General” metal type and are placed in the filtenna structure at the four locations marked for switching elements. For Graphene based switches, the dimension parameter L_s has a value of 0.1 mm. The programming software programs SonnetLab and MATLAB are used to electromagnetically simulate the filter in Sonnet using the programming code given in Appendix B. The filter is simulated twice: first with the Graphene based switches in switch OFF state and then with the Graphene based switches in switch ON state.

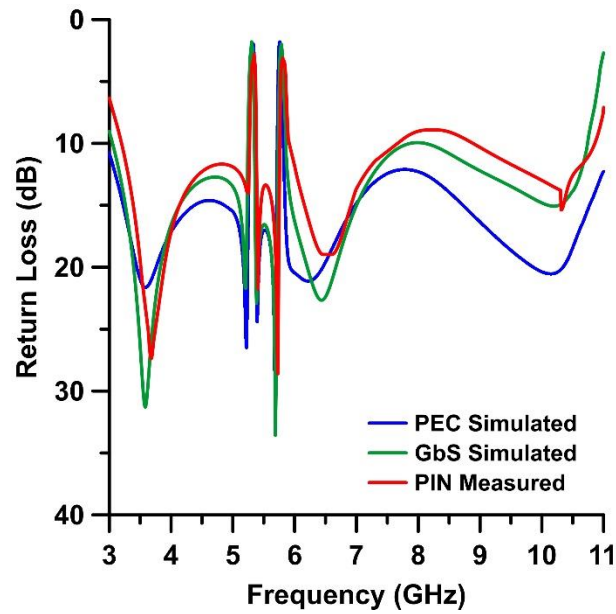
The return loss of the filtenna using the Graphene based switches in switch OFF state and switch ON state are given in Figure 4.3–8 (a) and Figure 4.3–8 (b) respectively. The results in both states are in good agreement with the results from the PEC based switches. The results in both states show the passband of the filtenna to be roughly from 3.07 GHz to 10.9 GHz at a return loss of more than 10 dB. In the switch OFF state, the passband region does not contain any notchband. This allows the filtenna to function at the 5.25 GHz and 5.8 GHz WLAN bands. In the switch ON state, sharp dual notchband are present at 5.3 GHz and 5.78 GHz at a return loss of 1.8 dB and 2 dB respectively. Thus, the two WLAN bands are rejected.

For a comparison with the PEC based switches and the Graphene based switches and for the verification of actual results, the fabricated prototype of the filtenna in Figure 4.3–5 is affixed with the same PIN diodes as the bandstop filter described previously.

The measured return loss of the filtenna using the PIN diodes in switch OFF state and switch ON state are given in Figure 4.3–8 (a) and Figure 4.3–8 (b) respectively. The measured results in both states reasonably agree with the results obtained using the PEC based switches and the Graphene based switches. The results in both state show the passband of the filtenna to be present from 3.09 GHz to 10.86 GHz at a return loss of more than 10 dB. In the switch OFF state, a complete bandpass response without any notchband is obtained. This allows the filtenna to operate at the two WLAN bands. In the switch ON state, sharp dual notchband are obtained at 5.34 GHz and 5.81 GHz at a return loss of 2.7 dB and 2.8 dB respectively. As a result, the two WLAN bands are successfully rejected.



(a)



(b)

Figure 4.3–8: Return loss of the filtenna in the (a) switch OFF and (b) switch ON states.

C) Radiation Patterns of Filtenna

The radiation patterns of the filtenna were simulated and measured at three various frequency points. These three points are at 3.1 GHz, 4.5 GHz and 6.5 GHz and are shown in Figure 4.3–9 (a), Figure 4.3–9 (b) and Figure 4.3–9 (c) respectively. The radiation patterns have been calibrated to the gain of the filtenna and the simulated and measured results have been attuned to obtain the best possible match with each other. As seen from the three results, the filtenna has stable bidirectional radiation patterns in the E-plane and omnidirectional radiation patterns in the H-plane. A reasonable match has been obtained between the simulated and the measured results.

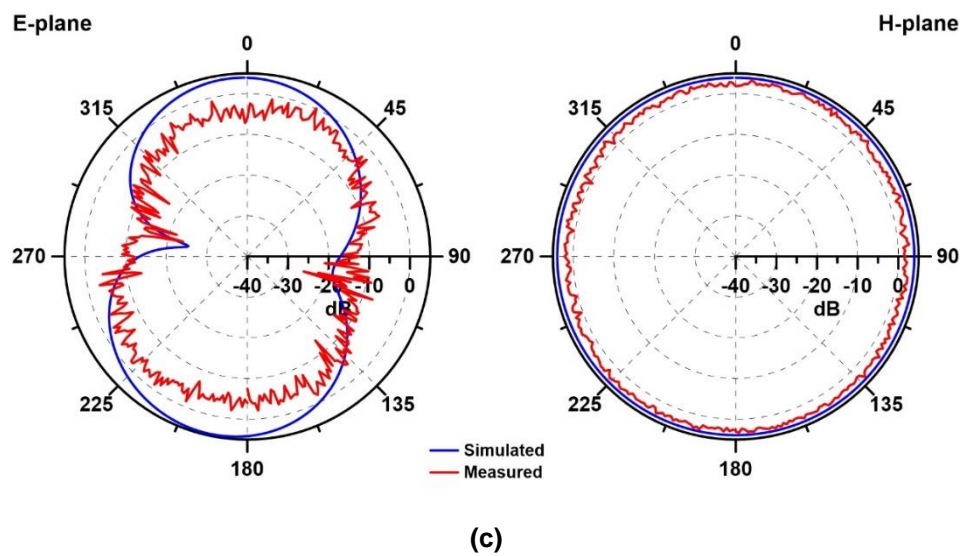
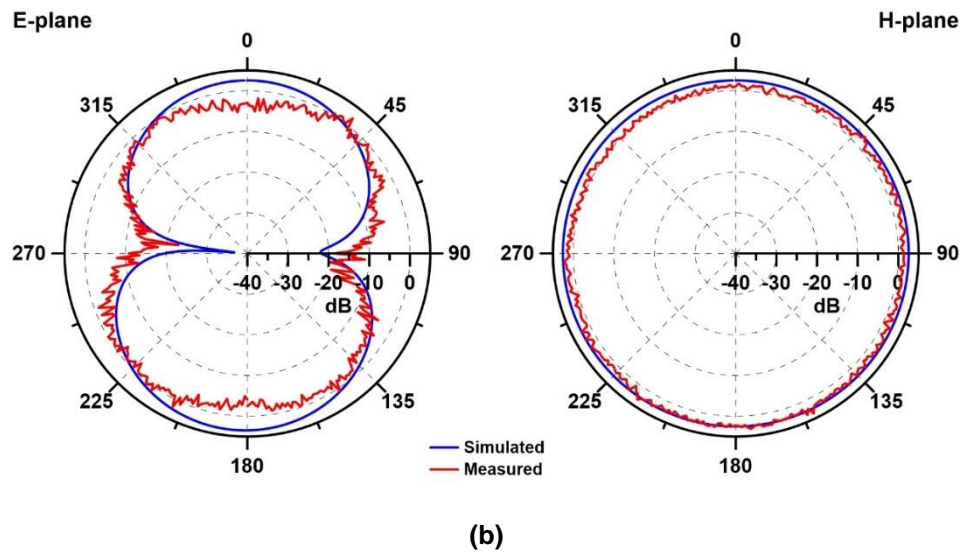
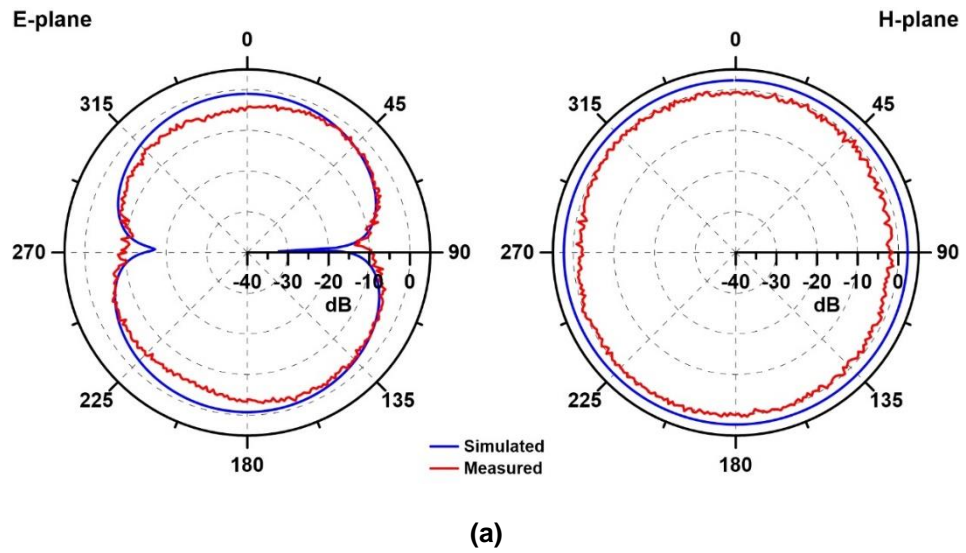


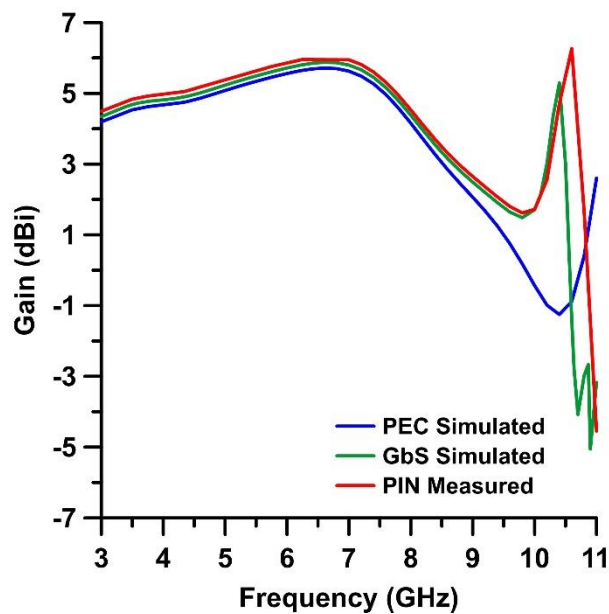
Figure 4.3–9: Radiation patterns of the filtenna at (a) 3.1 GHz, (b) 4.5 GHz and (c) 6.5 GHz.

D) Gain of Filtenna

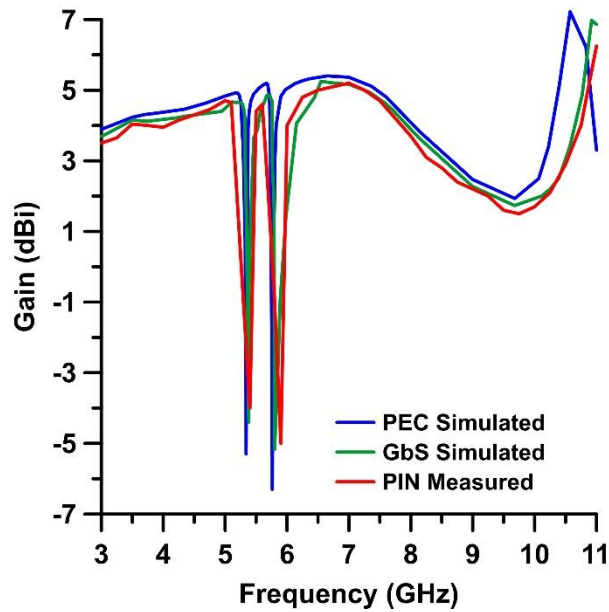
The gain of the filtenna using all three switches was obtained in both the switch OFF state and the switch ON state. The results in the switch OFF state are presented in Figure 4.3–10 (a) and the results in the switch ON state are presented in Figure 4.3–10 (b).

In the switch OFF state, the variance in the gain using Graphene based switches and the PIN diodes is within 4 dBi. At the dual notchband frequencies, the gains using the PEC based switches, Graphene based switches and PIN diodes are at an average of about 5.34 dBi, 5.5 dBi and 5.68 dBi respectively.

In the switch ON state, the only difference from the gains obtained in the switch OFF state is at the dual notchband frequencies. Because of band rejection, at these two frequency points, the gain, using all switches, drops significantly. The obtained gains at the respective dual notchband frequencies using PEC based switches are -5.3 dBi and -6.3 dBi, using Graphene based switches are -4.4 dBi and -5.17 dBi and using PIN diodes are -4 dBi and -5 dBi.



(a)



(b)

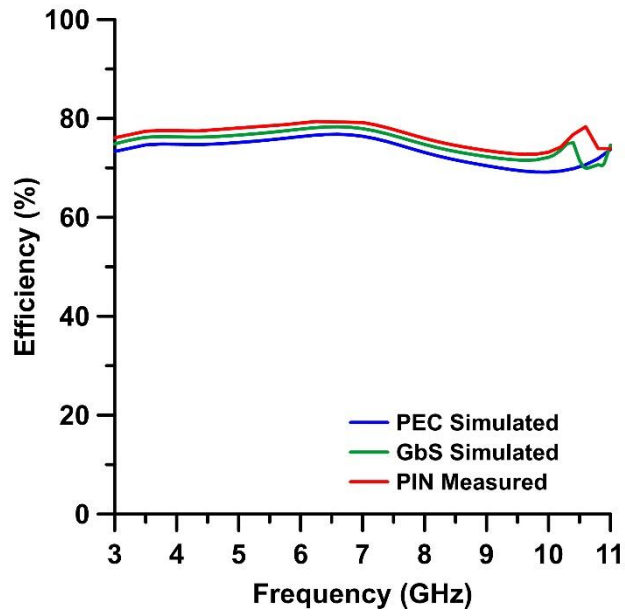
Figure 4.3–10: Gain of the filtenna in the (a) switch OFF and (b) switch ON states.

E) Efficiency of Filtenna

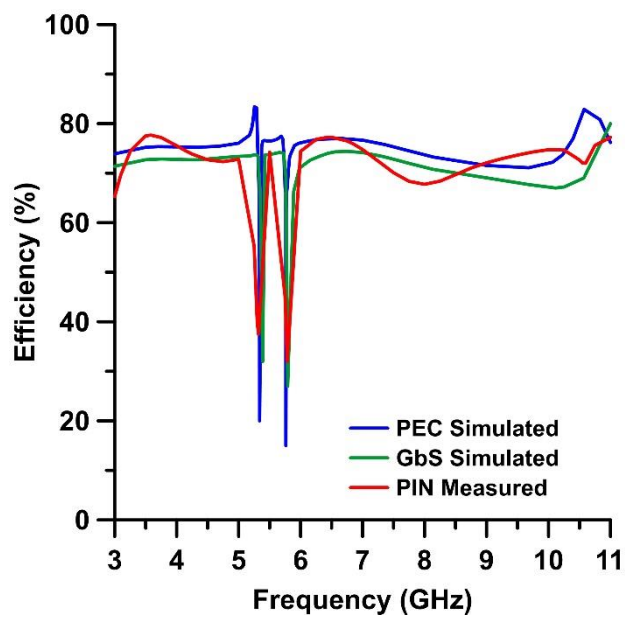
The efficiency of the filtenna using all three switches was acquired in both the switch OFF state and the switch ON state. The results in the switch OFF state are presented in Figure 4.3–11 (a) and the results in the switch ON state are presented in Figure 4.3–11 (b).

In the switch OFF state, the efficiency using all three switches varies between 70 % and 80 %. At the dual notchband frequencies, the efficiencies using the PEC based switches, Graphene based switches and PIN diodes are present at an average of about 75.7 %, 77.25 % and 78.65 % respectively.

In the switch ON state, the only major difference from the efficiencies obtained in the switch OFF state is at the dual notchband frequency points. Because of band rejection, at these two frequency points, the efficiency, using all switches, drops significantly. The obtained efficiencies at the respective dual notchband frequencies using PEC based switches are 20 % and 15 %, using Graphene based switches are 32 % and 27 % and using PIN diodes are 37.5 % and 32 %.



(a)



(b)

Figure 4.3–11: Efficiency of the filtenna in the (a) switch OFF and (b) switch ON states.

4.3.4: Summary of Presented Results

The results of the filtenna are summarised in Table 4.3–5.

Table 4.3–5: Summary of the results of the filtenna in the switch OFF and switch ON states using PEC based switches, Graphene based switches and PIN diodes.

Switch Type	Switch State	Passband (GHz)	FBW (%)	Dual Notchband			
				Frequency (GHz)	Rejection (dB)	Gain (dBi)	Efficiency (%)
PEC	OFF	3.06–10.67	133	None present	n/a	5.2 & 5.5	75.4 & 76
	ON	3.06–10.67	133	5.32 & 5.76	1.97 & 1.81	-5.3 & -6.3	20 & 15
GbS	OFF	3.07–10.90	135	None present	n/a	5.4 & 5.6	77 & 77.5
	ON	3.07–10.90	135	5.3 & 5.78	1.8 & 2	-4.4 & -5.2	32 & 27
PIN	OFF	3.09–10.86	134	None present	n/a	5.5 & 5.8	78 & 78.8
	ON	3.09–10.86	134	5.34 & 5.81	2.7 & 2.8	-4 & -5	37.5 & 32

4.4: Design of a Frequency Reconfigurable Filtenna with Dual Notchband for UWB Applications

4.4.1: Specifications

This section presents a broadband planar monopole filtenna based on the specifications given in Table 4.4–1. The specifications require a single-element monopole filtenna operating at the full UWB range of 3.1–10.6 GHz. The filtenna is required to have a microstrip-based feeding method; where the characteristic impedance of the feed network and the system should be 50Ω . The specifications further ask that the filtenna should be fabricated via PCB technology. Furthermore, the filtenna should have a dual notchband for the rejection of two interfering bands within the UWB range: the IEEE 802.16 WiMAX band operating at 3.5 GHz and the IEEE 802.11 WLAN band operating at 5.8 GHz.

Table 4.4–1: Required specifications of the filtenna.

Parameter	Description of Parameter	Value
Filtenna	Type of filtenna	Single Monopole
Technology	Fabrication technology	PCB
Feed	Feeding method	Microstrip
Z_0	Characteristic impedance of system	50Ω
f_L	Lower passband frequency	3.1 GHz
f_H	Upper passband frequency	10.6 GHz
f_C	Centre frequency	5.73 GHz
FBW	Fractional bandwidth	$\geq 130.84 \%$
n_{NB}	Number of notchband	Dual
f_{NB1} and f_{NB2}	Notchband frequencies	3.5 and 5.8 GHz

4.4.2: Realised Structure and Final Parameters

A) Final Layout

The final layout of the proposed filtenna which meets the specifications given above is illustrated in Figure 4.4–1; with the values of its dimension parameters given in Table 4.4–2. The antenna part of the filtenna is based on the same design as the one given in the section 4.2. Hence, the same equations and layout can be used.

The proposed filtenna utilises a defected ground structure with a partial ground plane. The length, L_G , of the partial ground plane is 13.1 mm. The filtenna has a microstrip-based feed network. The transmission feed line has a width, W_F , of 2.4 mm which corresponds to the required characteristic impedance of 50 Ω .

The required dual notchband are inserted in the passband of the filtenna by an integrated filter network. The filter network consists of three ring resonators: one circular ring resonator and two rectangular ring resonators.

The circular ring resonator, which produces a notchband at 3.5 GHz, is placed within the radiating element of the filtenna. Since, it is placed within the radiating element, metallisation of the shape of the circular ring resonator is cut out from the element. The radius of the inner edge, R_C , of the circular ring resonator is 5.35 mm. The thickness of the circular ring resonator, T_C , i.e. the distance between the inner edge and the outer edge of the resonator, is 0.5 mm. A splitting gap of a length, G_C , of 0.8 mm is present in the resonator. The circular ring resonator is half-wavelength, $\lambda_g/2$, long; where λ_g , is the guided wavelength at its respective notchband of 3.5 GHz. The total length of the resonator, L_{CRR} , can be calculated using (4.7).

$$L_{CRR} = \pi(2R_C + T_C) - G_C \quad (4.7)$$

The 5.8 GHz notchband is produced by the two rectangular ring resonators. Each resonator is laid on either side of the transmission feed line. These resonators are capacitively coupled with the main structure and, thus, two have been used so as to improve the coupling and achieve better notchband rejection results. The thickness of the resonators, T_R , i.e. the width of the resonators, is 0.5 mm. A splitting gap of a length, L_S , of 0.3 mm is present in the resonators. Each rectangular ring resonator is half-wavelength, $\lambda_g/2$, long; where λ_g , is the guided wavelength at its respective notchband of 5.8 GHz. The total length of the resonator, L_{RRR} , can be calculated using (4.8).

$$L_{RRR} = 2L1_R + 2L2_R - 4T_R - G_R \quad (4.8)$$

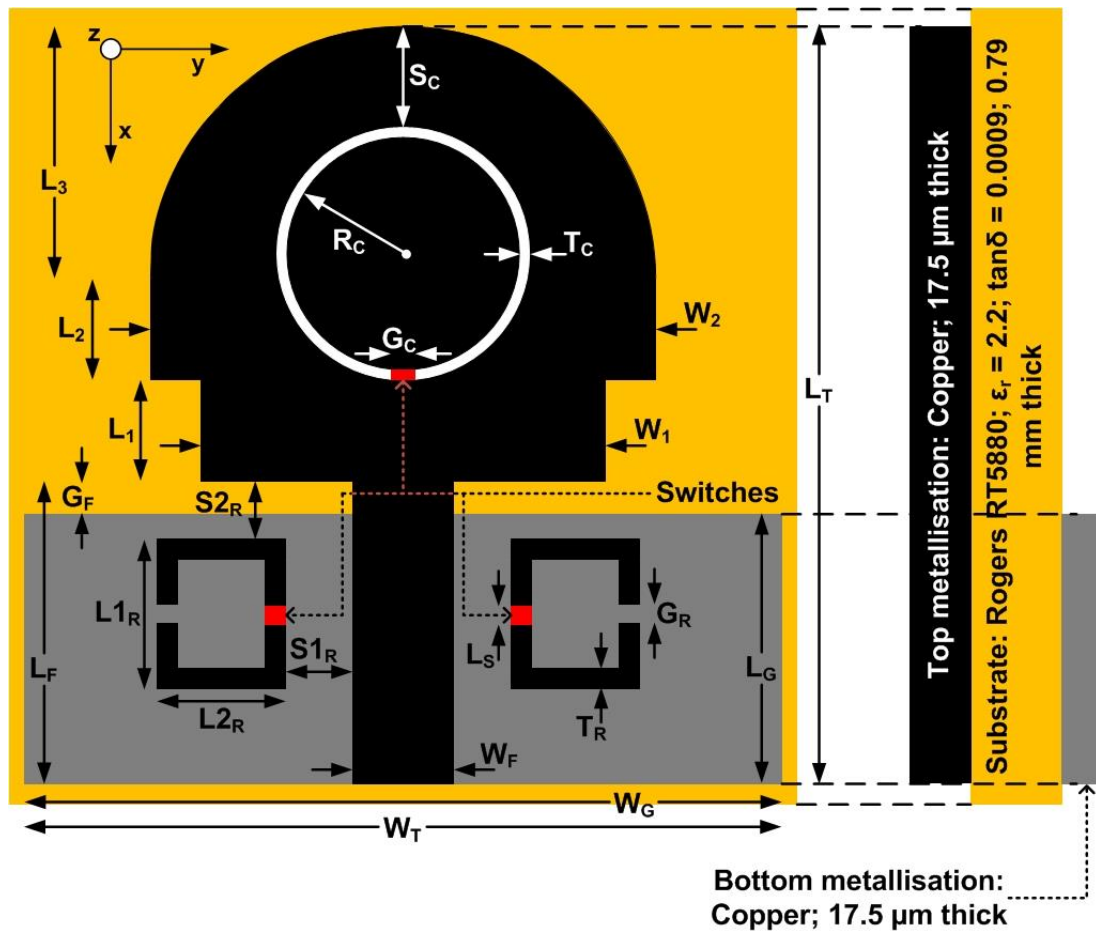


Figure 4.4–1: Geometry of the filtenna.

Table 4.4–2: Values of the dimension parameters of the filtenna.

Parameter	Value (mm)	Parameter	Value (mm)
W_T	32	L_{1R}	6.5
L_T	36.2	L_{2R}	4.5
W_G	32	T_R	0.5
L_G	13.1	G_R	0.5
W_F	2.4	S_{1R}	1
L_F	13.6	S_{2R}	1.1
G_F	0.5	L_S	0.3
W_1	15	R_C	5.35
L_1	4.3	T_C	0.5
W_2	23.8	G_C	0.8
L_2	6.4	S_C	6.26
L_3	11.9		

B) Attainment of Reconfigurability

In order to introduce reconfigurability in the filtenna to control the behaviour of the dual notchband, switching elements are placed at three positions in the integrated filter. Of these three positions, the first is at the point where the circular ring resonator connects to the rest of the filtenna metallisation and the other two are the mid-points of the longest transmission line of each rectangular ring resonator. The length of the gaps for the placement of the two switches in the rectangular ring resonators, L_S , is 0.3 mm and of the single switch in the circular ring resonator, G_C , is 0.8 mm. The three positions have been marked in red in the geometry of the filtenna given in Figure 4.4–1.

Switching element placed at the specified position in the circular ring resonator would act as a switch which can deny or allow the connection between the inner edge of the resonator and the rest of the filtenna metallisation. In its switch OFF state, the switching element would deny any connection between the two parts of the metallisation; thus, rejecting the flow of current into the inner edge of the resonator. On the other hand, in the switch ON state of the switching element, the metallisation within the resonator would be connected to the rest of the filtenna metallisation; thus, resulting in a notchband at the respective frequency of the circular ring resonator, i.e. at 3.5 GHz.

The other two switches, placed at the indicated positions in the rectangular ring resonators, would effectively be dividing each resonator into two sections of equal size. In other words, each rectangular ring resonator would consist of two transmission lines of an equal length — mirroring each other in the y-axis — conjoined with a switching element. When the switching elements are in their switch OFF state, there would be no connection between the two transmission lines of each resonator. As a result, the effective length of each resonator will be halved. This will result in the 5.8 GHz notchband not being present in the passband of the filtenna. Whereas, when the switching elements are in their switch ON state, the two transmission lines of each resonator will be connected to each other. In this state, the resulting length of both resonators will become equal to half-wavelength at the desired notchband frequency. This will result in a notchband being produced at the respective frequency of the rectangular ring resonators, i.e. at 5.8 GHz.

C) Fabrication of Final Layout

The final layout of the filtenna is designed on a Rogers RT5880 substrate of a thickness of 0.795 mm, having a dielectric permittivity of $\epsilon_r = 2.2$ and a dielectric loss

factor of $\tan \delta = 0.0009$. It is modelled and simulated using the commercial full-wave electromagnetic simulation software program Sonnet. A photograph of the top side and the bottom side of the fabricated PCB filtenna is shown in Figure 4.4–2 (a) and Figure 4.4–2 (b) respectively.

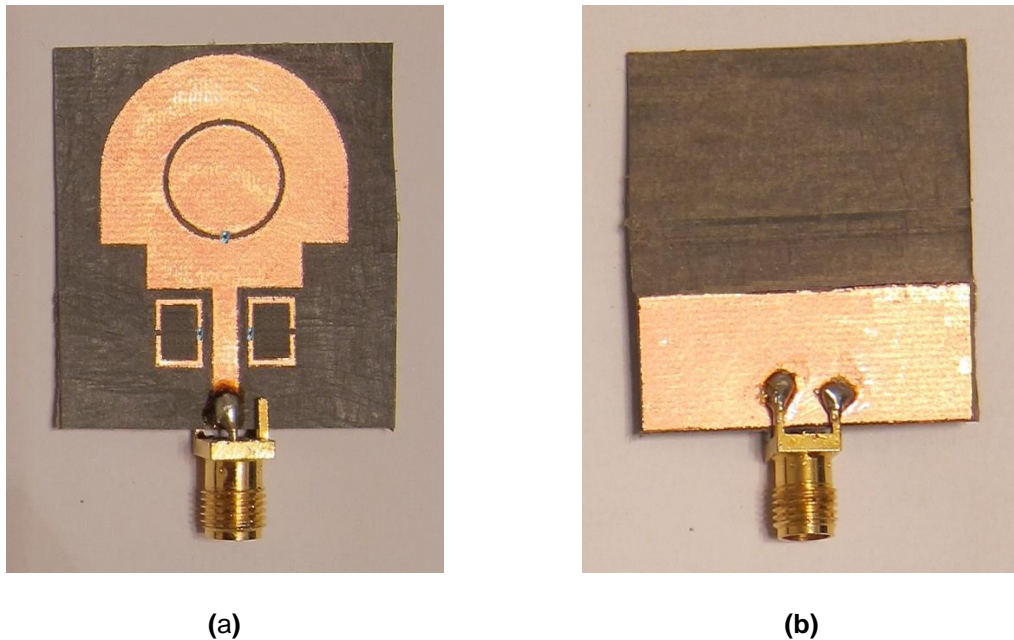


Figure 4.4–2: Photographs of (a) the top side and (b) the bottom side of the fabricated PCB filtenna.

4.4.3: Results

A) Return Loss of Filtenna

The filtenna from Figure 4.4–1 was simulated using the final values from Table 4.4–2. In order to determine the results of the filtenna in switch OFF state and switch ON state without the use of lossy switching elements, the simulations for the two states were carried out using gaps and PEC based switches. The switch OFF state was simulated by leaving gaps at the three points wherein the actual switches would be placed. The switch ON state was simulated by placing PEC metallic patches at the three locations.

The simulated return loss of the filtenna using the PEC based switches in switch OFF state and switch ON state are given in Figure 4.4–3 (a) and Figure 4.4–3 (b) respectively. The result in the switch OFF state shows the passband of the filtenna to be about 2.82 GHz to 11.45 GHz at a return loss of more than 10 dB. Furthermore, in the switch OFF state, a complete bandpass response without any

notchband is obtained. This allows the filtenna to operate at the 3.5 GHz WiMAX and the 5.8 GHz WLAN bands. In the switch ON state, the passband of the filtenna is obtained from 2.81 GHz to 11.91 GHz. Moreover, in the switch ON state, dual notchband are present at 3.45 GHz and 6.04 GHz at a return loss of 0.8 dB and 1.3 dB respectively. Thus, the WiMAX and the WLAN bands are rejected.

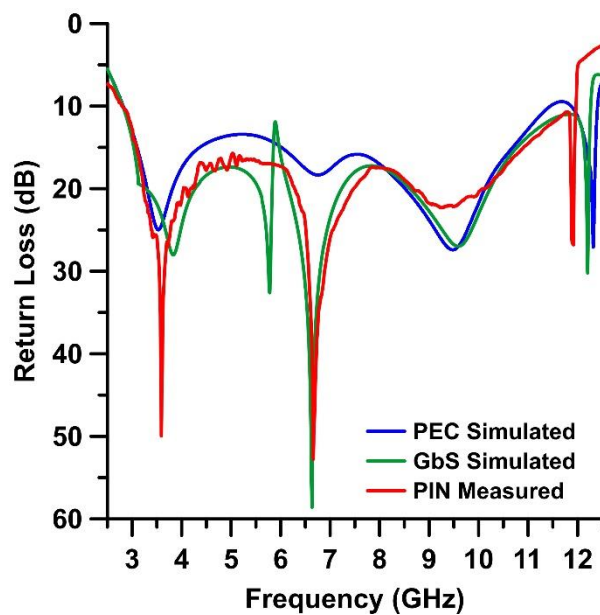
In order to obtain the results using Graphene based switches, the values of the varying surface resistance and the varying surface reactance of Graphene based switches were calculated using (3.1)–(3.4) in MATLAB; where the relaxation time, τ , was 125 ps. The Graphene based switches are implemented in Sonnet as a “General” metal type and are placed in the filtenna structure at the three locations marked for switching elements. The programming software programs SonnetLab and MATLAB are used to electromagnetically simulate the filter in Sonnet using the programming code given in Appendix B. The filtenna is simulated twice: first with the Graphene based switches in switch OFF state and then with the switches in switch ON state.

The return loss of the filtenna using the Graphene based switches in switch OFF state and switch ON state are given in Figure 4.4–3 (a) and Figure 4.4–3 (b) respectively. The results in both states are in reasonable agreement with the results from the PEC based switches. The results in both states show the passband of the filtenna to be roughly from 2.81 GHz to 11.94 GHz at a return loss of more than 10 dB. In the switch OFF state, the passband region does not contain any notchband. This allows the filtenna to function at the 3.5 GHz WiMAX and 5.8 GHz WLAN bands. In the switch ON state, dual notchband are present at 3.45 GHz and 6.03 GHz at a return loss of 1.6 dB and 1.54 dB respectively. Thus, the WiMAX and the WLAN bands are rejected.

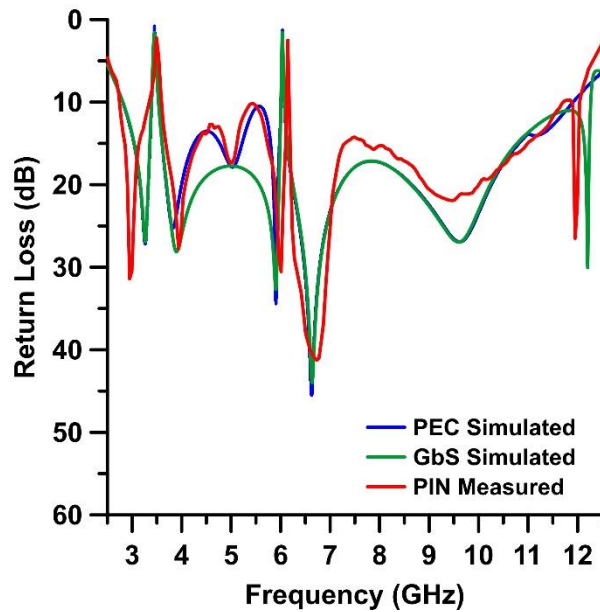
For a comparison with the PEC based switches and the Graphene based switches and for the verification of actual results, the fabricated prototype of the filtenna in Figure 4.4–2 is affixed with PIN diodes as the switching elements. The PIN diodes used are NXP BAP65–02. Each PIN diode has a resistance of 0.9Ω , an inductance of 0.6 nH and a capacitance of 0.8 pF [3-19]. The PIN diodes are powered on by supplying an external DC voltage of 3 V and a current of 1 mA. The DC blocking capacitance is 33 pF and a resistor of 1 k Ω is used for biasing. The return loss of the fabricated prototype of the filtenna with the PIN diodes reverse-biased and then forward-biased is measured using an Agilent E8361A PNA Network Analyser.

The measured return loss of the filtenna using the PIN diodes in switch OFF state and switch ON state are given in Figure 4.4–3 (a) and Figure 4.4–3 (b) respectively. The measured results in both states reasonably agree with the results obtained

using the PEC based switches and the Graphene based switches. The result in the switch OFF state shows the passband of the filtenna to be about 2.8 GHz to 11.97 GHz at a return loss of more than 10 dB. Additionally, in the switch OFF state, a bandpass response without any notchband is obtained. This allows the filtenna to operate at the 3.5 GHz WiMAX and the 5.8 GHz WLAN bands. In the switch ON state, the passband of the filtenna is obtained from 2.75 GHz to 11.7 GHz. Moreover, because the PIN diodes are forward-biased and the connections within the three ring resonators are complete, dual notchband are obtained. The dual notchband are present at 3.49 GHz and 6.15 GHz at a return loss of 2.2 dB and 2.5 dB respectively.



(a)



(b)

Figure 4.4–3: Return loss of the filtenna in the (a) switch OFF and (b) switch ON states.

B) Parametric Study of Position of both Ring Resonators

Parametric studies were carried out in order to check the rejection performance when the position of the circular ring resonator and the rectangular ring resonators was changed.

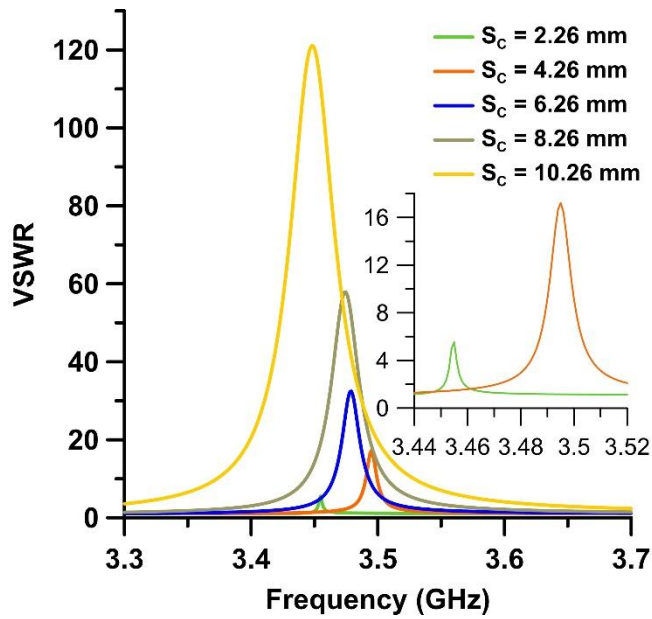
With regards to the circular ring resonator, it is expected that as it is moved closer to the top-end of the transmission feed line, the return loss rejection at the notchband frequency of 3.5 GHz will increase. Similarly, with regards to the rectangular ring resonators, it is expected that as they are moved further away from the radiating element and the top-end of the transmission feed line, the return loss rejection at the notchband frequency of 5.8 GHz will decrease.

So as to verify these statements, the filtenna was simulated with the circular ring resonator and the rectangular ring resonators relocated. The 3.5 GHz circular ring resonator was repositioned by varying the width, S_C , of the gap between the top-end of the filtenna and the top-end of the circular ring resonator. Whereas, the position of the 5.8 GHz rectangular ring resonators was altered by using various values for the width, S_{2R} , of the gap between the rectangular ring resonators and the radiating element. The results of these simulations are given in Figure 4.4–4. (For clarity purposes, rather than the return loss, the VSWR in a limited frequency range is plotted for the results. As the return loss decreases, the VSWR increases; inferring

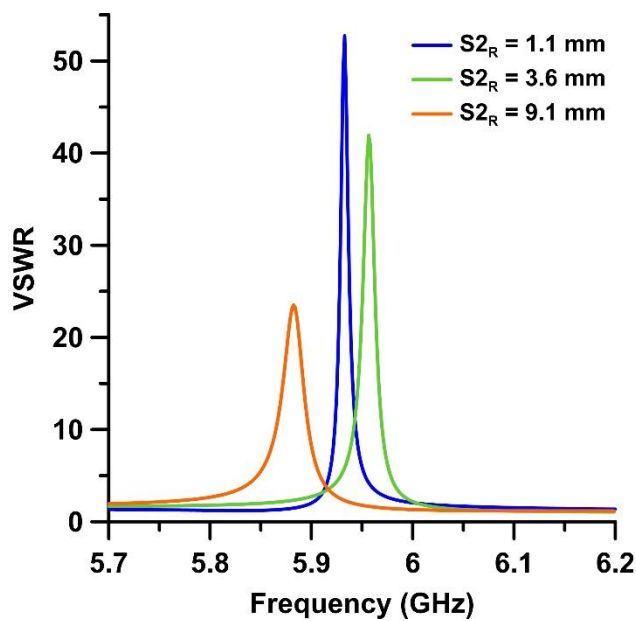
higher rejection characteristics. The vice versa situation would denote lower rejection characteristics.)

As can be seen from Figure 4.4–4 (a), the circular ring resonator was moved in the x -axis in increments of 2 mm from $S_C = 2.26$ mm to $S_C = 10.26$ mm. From the results, it is evident that as the circular ring resonator moves closer to the transmission feed line, the VSWR increases accordingly. In the final/original design when $S_C = 6.26$ mm, the VSWR at the notchband frequency is 32.44 ($S_{11} = 0.54$ dB). At the smaller values of $S_C = 2.26$ mm and $S_C = 4.26$ mm, i.e. when the resonator is located further away from the transmission feed line, the VSWR at the notchband frequency decreases to become 5.02 ($S_{11} = 3.51$ dB) and 17.22 ($S_{11} = 1.01$ dB) respectively. On the other hand, at the larger values of $S_C = 8.26$ mm and $S_C = 10.26$ mm, i.e. when the resonator is located closer to the transmission feed line, the VSWR at the notchband frequency increases to become 57.9 ($S_{11} = 0.3$ dB) and 121.09 ($S_{11} = 0.14$ dB) respectively. However, this repositioning of the circular ring resonator does not significantly affect the notchband frequency. In the presented results, the frequency shift is minor; averaging at ± 11.25 MHz (± 0.32 %).

As apparent from Figure 4.4–4 (b), the rectangular ring resonators were first moved 2.5 mm downwards in the x -axis — increasing the width, S_{2R} , of the gap to 3.6 mm — and then again moved a further of 5.5 mm downwards in the x -axis — increasing the width, S_{2R} , of the gap to 9.1 mm. From the results, it can be seen that as the rectangular ring resonators move further away from the radiating element, the VSWR decreases accordingly. In the final/original design, i.e. when $S_{2R} = 1.1$ mm, the VSWR at the notchband frequency is 52.73 ($S_{11} = 0.33$ dB). At $S_{2R} = 3.6$ mm, the VSWR at the notchband frequency decreases to 41.92 ($S_{11} = 0.41$ dB). Finally, at $S_{2R} = 9.1$ mm, the VSWR at the notchband frequency drops further to become 23.51 ($S_{11} = 0.74$ dB). However, this repositioning of the rectangular ring resonators does not significantly affect the notchband frequency. In the presented results, the frequency shift is minor; averaging at ± 40 MHz (± 0.68 %).



(a)



(b)

Figure 4.4–4: Parametric study of the effects on the VSWR of the filtenna by varying the position of (a) the 3.5 GHz resonator and (b) the 5.8 GHz resonators.

C) Current Densities of Filtenna

In order to show the effects of the circular and rectangular ring resonators on the filtenna during the switch OFF and switch ON operations, the current density of the filtenna was simulated at the dual notchband frequencies of 3.45 GHz and 6.03 GHz and at the passband frequency of 9.55 GHz.

The obtained results in the two reconfigurable states at the dual notchband frequencies are given in Figure 4.4–5 and Figure 4.4–6. In the switch OFF state at these two frequencies, the currents are present at places other than the resonators. When the filtenna is operated in the switch ON state at these two frequencies, the currents can be seen to be completely densely populated along the respective resonators. However, at the passband frequency, given in Figure 4.4–7, there is almost no difference between the two states. This indicates that the two reconfigurable states of the filtenna only affect the passband at the dual notchband frequencies.

Furthermore, if the distribution of the surface currents had been obtained at the dual notchband frequencies, it would have shown the currents to be concentrated along the edges of the respective resonators. The direction of the flow of the current along the inner edges and the outer edges of the resonators would have been opposite to each other. (The opposite directions would cancel the currents and produce notchband.)

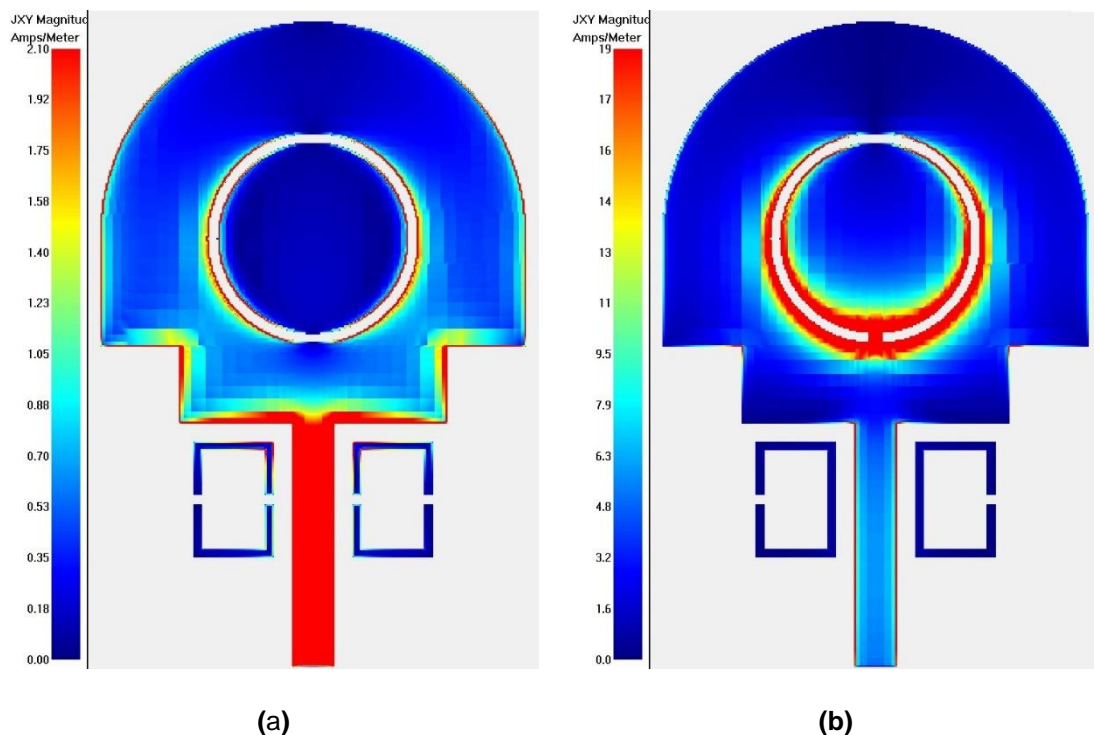


Figure 4.4–5: Current density of the filtenna at 3.45 GHz in the (a) switch OFF and (b) switch ON states.

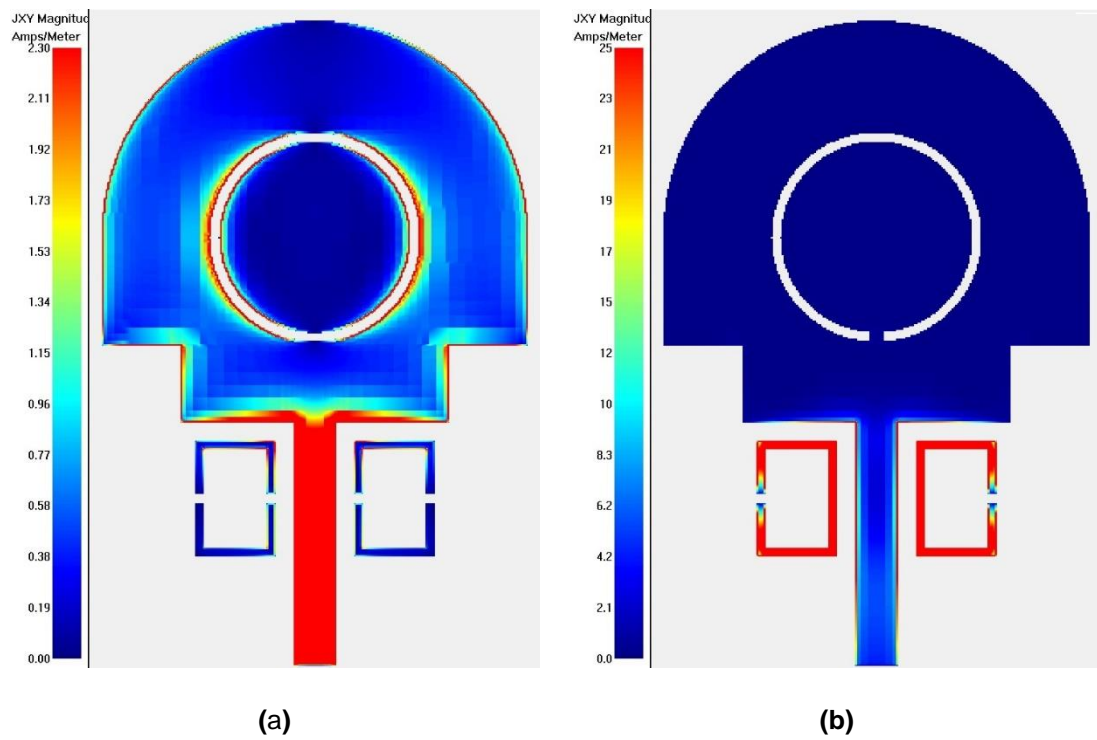


Figure 4.4-6: Current density of the filtenna at 6.03 GHz in the (a) switch OFF and (b) switch ON states.

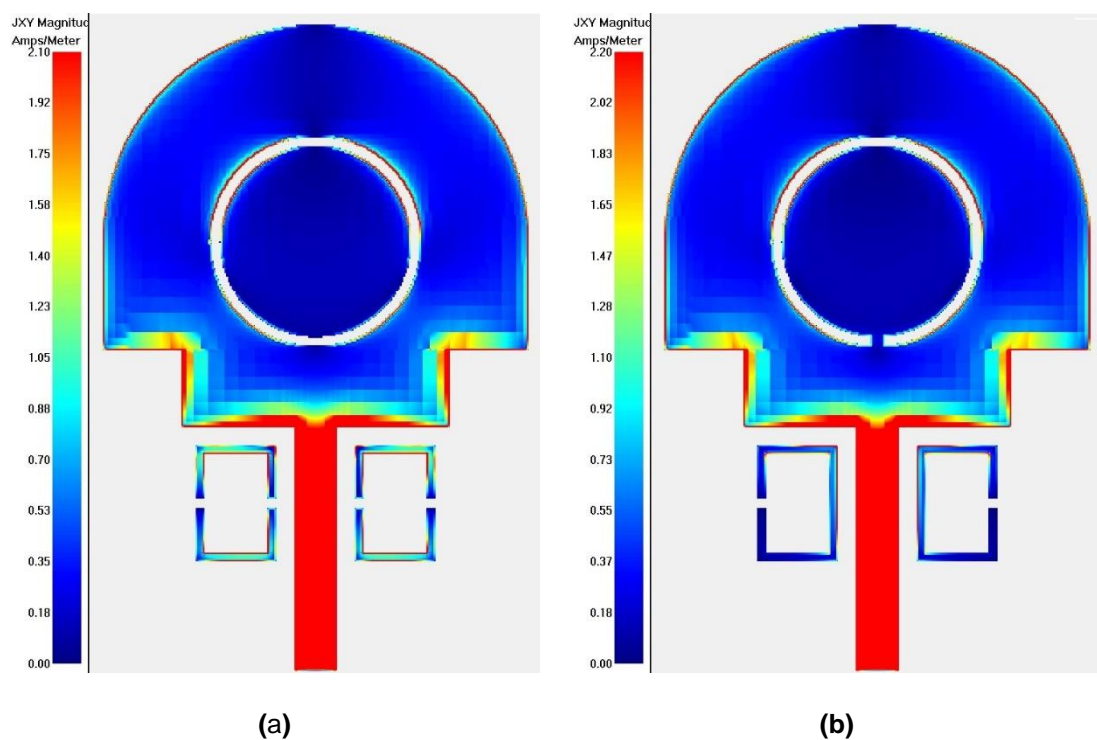


Figure 4.4-7: Current density of the filtenna at 9.55 GHz in the (a) switch OFF and (b) switch ON states.

D) Radiation Patterns of Filtenna

For the purpose of measuring its radiation patterns, the filtenna with PEC based switches was put in an anechoic chamber. The source/transmitting antenna is a horn antenna. A photograph of the filtenna under test is shown in Figure 4.4–8.

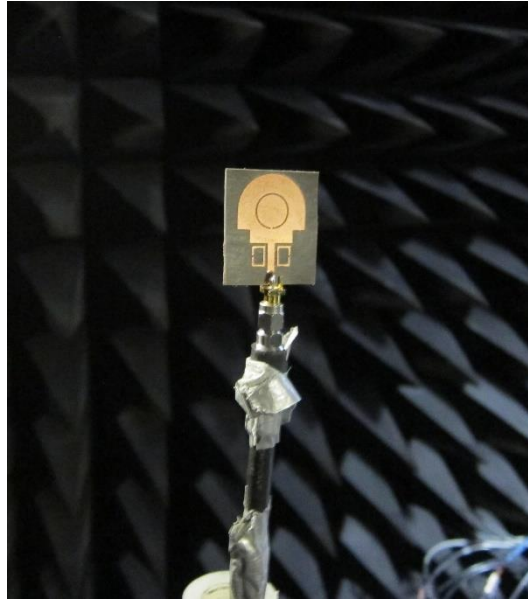


Figure 4.4–8: Photograph of the inside of an anechoic chamber showing the filtenna under test.

The radiation patterns of the filtenna were simulated and measured at three various frequency points. These three points are at 3.1 GHz, 4.5 GHz and 6.5 GHz and are shown in Figure 4.4–9 (a), Figure 4.4–9 (b) and Figure 4.4–9 (c) respectively. The radiation patterns have been calibrated to the gain of the filtenna and the simulated and measured results have been attuned to obtain the best possible match with each other. As seen from the three results, the filtenna has stable bidirectional radiation patterns in the E-plane and omnidirectional radiation patterns in the H-plane. A reasonable match has been obtained between the simulated and the measured results.

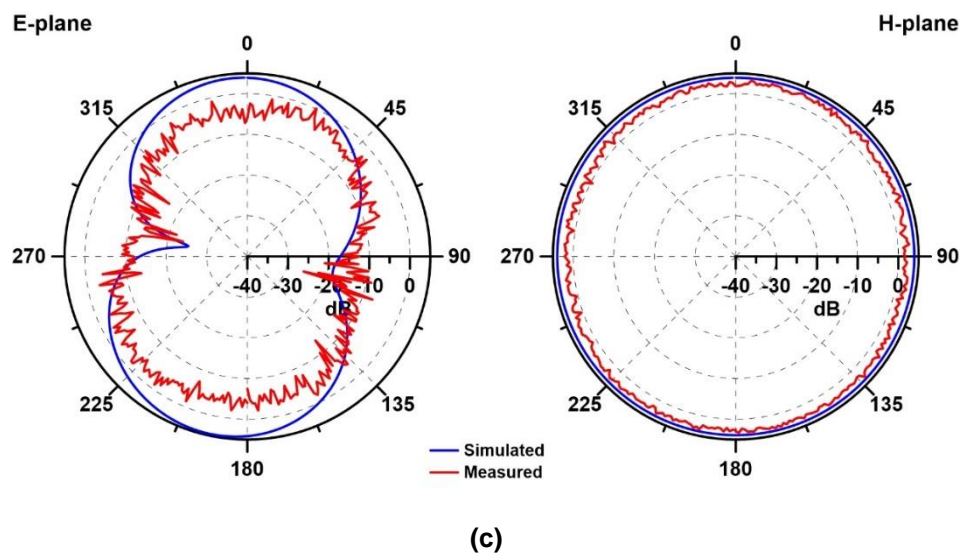
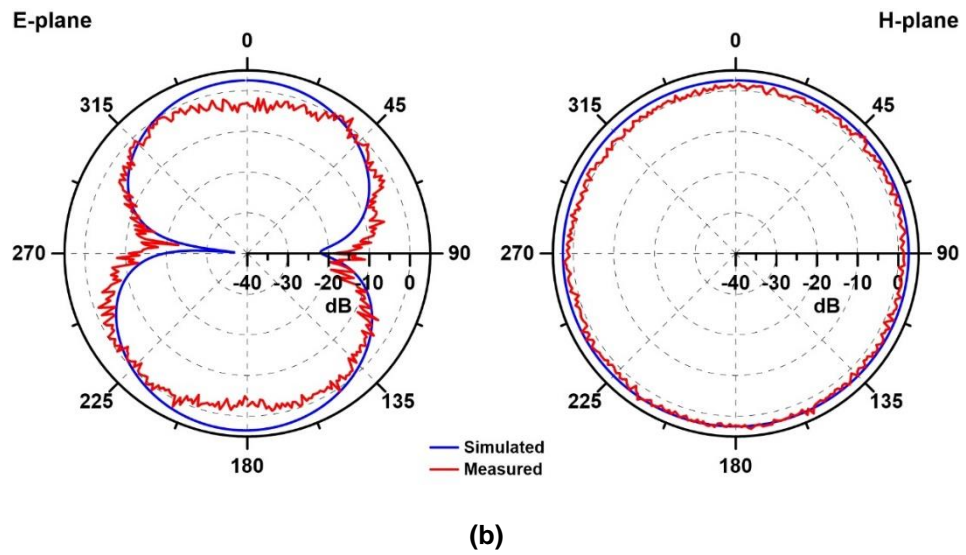
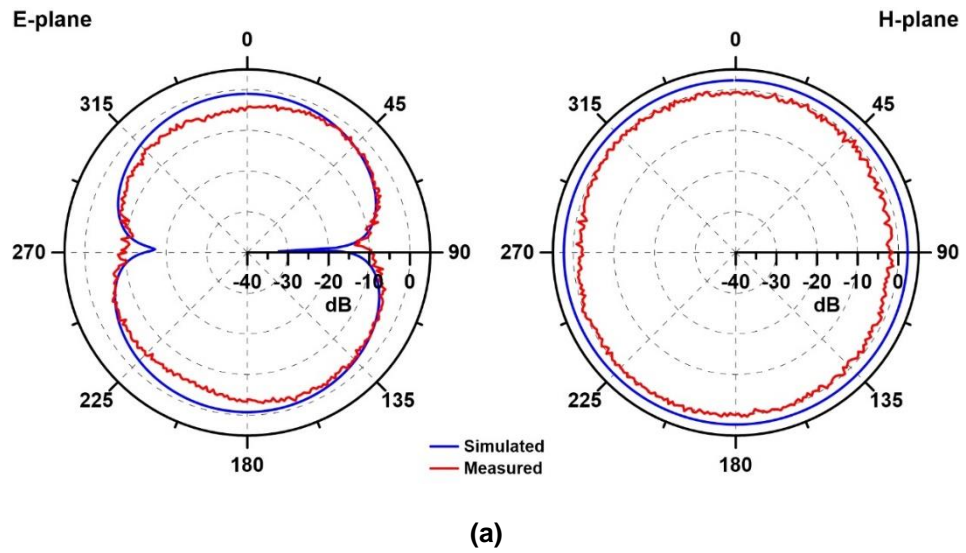


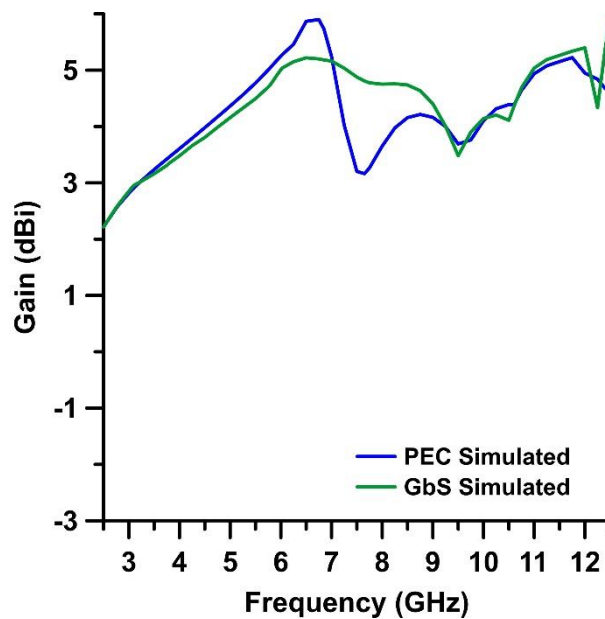
Figure 4.4–9: Radiation patterns of the filtenna at (a) 3.1 GHz, (b) 4.5 GHz and (c) 6.5 GHz.

E) Gain of Filtenna

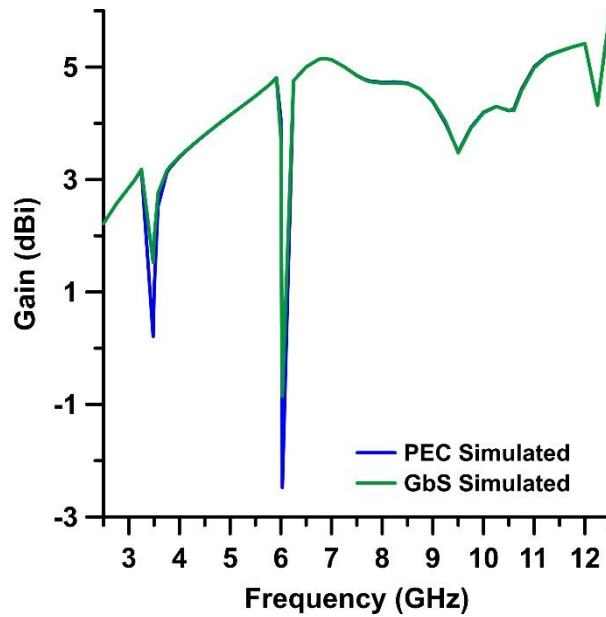
The simulated gain of the filtenna using PEC based switches and Graphene based switches was obtained in both the switch OFF state and the switch ON state. The results in the switch OFF state are presented in Figure 4.4–10 (a) and the results in the switch ON state are presented in Figure 4.4–10 (b).

In the switch OFF state, the variance in the gain using the two switches is within 3 dBi. At the dual notchband frequencies, the respective gains using PEC based switches are present at 3.22 dBi and 5.28 dBi and using Graphene based switches are present at 3.15 dBi and 5.04 dBi.

In the switch ON state, the only difference from the gains obtained in the switch OFF state is at the dual notchband frequencies. Because of band rejection, at these two frequency points, the gain, using both switches, drops considerably. The obtained gains at the respective dual notchband frequencies using PEC based switches are 0.21 dBi and -2.48 dBi and using Graphene based switches are 1.53 dBi and -0.85 dBi.



(a)



(b)

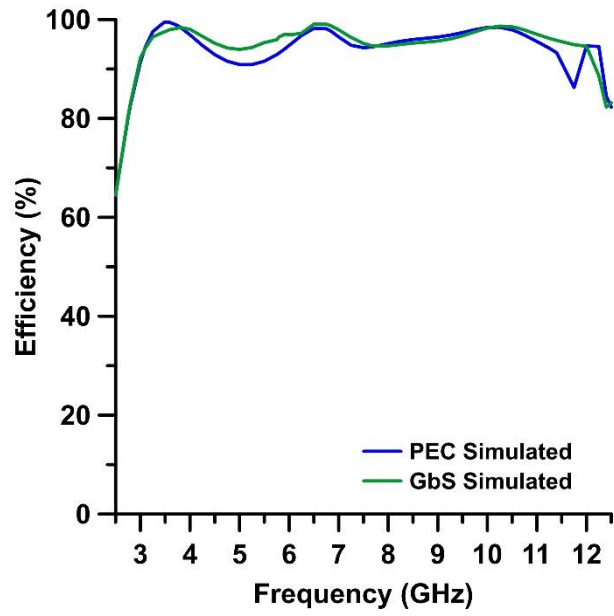
Figure 4.4–10: Gain of the filtenna in the (a) switch OFF and (b) switch ON states.

F) Efficiency of Filtenna

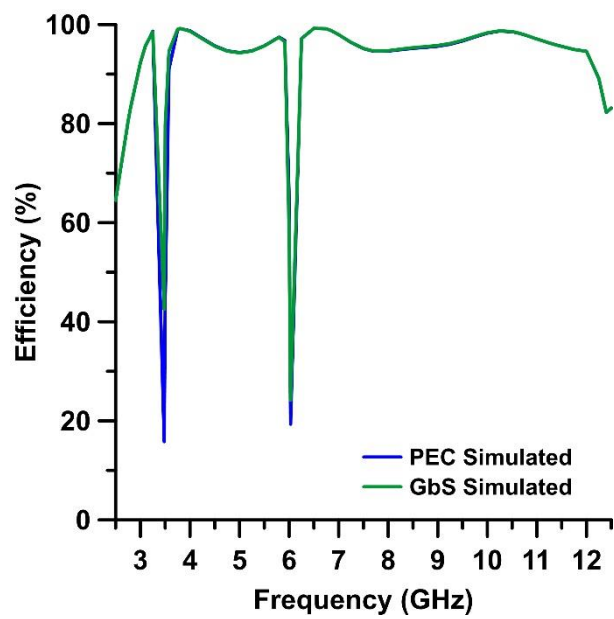
The simulated efficiency of the filtenna using the PEC based switches and the Graphene based switches was acquired in both the switch OFF state and the switch ON state. The results in the switch OFF state are presented in Figure 4.3–11 (a) and the results in the switch ON state are presented in Figure 4.3–11 (b).

In the switch OFF state, the efficiency across the passband using both switches varies between 90 % and 98 %. At the dual notchband frequencies, the respective efficiencies using the two switches are present at an average of about 98.5 % and 96 %.

In the switch ON state, the only major difference from the efficiencies obtained in the switch OFF state is at the dual notchband frequency points. Because of band rejection, at these two frequency points, the efficiency, using both switches, drops significantly. The obtained efficiencies at the respective dual notchband frequencies using PEC based switches are 15.8 % and 19.3 % and using Graphene based switches are 42.5 % and 24.1 %.



(a)



(b)

Figure 4.4–11: Efficiency of the filter antenna in the (a) switch OFF and (b) switch ON states.

4.4.4: Summary of Presented Results

The results of the filtenna are summarised in Table 4.4–3.

Table 4.4–3: Summary of the results of the filtenna in the switch OFF and switch ON states using PEC based switches, Graphene based switches and PIN diodes.

Switch Type	Switch State	Passband (GHz)	FBW (%)	Dual Notchband			
				Frequency (GHz)	Rejection (dB)	Gain (dBi)	Efficiency (%)
PEC	OFF	2.82–11.45	152	None present	n/a	3.2 & 5.3	99.5 & 95
	ON	2.81–11.91	157	3.45 & 6.04	0.8 & 1.3	0.2 & -2.5	15.8 & 19.3
GbS	OFF	2.81–11.94	158	None present	n/a	3.2 & 5.0	97.5 & 96.9
	ON	2.81–11.94	158	3.45 & 6.03	1.6 & 1.54	1.5 & -0.9	42.5 & 24.1
PIN	OFF	2.80–11.97	158	None present	n/a	n/p	n/p
	ON	2.75–11.70	158	3.49 & 6.15	2.2 & 2.5	n/p	n/p

4.5: Design of a Compact Inkjet-Printed Flexible Filtenna with Triple Notchband for S-band, ISM Band and UWB Applications

4.5.1: Specifications

This section presents a broadband planar monopole filtenna based on the specifications given in Table 4.5–1. The specifications require a single-element monopole filtenna operating in the frequency range of 1.5–10.6 GHz; which includes the 2 GHz S-band, 2.45 GHz ISM band and 3.1–10.6 GHz UWB. The filtenna is required to have a coplanar waveguide-based feeding method; where the characteristic impedance of the feed network and the system should be 97Ω . The specifications further ask that the filtenna should be fabricated via inkjet-printing technology. Furthermore, the filtenna should have a triple notchband for the rejection of three interfering bands within its broad operational range: the IEEE 802.16 WiMAX band operating at 3.5 GHz, the IEEE 802.11 WLAN band operating at 5.8 GHz and the ITU satellite communication system band operating at 8.2 GHz.

Table 4.5–1: Required specifications of the filtenna.

Parameter	Description of Parameter	Value
Filtenna	Type of filtenna	Single Monopole
Technology	Fabrication technology	Inkjet-Printed
Feed	Feeding method	CPW
Z_0	Characteristic impedance of system	97Ω *
f_L	Lower passband frequency	1.5 GHz
f_H	Upper passband frequency	10.6 GHz
f_C	Centre frequency	3.99 GHz
FBW	Fractional bandwidth	$\geq 228.21 \%$
n_{NB}	Number of notchband	Triple
$f_{NB1}, f_{NB2}, f_{NB3}$	Notchband frequencies	3.5, 5.8, 8.2 GHz

* Set to 97Ω due to inaccessibility of CPW probe stations capable of measuring standard 50Ω .

4.5.2: Realised Structures and Final Parameters

A) Final Layout

The final layout of the proposed filtenna which meets the specifications given above is illustrated in Figure 4.5–1; with the values of its dimension parameters given in Table 4.5–2. The filtenna is symmetrical with respect to its longitudinal direction in the x-axis. It has a total compact size of 33 mm × 47.2 mm.

The proposed filtenna has a coplanar waveguide-based feed network. The transmission feed line has a width, $W1_F$, of 3.3 mm and the width of the gap between the transmission feed line and the ground planes, G_G , is 0.85 mm. These values have been calculated using the commercial electronic design automation software program Keysight Advanced Design System. The characteristic impedance of the filtenna using these values corresponds to the required characteristic impedance of 97 Ω of the system.

The radiating element is directly connected to the transmission feed line and has a long oval shape. Due to the steady change in the radiating element of this shape, a broadband impedance bandwidth is easily achieved. This shape also provides a smooth shift from one resonant mode to another.

For the purpose of rejecting the three interfering signals, the inkjet-printed structure has been integrated with a filter network consisting of three pairs of resonators. One pair of resonators is for producing one notchband.

The notchband at 3.5 GHz is formed by the pair of slit resonators labelled “R1”. The two slit resonators are placed near the outer sides/edges of the radiating element. One end is placed within the radiating element and the other is placed at the edge of the radiating element. The resonators have a width of 0.3 mm. Since the slit resonators short-circuited at one end and open-circuited at the other end, they are quarter-wavelength, $\lambda_g/4$, long; where λ_g is the guided wavelength at 3.5 GHz. The required total length of the pair of slit resonators, L_{R1} , can be calculated using (4.9).

$$L_{R1} = \frac{L1_{R1} + L2_{R1}}{2} \quad (4.9)$$

A pair of rectangular ring resonators is used for producing the notchband at 5.8 GHz. The pair is labelled “R2” in the given geometry of the filtenna. The two 5.8 GHz resonators are positioned wholly within the radiating element and situated on either side of the symmetry plane; each at a distance, $S1_{R2}$, of 2.2 mm from the symmetry plane. The resonators have a width, T_{R2} , of 0.3 mm and a splitting gap,

G_{R2} , of 0.2 mm. The resonators are half-wavelength, $\lambda_g/2$, long; where λ_g is the guided wavelength at 5.8 GHz. The required total length of the pair of 5.8 GHz rectangular ring resonators, L_{R2} , can be calculated using (4.10).

$$L_{R2} = 2L1_{R2} + 2L2_{R2} - 4T_{R2} - G_{R2} \quad (4.10)$$

Another pair of rectangular ring resonators — labelled “R3” — is used for forming the notchband at 8.2 GHz. Unlike the 5.8 GHz pair which is located on either side of the symmetry plane, the 8.2 GHz pair of resonators is centred in the symmetry plane of the filtenna. The resonators have a width, T_{R3} , of 0.3 mm and a splitting gap, G_{R3} , of 0.2 mm. The resonators are half-wavelength, $\lambda_g/2$, long; where λ_g is the guided wavelength at 8.2 GHz. The required total length of the pair of 8.2 GHz rectangular ring resonators, L_{R3} , can be calculated using (4.11).

$$L_{R3} = 2L1_{R3} + 2L2_{R3} - 4T_{R3} - G_{R3} \quad (4.11)$$

The rejection performance of quarter-wavelength resonators becomes worse at higher frequencies. Therefore, half-wavelength resonators are better suited at higher frequencies. Another reason for the combination of using quarter-wavelength resonators and half-wavelength resonators is to show that both designs can work with inkjet-printed filtennas. With regards to choosing the positions of the three pairs of resonators, generally speaking, placing a resonator closer to the transmission feed line will increase the level of rejection. However, it should be noted that the proximity of a resonator to the transmission feed line is judged relative to the operating wavelength of the resonator. This means that resonators operating at lower frequencies can be positioned further from the transmission feed line without compromising their standard of rejection performance.

B) Fabrication of Final Layout

There are various dielectric substrates available which can be used for inkjet-printing. Paper and Kapton are two of the available products. Paper is probably the most used one for inkjet-printed circuits at the research-level. Although paper is cheap and very flexible, it has a low tensile strength of 17 MPa and introduces discontinuities when and where high levels of bending are required. Moreover, it has a relatively high dielectric loss factor of 0.07; which compromises the inkjet-printed circuits' efficiency. On the other hand, Kapton has a very good balance between its electrical and physical properties. Kapton is made of polyimide film. It has a comparatively low loss factor of 0.0021. Furthermore, even at the low thicknesses that it is predominantly manufactured at, i.e. 25–125 μm , it is very robust with a tensile strength of 231 MPa and a dielectric strength of 240 V/m. In addition, Kapton is able to operate within a broad temperature rating of -269°C – 400°C . More and detailed properties of Kapton can be found in Appendix A.3.

In this instance — and for all subsequent inkjet-printed circuits developed in this research work — Kapton has been chosen and used due to its desirable properties. The final layouts of the antenna and filter are designed on a flexible Kapton substrate of a thickness of 50 μm , having a dielectric permittivity of $\epsilon_r = 3.4$ and a dielectric loss factor of $\tan \delta = 0.0021$.

Inkjet-printing makes use of conductive and dielectric inks with various metallic nanoparticles in them. The commercially available various nanoparticles in inkjet inks are gold, silver, tungsten oxide, zinc oxide, copper, etc. While gold nanoparticle ink would have the best properties for inkjet-based circuits, it would also be the most costly. Therefore, the proposed circuits are printed using silver nanoparticle ink. The ink used is NovaCentrix JS-B80HV silver nanoparticle ink. The inkjet printer used is Dimatix Materials Printer DMP-3000. For the whole printed structure to be electrically conductive, the ink droplets from the inkjet printer should sufficiently overlap each other. The overlap of ink droplets is determined by the drop spacing setting in the printer. The drop spacing also determines the thickness of the inkjet-printed layers. For example, a small drop spacing, accompanied with a slow printing speed, would result in a thicker ink metallisation layer being printed since each succeeding droplet would be very near to the preceding one. Moreover, if the drop spacing is less than the size of the ink droplet, then each successive droplet would overlap the previous one. On this occasion, a drop spacing of 25 μm — corresponding to a printing resolution of 1016 dpi — is selected and shows to be optimal in terms of avoiding ink spillage and accumulation. The amplitude of the driving waveform is set to 25 V and the printing frequency is 2 kHz. Printing of the

two circuits is done using ink cartridges having a nozzle volume of 10 pL and arranged in a horizontal configuration. A polymer covering keeps the printed particles confined in a colloidal suspension. Once printed, the structures are sintered in a furnace at a curing temperature of 240°C for 45 minutes for the coarse ink lines to form continuous electrically conductive silver lines, providing a good channel for the flow of current. Although the conductivity of silver nanoparticle ink is less than traditional copper by about 3–4 times, depending on the curing temperature and time, it can be increased up to 2.5×10^7 S/m.

The depth of the top-layer ink metallisation where the skin effect is valid is calculated using (2.60). At the lower limit of the passband frequency and the maximum expected conductivity, the skin depth comes to be about 2.6 μm . Hence, the final thickness of the top-layer at 3 μm is passable — yet still not fully sufficient; unless it would have been at least 5.2 μm .

For reference purposes, the corresponding inkjet-printed antenna — formed by removing the three pairs of resonators from the filtenna — is also designed. The two circuits are modelled and simulated using the commercial full-wave electromagnetic simulation software program CST Microwave Studio. A photograph of the inkjet-printed antenna is shown in Figure 4.5–2 and of the inkjet-printed filtenna in Figure 4.5–3.



Figure 4.5–2: Photograph of the fabricated inkjet-printed antenna.

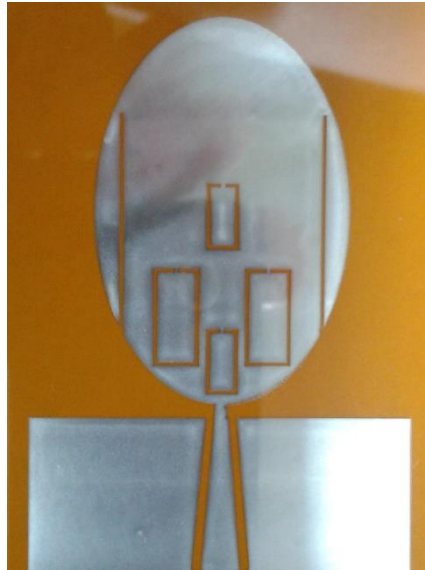


Figure 4.5–3: Photograph of the fabricated inkjet-printed filtenna.

4.5.3: Results

A) Return Loss of Antenna and Filtenna

The fabricated inkjet-printed structures were measured using a high frequency measurement system. The system comprised Cascade Microtech PM5 RF and Microtech coplanar APC50-GSG-250 probe stations and Agilent N5230A PNA-L and Agilent E8361A PNA network analysers. The measuring system was calibrated on a compatible impedance characterisation substrate using the standard Short-Open-Load calibration method. A photograph of one of the probe stations while having one of the inkjet-printed structures under test is shown in Figure 4.5–4.

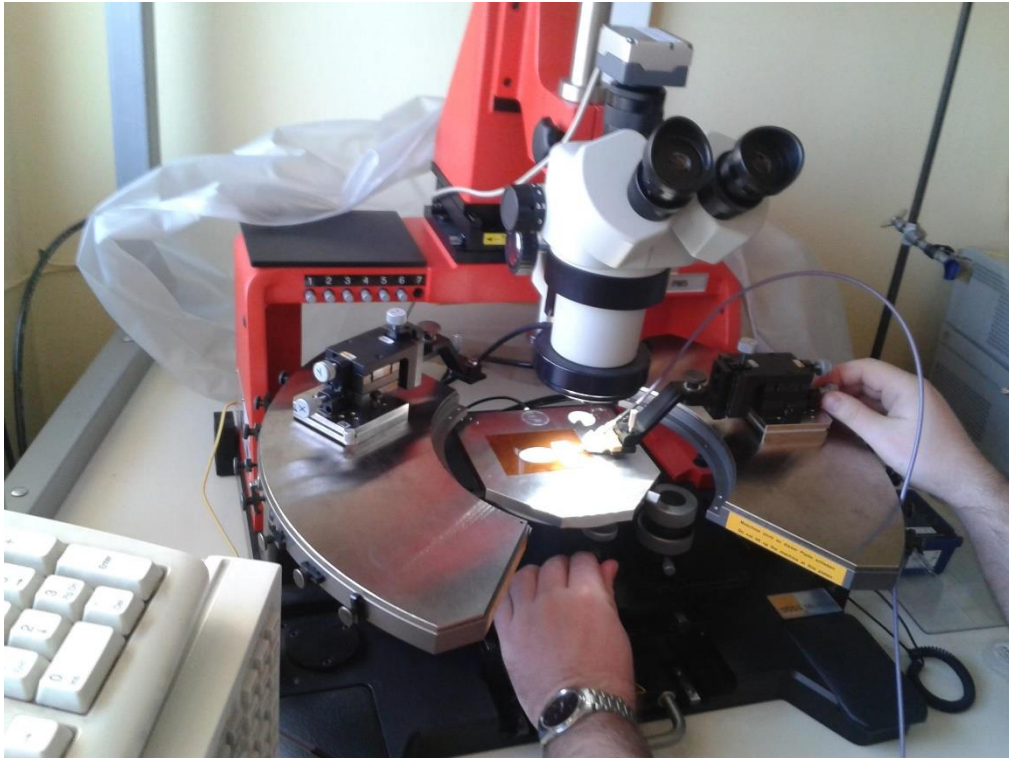


Figure 4.5–4: Photograph of a probe station having the filtenna under test.

The ensuing simulated and measured return loss of the inkjet-printed antenna is shown in Figure 4.5–5. The return loss obtained from the simulation shows that a full bandpass response at a return loss of more than 10 dB is obtained across the frequency range of 1.52 GHz to 10.61 GHz. The return loss acquired from the measurement shows the passband to be present from about 1.35 GHz to 10.5 GHz. Overall, there is a good match between the simulated and the measured results. Furthermore, since no filtering resonators are integrated with or within the radiating element, there are no notchband present in the results.

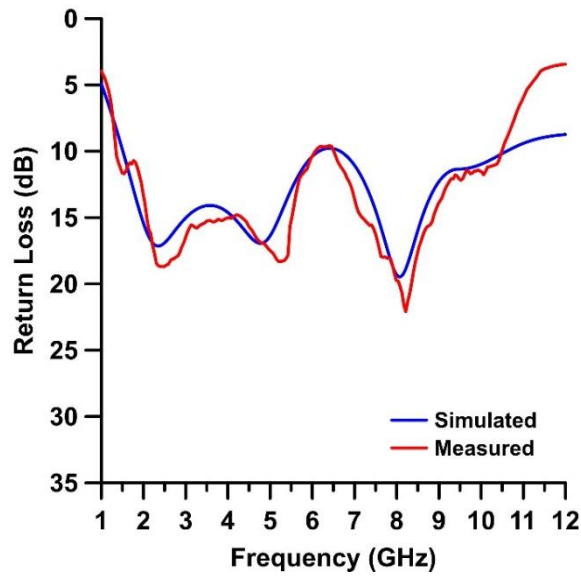


Figure 4.5-5: Return loss of the antenna.

The simulated return loss during the various four design steps/stages of the ink-jet-printed antenna leading to the final inkjet-printed filtenna is shown in Figure 4.5-6. The four stages are made of an antenna without any resonators (step 1), a filtenna with only the 3.5 GHz R1 pair of resonators (step 2), a filtenna with only the 5.8 GHz R2 pair of resonators (step 3) and a filtenna with only the 8.2 GHz R3 pair of resonators (step 4).

As can be seen from the four results, the passband at the four stages is relatively the same. The only difference is at the triple notchband frequencies; where each design step with a pair of resonators produces its respective notchband.

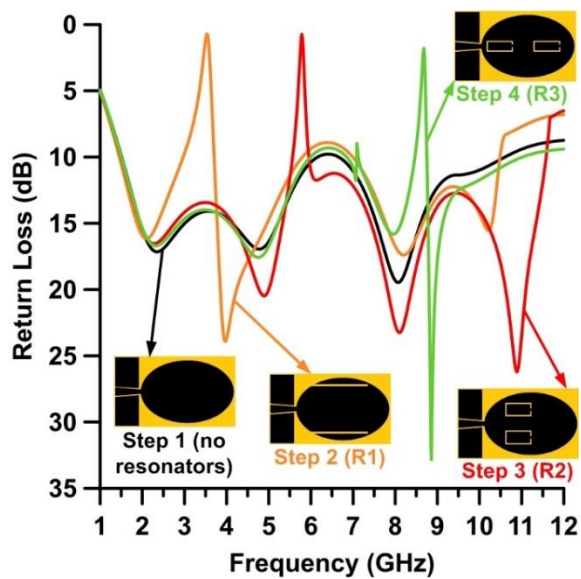


Figure 4.5-6: Return loss at the various design steps/stages of the filtenna.

The resulting simulated and measured return loss of the inkjet-printed filtenna is given in Figure 4.5–7. The result from the simulation shows that a full bandpass response at a return loss of more than 10 dB is obtained across the frequency range of 1.45 GHz to 10.32 GHz. Within this passband, three notchband are observed at 3.5 GHz, 5.78 GHz and 7.95 GHz with return losses of 0.82 dB, 0.87 dB and 2.11 dB respectively. The result from the measurement reasonably agrees with the simulation and show the passband to be present from about 1.6 GHz to 10.85 GHz. The triple notchband within the passband are present at the frequencies of 3.55 GHz, 5.65 GHz and 8.16 GHz. The return losses at these three notchband frequencies are 1.8 dB, 1.5 dB and 2.3 dB respectively. The slight shift in the frequencies of the obtained triple notchband from the desired values is due to the fabrication discrepancies and tolerances and the lower return loss is due to the low conductivity of the silver nanoparticle ink. The filtenna seems to be sensitive at the higher frequencies as seen from the increased variation between the simulated and the measured results after 9 GHz.

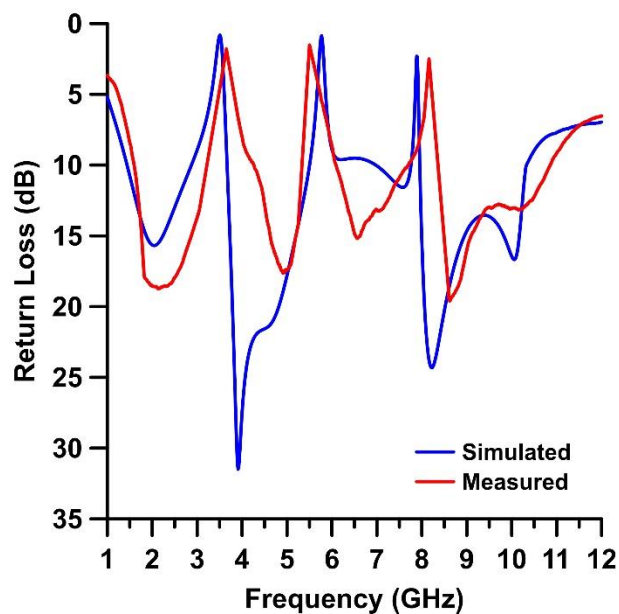


Figure 4.5–7: Return loss of the filtenna.

B) Parametric Study of Positions of R1 and R2 Resonators

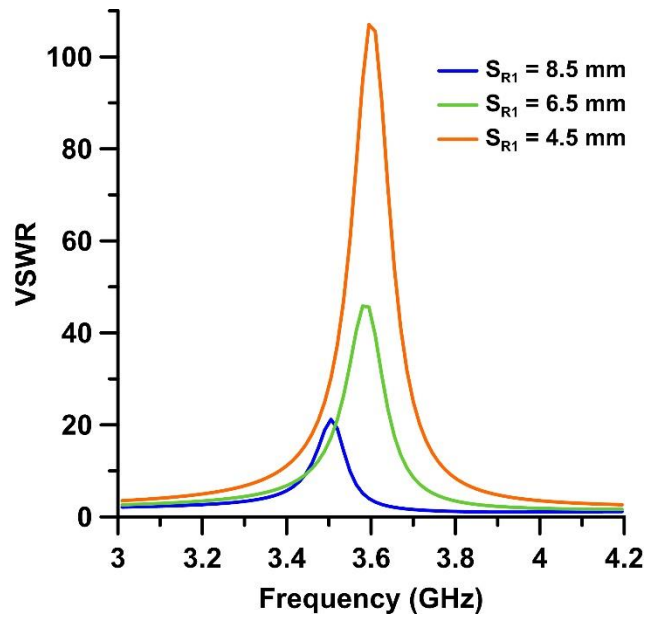
Parametric studies were carried out in order to check the rejection performance when the positions of the R1 pair (3.5 GHz) and the R2 pair (5.8 GHz) of resonators was altered in the y-axis.

With regards to both pairs of resonators, it is expected that as they are moved closer to the transmission feed line, the return loss rejection will increase, i.e. an

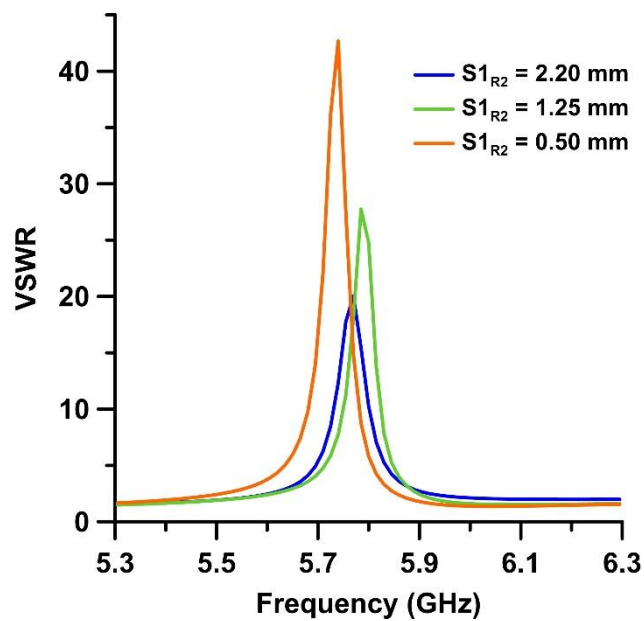
increase in the VSWR as well. With the purpose of verifying this, the filtenna was simulated with the position of the R1 resonators altered by using various values for the width, S_{R1} , and the position of the R2 resonators altered by using various values for the width, S_{R2} , of their respective gaps from the middle of the radiating element. The results of these simulations are given in Figure 4.5–8 (a) and Figure 4.5–8 (b) respectively. (For clarity purposes, rather than the return loss, the VSWR in a limited frequency range is plotted for the results.)

Each R1 resonator was first moved 2 mm, in the y-axis, closer to the middle of the radiating element/symmetry plane of the filtenna — decreasing the width, S_{R1} , of the gap to 6.5 mm — and then moved again a further of 2 mm — decreasing the width, S_{R1} , of the gap to 4.5 mm. From the results, it can be seen that as the R1 pair of resonators move closer to the transmission feed line, the VSWR increases accordingly. In the final/original design, i.e. when $S_{R1} = 8.5$ mm, the VSWR at the notchband frequency is 21.2 ($S_{11} = 0.82$ dB). At $S_{R1} = 6.5$ mm, the VSWR at the notchband frequency increases to 45.84 ($S_{11} = 0.38$ dB). Finally, at $S_{R1} = 4.5$ mm, the VSWR at the notchband frequency rises further to become 107.03 ($S_{11} = 0.16$ dB). However, the repositioning of the R1 pair of resonators in the y-axis does not significantly affect the notchband frequency. In the presented results, the frequency shift is minor; averaging at 80 MHz (2.27 %).

The R2 pair of resonators were repositioned in a similar manner. Each R2 resonator was first moved 0.95 mm, in the y-axis, closer to the middle of the radiating element/symmetry plane of the filtenna — decreasing the width, S_{R2} , of the gap to 1.25 mm — and then moved again a further of 0.75 mm — decreasing the width, S_{R2} , of the gap to 0.5 mm. From the results, it can be seen that as the R2 pair of resonators move closer to the transmission feed line, the VSWR increases accordingly. In the final/original design, i.e. when $S_{R2} = 2.2$ mm, the VSWR at the notchband frequency is 20.04 ($S_{11} = 0.87$ dB). At $S_{R2} = 1.25$ mm, the VSWR at the notchband frequency increases to 27.75 ($S_{11} = 0.63$ dB). Finally, at $S_{R2} = 0.5$ mm, the VSWR at the notchband frequency rises further to become 42.67 ($S_{11} = 0.41$ dB). However, same as the R1 pair of resonators, the repositioning of the R2 pair of resonators in the y-axis does not significantly affect the notchband frequency. In the presented results, the frequency shift is minor.



(a)



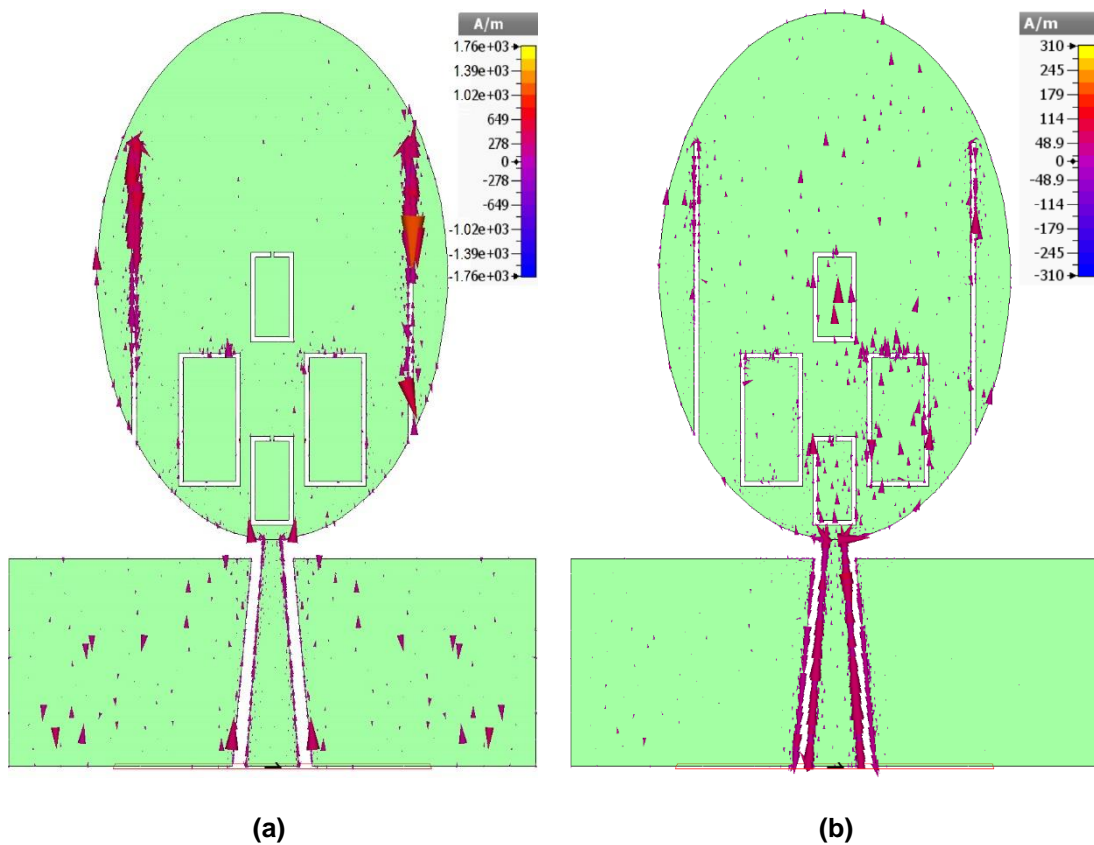
(b)

Figure 4.5–8: Parametric study of the effects on the VSWR of the filtenna by varying the position of (a) the 3.5 GHz R1 resonators and (b) the 5.8 GHz R2 resonators.

C) Distribution of Surface Currents in Filtenna

In order to further explain the effects of the three pairs of resonators and how the notchband are achieved, the distributions of the surface currents at the three notchband frequencies and a passband frequency were simulated. The four results are given in Figure 4.5–9.

At the three notchband frequencies, shown in Figure 4.5–9 (a), (c) and (d), stronger distributions of surface currents are concentrated within the three pairs of resonators. If observed closely, it can be seen that the direction of the flow of currents along the inner edges and the outer edges of the resonators is opposite to each other. Because of the opposite directions, the currents are cancelled by each other. Consequently, the filtenna does not radiate and notchband are obtained. Meanwhile, at the passband frequency of 4 GHz, shown in Figure 4.5–9 (b), the distribution of the surface current is almost uniform throughout the filtenna. (Although, a little concentration of the surface currents is seen within the R1 resonators as well. This is because the passband frequency of 4 GHz is quite near the notchband frequency of 3.5 GHz.)



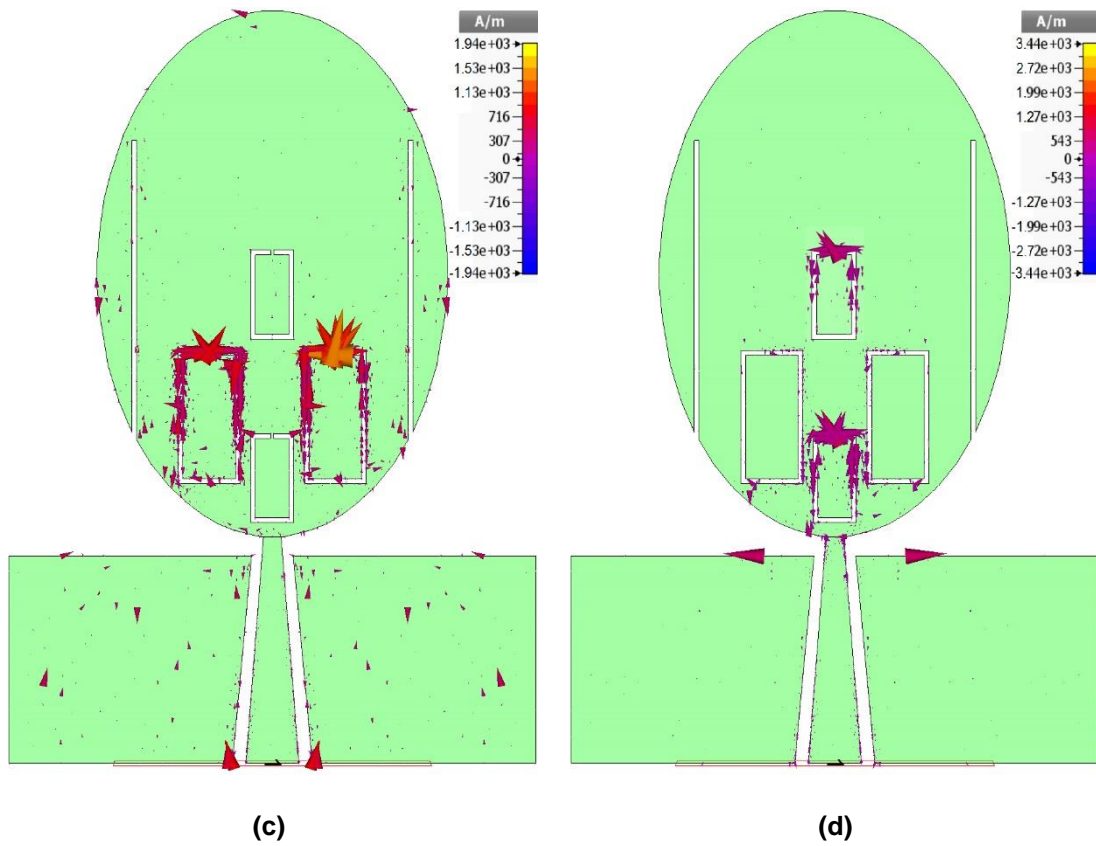


Figure 4.5–9: Distribution of the surface currents in the filtenna at (a) 3.55 GHz, (b) 4 GHz, (c) 5.65 GHz and (d) 8.16 GHz.

D) Radiation Patterns of Filtenna

For the purpose of measuring its radiation patterns, the filtenna was put in an anechoic chamber. The source/transmitting antenna is a horn antenna. Photographs of the horn antenna and the filtenna under test are shown in Figure 4.5–10.

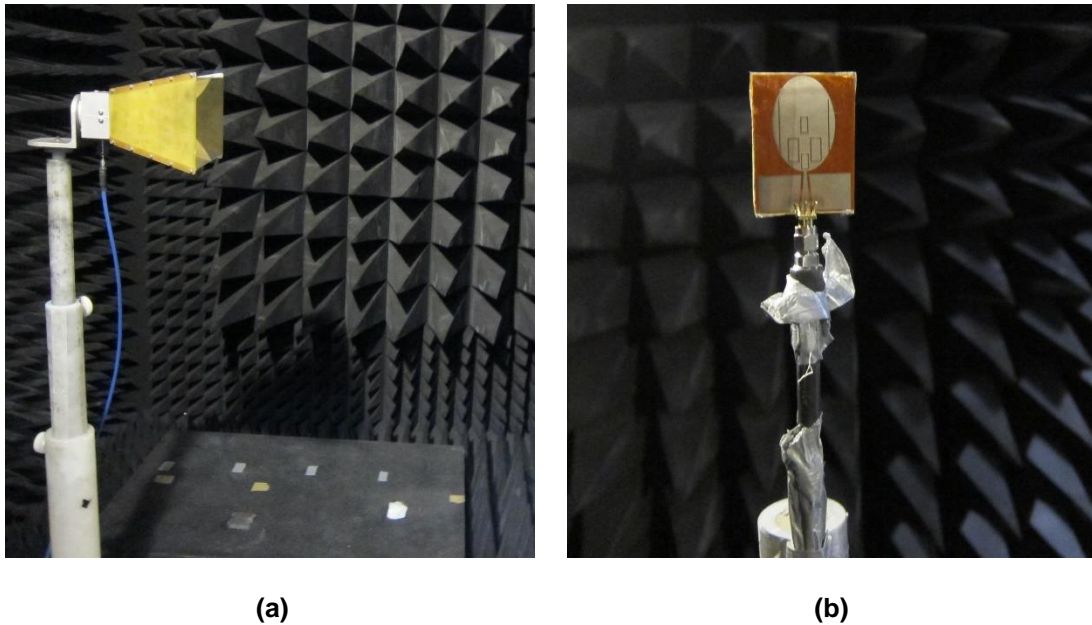


Figure 4.5–10: Photograph of the inside of an anechoic chamber showing (a) the horn antenna and (b) the filtenna under test.

The simulated and measured radiation patterns of the filtenna at two passband frequencies and one notchband frequency in the E-plane and the H-plane are presented in Figure 4.5–11. The radiation patterns have been calibrated to the gain of the filtenna and the simulated and measured results have been attuned to obtain the best possible match with each other. At the passband frequencies of 3.1 GHz and 4 GHz, given in Figure 4.5–11 (a) and Figure 4.5–11 (b) respectively, the filtenna displays stable bidirectional patterns in the E-plane and omnidirectional patterns in the H-plane. However, at the notchband frequency of 5.78 GHz, given in Figure 4.5–11 (c), the filtenna exhibits a deteriorated bidirectional pattern in the E-plane and a deteriorated omnidirectional pattern in the H-plane. This is to be as expected because of notchband suppression. The simulated results and the measured results match each other reasonably well.

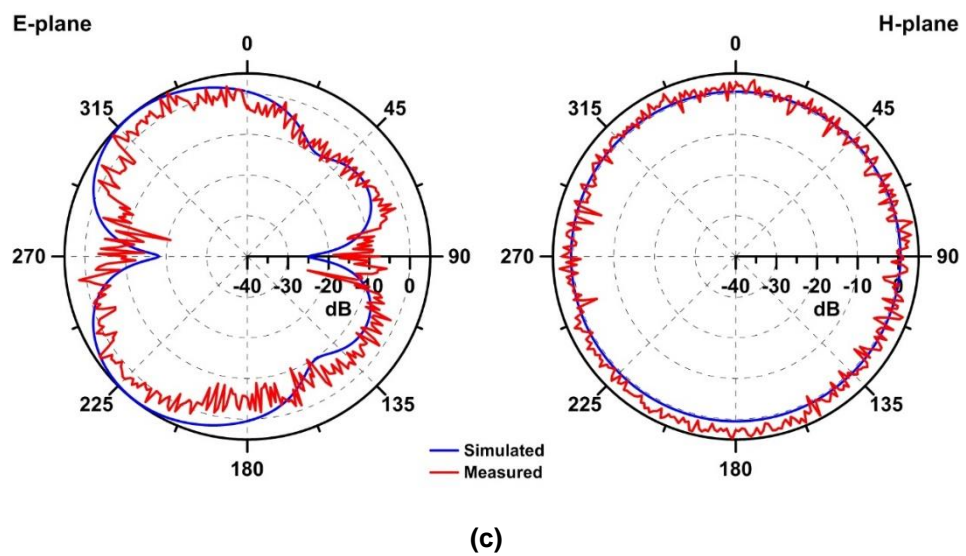
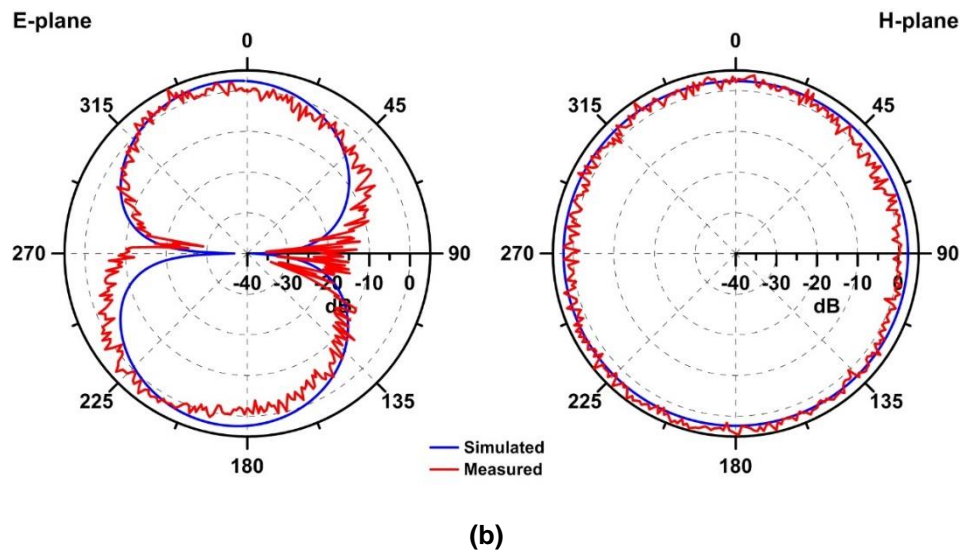
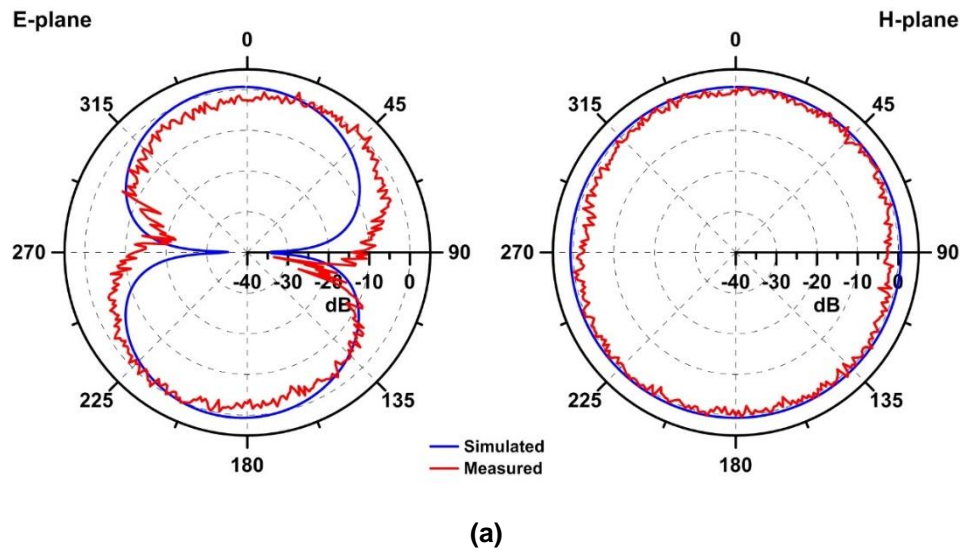


Figure 4.5–11: Radiation patterns of the filtenna at (a) 3.1 GHz, (b) 4 GHz and (c) 5.78 GHz.

E) Gain of Antenna and Filtenna

The simulated gain of the antenna and the simulated and measured gain of the filtenna were obtained. The results are presented in Figure 4.5–12.

Within the passband of 1.5 GHz to 10.85 GHz, the simulated average gain is 3.36 dBi and the variance of the gain across the operational range is within 5 dBi. The gain of the antenna and the filtenna echo each other across the broad frequency range except at the triple notchband frequencies. The gain of the antenna at the three notchband frequencies is 1.78 dBi, 3.61 dBi and 5.51 dBi. In the filtenna, these gains are significantly decreased to -3 dBi, -2 dBi and 2 dBi because of notchband suppression. The measured gain of the filtenna is a reasonable match with the simulated gain. Furthermore, similar to the simulated gain, the measured gain at the notchband frequencies is also reduced; becoming -2.25 dBi, -1.3 dBi and 2.6 dBi. The falls in the gain signify the rejection capability of the filtenna.

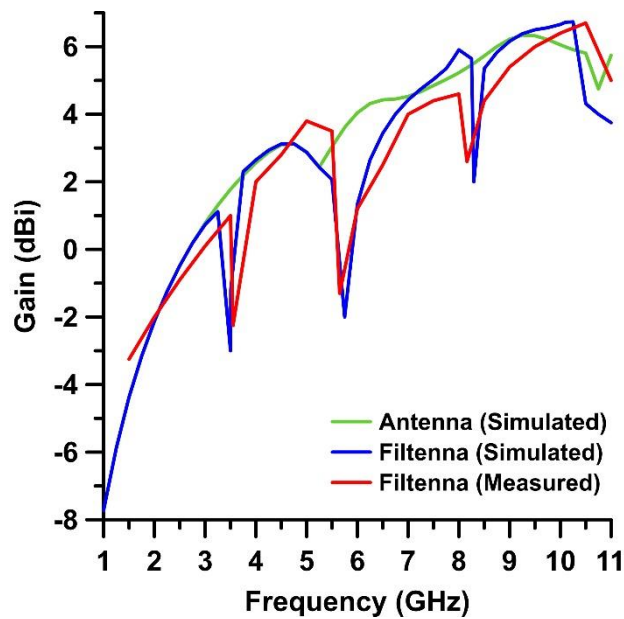


Figure 4.5–12: Gain of the antenna and the filtenna.

F) Efficiency of Antenna and Filtenna

The simulated efficiency of the antenna and the filtenna were obtained. The results are given in Figure 4.5–13.

Across the passband of 1.5 GHz to 10.85 GHz, the average efficiency is 89.8 %. Similar to the results of the gain, the efficiency of the antenna and the filtenna also echo each other except at the triple notchband frequencies. The efficiency of the filtenna drops to an average of about 21.3 % across the triple notchband. The

considerable reduction in the efficiency at the triple notchband indicates the rejection capability of the inkjet-printed filtenna.

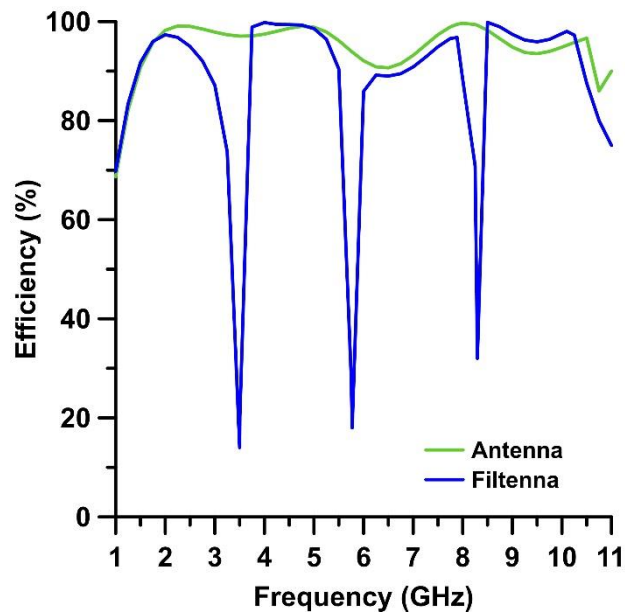


Figure 4.5–13: Efficiency of the antenna and the filtenna.

G) Flexibility Performance of Filtenna

Since the inkjet-printed filtenna is intended for flexible devices, the return loss needs to be checked in order to determine whether the passband and the triple notchband characteristics are retained at different levels of flexibility.

For these reasons, the filtenna was rolled on three foam cylinders; with each having a dielectric permittivity of $\epsilon_r = 1$ but a different radius. The three cylinders had a radius of 42.2 mm, 25 mm and 15 mm. The ensuing return loss of the filtenna for each radius was measured. The results are given in Figure 4.5–14.

From the presented results, it can be seen that there are differences between the flat and the bent cases, and within the bent cases themselves too. These differences are most evident at the higher frequencies, especially after 9 GHz. However, these differences are insignificant since, in all cases, the broad passband, alongside the triple notchband, is retained. For the bent/curved cases, the average shift in the triple notchband frequencies is ± 33.33 MHz and the average change in return loss is -0.13 dB. Furthermore, it was observed that the return loss of the filtenna between the flat case and the bent/curved cases was far closer to each other if the diameter of the curvature was larger than the filtenna's length, L_T , of 47.2 mm. Therefore, it can be said that the performance of the inkjet-printed filtenna remains reasonably acceptable at different levels of flexibility.

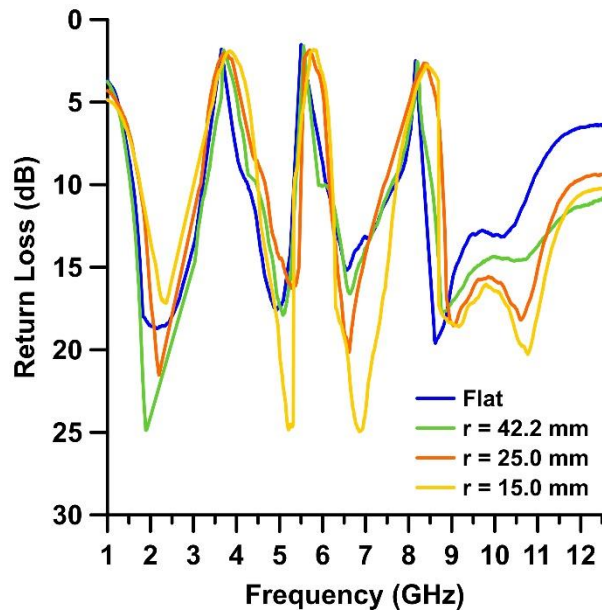


Figure 4.5–14: Measured return loss of the filtenna when bent/curved at various radii.

4.5.4: Summary of Presented Results

The results of the antenna and the filtenna are summarised in Table 4.5–3.

Table 4.5–3: Summary of the results of the antenna and the filtenna.

Structure	Response Type	Passband (GHz)	FBW (%)	Triple Notchband			
				Frequency (GHz)	Rejection (dB)	Gain (dBi)	Efficiency (%)
Antenna	Simulated	1.52–10.61	226	n/a	n/a	1.78 & 3.61 & 5.51	97 & 93 & 99
	Measured	1.35–10.50	243	n/a	n/a	n/p	n/p
Filtenna	Simulated	1.45–10.32	229	3.5 & 5.78 & 7.95	0.82 & 0.87 & 2.11	-3 & -2 & 2	14 & 17 & 32
	Measured	1.60–10.85	222	3.55 & 5.65 & 8.16	1.8 & 1.5 & 2.3	-2.25 & -1.3 & 2.6	n/p

4.6: References

- [4-1] D. Abed and H. Kimouche, "Design and characterization of microstrip UWB antennas," in *UltraWideband*. InTech, 2010, ch. 15, pp. 347–370.
- [4-2] W. Dou, Z. Shen, X. Li, and S. Xiao, "Broadband antennas and antenna arrays," *International Journal of Antennas and Propagation*, June 2014.
- [4-3] J. R. Kelly, P. S. Hall, and P. Gardner, "Band-notch UWB antenna incorporating a microstrip open-loop resonator," *IEEE Transactions on Antennas and Propagation*, vol. 59, no. 8, pp. 3045–3048, August 2011.
- [4-4] Y. Sung, "Triple band-notched UWB planar monopole antenna using a modified H-shaped resonator," *IEEE Transactions on Antennas and Propagation*, vol. 61, no. 2, pp. 278–280, February 2013.
- [4-5] I-J. Yoon, H. Kim, H. Yoon, Y. Yoon, and Y-H. Kim, "Ultra-wideband tapered slot antenna with band cutoff characteristic," *IET Electronics Letters*, vol. 41, no. 11, pp. 4–5, May 2005.
- [4-6] F. Zhu, S. Gao, A. Ho, R. Alhameed, C. See, T. Brown, J. Li, G. Wei, and J. Xu, "Multiple band-notched UWB antenna with band-rejected elements integrated in feed line," *IEEE Transactions on Antennas and Propagation*, vol. 61, no. 8, pp. 3952–3960, August 2013.
- [4-7] C. Lin, P. Jin, and R. Ziolkowski, "Single, dual and tri-band-notched UWB antennas using CLL resonators," *IEEE Transactions on Antennas and Propagation*, vol. 60, no. 1, pp. 102–109, January 2012.
- [4-8] W. Lui, C. Cheng, and H. Zhu, "Compact frequency notched UWB fractal printed slot antenna," *IEEE Microwave and Wireless Components Letters*, vol. 16, no. 4, pp. 224–226, April 2006.
- [4-9] J. Y. Siddiqui, C. Saha, and Y. Antar, "Compact SRR loaded UWB circular monopole antenna with frequency notch characteristics," *IEEE Transactions on Antennas and Propagation*, vol. 62, no. 8, pp. 4015–4020, August 2014.
- [4-10] B. S. Cook and A. Shamim, "Inkjet printing of novel wideband and high gain antennas on low-cost paper substrate," *IEEE Transactions on Antennas and Propagation*, vol. 60, no. 9, pp. 4148–4156, September 2012.

- [4-11] A. R. Maza, B. Cook, G. Jabbour, and A. Shamim, "Paper-based inkjet-printed ultra-wideband fractal antennas," *IET Microwaves, Antennas & Propagation*, vol. 6, no. 12, p. 1366–1373, April 2012.
- [4-12] G. Shaker, S. Safavi-Naeini, N. Sangary, and M. M. Tentzeris, "Inkjet printing of ultrawideband antennas on paper-based substrates," *IEEE Antennas and Wireless Propagation Letters*, vol. 10, pp. 111–114, 2011.
- [4-13] H. R. Khaleel, "Design and fabrication of compact inkjet printed antennas for integration within flexible and wearable electronics," *IEEE Transactions on Components, Packaging and Manufacturing Technology*, vol. 4, no. 10, pp. 1722–1728, October 2014.
- [4-14] D. Unnikrishnan, D. Kaddour, S. Tedjini, E. Bihar, and M. Saadaoui, "CPW-fed inkjet printed UWB antenna on ABS-PC for integration in molded interconnect devices technology," *IEEE Antennas and Wireless Propagation Letters*, vol. 14, pp. 1125–1128, 2015.
- [4-15] H. R. Khaleel, H. M. Al-Rizzo, D. G. Rucker, and S. Mohan, "A compact polyimide-based UWB antenna for flexible electronics," *IEEE Antennas and Wireless Propagation Letters*, vol. 11, pp. 564–567, 2012.
- [4-16] N. C. Azenui and H. Y. D. Yang, "A printed crescent patch antenna for ultrawideband applications," *IEEE Antennas and Wireless Propagation Letters*, vol. 6, pp. 113–116, 2007.
- [4-17] O. Haraz and A-R Sebak, "UWB antennas for wireless applications," in *Advancement in Microstrip Antennas with Recent Applications*. InTech, 2013, ch. 6, pp. 125–152.
- [4-18] C. A. Balanis, *Antenna Theory: Analysis and Design*. Hoboken, New Jersey, United States of America: John Wiley & Sons, Inc., 2005.
- [4-19] K. Chang, I. Bahl, and V. Nair, *RF and Microwave Circuit and Component Design for Wireless Systems*. New York, United States of America: John Wiley & Sons, 2002.
- [4-20] J-S. Hong and M. J. Lancaster, *Microstrip Filters for RF/microwave Applications*. New York, United States of America: John Wiley & Sons, 2001.

Chapter 5:

Development of Broadband MIMO-Element Planar Monopole Filtennas

5.1: Introduction

MIMO technology is the use of multiple antenna elements at both the transmitter-ends and the receiver-ends in the wireless transceivers of wireless communication systems. MIMO technology is used to significantly enhance the data throughput, data transmission performance and channel capacity without additional bandwidth or increasing transmit power [5-1]–[5-4]. Furthermore, MIMO technology can be used to provide diversity gain and multiplexing gain — which improve the link quality and the capacity respectively of wireless communication systems [5-5]–[5-6].

MIMO technology is already being implemented with narrowband systems. However, in recent times, MIMO technology has been adapted for use in various wireless communication systems which it was not originally intended for. These include broadband systems; such as UWB communication systems [5-7].

The combination of MIMO technology and UWB communication systems can further increase the channel capacity as compared to conventional MIMO systems for narrowband applications [5-8]. Additionally, the combination can also be employed to increase the range, raising link reliability and improving the interference cancellation [5-8]–[5-11]. To combat the multipath fading issue in UWB communication systems, UWB diversity antenna systems with MIMO technology are promising candidates [5-5] and [5-8].

Such applications require compact wideband MIMO antennas because of the space and size limitations in wireless transceivers. MIMO antennas should be of the printed type because they are best able to integrate with the small wireless devices manufactured nowadays. Furthermore, there should be a high isolation, i.e. low mutual coupling, amongst the individual antenna elements with low envelope correlation coefficients. Moreover, the interference bands within the UWB should be rejected.

Various MIMO filter antennas and MIMO antennas for UWB systems have been proposed [5-12]–[5-27]. Some configurations are aimed at reducing coupling. A common approach is to depolarize antennas, while not making them fully orthogonal to each other [5-17]–[5-19]. On the other hand, such antennas are not able to attain a high isolation due to the volume constraints and the lack of orthogonality. Another methodology is to introduce ground-plane slots or parasitic elements [5-20]–[5-23]. Although these designs provide significant improvements in isolation in very small volumes, they are fundamentally narrowband. Another method used in [5-24] offers

wideband isolation by completely shadowing the closely-spaced antenna elements from each other. However, this requires a high-profile separator between the antenna elements to achieve the high isolation. In [5-25]–[5-26], antenna elements of different types were combined to achieve pattern diversity. The antenna elements had distinct radiation patterns and polarizations, and so were able to receive signals with low correlation. The antenna presented in [5-27] is difficult to integrate in modern wireless transceivers of mobile devices because of its large size. Moreover, the antenna does not reject the interfering WLAN band. Thus, it can be said that these works do not satisfy all the main challenges in MIMO filter antenna design; such as placing multiple elements closely while maintaining a high isolation, wide operation band and rejection of interfering bands.

Therefore, despite the broad published work on broadband MIMO-element planar monopole filter antennas and antennas for wireless transceivers, there is still a scope of some further research and development. In addition, some essential points which necessitate to be addressed, especially in light of the limitations in the published literature, are as follows:

- Development of broadband MIMO-element planar monopole filter antennas by the integration of filter structures with broadband MIMO-element planar monopole antennas.
- Complete rejection of any interfering frequency bands present within the passband of the monopole antennas.
- Development of broadband MIMO-element planar monopole filter antennas which are able to provide a high isolation.
- Development of broadband MIMO-element planar monopole filter antennas which have a high diversity performance.

The purpose of the overall chapter is to integrate filters with or within MIMO-element planar monopole antennas to form broadband MIMO-element planar monopole filter antennas which address the points listed above. Therefore, in this chapter, the fourth, and last, PCB filter antenna for wireless transceivers of UWB applications has been developed.

The filter antenna, presented in section 5.2, combines MIMO technology for UWB applications. The MIMO filter antenna is formed of four individual antenna elements; with each operating in the UWB. Each element of the MIMO antenna is then integrated with three ring resonators, which have a bandstop effect, to form a MIMO filter antenna. Thus, the MIMO filter antenna is able to produce a dual notchband which filters out the two interfering IEEE 802.16 WiMAX 3.5 GHz and IEEE 802.11 WLAN 5.8 GHz

frequency bands. At the same time, each element of the MIMO filtenna is able to achieve an UWB bandwidth. Furthermore, the developed filtenna is able to provide a high isolation amongst its multiple antenna elements and a high diversity performance. The MIMO filtenna, alongside the reference MIMO antenna, has been fabricated using conventional PCB technology on a rigid substrate with copper as the metallisation.

5.2: Design of a Compact MIMO Filtenna with Dual Notchband, High Isolation and High Diversity for UWB Applications

5.2.1: Specifications

This section presents a broadband planar monopole filtenna based on the specifications given in Table 5.2–1. The specifications require a MIMO four-element monopole filtenna operating at the full UWB range of 3.1–10.6 GHz. The four elements of the MIMO filtenna should be arranged in a 4 × 4 configuration. The filtenna is required to have a microstrip-based feeding method; where the characteristic impedance of the feed network and the system should be 50 Ω. The specifications further ask that the filtenna should be fabricated via PCB technology. Furthermore, the filtenna should have a dual notchband for the rejection of two interfering bands within the UWB range: the IEEE 802.16 WiMAX band operating at 3.5 GHz and the IEEE 802.11 WLAN band operating at 5.8 GHz.

Table 5.2–1: Required specifications of the filtenna.

Parameter	Description of Parameter	Value
Filtenna	Type of filtenna	MIMO Monopole
Configuration	Arrangement of MIMO elements	4 × 4
Technology	Fabrication technology	PCB
Feed	Feeding method	Microstrip
Z_0	Characteristic impedance of system	50 Ω
f_L	Lower passband frequency	3.1 GHz
f_H	Upper passband frequency	10.6 GHz
f_C	Centre frequency	5.73 GHz
FBW	Fractional bandwidth	≥ 130.84 %
Isolation	Isolation between elements	> 20 dB
n_{NB}	Number of notchband	Dual
f_{NB1} and f_{NB2}	Notchband frequencies	3.5 and 5.8 GHz

5.2.2: Realised Structures and Final Parameters

A) Final Layouts

Apart from being a 4×4 MIMO filtenna, the required specifications of the filtenna are the same as the given in section 4.4. Hence, the same design can be used. The final layout of the proposed antenna which meets all but the notchband specifications is illustrated in Figure 5.2–1, with the values of its dimension parameters given in Table 5.2–2, and the final layout of the proposed filtenna which meets all the required specifications is illustrated in Figure 5.2–2, with the values of its dimension parameters given in Table 5.2–3. As can be seen, the MIMO structures have been formed by laying four individuals radiating elements adjacent to each other; with each successive element rotated 90° clockwise to the left of the adjacent one. Such a layout results in a square 4×4 configuration as exemplified in the two geometries. Each radiating element is symmetrical with respect to its longitudinal direction.

The proposed MIMO filtenna utilises a defected ground structure with a partial ground plane for each element. The length, L_G , of each partial ground plane is 13.1 mm. The filtenna has a microstrip-based feed network. The transmission feed line of each element has a width, W_F , of 2.4 mm. The width corresponds to the required characteristic impedance of 50Ω of the system.

The required dual notchband to reject the two interfering bands are inserted in the passbands of the MIMO filtenna by an integrated filter network for each of the four elements. The filter network is the same as the one used in section 4.4 and consists of three ring resonators: one circular ring resonator and two rectangular ring resonators.

The circular ring resonator, which produces a notchband at 3.5 GHz, is placed within each radiating element of the MIMO filtenna. The two rectangular ring resonators, which produce a notchband at 5.8 GHz, are placed next to the transmission feed line of each of the four elements. Both the circular ring resonator and the rectangular ring resonators are half-wavelength, $\lambda_g/2$, long; where λ_g is the guided wavelength at their respective notchband frequencies. The perimeters of the circular ring resonator and the rectangular ring resonators can be calculated using (4.7) and (4.8) respectively.

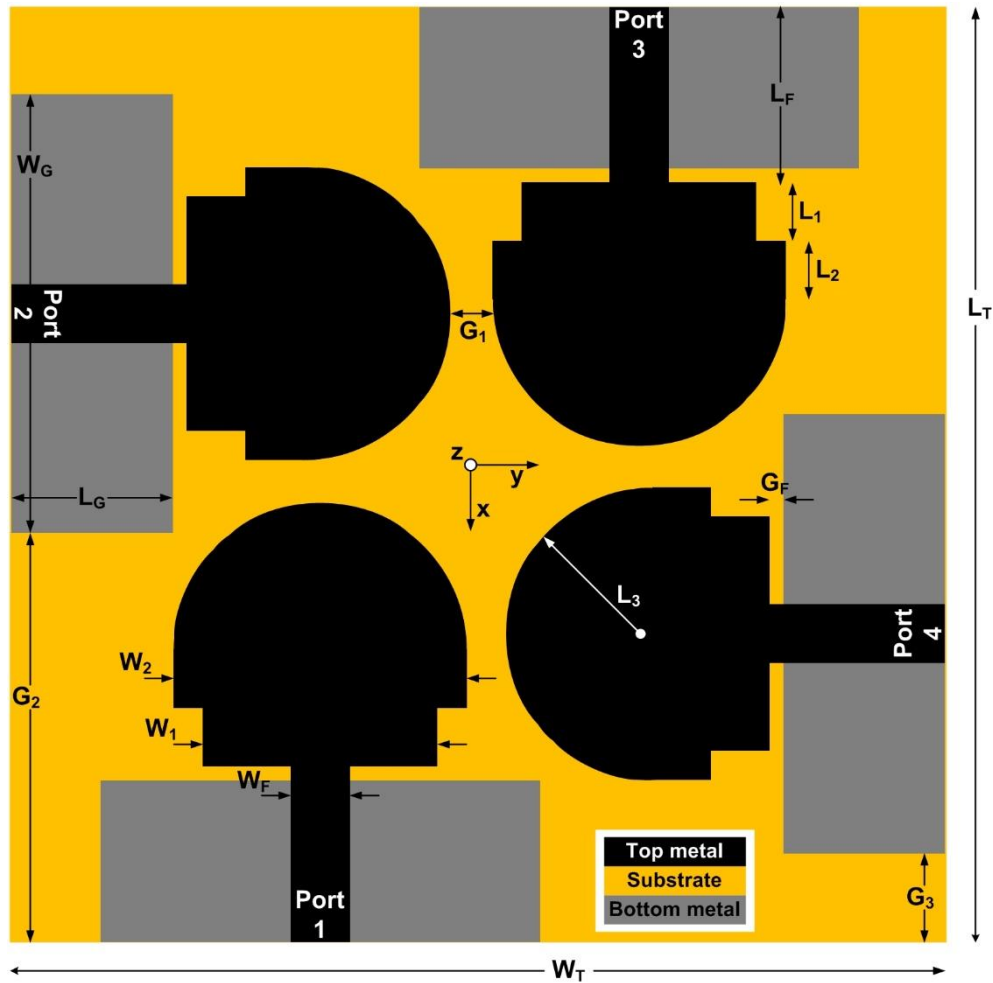


Figure 5.2-1: Geometry of the antenna.

Table 5.2-2: Values of the dimension parameters of the antenna.

Parameter	Value (mm)	Parameter	Value (mm)
W_T	77.2	L_1	4.3
L_T	77.2	W_2	23.8
W_G	32	L_2	6.4
L_G	13.1	L_3	11.9
W_F	2.4	G_1	3.2
L_F	13.6	G_2	35.1
G_F	0.5	G_3	10.1
W_1	15		

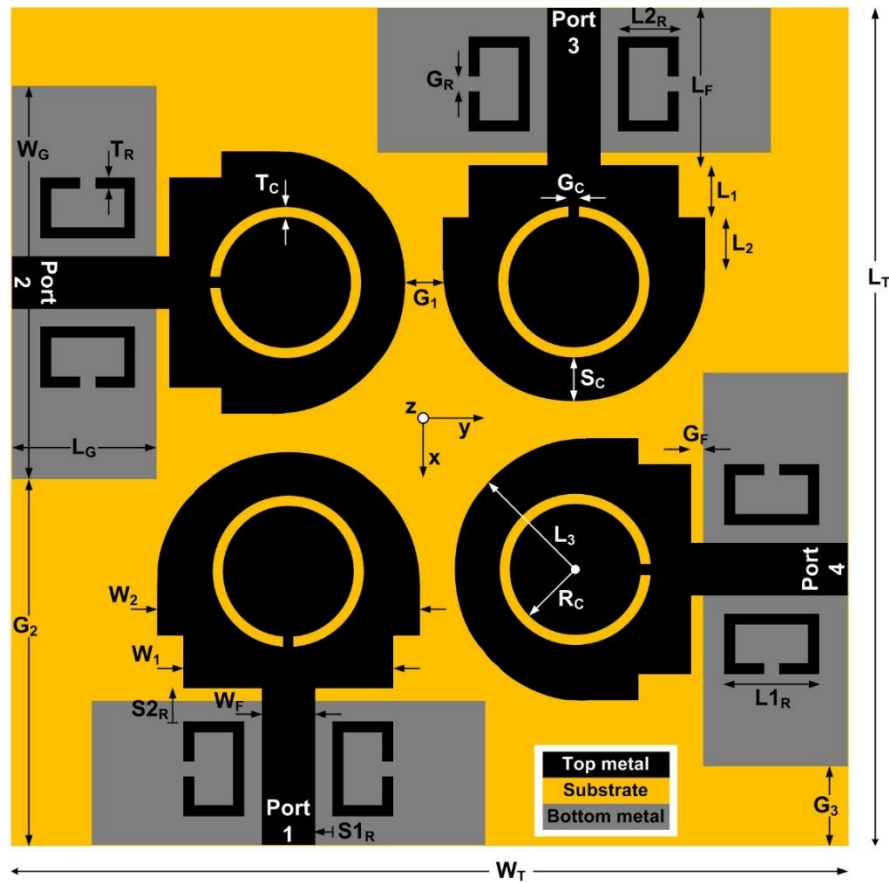


Figure 5.2-2: Geometry of the filtenna.

Table 5.2-3: Values of the dimension parameters of the filtenna.

Parameter	Value (mm)	Parameter	Value (mm)
W_T	77.2	L_{2R}	4.5
L_T	77.2	T_R	0.5
W_G	32	G_R	0.5
L_G	13.1	S_{1R}	1
W_F	2.4	S_{2R}	1.1
L_F	13.6	R_C	5.35
G_F	0.5	T_C	0.5
W_1	15	G_C	0.8
L_1	4.3	S_C	6.26
W_2	23.8	G_1	3.2
L_2	6.4	G_2	35.1
L_3	11.9	G_3	10.1
L_{1R}	6.5		

B) Fabrication of Final Layouts

The final layouts of the antenna and the filtenna are designed on a Rogers RT5880 substrate of a thickness of 0.795 mm, having a dielectric permittivity of $\epsilon_r = 2.2$ and a dielectric loss factor of $\tan \delta = 0.0009$. They are modelled and simulated using the commercial full-wave electromagnetic simulation software program Sonnet. Photographs of both sides of the fabricated PCB antenna and the PCB filtenna are shown in Figure 5.2–3 and Figure 5.2–4 respectively.

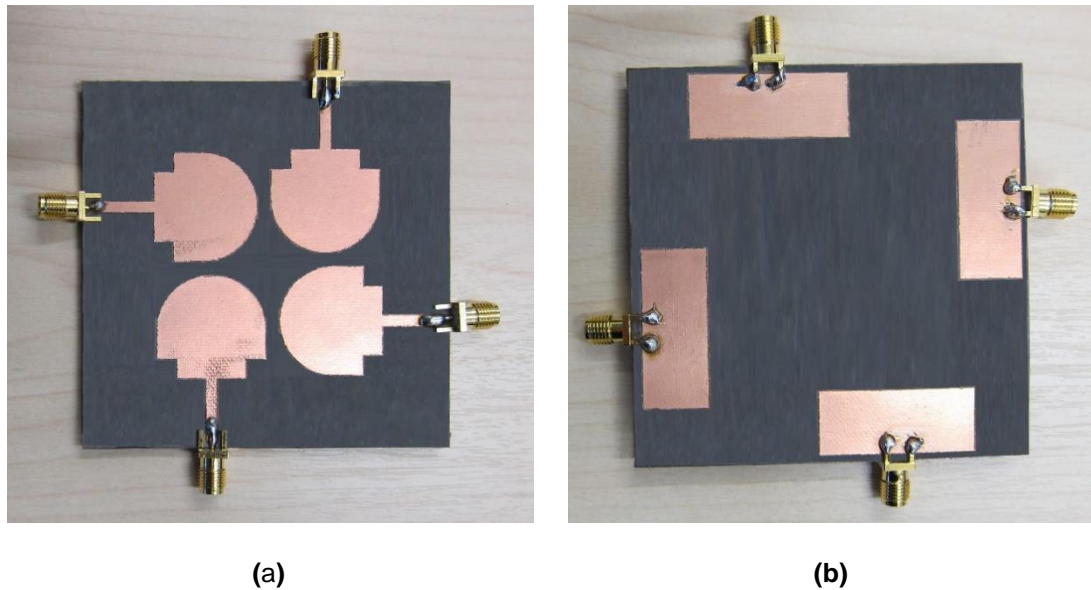


Figure 5.2–3: Photographs of (a) the top side and (b) the bottom side of the fabricated PCB antenna.

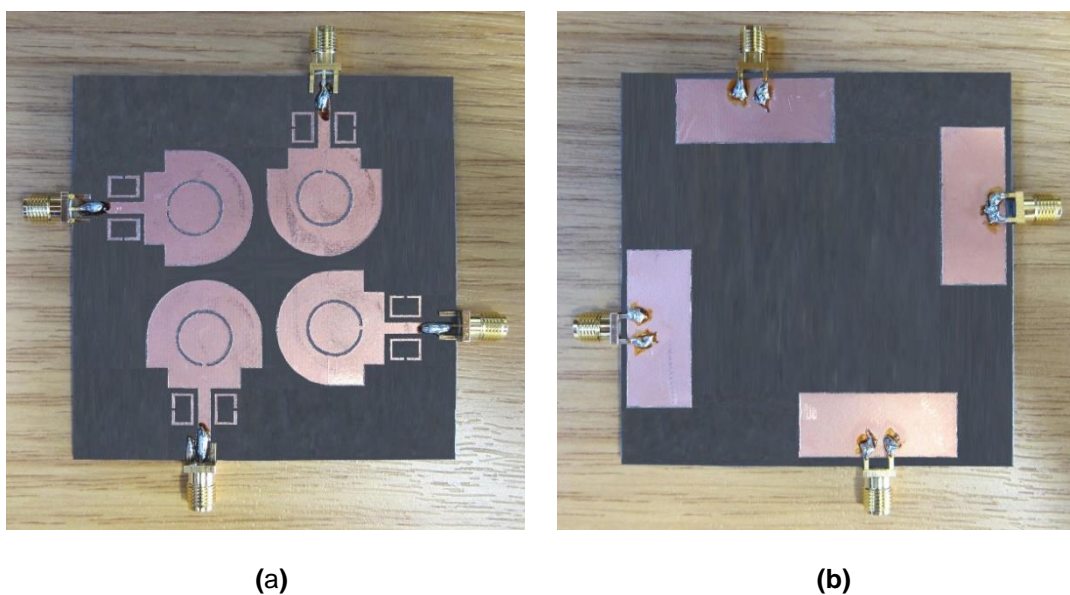


Figure 5.2–4: Photographs of (a) the top side and (b) the bottom side of the fabricated PCB filtenna.

5.2.3: Results

A) Return Loss of Antenna and Filtenna

The antenna from Figure 5.2–1 was simulated using the final values from Table 5.2–2 and the filtenna from Figure 5.2–2 was simulated using the final values from Table 5.2–3. Thereafter, the fabricated antenna in Figure 5.2–3 and the fabricated filtenna in Figure 5.2–4 were measured using an Agilent E8361A PNA Network Analyser.

The ensuing simulated and measured return loss of the MIMO antenna is shown in Figure 5.2–5. The return loss obtained from the simulation shows that a full bandpass response at a return loss of more than 10 dB is obtained across the frequency range of 2.75 GHz to 12 GHz for all four elements. The measured return loss of each element was acquired by stimulating each port one by one while, at the same time, the other three ports were terminated using 50 Ω loads. These obtained results show the average passband of the four elements to be present from about 2.98 GHz to 11.72 GHz. The antenna seems to be sensitive at the higher frequencies as seen from the deviation between the individual measured results of each element after 7.5 GHz. Furthermore, since there are no filtering resonators integrated with or within the radiating elements, there are no notchband present in the results.

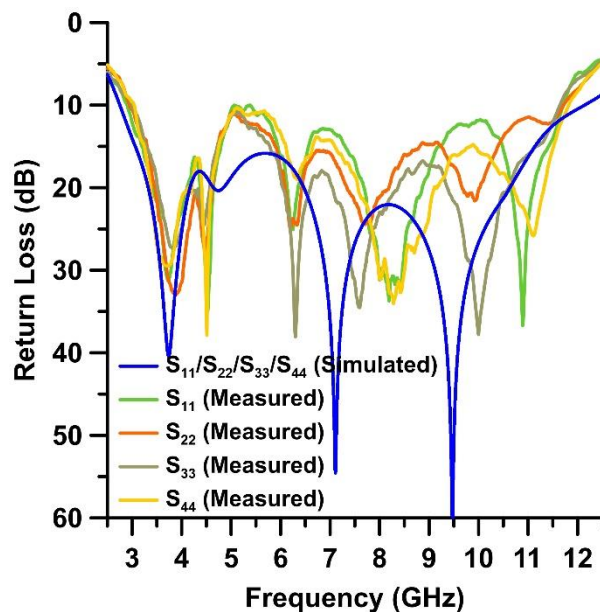


Figure 5.2–5: Return loss of the antenna.

The resulting simulated and measured return loss of the MIMO filtenna is shown in Figure 5.2–6. The simulated return loss shows that a full bandpass response at a return loss of more than 10 dB is obtained across the frequency range of 2.69 GHz to 12 GHz for all four elements. Additionally, within the passband, dual notchband are present. The simulated dual notchband have been attained at 3.45 GHz and 6.04 GHz at a return loss of 0.85 dB and 1.4 dB respectively.

Same as the MIMO antenna, the measured return loss of each element of the MIMO filtenna was obtained by stimulating each port one by one while, at the same time, the other three ports were terminated using 50 Ω loads. The attained results show the average passband of the four elements to be present from about 2.96 GHz to 11.56 GHz. There is a negligible difference between the individual elements' lower limit of the passband frequency and a slight difference between the individual elements' upper limit of the passband frequency. Furthermore, measurements show the dual notchband at the marginally shifted frequencies of 3.52 GHz, at an average return loss of 1.75 dB, and of 6.05 GHz, at an average return loss of 2.4 dB.

Although not as much as the antenna, the filtenna also seems to be sensitive at the higher frequencies as seen from the variance between the individual measured results of each element after 8 GHz.

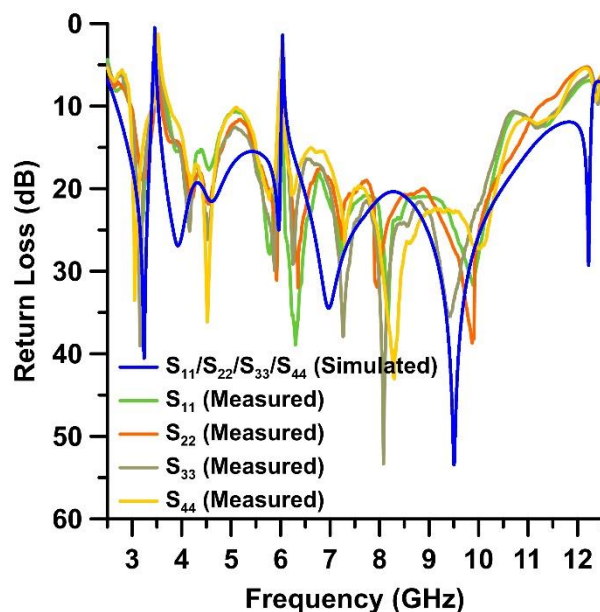
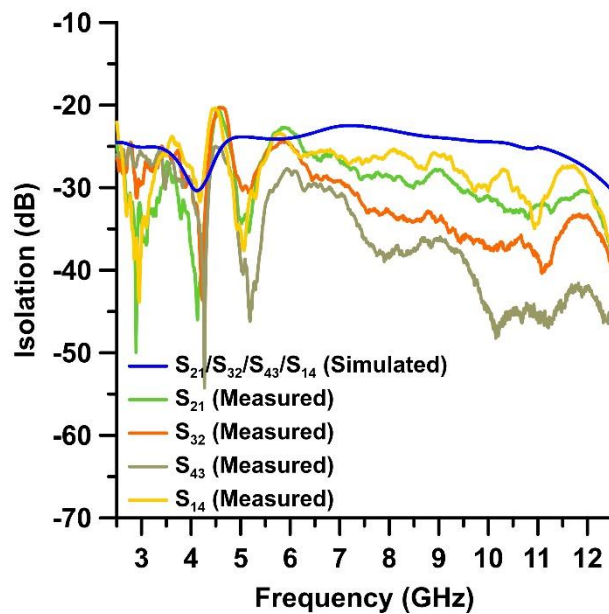


Figure 5.2–6: Return loss of the filtenna.

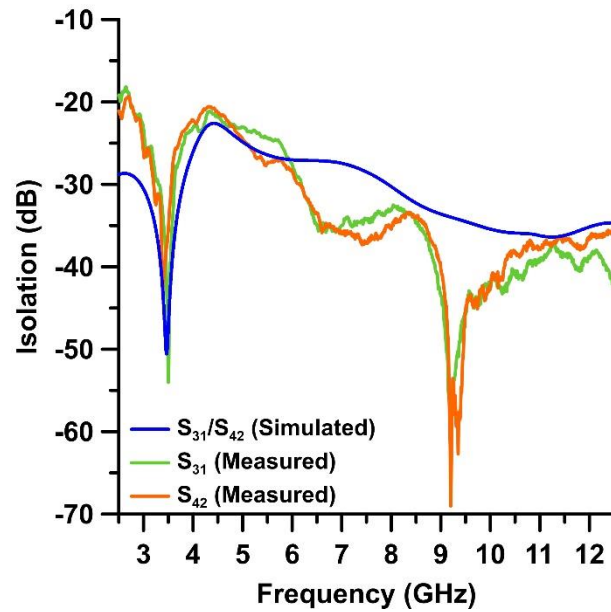
B) Isolation in Antenna and Filter

The simulated and measured results of the isolation between the adjacent elements of the MIMO antenna are given in Figure 5.2–7 (a) and of the opposite elements are given in Figure 5.2–7 (b).

The simulated isolation is more than 20 dB across the operational passband. The isolations amongst the adjacent and opposite elements were measured by stimulating two ports at a time, while the other two ports were terminated using 50 Ω loads. Between both the adjacent elements and the opposite elements, the measured results show the isolation to be more than 20 dB throughout the whole passband. Nevertheless, as can be seen from both figures, at 4.5 GHz, the isolation becomes very close to being less than 20 dB.



(a)

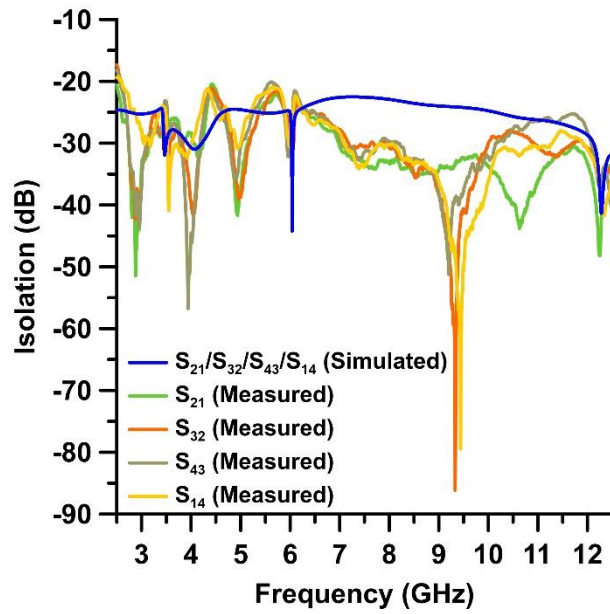


(b)

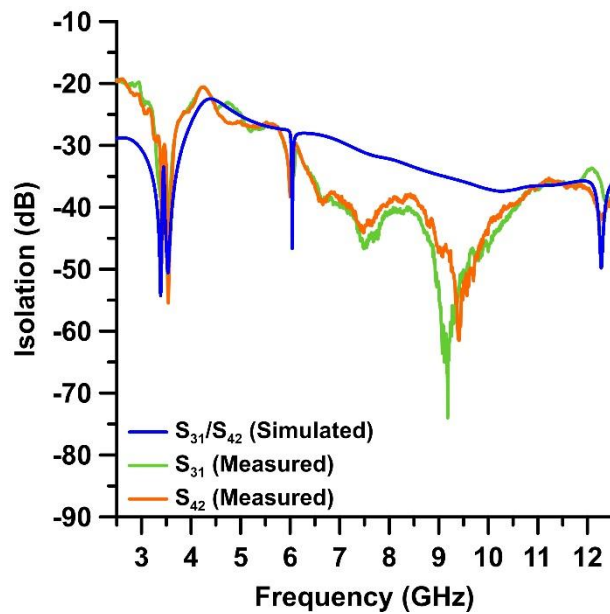
Figure 5.2–7: Isolations between (a) the adjacent elements and (b) the opposite elements of the antenna.

The simulated and measured results of the isolation between the adjacent elements of the MIMO filtenna are given in Figure 5.2–8 (a) and of the opposite elements are given in Figure 5.2–8 (b).

The simulated isolation is more than 20 dB throughout the passband range. The isolations amongst the adjacent and opposite elements were measured by exciting two ports at the same time, while the other two ports were terminated using 50 Ω loads. The measured results show the isolation to be more than 20 dB across the entire passband between both the adjacent elements and the opposite elements. This satisfies one of the requirements of the MIMO filtenna. However, between 4.25 GHz and 4.5 GHz, the isolation approaches very close to being less than 20 dB as can be seen from both figures. The isolation at these frequencies could be easily increased by placing a stub or a multi-mode resonator, of a quarter-wavelength length at 4.375 GHz, in the middle of the filtenna and connecting the four radiating elements or the ground planes to it; similar to the procedure given in [5-15]. This would result in the current at 4.375 GHz being focused only on the stub or the multi-mode resonator. This would reduce the mutual coupling, i.e. increase the isolation, amongst the elements of the filtenna. It is also possible to further improve the overall isolation amongst the adjacent and opposite elements of the MIMO filtenna, but this would be at the cost of a deterioration in the overall return loss of the filtenna [5-16].



(a)



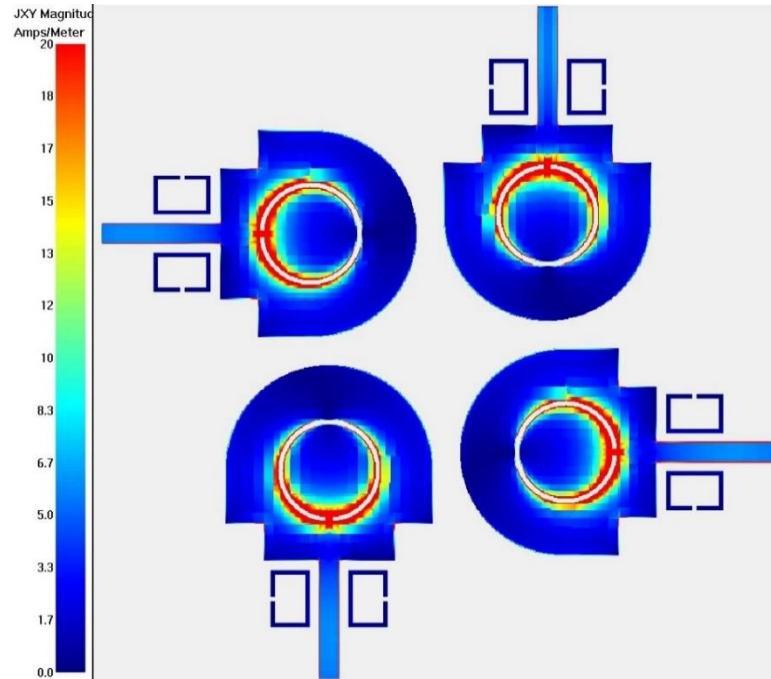
(b)

Figure 5.2–8: Isolations between (a) the adjacent elements and (b) the opposite elements of the filtenna.

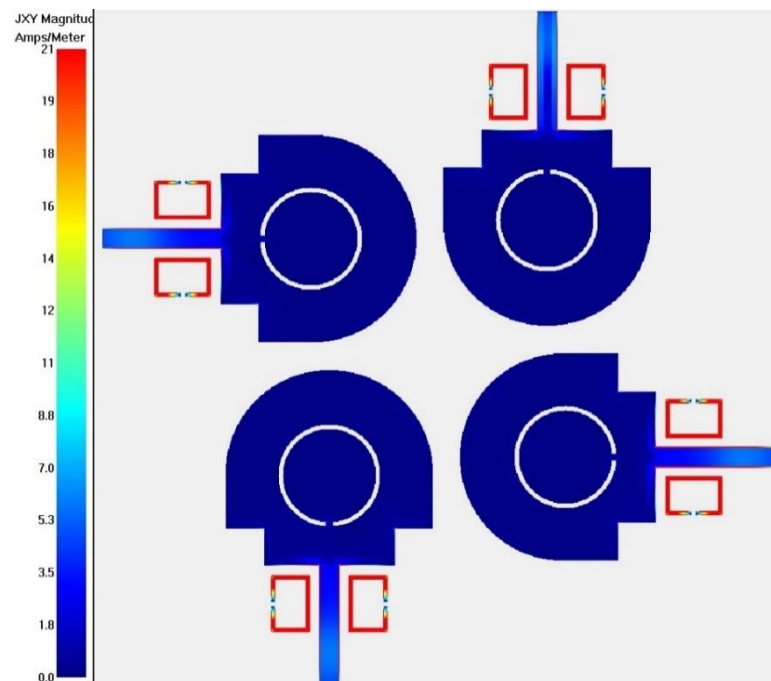
C) Current Densities of Filtenna

So as to show the effects of each element’s ring resonators on the MIMO filtenna during operation, the current density of the filtenna was simulated with all four ports excited at the dual notchband frequencies of 3.45 GHz and 6.04 GHz. The obtained results at the two frequencies are given in Figure 5.2–9.

From the two figures, it can be seen that at the two notchband frequencies, the currents are completely densely populated along their respective notchband resonators. This holds true for each radiating element.



(a)



(b)

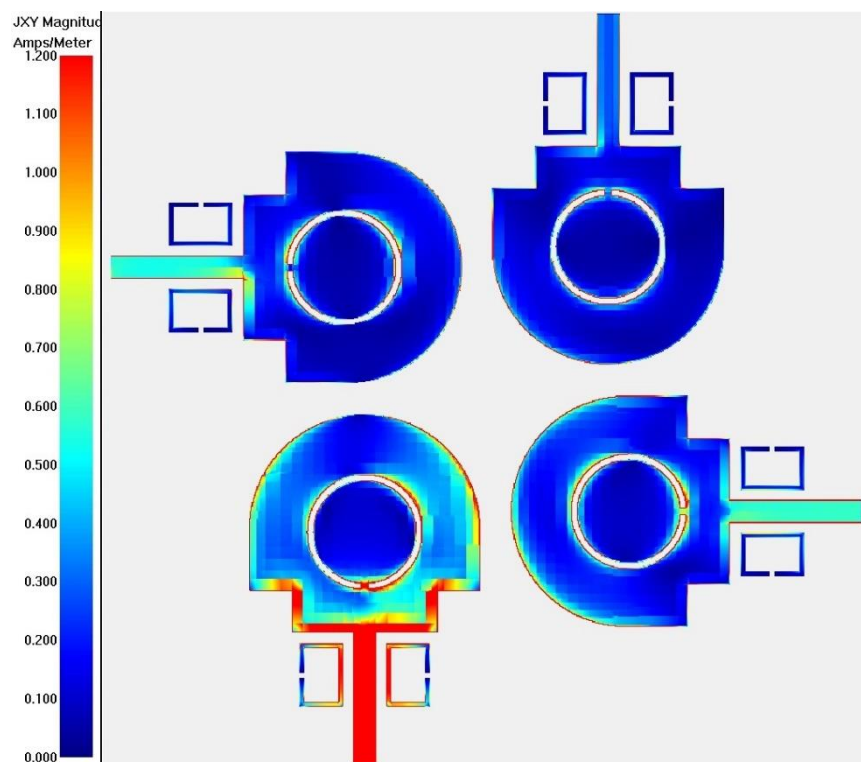
Figure 5.2-9: Current density of the filtenna at the dual notchband frequencies of (a) 3.45 GHz and (b) 6.04 GHz.

In order to expand on the isolation results of the filtenna from Figure 5.2–8, the current density of the filtenna with only port 1 excited was obtained at two frequencies. According to Figure 5.2–8, the first frequency, 7.32 GHz, and the second frequency, 4.36 GHz, are the points where the isolation is at a minimum for the adjacent elements and the opposite elements respectively.

Figure 5.2–10 (a) shows that while the main currents are being driven in the first radiating element, there is a leakage of the currents across to the other elements because of mutual capacitive coupling. Almost all of this leakage is through to the second and the fourth adjacent elements. This is evident from the higher current density present in the transmission feed lines of the two adjacent elements than the opposite element.

On the other hand, Figure 5.2–10 (b) shows that at 4.36 GHz, the leakage of the currents from the first radiating element is mostly across to the third opposite element rather than through to the adjacent elements.

Therefore, it can be inferred that the current densities at the two frequencies emulate the isolation results from Figure 5.2–8.



(a)

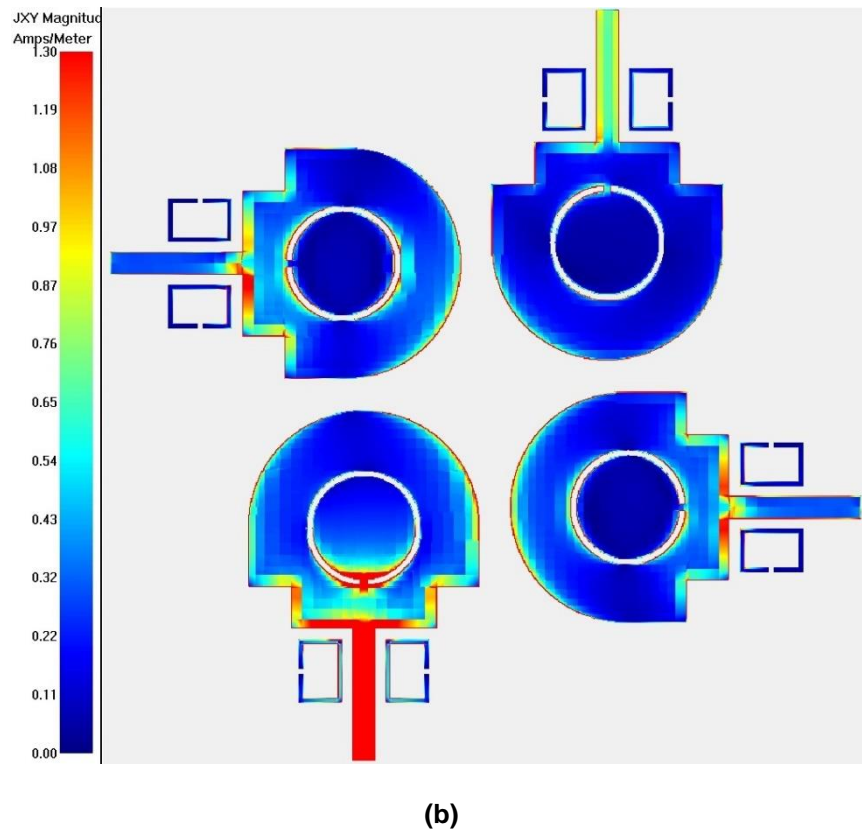


Figure 5.2–10: Current density of the filtenna at the frequencies of (a) 7.32 GHz and (b) 4.36 GHz.

D) Radiation Patterns of Filtenna

The radiation patterns of the filtenna were simulated and measured at three various frequency points. These three points are at 3.1 GHz, 4.5 GHz and 6.5 GHz and are shown in Figure 5.2–11 (a), Figure 5.2–11 (b) and Figure 5.2–11 (c) respectively. The radiation patterns have been calibrated to the gain of the filtenna and the simulated and measured results have been attuned to obtain the best possible match with each other. As seen from the three results, the filtenna has stable bidirectional radiation patterns in the E-plane and omnidirectional radiation patterns in the H-plane. A reasonable match has been obtained between the simulated and the measured results.

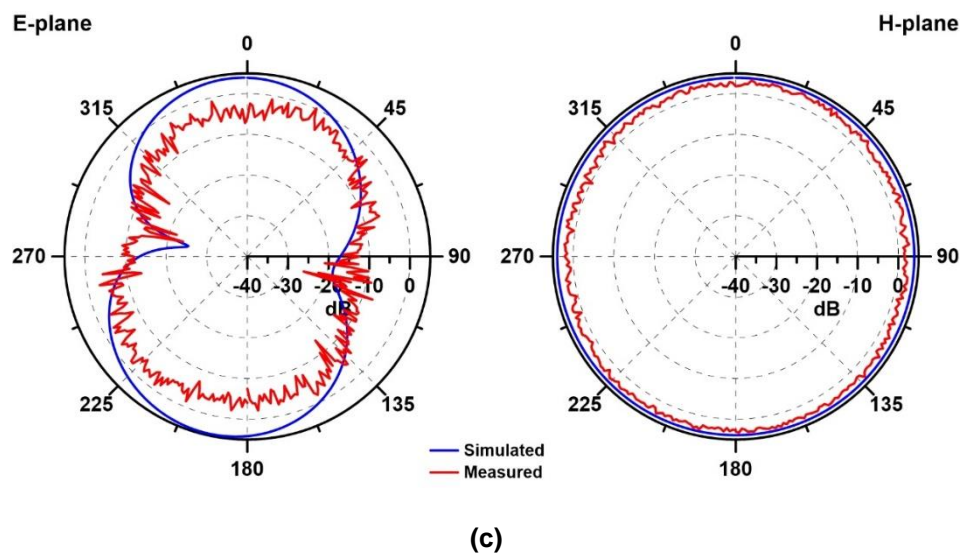
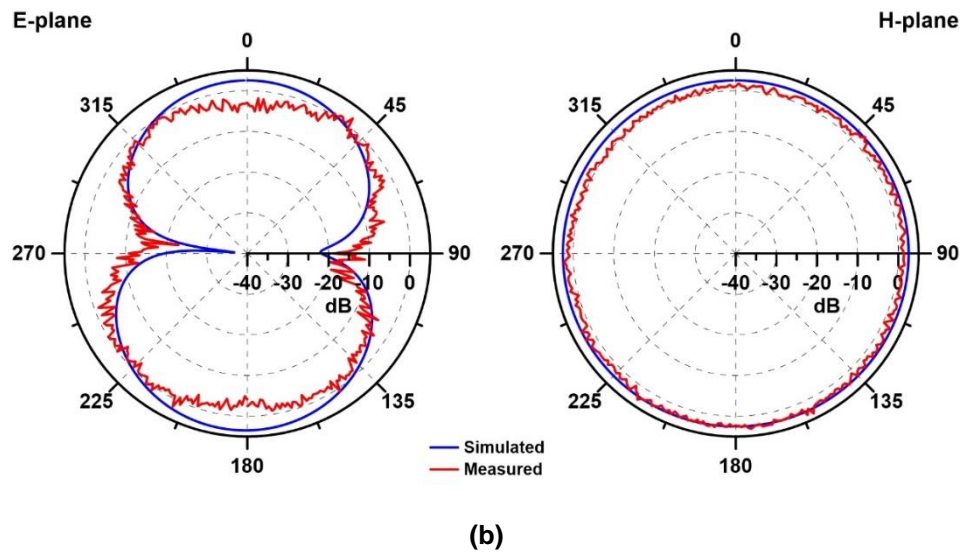
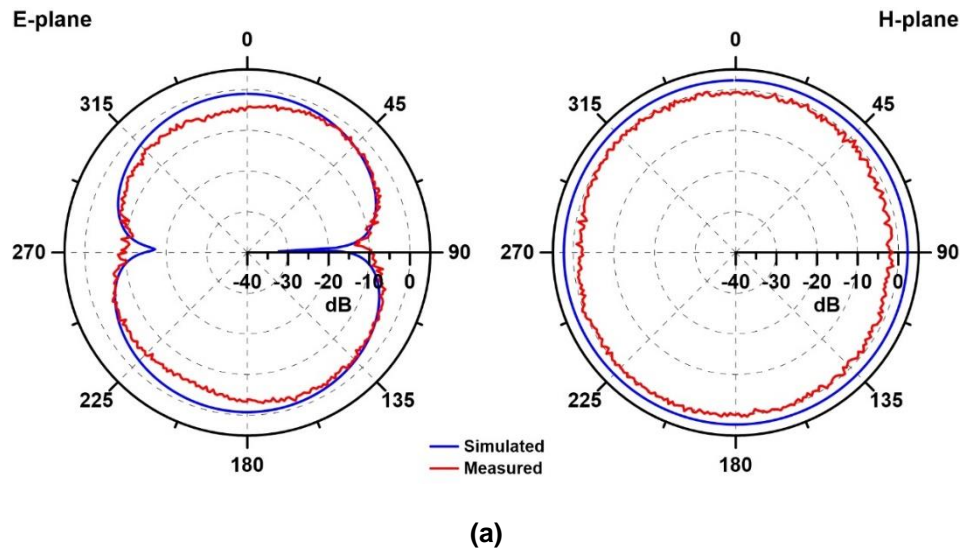


Figure 5.2–11: Radiation patterns of the filtenna at (a) 3.1 GHz, (b) 4.5 GHz and (c) 6.5 GHz.

E) Gain of Antenna and Filtenna

The simulated gain of the antenna and the filtenna were obtained. The results are presented in Figure 5.2–12.

Within the passband of the antenna and the passband of the filtenna, the simulated average gain is 5.23 dBi and 5.49 dBi respectively and the variance of the gain is within 2 dBi and 2.15 dBi respectively. The gain of the antenna and the filtenna almost mirror each other across the operational frequency range except at the dual notchband frequencies. The gain of the antenna at the dual notchband frequencies is 5.1 dBi and 4.57 dBi. However, in the filtenna, these gains are reduced to 1.54 dBi and -0.61 dBi respectively because of notchband suppression. The falls in the gain signify the rejection capability of the filtenna.

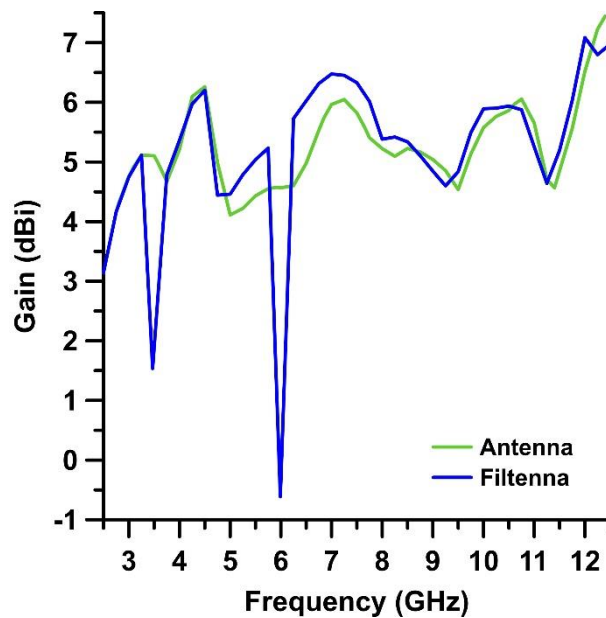


Figure 5.2–12: Gain of the antenna and the filtenna

F) Efficiency of Antenna and Filtenna

The simulated efficiency of the antenna and the filtenna were obtained. The results are given in Figure 5.2–13.

Across the passband of the antenna and the passband of the filtenna, the average efficiency is 90.7 %. Similar to the results of the gain, the efficiency of the antenna and the filtenna also echo each other except at the dual notchband frequencies. The efficiency of the filtenna drops from about 96 % and 89.5 % to about 24.4 % and 20.5 % at the dual notchband frequencies. The substantial decrease in the efficiency at the dual notchband also indicates the rejection capability of the filtenna.

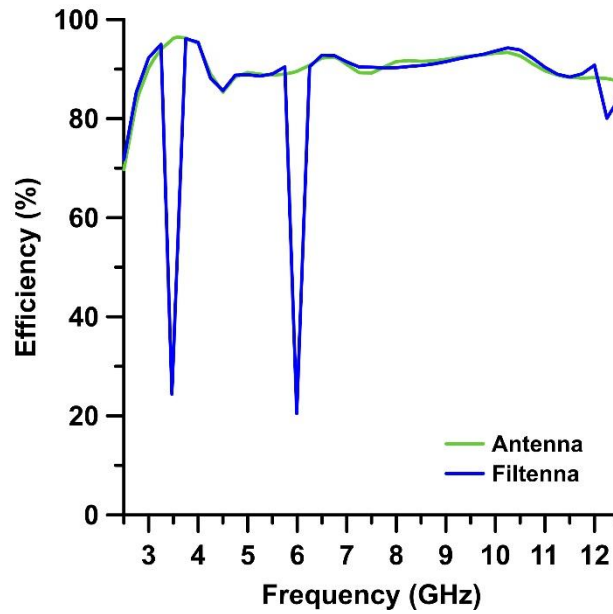


Figure 5.2-13: Efficiency of the antenna and the filtenna

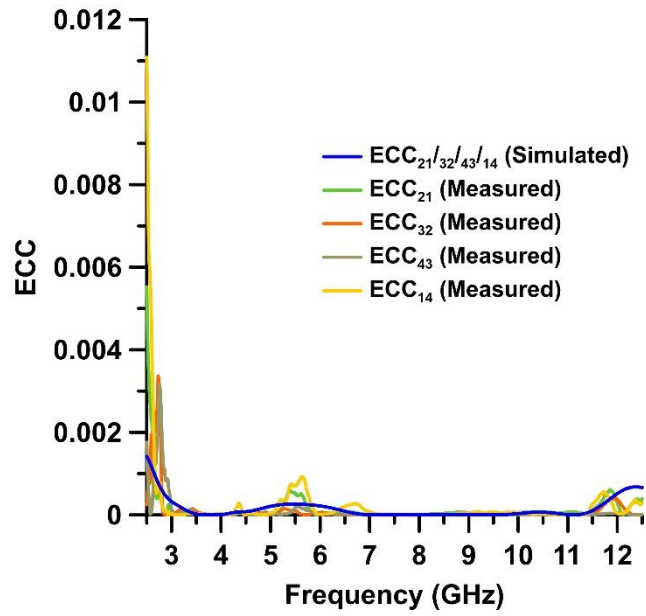
G) Diversity Performance of Antenna and Filtenna

The Envelope Correlation Coefficient is an important parameter for evaluating the diversity performance of antennas and filtennas which are intended for MIMO applications. The Envelope Correlation Coefficient, ρ_e , should have a value less than 0.25 for an antenna or a filtenna to meet the requirement of a good diversity performance [5-7]. According to the method proposed in [5-28] for four-port lossless MIMO antennas/filtennas in a uniform propagation environment, the Envelope Correlation Coefficient can be calculated by the formula given in (5.1).

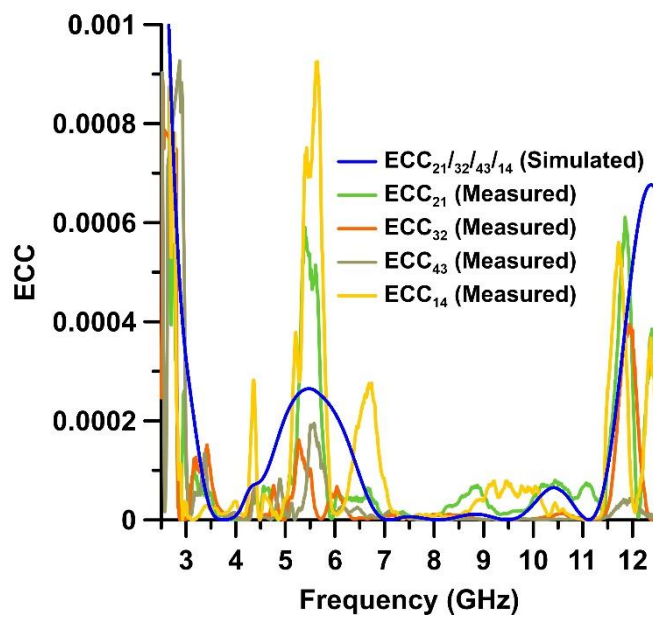
$$\rho_e = \frac{|S_{ii}^* S_{ij} + S_{ji}^* S_{jj}|^2}{(1 - |S_{ii}|^2 - |S_{ji}|^2) \times (1 - |S_{jj}|^2 - |S_{ij}|^2)} \quad (5.1)$$

where i and j denote the port numbers 1, 2, 3, or 4 of their respective radiating elements 1, 2, 3, or 4 and $i \neq j$.

The simulated and measured values of the Envelope Correlation Coefficient of the adjacent elements and the opposite element of the antenna are given in Figure 5.2-14 and Figure 5.2-15 respectively. For the simulated passband range, the Envelope Correlation Coefficient for the adjacent elements and the opposite elements is below 0.0003. Across the measured passband, it is below 0.0009 and 0.0020 for the adjacent elements and the opposite elements respectively.

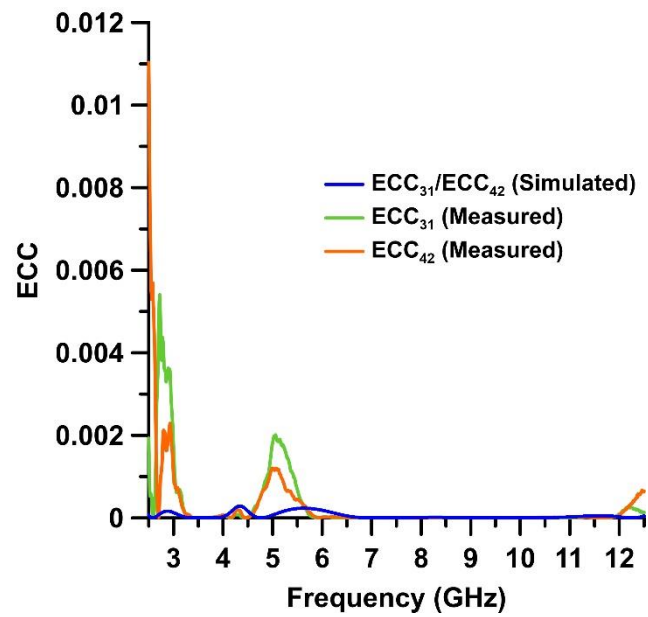


(a)

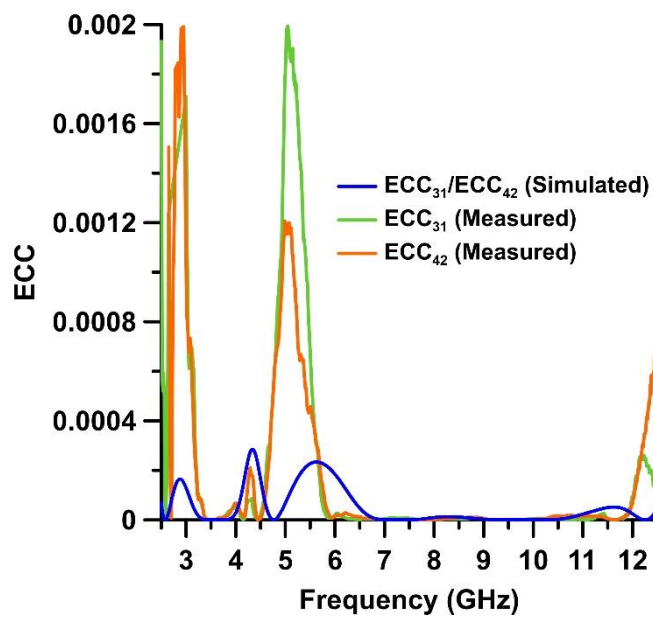


(b)

Figure 5.2–14: Envelope correlation coefficient of the adjacent elements of the antenna: (a) full view and (b) zoomed-in view.



(a)



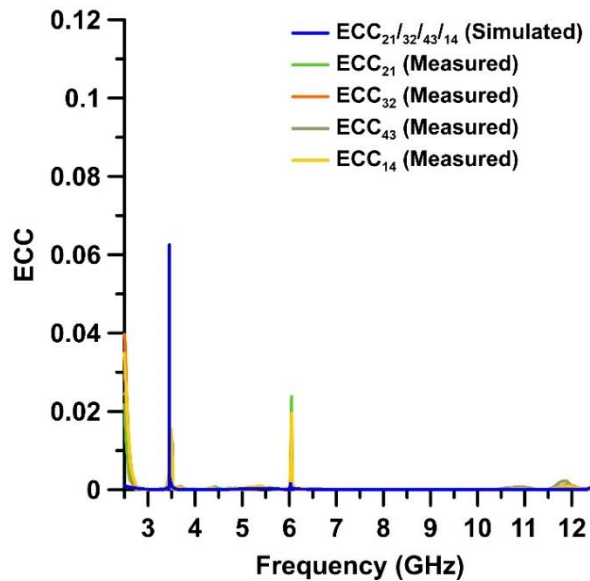
(b)

Figure 5.2–15: Envelope correlation coefficient of the opposite elements of the antenna: (a) full view and (b) zoomed-in view.

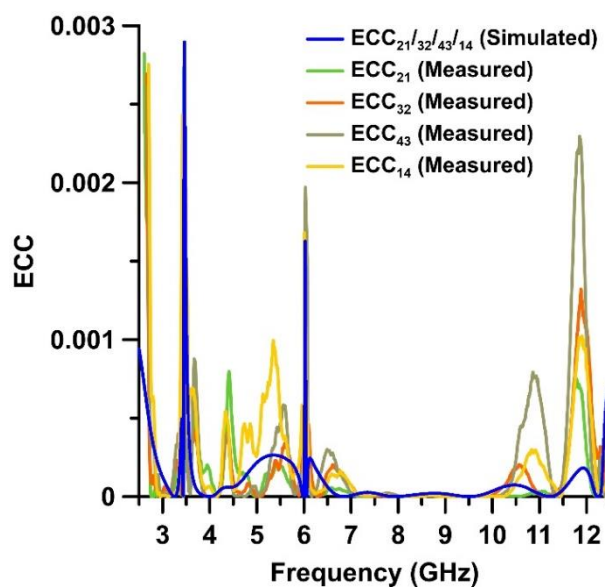
The simulated and measured values of the Envelope Correlation Coefficient of the adjacent elements and the opposite element of the filtenna are given in Figure 5.2–16 and Figure 5.2–17 respectively. For the simulated passband range (excluding the dual notchband frequencies), the Envelope Correlation Coefficient for the adjacent elements and the opposite elements is below 0.0003. Across the

measured passband (excluding the dual notchband frequencies), it is below 0.0010 for both the adjacent elements and the opposite elements. Whereas, at the first and the second notchband frequencies, the values are at a maximum of 0.0160 and 0.0240 respectively for the adjacent elements and at a maximum of 0.0017 and 0.0040 respectively for the opposite elements.

Since the acquired values of the Envelope Correlation Coefficient are less than 0.25, a good diversity performance is ensured by the designed MIMO filtenna.

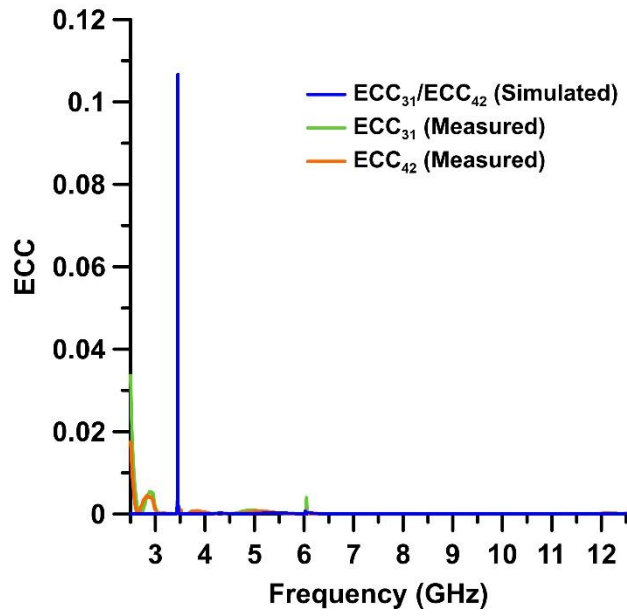


(a)

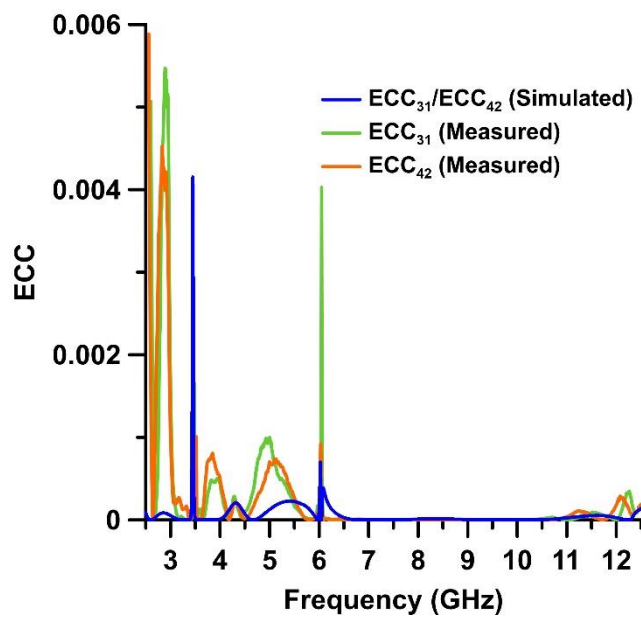


(b)

Figure 5.2–16: Envelope correlation coefficient of the adjacent elements of the filtenna: (a) full view and (b) zoomed-in view.



(a)



(b)

Figure 5.2–17: Envelope correlation coefficient of the opposite elements of the filtenna: (a) full view and (b) zoomed-in view.

5.2.4: Summary of Presented Results

The results of the antenna and the filtenna are summarised in Table 5.2–4.

Table 5.2–4: Summary of the results of the antenna and the filtenna.

Structure	Response Type	Passband (GHz)	FBW (%)	Dual Notchband			
				Frequency (GHz)	Rejection (dB)	Gain (dBi)	Efficiency (%)
Antenna	Simulated	2.75–12.00	161	n/a	n/a	5.1 & 4.57	96 & 89.5
	Measured	2.98–11.72	148	n/a	n/a	n/p	n/p
Filtenna	Simulated	2.69–12.00	164	3.45 & 6.04	0.85 & 1.4	1.54 & -0.61	24.4 & 20.5
	Measured	2.96–11.56	147	3.52 & 6.05	1.75 & 2.4	n/p	n/p

5.3: References

- [5-1] A. Al-Rawi, A. Hussain, J. Yang, M. Franzén, C. Orlenius, and A. A. Kishk, "A new compact wideband MIMO antenna—the double-sided tapered self-grounded monopole array," *IEEE Transactions on Antennas and Propagation*, vol. 62, no. 6, pp. 3365–3369, June 2014.
- [5-2] G. G. Raleigh and J. M. Cioffi, "Spatio-temporal coding for wireless communication," *IEEE Transactions on Communications*, vol. 46, no. 3, pp. 357–366, March 1998.
- [5-3] V. Tarokh, N. Seshadri, and A. R. Calderbank, "Space-time codes for high data rate wireless communication: performance criterion and code construction," *IEEE Transactions on Information Theory*, vol. 44, no. 2, pp. 744–765, March 1998.
- [5-4] J-M. Lee, K-B. Kim, H-K. Ryu, and J-M. Woo, "A compact ultrawideband MIMO antenna with WLAN band-rejected operation for mobile devices," *IEEE Antennas and Wireless Propagation Letters*, vol. 11, pp. 990–993, 2012.
- [5-5] L. Liu, S. W. Cheung, and T. I. Yuk, "Compact MIMO antenna for portable devices in UWB applications," *IEEE Transactions on Antennas and Propagation*, vol. 61, no. 8, pp. 4257–4264, August 2013.
- [5-6] L. Zheng and C. Tse, "Diversity and multiplexing: a fundamental tradeoff in multiple-antenna channels," *IEEE Transactions on Information Theory*, vol. 49, no. 5, pp. 1073–1096, May 2003.
- [5-7] T. Kaiser, F. Zheng, and E. Dimitrov, "An overview of UWB systems with MIMO," *IEEE Proceedings*, vol. 97, no. 2, pp. 285–312, February 2009.
- [5-8] S. Zhang, Z. Ying, J. Xiong, and S. He, "Ultrawideband MIMO/diversity antennas with a tree-like structure to enhance wideband isolation," *IEEE Antennas and Wireless Propagation Letters*, vol. 8, pp. 1279–1282, 2009.
- [5-9] G. J. Foschini, "Layered space-time architecture for wireless communication in a fading environment when using multi-element antennas," *Bell Labs Technical Journal*, vol. 1, no. 2, pp. 41–59, 1996.
- [5-10] J. W. Wallace, M. A. Jensen, A. L. Swindlehurst, and B. D. Jeffs, "Experimental characterization of the MIMO wireless channel: data acquisition and analysis," *IEEE Transactions on Communications*, vol. 2, no. 2, pp. 335–343, March 2003.

- [5-11] V. P. Tran and A. Sibille, "Spatial multiplexing in UWB MIMO communications," *IET Electronics Letters*, vol. 42, no. 16, pp. 931–932, August 2006.
- [5-12] J-F. Li, Q-X. Chu, Z-H. Li, and X-X. Xia, "Compact dual band-notched UWB MIMO antenna with high isolation," *IEEE Transactions on Antennas and Propagation*, vol. 61, no. 9, pp. 4759–4766, September 2013.
- [5-13] X-L. Liu, Z-D. Wang, Y-Z. Yin, J. Ren, and J-J. Wu, "A compact UWB MIMO antenna using QSCA for high isolation," *IEEE Antennas and Wireless Propagation Letters*, vol. 13, pp. 1497–1500, 2014.
- [5-14] J. Ren, W. Hu, Y. Yin, and R. Fan, "Compact printed MIMO antenna for UWB applications," *IEEE Antennas and Wireless Propagation Letters*, vol. 13, pp. 1517–1520, 2014.
- [5-15] N. K. Kiem, H. N. B. Phuong, Q. N. Hieu, and D. N. Chien, "A compact printed 4×4 MIMO-UWB antenna with WLAN band rejection," *IEEE International Symposium on Antennas and Propagation and North American Radio Science Meeting*, pp. 2245–2246, July 2013.
- [5-16] Y. Li, W. Li, C. Liu, and T. Jiang, "Two UWB-MIMO antennas with high isolation using sleeve coupled stepped impedance resonators," *IEEE Asia-Pacific Conference on Antennas and Propagation*, August 2012.
- [5-17] S. W. Sou, "High-gain dual-loop antennas for MIMO access points in the 2.4/5.2/5.8 GHz bands," *IEEE Transactions on Antennas and Propagation*, vol. 58, no. 7, pp. 2412–2419, July 2010.
- [5-18] J-H. Chou and S-W. Sou, "Internal wideband monopole antenna for MIMO access-point applications in WLAN/WIMAX bands," *Microwave and Optical Technology Letters*, vol. 50, no. 5, pp. 1146–1148, May 2008.
- [5-19] S. W. Sou and C. T. Lee, "Low-cost dual-loop-antenna system for dual-WLAN-band access points," *IEEE Transactions on Antennas and Propagation*, vol. 58, no. 5, pp. 1652–1659, May 2011.
- [5-20] J. O. Yang, F. Yang, and Z. M. Wang, "Reducing mutual coupling of closely spaced microstrip MIMO antennas for WLAN application," *IEEE Antennas and Wireless Propagation Letters*, vol. 10, pp. 310–313, 2011.
- [5-21] L. Minz and R. Garg, "Reduction of mutual coupling between closely spaced PIFAs," *IET Electronics Letters*, vol. 46, no. 6, pp. 392–394, March 2012.
- [5-22] C. Y. Chiu, C. H. Cheng, R. D. Murch, and C. R. Rowell, "Reduction of mutual coupling between closely-packed antenna elements," *IEEE*

- Transactions on Antennas and Propagation*, vol. 55, no. 6, pp. 1732–1738, June 2007.
- [5-23] F. G. Zhu, J. D. Xu, and Q. Xu, “Reduction of mutual coupling between closely-packed antenna elements using defected ground structure,” *IEEE International Symposium on Microwave, Antenna, Propagation and EMC Technologies for Wireless Communications*, pp. 1–4, 2009.
- [5-24] Z. Bayraktar, M. Gregory, and D. H. Werner, “Composite planar double-sided AMC surfaces for MIMO applications,” *IEEE International Symposium on Antennas and Propagation and North American Radio Science Meeting*, pp. 1–4, 2009.
- [5-25] A. Rajagopalan, G. Gupta, A. S. Konanur, B. Hughes, and G. Lazzi, “Increasing channel capacity of an ultrawideband MIMO system using vector antennas,” *IEEE Transactions on Antennas and Propagation*, vol. 55, no. 10, pp. 2880–2887, October 2007.
- [5-26] S. Zhang, B. K. Lau, A. Sunesson, and S. He, “Closely-packed UWB MIMO/diversity antenna with different patterns and polarizations for USB dongle applications,” *IEEE Transactions on Antennas and Propagation*, vol. 60, no. 9, pp. 4372–4380, September 2012.
- [5-27] A. I. Najam, Y. Duroc, and S. Tedjni, “UWB-MIMO antenna with novel stub structure,” *Progress in Electromagnetics Research C*, vol. 19, pp. 245–257, February 2011.
- [5-28] S. Blanch, J. Romeu, and I. Corbella, “Exact representation of antenna system diversity performance from input parameter description,” *IET Electronics Letters*, vol. 39, no. 9, pp. 705–707, May 2003.

Chapter 6:

**Development of
Narrowband Planar Microstrip
Filtennas**

6.1: Introduction

For a given power and frequency (often set by governmental radio frequency protocols), the range of the radio frequency link is determined by the data rate. A lower data rate provides a longer range due to an increased sensitivity of the wireless transceivers. At the same time, there is a compromise: since very low data rates mean a very long time on air, this, in turn, reduces the lifetime of devices and also increases the probability of interference with other wireless communication systems. Accordingly, in practical designs, long-range systems typically use a reasonably low data rate to optimise and acquire a good balance between the range and the transmission time. The narrowband technique for a long range and a reasonably low data rate is widely accepted since it gives the best possible balance between the range and the transmission time.

Wireless communication systems used by police, ambulance, fire services, maritime communications and for smart metering are some applications of narrowband communication systems.

Most people incorrectly interpret that if, for example, a frequency range of 450–500 MHz is stated for a narrowband antenna, then “the antenna will no longer operate at 440 MHz or 510 MHz” and that a narrowband antenna works similar to filters. Consequently, it is also assumed that the decoupling between two narrowband antennas with adjacent frequency bands will be better than the decoupling between two similar broadband versions. However, this is, evidently, not the case. Modern antennas exhibit bandwidths that extend far beyond the specified frequency range, for which the stated values as provided in the data sheet apply, such as VSWR, return loss, gain, half-power beamwidth, etc. In other words, the functionality of the antenna still remains above and below this specified frequency range, but with increasing deviations from the given specifications. The situation can be likened to that of an electric light bulb which is designed for a voltage rating of 230–240 V to achieve its full brightness. Although it will still function at 200 V, it will not shine at its full brightness. In narrowband antennas, the fluctuating functionality outside their specified frequency range can be classified as — and leads to the reception of — frequency harmonics and noise.

For the purpose of suppressing these frequency harmonics and noise near the passband(s) of narrowband antennas, filters can be integrated with the antennas.

Unlike broadband antennas, integrating bandstop filters with narrowband antennas would be an inappropriate choice. The reasons being that, firstly, the exact position of the frequencies that must be suppressed would be unknown beforehand and, secondly, the number of these frequencies may be probably too many. For these reasons, bandstop filter networks could become complex to design and/or be size-unfriendly.

On the other hand, bandpass filters are a better choice. Bandpass filters, with the same number and position of passbands as the narrowband antennas they are being integrated with, would only let specific frequencies of interest to pass through them and reject and/or suppress any out-of-band noise and harmonics. Logically speaking, this would be better since there can be only so many number of passbands in narrowband antennas. This integration results in the formation of narrowband filtennas for wireless transceivers.

Several new fabrication technologies have emerged in the recent years. They usually have different fabrication approaches as compared with conventional PCB technology. Moreover, they use different metallisation and dielectric substrates as well. One of these emerging technologies is inkjet-printing. Thus, it is important to demonstrate the practicability of inkjet-printed planar monopole antennas for wireless transceivers of narrowband applications.

For the above reasons, some work has been carried out [6-1]–[6-10]. In these works, antenna arrays for the 2.4 GHz and 5.8 GHz bands have been reported in [6-1]. However, the 2.4 GHz and 5.8 GHz point-to-point antenna arrays are mounted separately with discrete ports [6-1]. It is difficult to achieve a planar antenna array with stable directional radiation patterns from 2–6 GHz; as gain is proportional to the radiation aperture [6-1]. Hence, a dual-band array structure is preferred due to its simple system configuration and minimisation of cost. Although similar work has been proposed in [6-1]–[6-2], it is disadvantageous with respect to quite a number of factors; such as, large 2×2 array structures, single-band operation, final response not being sufficiently sharp and, most importantly, spurious harmonics not being fully rejected. Similarly, [6-3]–[6-4] are unfavourable as well since the filters employed are of 3rd and 4th orders, and again the spurious harmonics have not been fully rejected. As extensively discussed in the first and fourth chapters, inkjet-printing technology has been implemented in a wide range of applications; such as displays and lighting to radio frequency and microwave applications, including inkjet-printed antennas [6-5]–[6-7], sensor applications [6-5], broadband systems [6-6] and RFID applications [6-7]. Since 4G has almost achieved maturity, researchers and industries are focusing on the development of 5G communications. 5G is

projected to have higher data rates, faster latency rates, low costs and usage of energy and more supported devices [6-8]. The evolving 5G mobile networks will be required to support capacities of as much as 100x of today's capacity by 2020 and as much as 1000x by 2030 [6-9]–[6-10]. In order to meet these demands, the use of mm-wave bands seems the best option owing to the large amount of available spectrum which could be used for that purpose [6-10]. Despite the wide implementation of inkjet-printing, there has been no reported work on employing it for mm-wave 5G antennas.

Despite the work on narrowband planar microstrip filtennas for wireless transceivers, there is still a scope of some further research. In addition, some essential points which necessitate to be addressed, especially in light of the limitations in the published literature, are as follows:

- Development of narrowband planar microstrip filtennas by the integration of bandpass filters with narrowband planar microstrip antennas.
- Development of narrowband planar microstrip filtennas for wireless transceivers of various wireless communication systems.
- Development of single-band and multi-band narrowband planar microstrip filtennas.
- Rejection or significant suppression of any interfering noise and harmonics present near the passband(s) of the narrowband planar microstrip antennas.
- Using new fabrication technologies for the development of narrowband planar microstrip filtennas.

The purpose of the overall chapter is to integrate planar bandpass filters with narrowband planar microstrip antennas to form narrowband planar microstrip filtennas which address the points listed above. Therefore, in this chapter, three filtennas for wireless transceivers of narrowband applications have been developed. Of the three, one is a PCB filtenna and two are inkjet-printed flexible filtennas.

Section 5.2 introduces the topology of an antenna whose variants will be used in this chapter. Alongside an analysis of its geometry, the section also details its theoretical working, design method and design equations. Additionally, the results based on the design method and design equations are also presented.

Section 5.3 presents a 1×2 filtenna array for dual-band WLAN applications. A 1×2 antenna array for IEEE 802.11 WLAN dual-band frequencies of 2.4 GHz and 5.8 GHz was first designed and consisted of two radiating elements with a single feed network. When tested, in addition to the two main frequencies, the antenna

array displayed noise and harmonics near the two main passbands. Hence, two pseudo-interdigital bandpass filters were designed and integrated within the antenna array for each radiating element. The resultant filtenna array gave a better performance. The filtenna array has been fabricated using conventional PCB technology on a rigid substrate with copper as the metallisation.

Section 5.4 presents the development of an inkjet-printed filtenna for wireless transceivers of single-band WLAN applications. An antenna for IEEE 802.11 WLAN 5.8 GHz band was first designed. Since the antenna exhibited heavy noise and harmonics near its passband, a CPW-fed pseudo-interdigital bandpass filter was designed and integrated with the antenna. The subsequent filtenna was able to give a much performance due to the suppression of noise and harmonics. The filtenna has been developed using inkjet-printing technology on flexible Kapton substrate with silver nanoparticle ink as the metallisation.

In section 5.5, an inkjet-printed flexible antenna for wireless transceivers of 5G applications has been developed. Since there are no interfering wireless services present near or around 28 GHz, filters were not integrated with the antenna. The antenna was designed for 5G applications operating at 28 GHz. The antenna has been developed using inkjet-printing technology on Kapton substrate. The metallisation used are silver nanoparticle ink and copper. Because of inkjet-printing technology and the choice of the printing substrate, the developed 5G antenna is flexible.

6.2: Design of Narrowband Planar Microstrip Antennas

6.2.1: Geometry of the Narrowband Planar Microstrip Antenna

The geometry of a narrowband planar microstrip antenna is given in Figure 6.2–1. This and slight variations of this geometry will be used for the later sections as well. The top metallisation consists of three transmission lines. These are the transmission feed line, the quarter-wavelength impedance transformer and the radiating element. All three transmission lines have a rectangular shape but different sizes. A complete ground covers the entire bottom side of the dielectric substrate. Hence, it has the same size as that of the dielectric substrate.

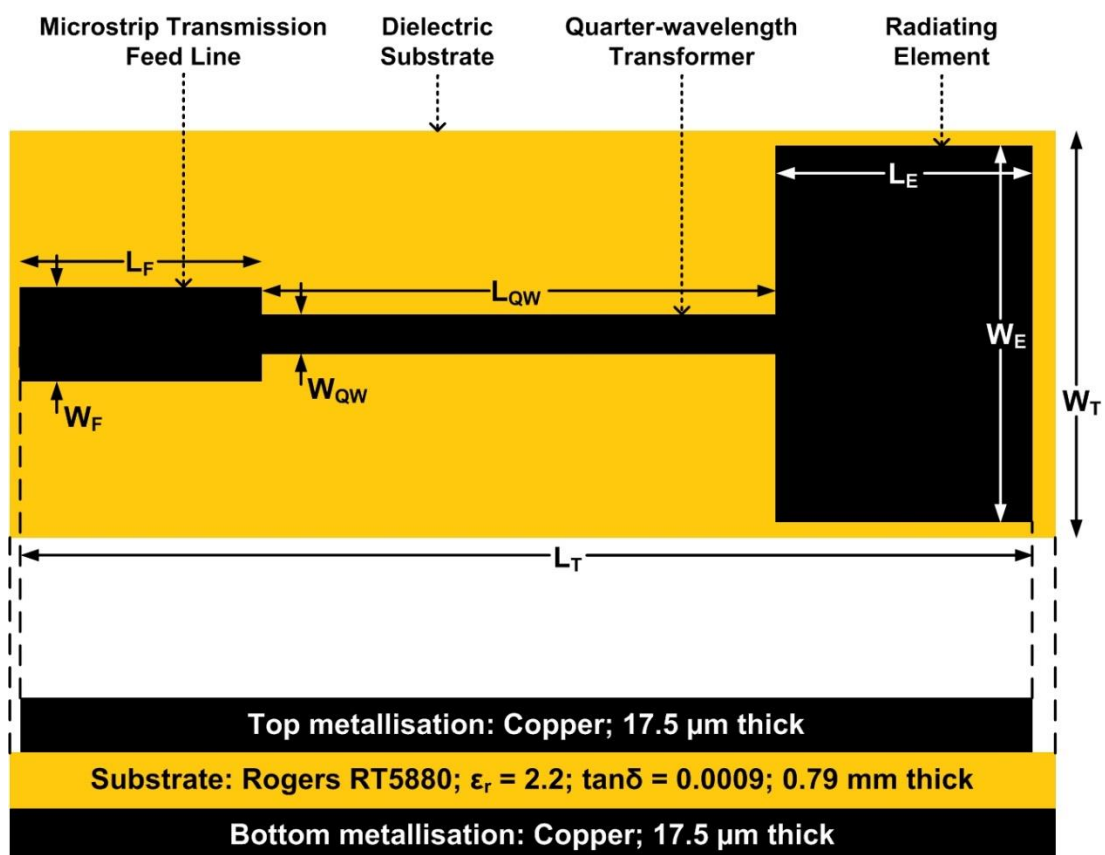


Figure 6.2–1: Geometry of the antenna.

6.2.2: Operating Mechanism of Narrowband Planar Microstrip Antennas

In order to design and determine the initial parameters of narrowband planar microstrip antennas, their operating mechanism needs to be understood first.

Narrowband planar microstrip antennas with a complete ground plane, such as the one shown above, are capable of operating at only one resonant mode — as signified in Figure 6.2–2 — instead of at multiple resonant modes as in the case of broadband planar monopole antennas with a finite ground plane.

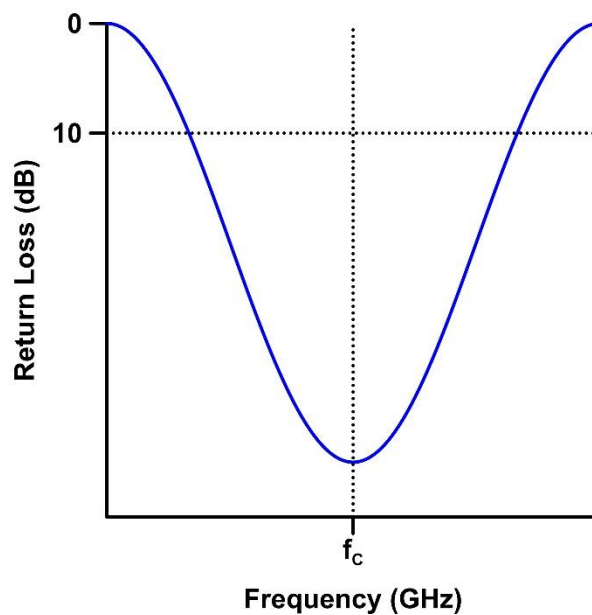


Figure 6.2–2: Single resonant mode of narrowband planar microstrip antennas.

At the resonant mode, the current modes which exist in the radiating elements of the narrowband planar microstrip antennas are bigger at the centre of the radiating elements and mostly concentrated on the boundaries of the length of the radiating elements.

6.2.3: Analysis of the Geometry of the Narrowband Planar Microstrip Antenna

Narrowband planar microstrip antennas can be fed using various feeding methods. The five most popular are microstrip line feed, coplanar waveguide feed, coaxial probe feed, proximity coupling feed and aperture coupling feed. For the undertaken

research work, the two feeding techniques used for the developed narrowband antennas are microstrip line feed and coplanar waveguide feed.

The procedure to be followed and the equations to be used for the design of the narrowband planar microstrip antennas of the shape given in Figure 6.2–1 were derived in [6-11] and are provided below.

A) Determining Size of Radiating Element

The equations (6.1)–(6.4) given below can be used to calculate the size of the transmission line placed in the last, i.e. the radiating element.

The size of the radiating element can be determined by the frequency of the dominant resonant mode. At this resonant mode, the antenna behaves like a half-wavelength transmission line. Equation (6.1) gives an expression for the calculation of the width, W_E , of the radiating element. Moreover, the expression shows that the width is a function of the half-wavelength and the relative permittivity of the medium of radiation.

$$W_E = \frac{c}{2f_c} \sqrt{\frac{2}{\epsilon_r + 1}} \quad (6.1)$$

Since the antenna behaves like a half-wavelength transmission line, the length of the entire radiating element is approximately $\lambda/2$ at the resonant frequency. However, within this length, the length of fringing fields on both sides of the radiating element are also included [6-11]. Therefore, in order to obtain the exact length of the radiating element, the length of these fields needs to be subtracted from the approximate half-wavelength. This is achieved in three steps. In the first, the effective dielectric constant, ϵ_{eff} , is calculated using (6.2). This is then used to calculate the length, Δl , of the fringing fields on one side of the radiating element using (6.3). Lastly, the length, L_E , of the radiating element is calculated by subtracting the length of the fringing fields on both sides from the half-wavelength of the radiating element; as given by (6.4).

$$\epsilon_{eff} = \left(\frac{\epsilon_r + 1}{2} \right) + \left[\left(\frac{\epsilon_r - 1}{2} \right) \times \left\{ \left(1 + \frac{12h}{W_E} \right)^{-\frac{1}{2}} \right\} \right] \quad (6.2)$$

$$\Delta l = (0.412h) \times \left(\frac{\varepsilon_{eff} + 0.3}{\varepsilon_{eff} - 0.258} \right) \times \left(\frac{\frac{W_E}{h} + 0.264}{\frac{W_E}{h} + 0.8} \right) \quad (6.3)$$

$$L_E = \frac{c}{2f_c \sqrt{\varepsilon_{eff}}} - 2\Delta l \quad (6.4)$$

B) Determining Size of Quarter-wavelength Transformer

The equations (6.5)–(6.11) given below can be used to calculate the size of the transmission line in the middle, i.e. the quarter-wavelength impedance transformer.

In order to calculate the width, W_{QW} , the following four steps are taken. Firstly, the input admittance, Y_{in} , of the line when looking into the quarter-wavelength impedance transformer from the transmission feed line is calculated. This is given by (6.5) or (6.6). Then, the obtained input admittance is converted to its corresponding input impedance, Z_{in} ; as given by (6.7). Thirdly, the actual impedance, Z_{QW} , of the quarter-wavelength transmission line — which is a function of the characteristic impedance — is then calculated using (6.8).

when $W_E < \lambda_0$, use (6.5):

$$Y_{in} = \frac{1}{45} \times \left[\left(\frac{1}{2} \sqrt{\frac{2}{\varepsilon_r + 1}} \right)^2 \right] \quad (6.5)$$

when $W_E > \lambda_0$, use (6.6):

$$Y_{in} = \frac{1}{60} \times \left[\left(\frac{1}{2} \sqrt{\frac{2}{\varepsilon_r + 1}} \right)^2 \right] \quad (6.6)$$

$$Z_{in} = \frac{1}{Y_{in}} \quad (6.7)$$

$$Z_{QW} = \sqrt{Z_{in} \times Z_0} \quad (6.8)$$

Fourthly and lastly, once the value of the impedance of the quarter-wavelength transformer is attained using (6.8), the equations from section 2.1 or a commercial

electronic design automation software program, such as Keysight Advanced Design System, can be used to convert the impedance to a value for its corresponding width.

In order to calculate the length of the quarter-wavelength transmission line, the following three steps are taken. Firstly, the operating wavelength, λ_c , of antenna is calculated using (6.9). Then, the guided wavelength, λ_g , is obtained using the values obtained for the operating wavelength. The expression to calculate the guided wavelength is given in (6.10). Lastly, the length, L_{QW} , of the transmission line is one-quarter of the guided wavelength and is given by (6.11).

$$\lambda_c = \frac{c}{f_c} \quad (6.9)$$

$$\lambda_g = \frac{\lambda_c}{\sqrt{\epsilon_{eff}}} \quad (6.10)$$

$$L_{QW} = \frac{\lambda_g}{4} \quad (6.11)$$

C) Determining Size of Transmission Feed Line

Since the antennas should have a characteristic impedance according to the given specifications of the system, the width of a microstrip line feed and a CPW feed can be calculated from the equations given in section 2.1. The length of a microstrip line feed does not affect the resonant frequency of antennas. Hence, the value for the length can be chosen which is just enough to provide an adequate connection required for an SMA connector.

6.2.4 Realised Structure of the Narrowband Planar Microstrip Antenna

A) Initial and Final Parameters

The dielectric substrate used for the antenna is a Rogers RT5880 substrate of a thickness of 0.79 mm, having a dielectric permittivity of $\epsilon_r = 2.2$ and a dielectric loss factor of $\tan \delta = 0.0009$. The antenna is modelled and simulated using the commercial full-wave electromagnetic simulation software programs Sonnet and CST Microwave Studio.

By using the design method and (6.1)–(6.11) given above, the values of the dimension parameters of the antenna were determined for a sample frequency of 5.8 GHz and a sample characteristic impedance of 50 Ω . The calculated values obtained using the design equations are given in Table 6.2–1 and the optimised values obtained using full-wave electromagnetic analysis are given in Table 6.2–2.

Table 6.2–1: Initial values of the dimension parameters of the antenna.

Parameter	Value (mm)	Parameter	Value (mm)
W_T	25	W_{QW}	0.46
L_T	50	L_{QW}	12.31
W_F	2.2	W_E	20.45
L_F	10	L_E	23.55

Table 6.2–2: Final values of the dimension parameters of the antenna.

Parameter	Value (mm)	Parameter	Value (mm)
W_T	25	W_{QW}	0.6
L_T	50	L_{QW}	8.9
W_F	2.2	W_E	20.4
L_F	10	L_E	16.7

B) Fabrication of Final Layout

The antenna from Figure 6.2–1 using the final values from Table 6.2–2 is designed on a Rogers RT5880 substrate of a thickness of 0.795 mm, having a dielectric permittivity of $\epsilon_r = 2.2$ and a dielectric loss factor of $\tan \delta = 0.0009$. It is modelled and simulated using the commercial full-wave electromagnetic simulation software program Sonnet. Photographs of the top side and the bottom side of the fabricated antenna are shown in Figure 6.2–3.

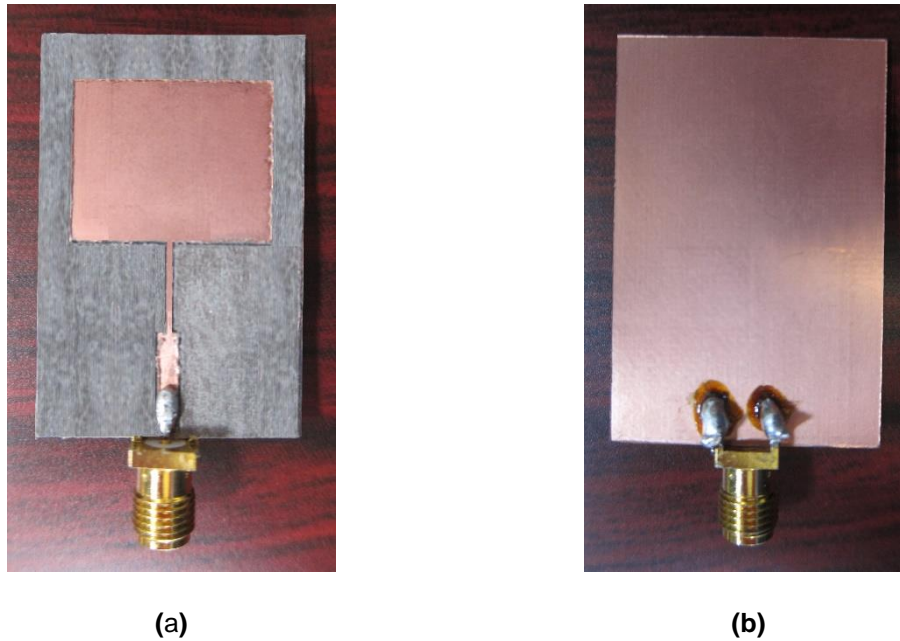


Figure 6.2-3: Photographs of (a) the top side and (b) the bottom side of the fabricated antenna.

6.2.5 Results of the Narrowband Planar Microstrip Antenna

A) Return Loss

The antenna in Figure 6.2-1 was simulated twice: first, using the initial/calculated values from Table 6.2-1 and second, using the final/optimised values from Table 6.2-2. The fabricated prototype of the antenna was measured using an Agilent E8361A PNA Network Analyser. The obtained measured results, alongside the two simulated results, are given in Figure 6.2-4.

Although both simulated results show the return loss of the antenna to be sharp and more than 10 dB, there are considerable differences present between them. The response from the calculated values shows the resonant frequency of the antenna to be at 4.17 GHz. On the other hand, using the optimised values, the antenna resonates at 5.79 GHz. Furthermore, there is a substantial difference between the magnitudes of the return loss at both frequencies too: from the calculated response, it is 12.5 dB and from the optimised response, it is 43.39 dB.

The measured and the simulated results using the optimised values are in a reasonable agreement with each other. The measured response shows the resonant frequency of the antenna has slightly shifted and is present at 5.85 GHz. In addition, the measured return loss at the resonant frequency has considerably decreased and is present at 21.88 dB.

The slight shift in the frequency of the resonant mode between the measured and the simulated results could be to fabrication discrepancies; specifically the length of the radiating element of the fabricated prototype. The lower measured return loss at the resonant frequency could be due to the losses experienced because of the SMA connector which was not modelled in the simulation and/or due to the metallisation and substrate losses.

More and detailed variances between the three results are summarised in Table 6.2–3.

The differences between the calculated and the optimised results show that while the design procedure and equations given in the previous section can be used to obtain initial values for the dimension parameters of the narrowband planar microstrip antennas, these values will always need to be optimised further using full-wave electromagnetic analysis in order to obtain a better response.

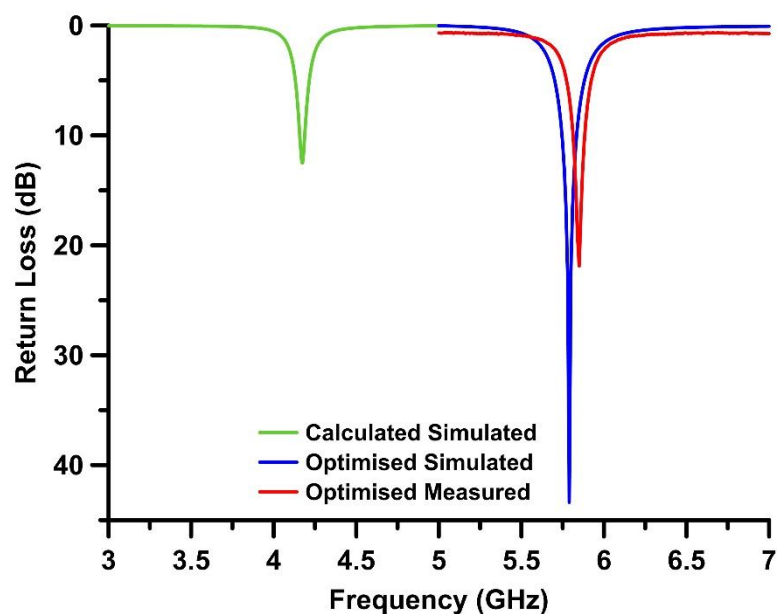


Figure 6.2–4: Return loss of the antenna.

Table 6.2–3: Summary of the resulting return loss of the antenna using the initial/calculated values and the final/optimised values.

Response Type	f_c (GHz)	Return Loss (GHz)	Passband (GHz)	ABW (GHz)	FBW (%)
Calculated Simulated	4.17	12.5	4.155–4.185	0.03	0.72
Optimised Simulated	5.79	43.39	5.745–5.835	0.09	1.55
Optimised Measured	5.85	21.88	5.813–5.883	0.07	1.20

B) Parametric Study of Various Parameters

With the aim of gaining a better understanding of how the various parameters of the presented narrowband planar microstrip antenna affect its return loss, parametric studies were undertaken. These included studies of the width of the radiating element, the length of the radiating element and the width of the quarter-wavelength transformer.

In the first instance, the width, W_E , of the radiating element was varied. The resulting effects are shown in Figure 6.2–5 (a).

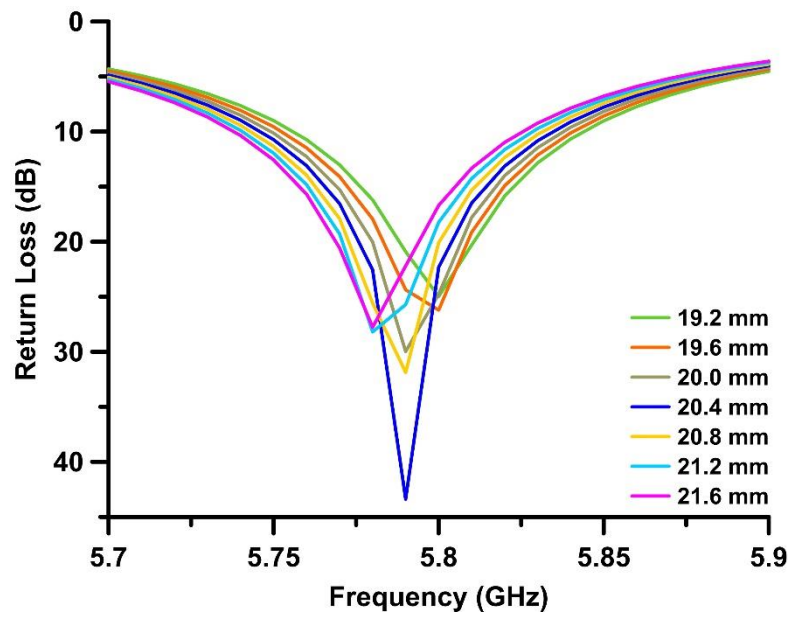
The passband matching was found to be very sensitive to the value of the width, i.e. as the width of the radiating element changes, the return loss at the resonant frequency also changes. The said change is a reduction in the return loss when the optimal value of the width is changed. This is evident from the six curves when the width is reduced from the optimal value of 20.4 mm to 20 mm, 19.6 mm and 19.2 mm and when it is increased to 20.8 mm, 21.2 mm and 21.6 mm. As can be seen from the given results, the respective return loss of each curve at the resonant frequency is always less than the response obtained when using the optimal value of 20.4 mm. This is because the width of the radiating element is an impedance and must be of a specific value in order to match the stepped impedance matching of the transmission lines which make up the antenna. Furthermore, when the width of the radiating element is varied, slight downwards shifts in the resonant frequency are also observed. As the width is increased from 19.2 mm to 21.6 mm, the resonant frequency shifts downwards by a margin of 20 MHz.

In the second case, the effects of changing the length, L_E , of the radiating element were observed. The results are shown in Figure 6.2–5 (b).

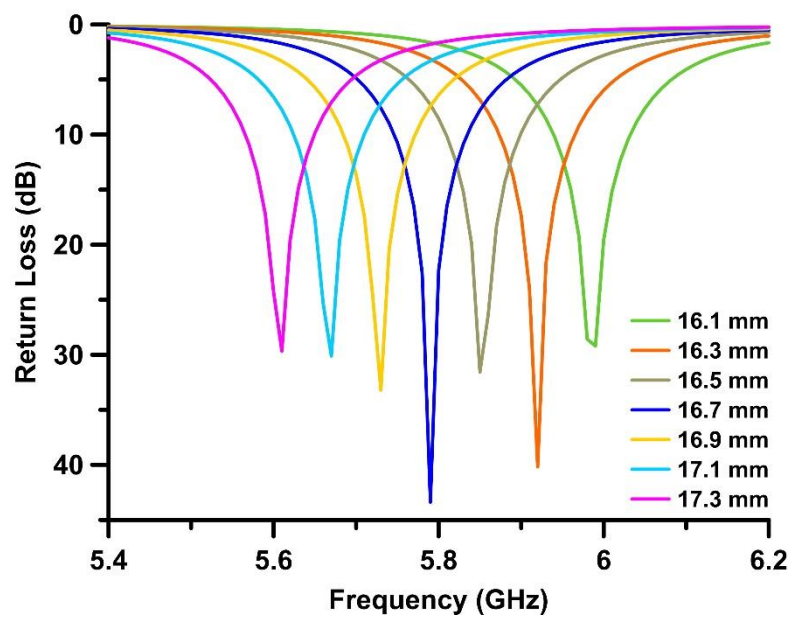
The results show that the position of the resonant frequency is significantly affected because of a change in the length of the radiating element. The antenna was simulated with seven values for the length of the radiating element. The values used are in the range of 16.1 mm to 17.3 mm in increments of 0.2 mm. Even a change of just ± 0.2 mm considerably affected the resonant frequency. An increase in the length reduced the resonant frequency and a decrease in the length increased the resonant frequency. The first scenario is shown from the three curves when the length of the radiating element is reduced from the optimal value of 16.7 mm to 16.5 mm, 16.3 mm and 16.1 mm. For these length, the resonant frequency of the antenna shifts to 5.85 GHz, 5.92 GHz and 5.99 GHz respectively. Similarly, when the length is increased from the optimal value of 16.7 mm to 16.9 mm, 17.1 mm and 17.3 mm, the antenna resonates at 5.73 GHz, 5.67 GHz and 5.61 GHz respectively. Such results have been obtained because the length of the radiating element is a direct function of the resonant frequency; as was expressed in (6.4). Hence, by tuning the length of the radiating element, a desired resonant frequency can be achieved. Furthermore, although the return loss at each of the six studied values of the length is more than 10 dB, it is, nevertheless, much less than the return loss obtained using the optimal value of 16.7 mm. This implies that the width of the radiating element will also have to be optimised for each change in the length of the radiating element.

In the third, and last, case, the effects of changing the width, W_{qw} , of the quarter-wavelength transformer were observed. The results are shown in Figure 6.2–5 (c). Since the quarter-wavelength transmission line is an impedance transformer, which provides impedance matching between the transmission feed line and the radiating element of the antenna, its width significantly impacts the response at the resonant frequency of the antenna. In order to show this, the antenna was simulated with seven different values for the width of the quarter-wavelength transformer. The seven values were 0.3 mm to 0.9 mm in increments of 0.1 mm. When the value of the width was decreased or increased even slightly from the optimal value of 0.6 mm, the return loss at the resonant frequency significantly dropped. At 0.5 mm and 0.7 mm, i.e. near the optimal value, although the return loss is around 22.5 dB, the response is not sharp. At the farther values of 0.3 mm, 0.4 mm, 0.8 mm and 0.9 mm, the return loss becomes less than 17.5 dB and even more flatter. Moreover, while a change in the return loss was clearly seen due to varying the width of the quarter-wavelength transformer, almost no change was observed in the position of the resonant frequency.

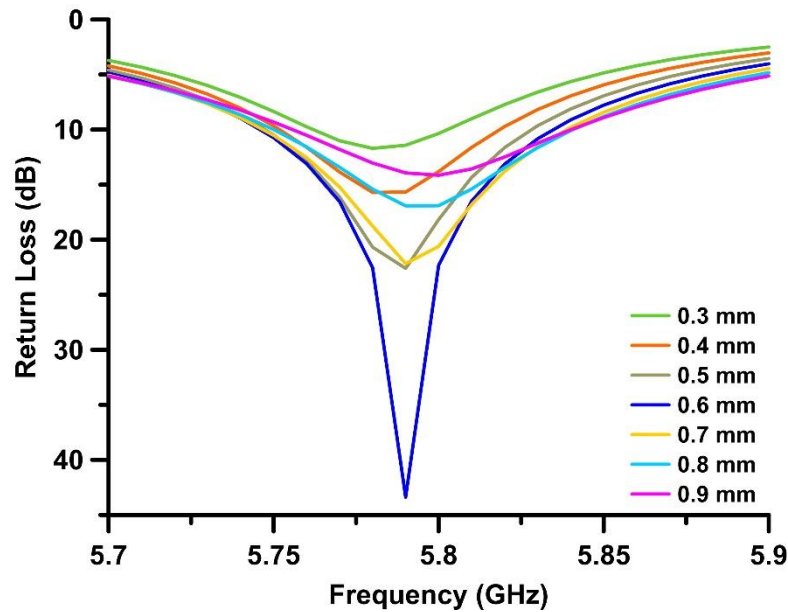
Amongst the numerous values studied for the three aforementioned parameters of the antenna, the best and the optimal value for the width, W_E , of the radiating element is 20.4 mm, for the length, L_E , of the radiating element is 16.7 mm and for the width, W_{QWT} , of the quarter-wavelength transformer is 0.6 mm. These value were obtained from multiple iterations using the full-wave electromagnetic software program.



(a)



(b)



(c)

Figure 6.2–5: Parametric study of the effects on the return loss of the antenna by varying (a) the width of the radiating element, (b) the length of the radiating element and (c) the width of the quarter-wavelength transmission line.

C) Current Density

The current density of the antenna was simulated at the resonant frequency of 5.79 GHz. The obtained result is given in Figure 6.2–6.

It can be seen from the result that when the antenna is resonating, the current is densely populated in the middle and along the length of the radiating element. This is true as per stated earlier in the operating mechanism of narrowband planar microstrip antennas, i.e. that the currents in narrowband planar microstrip antennas are mostly concentrated in the middle of the antenna elements.

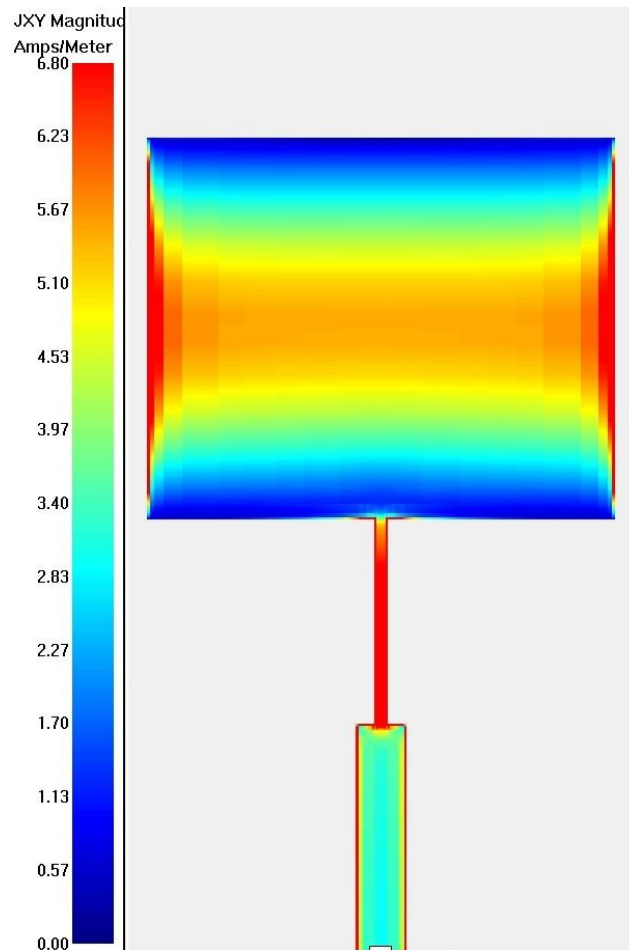


Figure 6.2-6: Current density of the antenna at 5.79 GHz.

D) Radiation Patterns

The simulated radiation patterns of the antenna at 5.79 GHz in the E-plane and the H-plane are given in Figure 6.2-7. The radiation patterns have been calibrated to the gain of the antenna.

The antenna is a directional antenna as shown by the E-plane. In that plane, a major radiation lobe is shown at the top of the antenna. Although not shown here, there will be a minor radiation lobe and side radiation lobes on the bottom side of the antenna. On the other hand, the H-plane exhibits an omnidirectional radiation pattern; inferring that the antenna radiates in all directions in that plane.

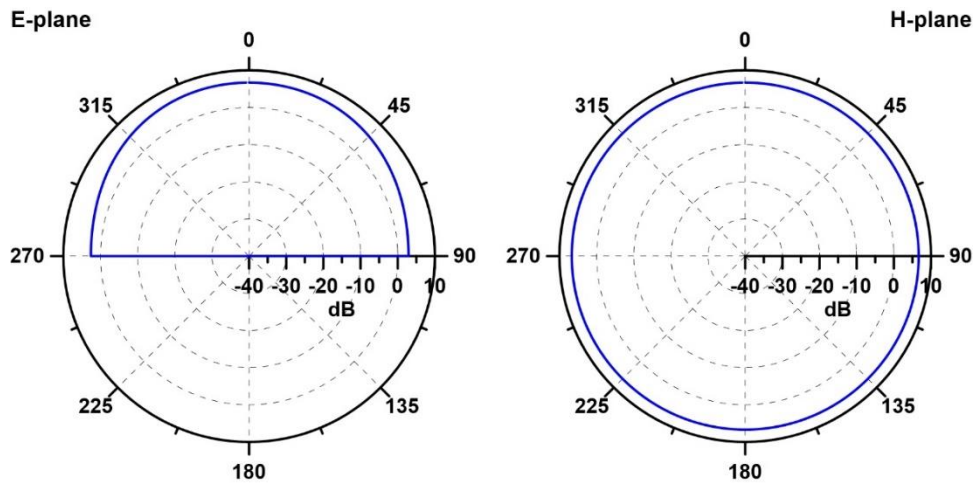


Figure 6.2–7: Radiation patterns of the antenna at 5.8 GHz.

E) Gain

The simulated gain of the antenna was obtained between a frequency range of 5 GHz and 7 GHz. The acquired result is given in Figure 6.2–8.

At the resonant frequency of 5.79 GHz, the gain of the antenna is about 6.68 dBi.

The obtained value is typical of narrowband planar microstrip antennas.

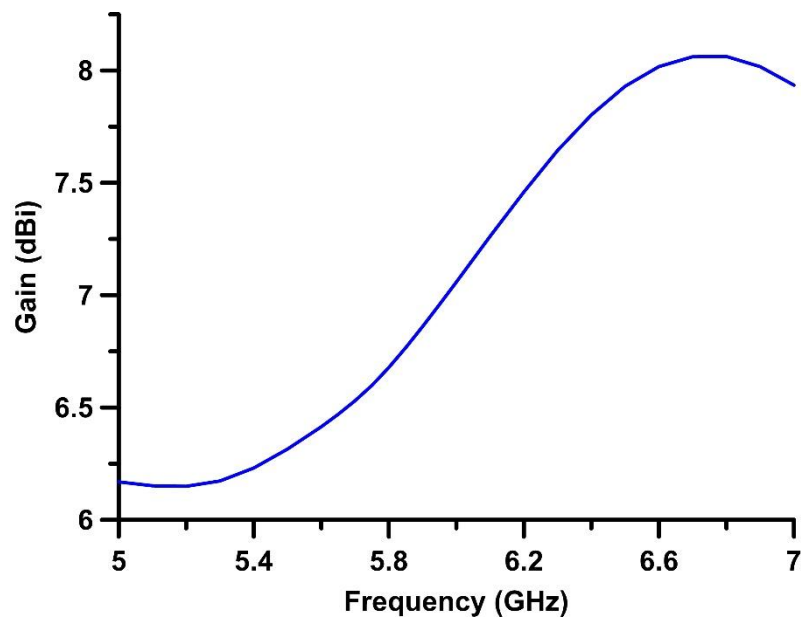


Figure 6.2–8: Gain of the antenna.

F) Efficiency

The efficiency of the antenna was simulated and the obtained result is given in Figure 6.2–9.

The average efficiency across the passband is at least 80 %. The efficiency peaks at the resonant frequency of 5.79 GHz to 96.18 %. The exceptionally high value is due to the presented result being a simulation which excludes most metallisation and dielectric losses and actual fabrication discrepancies.

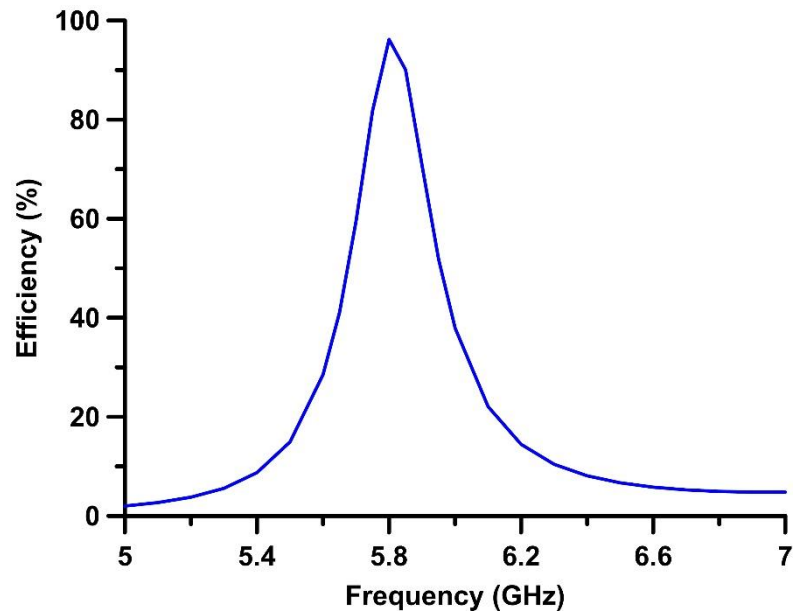


Figure 6.2–9: Efficiency of the antenna.

6.3: Design of a Filtenna Array for Dual-band WLAN Applications

6.3.1: Specifications

This section presents a narrowband planar microstrip filtenna array based on the specifications given in Table 6.3–1. The specifications require a dual-element planar microstrip filtenna array operating at the dual IEEE 802.11 WLAN bands of 2.4 GHz and 5.8 GHz. The filtenna array is required to have a microstrip-based feeding method; where the characteristic impedance of the feed network and the system should be 50Ω . The specifications further ask that the filtenna array should be fabricated via PCB technology. Furthermore, the filtenna array should be able to suppress any interfering frequency harmonics and noise present near and between the two passbands.

Table 6.3–1: Required specifications of the filtenna array.

Parameter	Description of Parameter	Value
Filtenna	Type of filtenna	Array Element
Configuration	Arrangement of array elements	1×2
Technology	Fabrication technology	PCB
Feed	Feeding method	Microstrip
Z_0	Characteristic impedance of system	50Ω
n_{PB}	Number of passbands	Dual
f_{1C}	Resonant frequency of first element	2.4 GHz
f_{2C}	Resonant frequency of second element	5.8 GHz

6.3.2: Realised Structure and Final Parameters

A) Final Layout

The geometry of the initial antenna array is given in Figure 6.3–1; with the values of its dimension parameters given in Table 6.3–2. In addition, for a better understanding, the equivalent transmission line circuit model of the antenna array is

presented in Figure 6.3–2; with the impedances and the electrical lengths of the respective transmission lines, before optimisation, given in Table 6.3–3.

The antenna array is inductively coupled to the source. It is stimulated via a single input port. The input port is connected to the transmission feed line, A , of the antenna array; where the characteristic impedance, Z_0 , of the transmission feed line is 50Ω . The corresponding value of the width, W_F , of the transmission feed line is calculated using the equations from section 2.1. Since the length of the transmission feed line does not affect the operation of the array, the value of the length, L_F , is chosen such that it is just sufficient to connect an SMA connector.

The power from the input port and the transmission feed line is then split into two branches through a transmission line (a combination of lines B and C) of an impedance of 76.71Ω and a length of $2\lambda_g$; where λ_g is the guided wavelength at 5.8 GHz. The top branch of the array is for the 2.4 GHz radiating element and the bottom branch is for the 5.8 GHz radiating element.

At both ends of the power-splitting transmission line, a transmission line extends the overall length of each branch. In the 2.4 GHz branch, this is line D and has a length of $1\lambda_g/8$; where λ_g is the guided wavelength at 2.4 GHz. Whereas, in the 5.8 GHz branch, this is line G and has a length of $5\lambda_g/8$; where λ_g is the guided wavelength at 5.8 GHz. In both cases, the impedance of the lines i.e. D and G , is 50Ω .

Thereafter, both branches carry on forward with quarter-wavelength transformers; with each having an impedance of 76.71Ω . In the top and the bottom branches, these are line E and line H respectively and are quarter-wavelength, $\lambda_g/4$, long each; where λ_g is the guided wavelength at 2.4 GHz and 5.8 GHz respectively.

Lastly, both branches end in their respective radiating elements (line F and line I). The elements are designed using (6.1)–(6.11) to radiate at the frequencies of 2.4 GHz and 5.8 GHz. Before optimisation, each element would have a length of half-wavelength, $\lambda_g/2$; where λ_g is the guided wavelength at each element's respective resonant frequency. The two elements are located from each other at a distance, G_1 , of 43 mm, which is equivalent to $1\lambda_g$; where λ_g is the guided wavelength at 2.4 GHz.

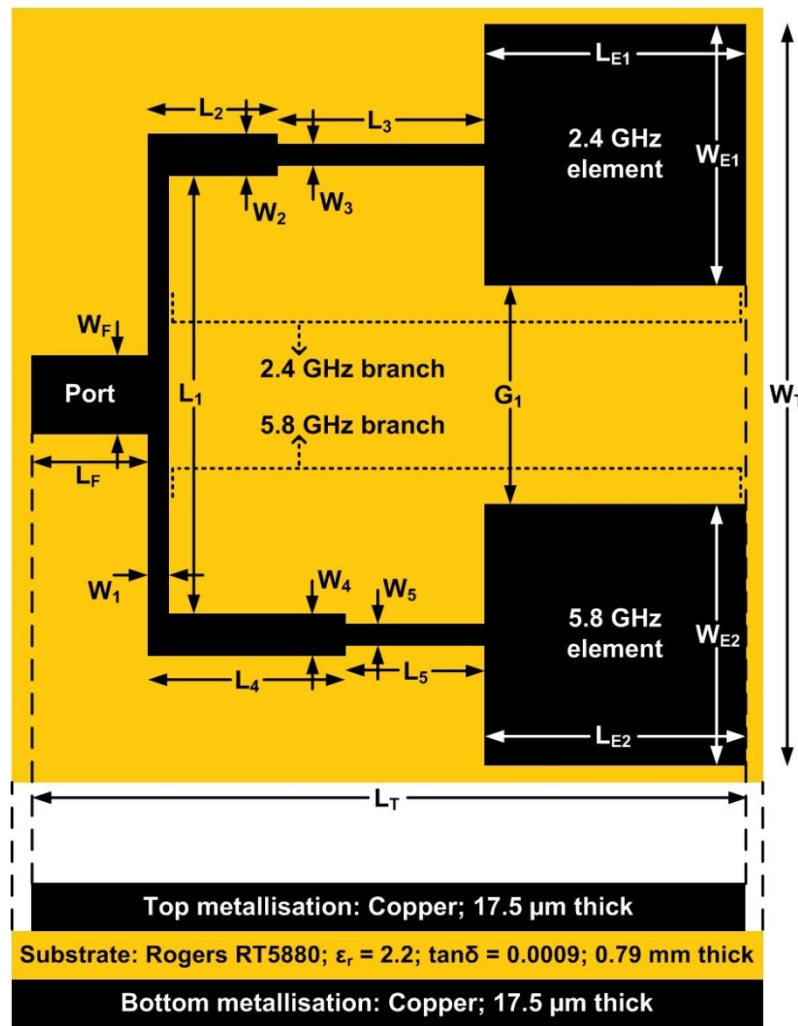


Figure 6.3-1: Geometry of the antenna array.

Table 6.3-2: Values of the dimension parameters of the antenna array.

Parameter	Value (mm)	Parameter	Value (mm)
W_T	112.9	W_4	2.2
L_T	84.3	L_4	23.6
W_F	2.2	W_5	1.2
L_F	3.5	L_5	8.9
W_1	1.2	W_{E1}	49.4
L_1	75.8	L_{E1}	41.8
W_2	2.2	W_{E2}	20.5
L_2	11.2	L_{E1}	17
W_3	1.2	G_1	43
L_3	21.3		

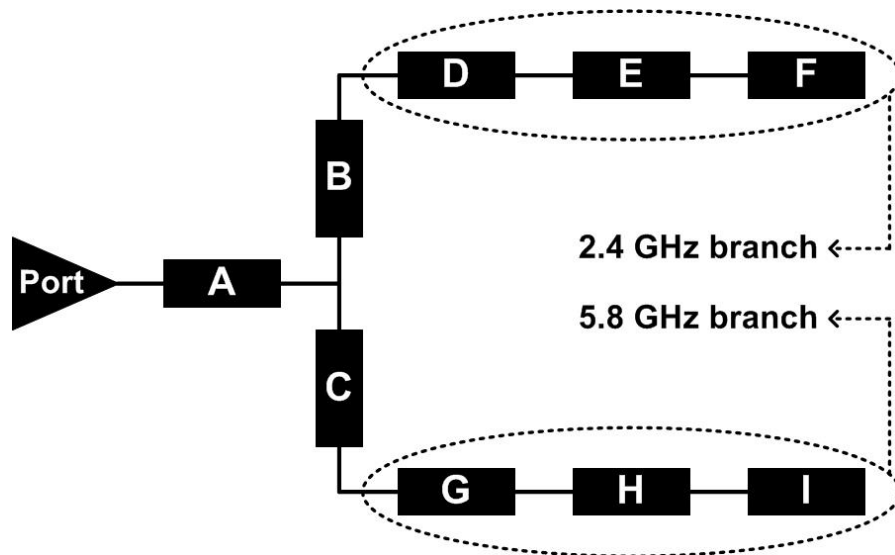


Figure 6.3–2: Equivalent transmission line circuit model of the antenna array.

Table 6.3–3: Values of the transmission line parameters of the antenna array.

Transmission Line	Impedance (Ω)	Electric Length (degrees)
A	50	n/a
B	76.71	λ_g at 5.8 GHz
C	76.71	λ_g at 5.8 GHz
D	50	$1\lambda_g/8$ at 2.4 GHz
E	76.71	$\lambda_g/4$ at 2.4 GHz
F	3.66	$\lambda_g/2$ at 2.4 GHz
G	50	$5\lambda_g/8$ at 5.8 GHz
H	76.71	$\lambda_g/4$ at 5.8 GHz
I	8.87	$\lambda_g/2$ at 5.8 GHz

For the purpose of suppressing any frequency harmonics and noise near and between the two passbands, bandpass filters can be integrated within the designed antenna array. Bandpass filters — either two filters with a single passband each or one filter with a dual passband — would only let the two desired frequencies of operation to pass through them and reject all others.

The selected filters are pseudo-interdigital bandpass filters and their detailed design is based on the procedure given originally in [6-12]. Since there are two passbands, two filters — one for each antenna element — are designed for integration. The geometry of both filters is the same and is illustrated in Figure 6.3–3. The centre frequency of each filter is the resonant frequency of each antenna element, i.e.

2.4 GHz and 5.8 GHz. The designed filters are of a second-order each. The folded interdigital resonators of each filter are half-wavelength, $\lambda_g/2$, long; where $\lambda_g/2$ is the guided wavelength at the respective centre frequency of each filter. The total length, L_R , of each interdigital resonator can be calculated using (6.12). The obtained values of the dimension parameters of the 2.4 GHz filter and the 5.8 GHz filter after their final design are given in Table 6.3–4 and in Table 6.3–5 respectively.

$$L_R = L_7 + L_8 + L_9 - 0.5W_7 - 0.5W_8 + W_9 \tag{6.12}$$

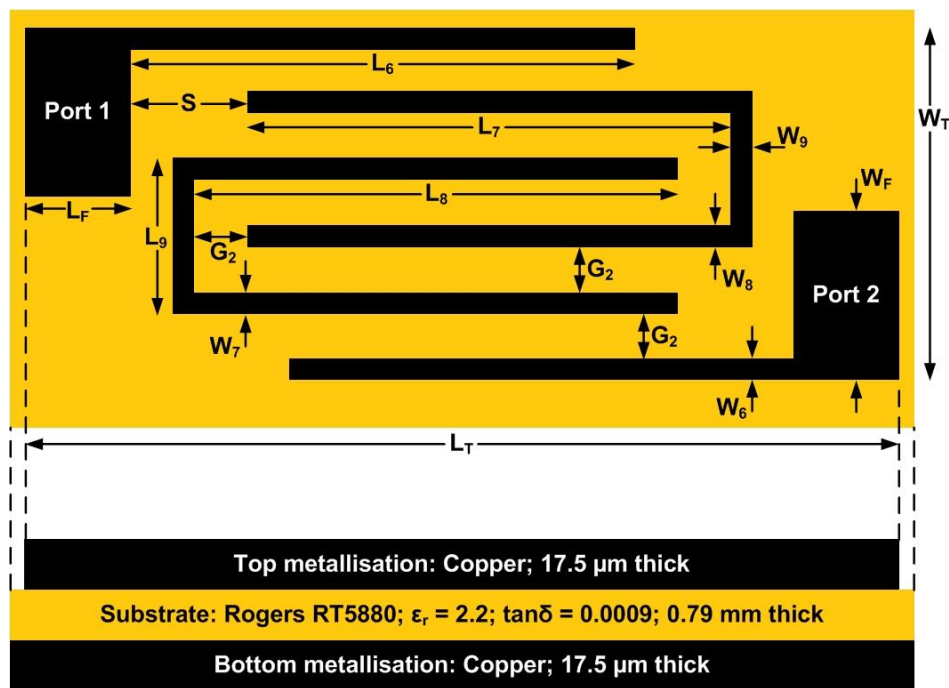


Figure 6.3–3: Geometry of the filters.

Table 6.3–4: Values of the dimension parameters of the 2.4 GHz filter.

Parameter	Value (mm)	Parameter	Value (mm)
W_T	3.3	W_8	0.3
L_T	32.3	L_8	23.8
W_F	2.2	W_9	0.3
L_F	3.5	L_9	1.5
W_6	0.3	G_2	0.3
L_6	23.8	G_3	0.3
W_7	0.3	S	0.9
L_7	23.8		

Table 6.3–5: Values of the dimension parameters of the 5.8 GHz filter.

Parameter	Value (mm)	Parameter	Value (mm)
W_T	8.2	W_8	0.6
L_T	15.1	L_8	8.3
W_F	2.2	W_9	0.6
L_F	3.5	L_9	3.4
W_6	0.6	G_2	0.8
L_6	8.1	G_3	0.3
W_7	0.6	S	0.3
L_7	8.3		

The final layout of the proposed filtenna array which meets the specifications given in Table 6.3–1 is illustrated in Figure 6.3–4; with the values of its dimension parameters given in Table 6.3–6.

The arrangement of the transmission lines which make up the filtenna array is mostly the same as the antenna array. The only major difference is the integration of the two designed pseudo-interdigital bandpass filters. Minor differences include changes in some of the dimensions of the array. These have been reflected in the provided table. Furthermore, the size, G_1 , of the gap between the two antenna elements has been decreased to 28.3 mm, which is equivalent to $0.33\lambda_g$; where λ_g is the guided wavelength at 2.4 GHz. This has been done so as to reduce the size of the filtenna array.

The interdigital resonators of each filter are integrated with their respective branch of the array, i.e. the 2.4 GHz resonators with the 2.4 GHz branch and the 5.8 GHz resonators with the 5.8 GHz branch. The integration of both filters is done in such a way that the power-splitting transmission line now acts as the transmission feed line for the filters. Additionally, the outer fingers of the resonators of both filters are now directly coupled with the transmission feed lines of the two antenna elements.

Such a design would result in taking all the frequencies as an input for the port of the filtenna array. These would then travel in the power-splitting transmission line (now a transmission feed line for the filters). Thereafter, upon reaching the bandpass filters, only the respective bandpass frequency of the filter would be allowed to pass through each filter and all the other frequencies would be rejected. Each “allowed” frequency is the same as the respective resonant frequency of the

antenna elements. Hence, each element will then radiate at its respective frequency of operation.

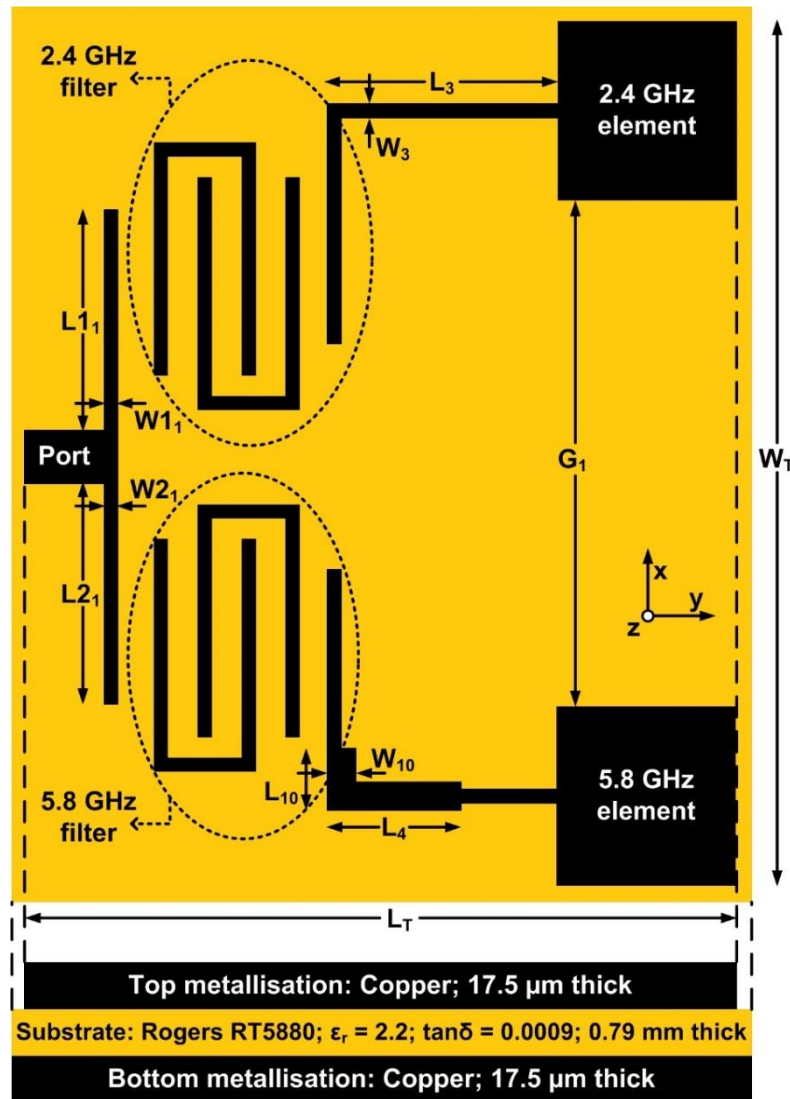


Figure 6.3-4: Geometry of the filtenna array.

Table 6.3-6: Values of the dimension parameters of the filtenna array.

Parameter	Value (mm)	Parameter	Value (mm)
W_T	98.2	W_3	1.2
L_T	73.1	L_3	21.3
W_{1_1}	0.3	L_4	24.6
L_{1_1}	24.4	W_{10}	2.2
W_{2_1}	0.6	L_{10}	28.2
L_{2_1}	8.7	G_1	28.3

B) Fabrication of Final Layout

The final layout of the filtenna array is designed on a Rogers RT5880 substrate of a thickness of 0.79 mm, having a dielectric permittivity of $\epsilon_r = 2.2$ and a dielectric loss factor of $\tan \delta = 0.0009$. It is modelled and simulated using the commercial full-wave electromagnetic simulation software program Sonnet. A photograph of the fabricated PCB filtenna array is shown in Figure 6.3–5.

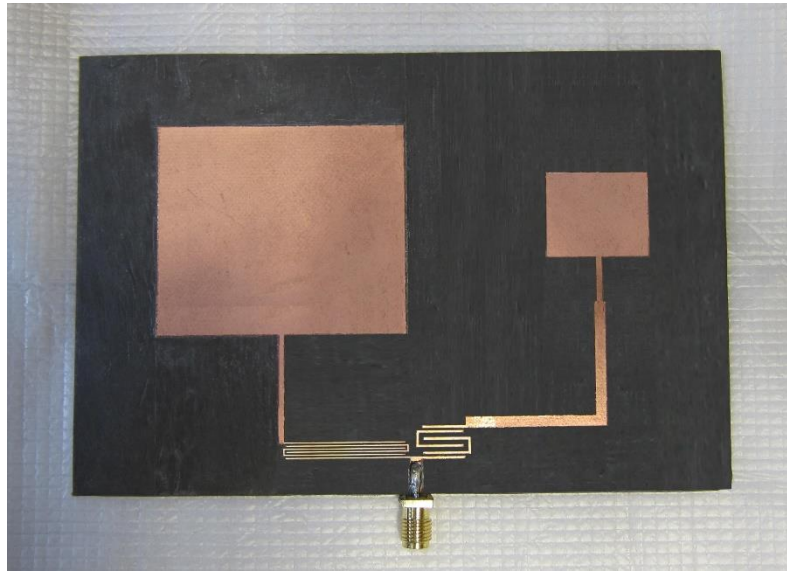


Figure 6.3–5: Photograph of the fabricated PCB filtenna array.

6.3.3: Results

A) Return Loss of Antenna Array

The standalone antenna array from Figure 6.3–1 was simulated using the values provided in Table 6.3–2. The ensuing return loss is presented in Figure 6.3–6.

The simulated frequency range is 1 GHz to 7 GHz. As can be seen, the array fundamentally resonates at the two WLAN bands of 2.4 GHz and 5.8 GHz. The attained return loss at each of these two points is almost 30 dB. However, the result also shows that multiple frequency harmonics and noise are present at various other frequencies. These interfere with the two main signals by causing distortion and loss of sensitivity.

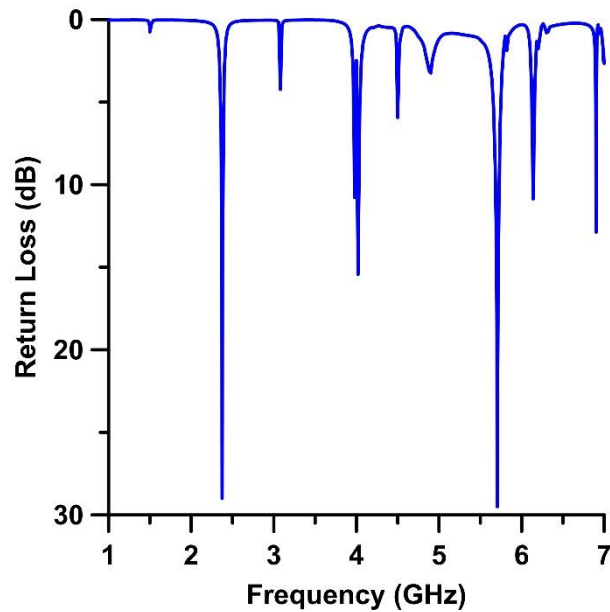


Figure 6.3-6: Return loss of the antenna array.

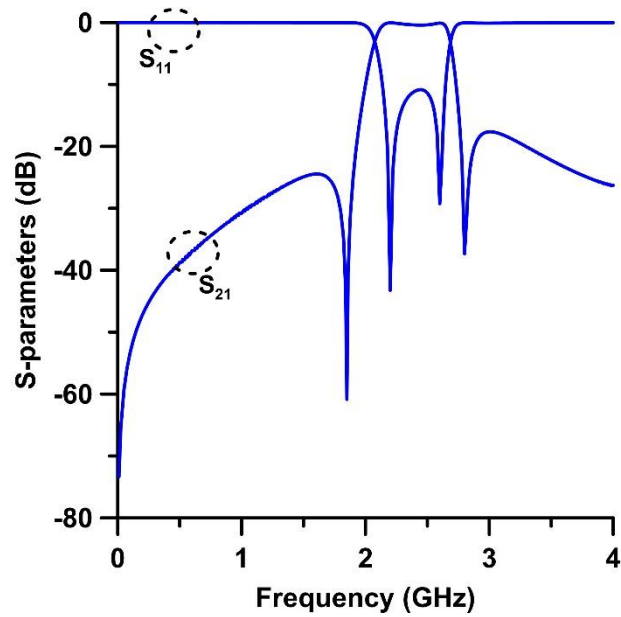
B) S-parameters of Filters

The bandpass filter from Figure 6.3-3 was electromagnetically simulated. For the 2.4 GHz filter, the values provided in Table 6.3-4 were used and for the 5.8 GHz filter, the values from Table 6.3-5 were used.

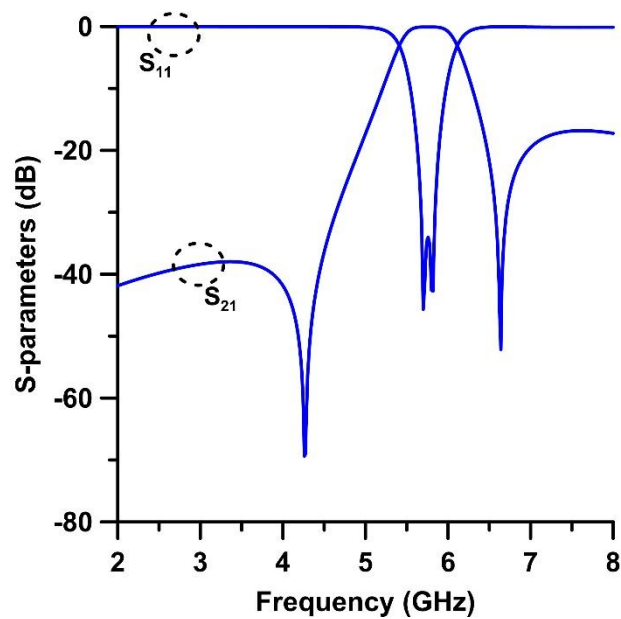
The obtained S-parameters of the 2.4 GHz bandpass filter are shown in Figure 6.3-7 (a). The results show the 3 dB passband of the filter to be present from about 2.08 GHz to 2.69 GHz. The centre frequency of the filter is shifted slightly downwards to 2.37 GHz. From these values, the obtained fractional bandwidth of the filter is 25.8 %. The insertion loss at the centre frequency is about 0.1 dB. The return loss is more than 13 dB across the passband.

The obtained S-parameters of the 5.8 GHz bandpass filter are given in Figure 6.3-7 (b). The results show the 3 dB passband of the filter to be present from about 5.51 GHz to 6.11 GHz. The centre frequency of the filter is obtained at exactly 5.8 GHz. The insertion loss of the filter at this point is about 0.1 dB. From these values, the calculated fractional bandwidth of the filter is about 10.3 %.

In the results of both filters, two transmission zeroes appear at frequencies below and above the passband. These transmission zeroes improve the selectivity of the filters.



(a)



(b)

Figure 6.3–7: S-parameters of (a) the 2.4 GHz filter and (b) the 5.8 GHz filter.

C) Return Loss of Filtenna Array

The final filtenna array from Figure 6.3–4 was simulated and its fabricated prototype from Figure 6.3–5 was measured using an Agilent E8361A PNA Network Analyser. The resulting return losses obtained from the simulation and the measurement are shown in Figure 6.3–8.

An excellent match has been obtained between the two results. There is a negligible shift in the position of the two resonant frequencies. Both results show the filtenna array to exhibit dual resonant frequencies of 2.4 GHz and 5.8 GHz. In the simulated result, the return loss at the two frequencies is about 23 dB. However, the measured return loss is about 35 dB at 2.4 GHz and almost 30 dB at 5.8 GHz. Furthermore, both results show a major suppression of the frequency harmonics and noise. However, the harmonic at 4.5 GHz has not been fully rejected. This could be rectified by shifting forwards the first transmission zero of the 5.8 GHz bandpass filter.

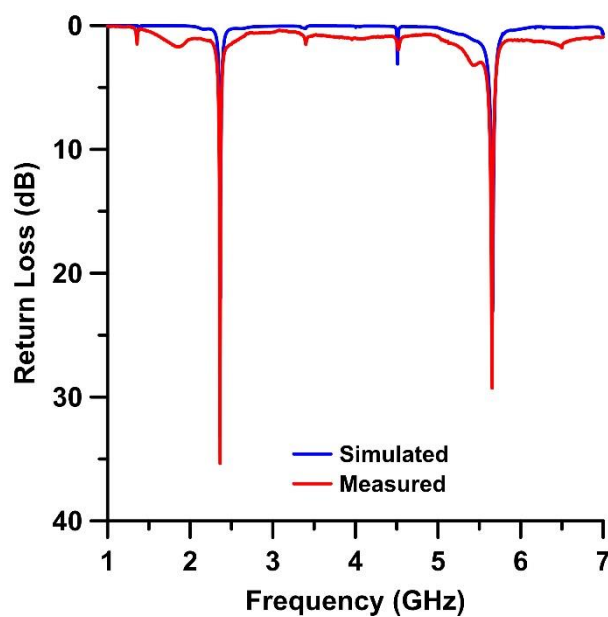


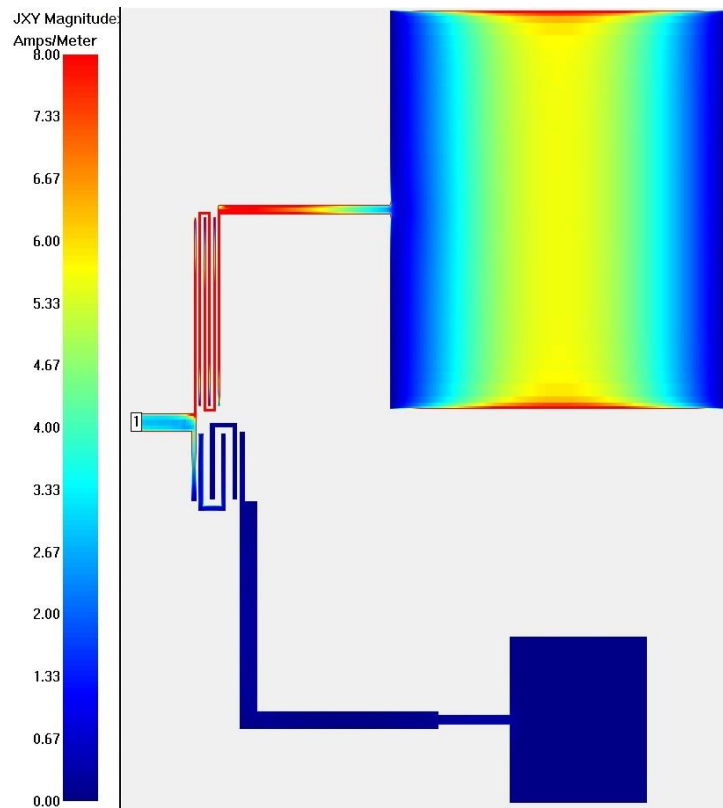
Figure 6.3–8: Return loss of the filtenna array.

D) Current Densities of Filtenna Array

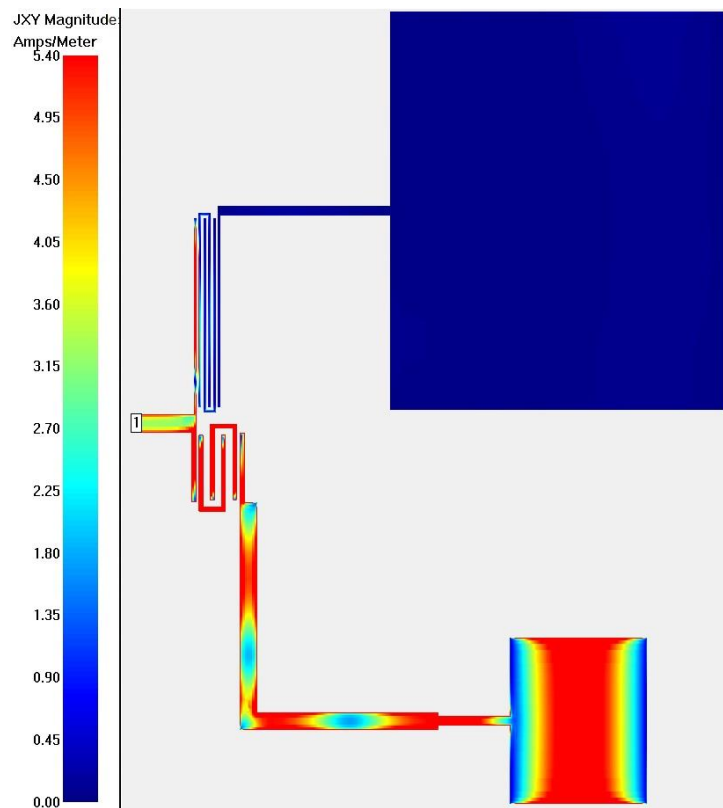
The current density of the filtenna array was simulated at the dual resonant frequencies of 2.4 GHz and 5.8 GHz. The obtained results are given in Figure 6.3–9.

It can be seen from Figure 6.3–9 (a) that at 2.4 GHz, the current is present in only the top branch of the filtenna array. Moreover, at the resonant frequency, the current is densely present in the middle and the sides of the 2.4 GHz antenna element.

Similarly, at 5.8 GHz, as can be seen in Figure 6.3–9 (b), the flow of current is solely in the bottom 5.8 GHz branch of the filtenna array. Furthermore, the current can be seen to be densely populated in the middle and along the edges of the 5.8 GHz antenna element.



(a)



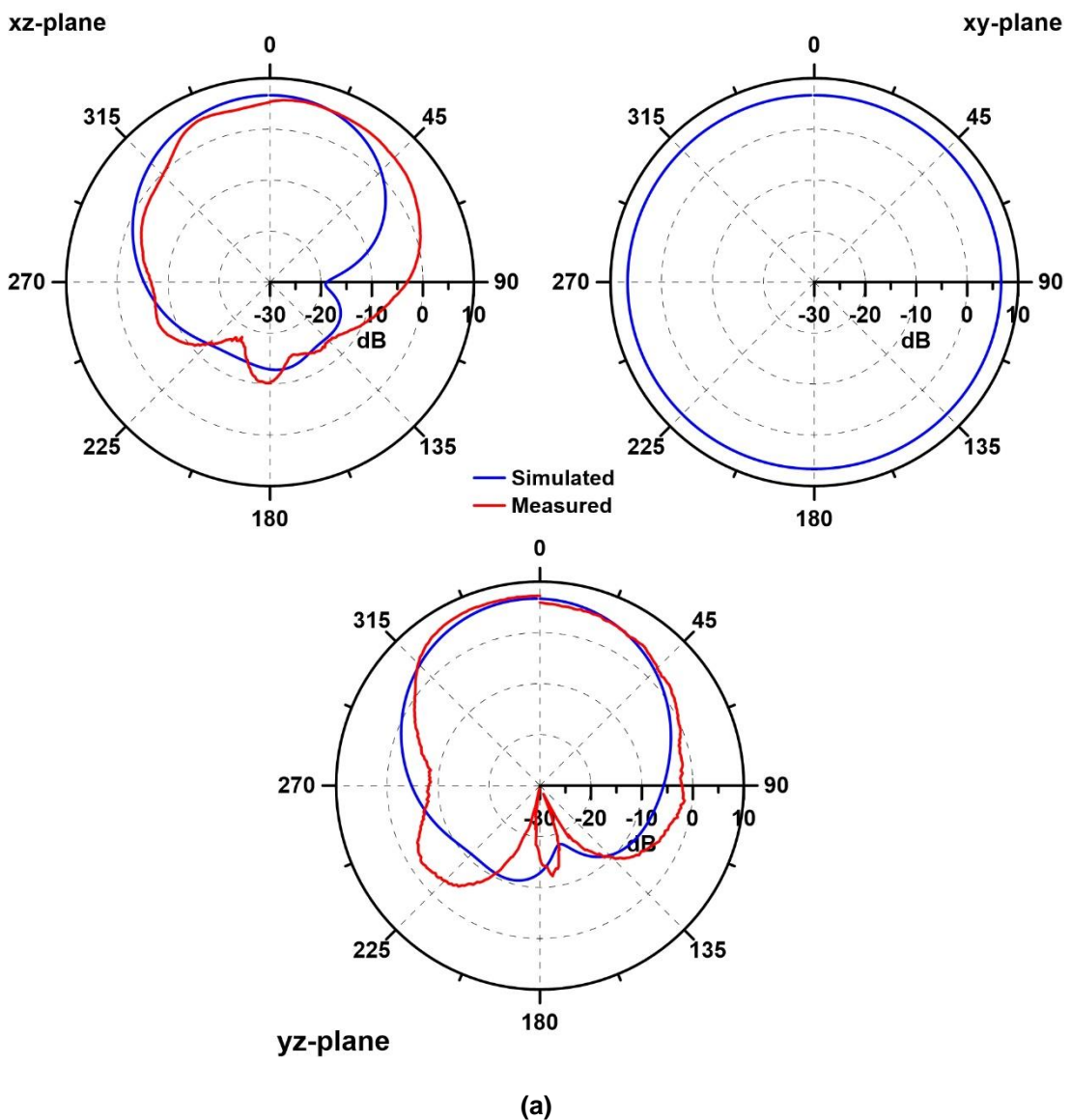
(b)

Figure 6.3–9: Current density of the filtenna array at (a) 2.4 GHz and (b) 5.8 GHz.

E) Radiation Patterns of Filtenna Array

The radiation patterns of the filtenna array were simulated and measured in its three planes at the two resonant frequencies of 2.4 GHz and 5.8 GHz. The radiation patterns have been calibrated to the gain of the filtenna array and the simulated and measured results have been attuned to obtain the best possible match with each other. The results are given in Figure 6.3–10.

The obtained results at both frequencies in the xz-plane and the yz-plane show a major radiation lobe present at the top of the filtenna array. At the same time, there are minor and side radiation lobes present on the bottom side of the filtenna array. Moreover, in the xy-plane, the filtenna array can be seen to have omnidirectional patterns and, hence, radiating in all directions in that plane at both frequencies.



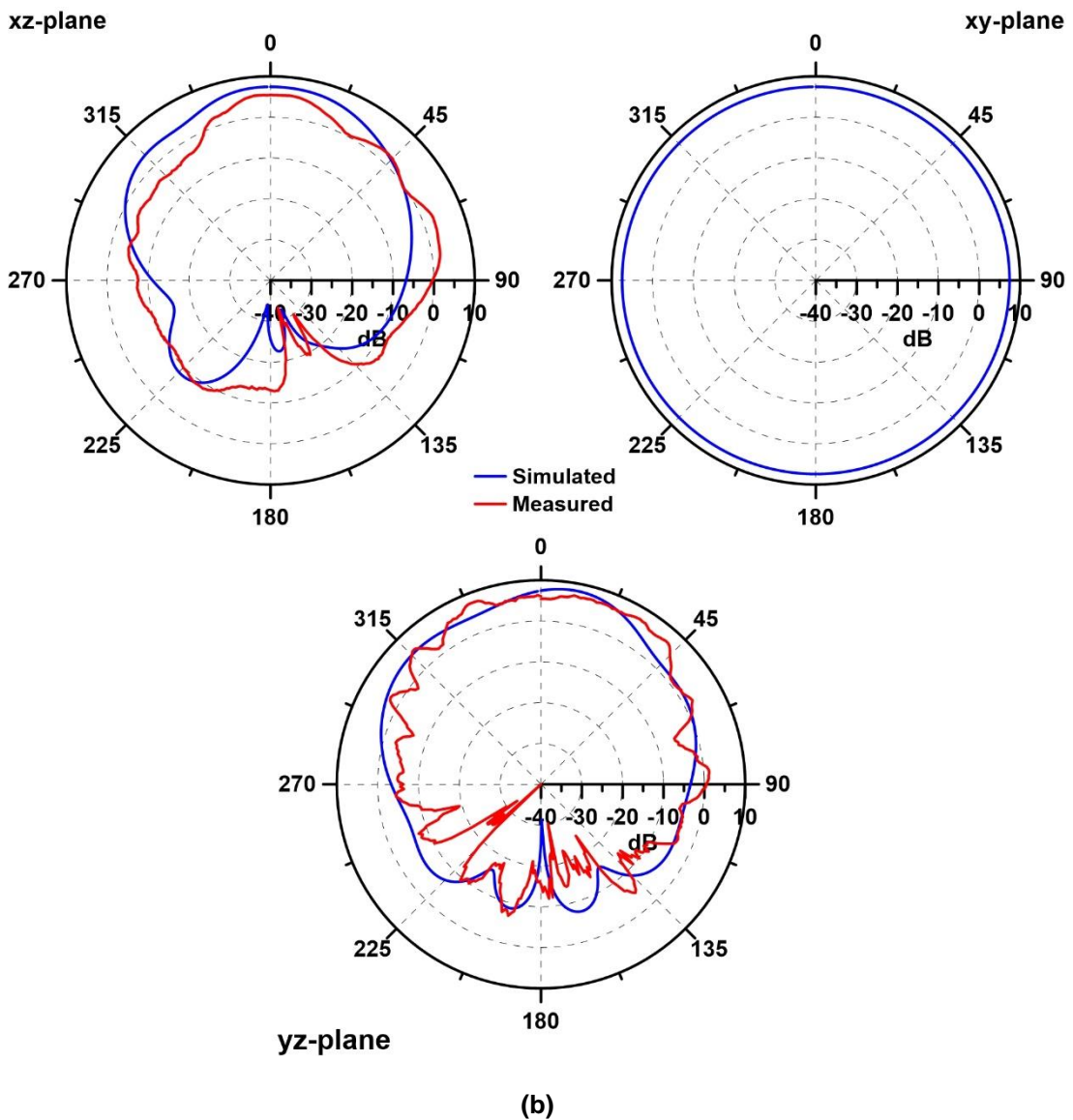


Figure 6.3–10: Radiation patterns of the filtenna array at (a) 2.4 GHz and (b) 5.8 GHz.

F) Gain of Antenna Array and Filtenna Array

The simulated gain of the antenna array and the filtenna array was obtained in the frequency range of 1 GHz to 7 GHz. The results are presented in Figure 6.3–11.

Within the simulated frequency range of the filtenna array, the gain varies from about -11.3 dBi to 7.4 dBi. As can be seen, there are two peaks in the result. The two peaks are present at the frequencies of 2.4 GHz and 5.8 GHz at a gain of about 6.65 dBi and 7.43 dBi respectively. Compared with the gain of the antenna array, the line representing the gain of the filtenna array is smoother and has a less variance across the frequency range.

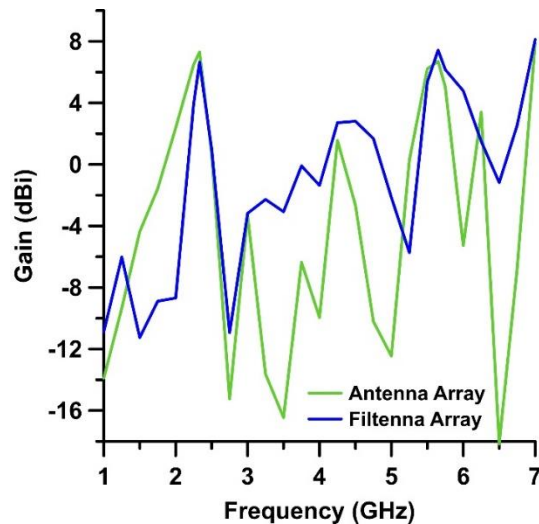


Figure 6.3–11: Gain of the antenna array and the filtenna array.

G) Efficiency of Antenna Array and Filtenna Array

The efficiency of the antenna array and the filtenna array was simulated in the frequency range of 1 GHz to 7 GHz. The results are presented in Figure 6.3–12.

The ensuing efficiency of the filtenna array echoes the result of the gain presented above. Within the simulated frequency range, the efficiency, too, shows two peaks corresponding to the two frequencies of 2.4 GHz and 5.8 GHz. The efficiency at 2.4 GHz is 69.3 % and at 5.8 GHz is 81.3 %. In the rest of the frequency range, the efficiency is less than 15 %. Furthermore, all the other peaks or fluctuations present in the efficiency of the antenna array across the frequency range are suppressed in the efficiency of the filtenna array.

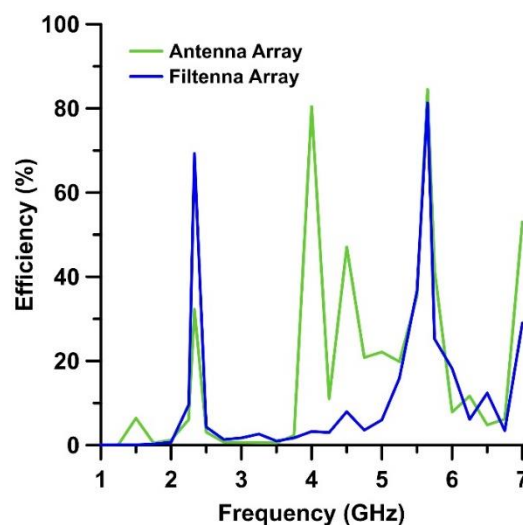


Figure 6.3–12: Efficiency of the antenna array and the filtenna array.

6.4: Design of an Inkjet-Printed Filtenna for WLAN Applications

6.4.1: Specifications

This section presents a narrowband planar microstrip filtenna based on the specifications given in Table 6.4–1. The specifications require a single-element planar microstrip filtenna operating at the IEEE 802.11 WLAN band of 5.8 GHz. The filtenna is required to have a coplanar waveguide-based feeding method; where the characteristic impedance of the feed network and the system should be 95Ω . The specifications further ask that the filtenna should be fabricated via inkjet-printing technology. Furthermore, the filtenna should be able to suppress any interfering frequency harmonics and noise present near the resonant frequency.

Table 6.4–1: Required specifications of the filtenna.

Parameter	Description of Parameter	Value
Filtenna	Type of filtenna	Single Element
Technology	Fabrication technology	Inkjet-Printed
Feed	Feeding method	CPW
Z_0	Characteristic impedance of system	95Ω *
n_{PB}	Number of passbands	Single
f_c	Resonant frequency	5.8 GHz

* Set to 95Ω due to inaccessibility of CPW probe stations capable of measuring standard 50Ω .

6.4.2: Realised Structure and Final Parameters

A) Final Layout

The geometry of the initial antenna is given in Figure 6.4–1; with the values of its dimension parameters given in Table 6.4–2.

The antenna is stimulated via the port connected to the transmission feed line of the antenna. Since, the final filtenna should have a CPW feed network, the initial

antenna has a CPW-fed configuration as well. Rectangular transmission lines on each side of the transmission feed line serve as the ground planes of the antenna. This also eliminates the need for bottom-layer ground metallisation. Hence, the designed antenna is a single-layer circuit. Since the required characteristic impedance, Z_0 , of the transmission feed line is 95Ω , the corresponding value of the width, W_F , of the transmission feed line and the value of the width, G_G , of the gap between the transmission feed line and the ground plane are calculated using the commercial electronic design automation software program Keysight Advanced Design System. The transmission feed line is directly connected to the radiating element. As can be seen from the given geometry, inset transmission line feeding technique was adopted. This also reduces the total area occupied by the antenna. Moreover, a change in the length of the inset-feed affects the input impedance of the antenna at the resonant frequency. Hence, such a feeding technique provides a better control of the impedance of the antenna. The radiating element has a standard shape and is designed using (6.1)–(6.11) to radiate at the frequency of 5.8 GHz. Before optimisation, the element would have a length of half-wavelength, $\lambda_g/2$; where λ_g is the guided wavelength at 5.8 GHz.

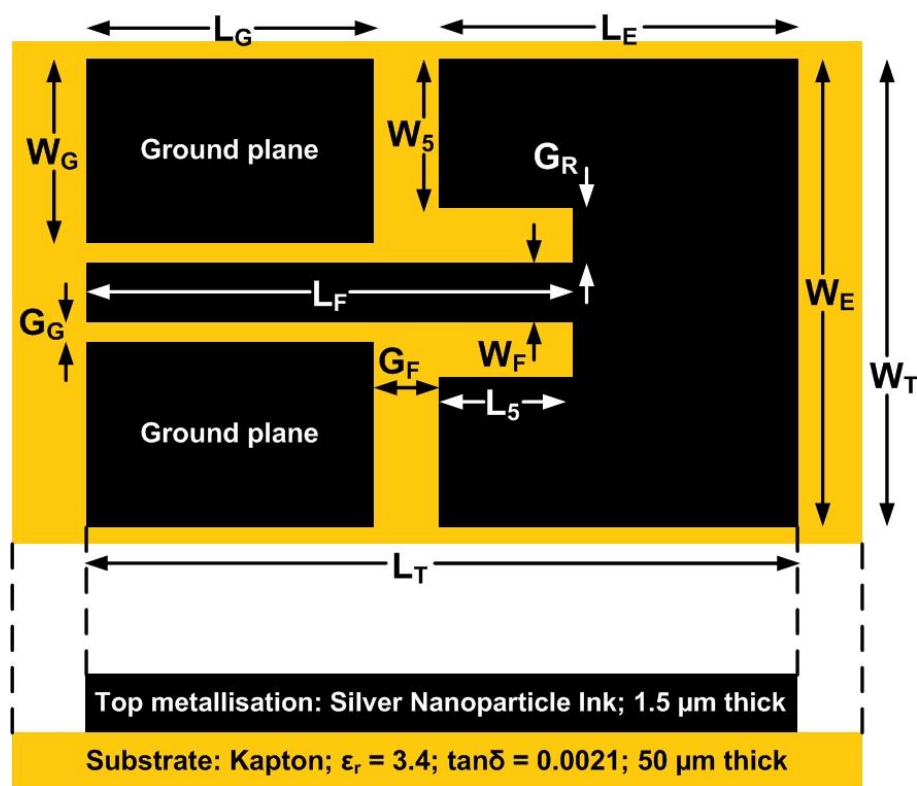


Figure 6.4–1: Geometry of the antenna.

Table 6.4–2: Values of the dimension parameters of the antenna.

Parameter	Value (mm)	Parameter	Value (mm)
W_T	50	L_F	26.1
L_T	41.1	W_5	24.22
W_G	5.95	L_5	11.2
L_G	14.7	W_E	49.74
G_G	0.12	L_E	26.2
G_F	0.2	G_R	0.55
W_F	0.2		

So as to suppress any frequency harmonics and noise near the resonant frequency of the antenna, a bandpass filter can be integrated within the structure. The bandpass filter would only allow one frequency to pass through it and reject any other.

Since the antenna is meant to resonant at only one frequency, only one filter is designed for the integration. The chosen filter is a pseudo-interdigital bandpass filter and its detailed design is based on the procedure given originally in [6-12]. The geometry of the filter is given in Figure 6.4–2; with the values of its dimension parameters given in Table 6.4–3. As can be seen from the geometry, the configuration of the filter is mostly the same as the two filters designed in the previous section. The only difference is that since the final filtenna should have a CPW feeding method, the integrated filter has a CPW feeding network as well. The filter has rectangular transmission lines around it on both sides. These serve as its ground plane and act as a replacement for a bottom-layer ground metallisation. The filter is designed at a centre frequency which is the same as the resonant frequency of the antenna, i.e. 5.8 GHz. The designed filter is of a second-order. Each folded interdigital resonator of the filter is half-wavelength, $\lambda_g/2$, long; where $\lambda_g/2$ is the guided wavelength at 5.8 GHz. The total length, L_R , of each interdigital resonator can be calculated using (6.13).

$$L_R = L_2 + L_3 + L_4 - 0.5W_2 - 0.5W_3 + W_4 \quad (6.13)$$

The width, G_2 , of the gap between all fingers of the filter is the same. Decreasing the width of this gap would broaden the bandwidth of the filter. On the other hand, increasing the width would result in a higher insertion loss.

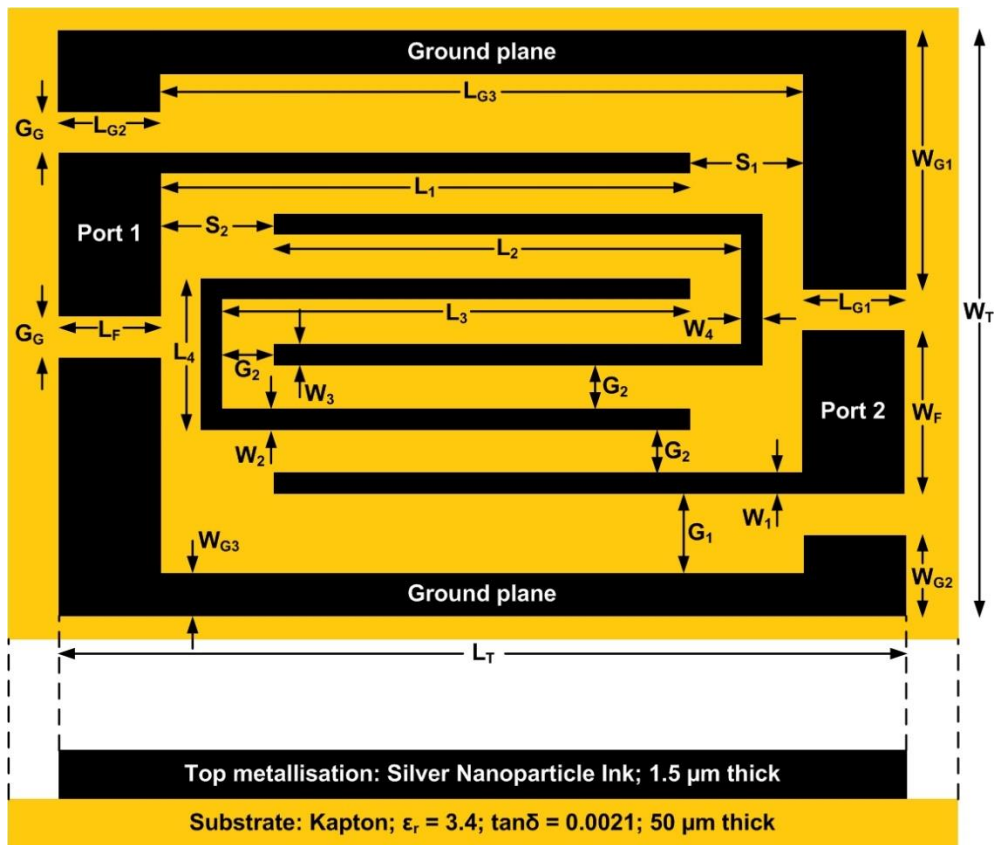


Figure 6.4-2: Geometry of the filter.

Table 6.4-3: Values of the dimension parameters of the filter.

Parameter	Value (mm)	Parameter	Value (mm)
W_T	5.48	L_1	10.1
L_T	14.7	W_2	0.15
W_{G1}	3.47	L_2	10.1
L_{G1}	2	W_3	0.15
W_{G2}	1.57	L_3	9.65
L_{G2}	2	W_4	0.15
W_{G3}	1.52	L_4	1.05
L_{G3}	10.7	G_1	0.17
G_G	0.12	G_2	0.15
W_F	0.2	S_1	0.6
L_F	2	S_2	0.3
W_1	0.15		

The final filtenna is formed by replacing the inset transmission feed line of the antenna by the designed bandpass filter. The geometry of the final filtenna is given in Figure 6.4–3. Apart from the overall size of the final structure, the dimensions of the integrated filter and the integrated radiating element remain the same as the values given in the previous tables. The new total size of the filtenna, $W_T \times L_T$, is 50 mm \times 41.5 mm.

For the filtenna, the input port is the previously named “Port 1” of the bandpass filter. When the port is excited, it would take all frequencies as an input. However, immediately, the bandpass filter would allow only the bandpass frequency of the filter, while all others would be rejected. This “allowed” frequency is the same as the resonant frequency of the antenna element, i.e. 5.8 GHz. The element will then radiate at only this frequency.

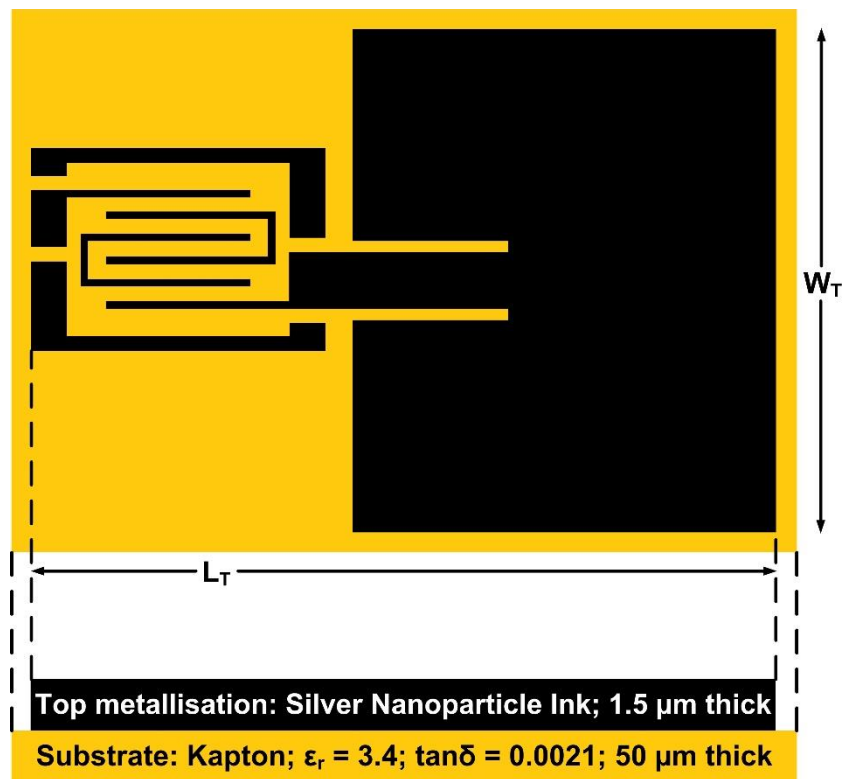


Figure 6.4–3: Geometry of the filtenna.

B) Fabrication of Final Layouts

The final layouts of the three circuits are designed on a flexible Kapton substrate of a thickness of 50 μm , having a dielectric permittivity of $\epsilon_r = 3.4$ and a dielectric loss factor of $\tan \delta = 0.0021$. It is modelled and simulated using the commercial full-wave electromagnetic simulation software program Sonnet. The proposed circuits are

printed using silver nanoparticle ink. The ink used is NovaCentrix JS-B80HV silver nanoparticle ink. The inkjet printer used is Dimatix Materials Printer DMP-3000.

The detailed fabrication process has been previously given in section 4.6. Therefore, only the main settings for the current fabrications are mentioned here. The drop spacing of the inkjet printer is set to 25 μm ; which corresponds to a printing resolution of 1016 dpi. The amplitude of the driving waveform and the printing frequency are fixed to 25 V and 2 kHz respectively. The ink cartridges have a nozzle volume of 10 pL and are arranged in a horizontal configuration. After the structures are printed, they are sintered in a furnace at a curing temperature of 180°C for 20 minutes for the coarse ink lines to form continuous electrically conductive silver lines, providing a good channel for the flow of current. Although the conductivity of silver nanoparticle ink is less than traditional copper by about 3–4 times, depending on the curing temperature and time, it can be increased up to 2.5×10^7 S/m. However, in this instance, since the structures are cured quicker than and at a lower temperature compared with the structures in section 4.6, the conductivity of the printed layers is expected to be at a maximum of 1.0– 1.5×10^7 S/m.

The depth of the top-layer ink metallisation where the skin effect is valid is calculated using (2.60). At the upper end of the maximum expected conductivity, the skin depth comes to be about 1.71 μm . Hence, the final thickness of the top-layer at 1.5 μm is inadequate. However, the thickness of 1.5 μm had to be used because of a mechanical fault with the inkjet printer which was resulting in being able to print only one layer of 1.5 μm . Conversely, if the conductivity of 2.5×10^7 S/m had been achieved, the skin depth would have been 1.32 μm and, hence, the final thickness of 1.5 μm would have been passable — yet still not fully sufficient; unless it would have been at least 2.64 μm .

6.4.3: Results

A) Return Loss of Antenna

The antenna from Figure 6.4–1 was simulated using the values given in Table 6.4–2. The frequency range of the simulation was from 1 GHz to 10 GHz. The obtained return loss from the simulation is shown in Figure 6.4–4. The result shows that the antenna has a fundamental resonant frequency at 5.8 GHz at a return loss of about 26.82 dB. However, at the same time, the result shows that the simulated range is full of various frequency harmonics and noise. Almost all of these are present at a

return loss of more than 3 dB; some even reaching more than 10 dB. These interfere with the fundamental frequency of the antenna.

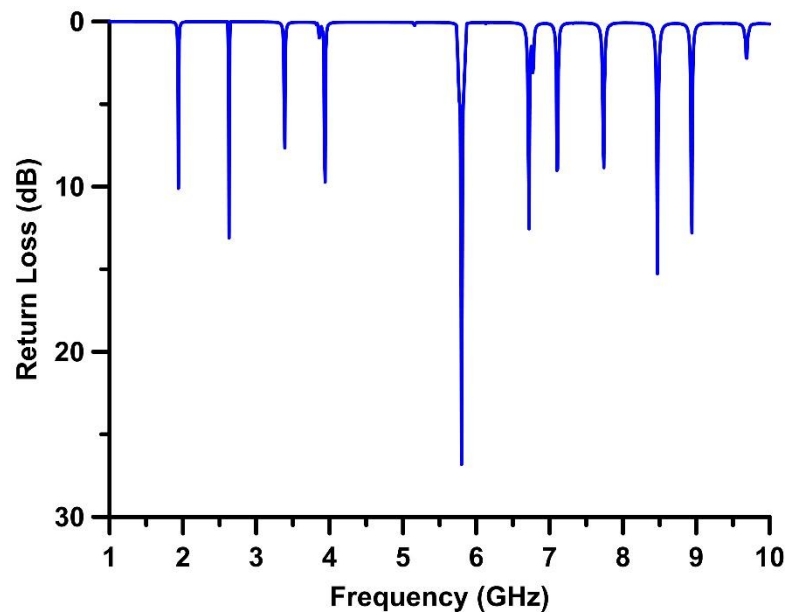


Figure 6.4-4: Return loss of the antenna.

B) S-parameters of Filter

The bandpass filter from Figure 6.4-2, was electromagnetically simulated using the values provided in Table 6.4-3 and then the fabricated prototype was measured for the verification of actual results. The measuring system comprised Cascade Microtech PM5 RF and Microtech coplanar APC50-GSG-250 probe stations and Agilent N5230A PNA-L and Agilent E8361A PNA network analysers. The system was calibrated on a compatible impedance characterisation substrate using the standard Short-Open-Load calibration method. The obtained S-parameters from the simulation and the measurement are shown in Figure 6.4-5.

The simulated result shows the filter to have a fractional bandwidth of 14.8 %. The 3 dB passband of the filter is present from about 5.26 GHz to 6.1 GHz. The centre frequency of the filter is slightly lessened to 5.7 GHz. The insertion loss in the passband at this point is 2.03 dB. The return loss is more than 15 dB for most of the passband bandwidth. Two transmission zeros appear at frequencies below and above the passband. The transmission zeroes improve the selectivity of the filter.

On the other hand, the measured result of the filter from the network analysers shows an insertion loss of about 5 dB in the same frequency range. The substantial difference between the simulated and the measured results is due to the thickness

of the printed metallic layers, high dielectric losses and the low conductivity of ink. The return loss is more than 12 dB for most of the passband bandwidth.

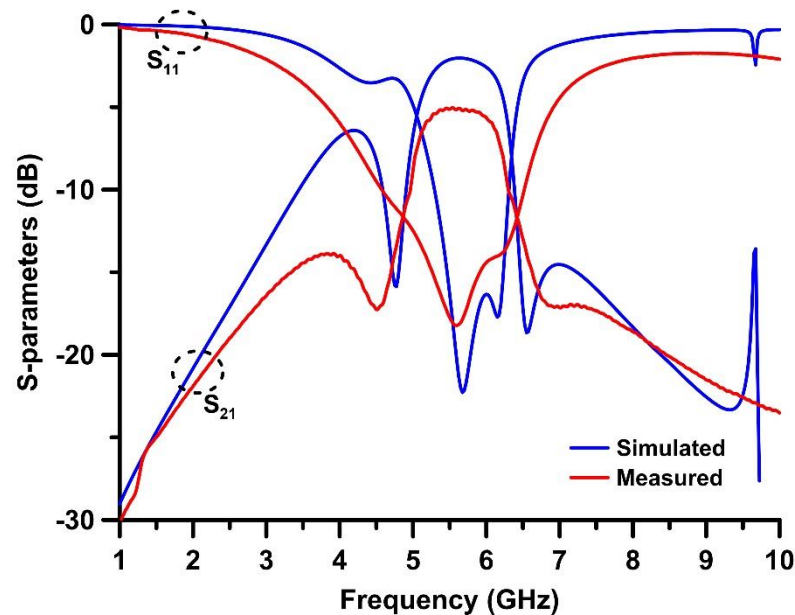


Figure 6.4-5: S-parameters of the filter.

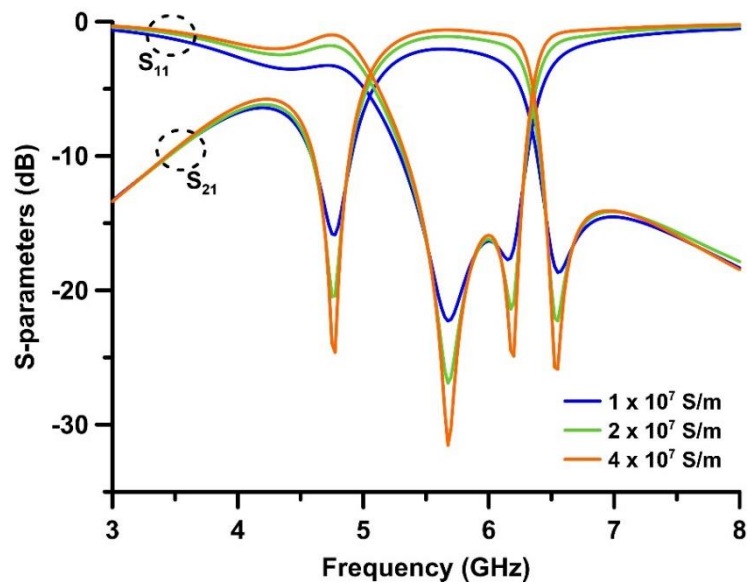
C) Parametric Study of Conductivity and Thickness of Ink

In order to explain the high losses exhibited by the bandpass filter, further investigations were carried out. Since the conductivity of the silver nanoparticle ink and the thickness of the ink metallisation are assumed to be the biggest contributors towards the obtained loss, the filter was simulated with the values of these two parameters varied.

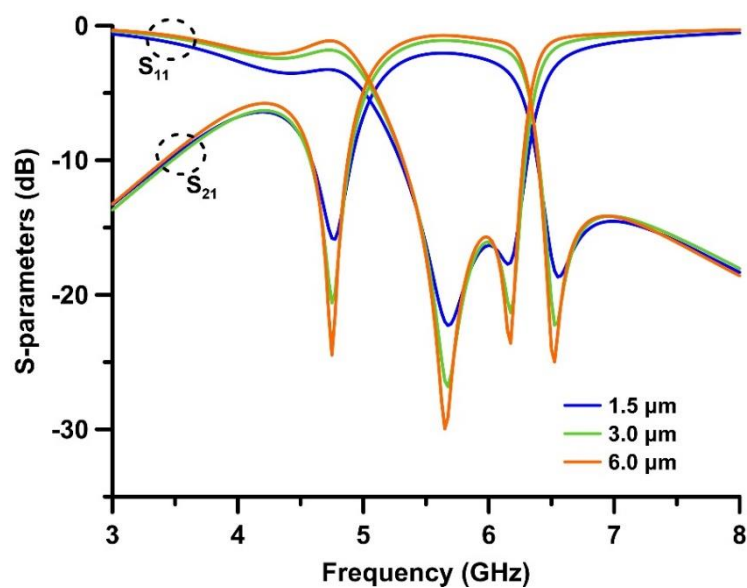
The results of the filter with a varying conductivity of ink — while the thickness of the ink metallisation was kept constant to the final value of $1.5 \mu\text{m}$ — are given in Figure 6.4-6 (a). As can be seen from the results, doubling the electrical conductivity from the initial value of $1.0 \times 10^7 \text{ S/m}$ to $2.0 \times 10^7 \text{ S/m}$ decreased the insertion loss by almost 1 dB. When the conductivity was again doubled from $2.0 \times 10^7 \text{ S/m}$ to $4.0 \times 10^7 \text{ S/m}$, the results showed a further decrease in the loss by about 0.5 dB. These results indicate the main source of the losses experienced by the filter to be the considerably low conductivity of the ink. Practically, the conductivity of the silver nanoparticle ink can be increased by increasing the curing temperature and the curing time.

As shown in Figure 6.4-6 (b), the thickness of the ink metallisation was found to be the second major contributor towards the insertion loss of filter. The filter was simulated for various values of the thickness of the ink metallisation, while the

conductivity of the ink was kept constant to the final value of 1.0×10^7 S/m. When the thickness was doubled from the initial value of $1.5 \mu\text{m}$ to $3.0 \mu\text{m}$, the insertion loss was reduced by 0.9 dB. Increasing the thickness two-fold further to $6.0 \mu\text{m}$, showed a further reduction in the loss by about 0.4 dB. Any further increases in the thickness of the ink metallisation (not shown) gave no significant reduction in the insertion loss. Practically, the thickness of the ink metallisation can be increased by decreasing the drop spacing of the inkjet printer.



(a)



(b)

Figure 6.4–6: Parametric study of the effects on the S-parameters of the filter by varying (a) the conductivity of the ink and (b) the thickness of the ink metallisation.

D) Return Loss of Filtenna

The simulated return loss between a range of 1 GHz to 10 GHz of the final filtenna is shown in Figure 6.4–7. As can be seen, the antenna resonates at only one frequency. This resonant frequency has shifted slightly downwards to about 5.75 GHz. This is because the centre frequency of the integrated bandpass filter had been reduced. The ensuing return loss of the filtenna at the resonant frequency is 18.5 dB. Furthermore, because of the integrated bandpass filter, the frequency harmonics and noise around the resonant frequency of the antenna have been reasonably suppressed. Only three points can be seen; all of which are at a return loss of less than 2 dB. Hence, they do not interfere with the operational band of the filtenna.

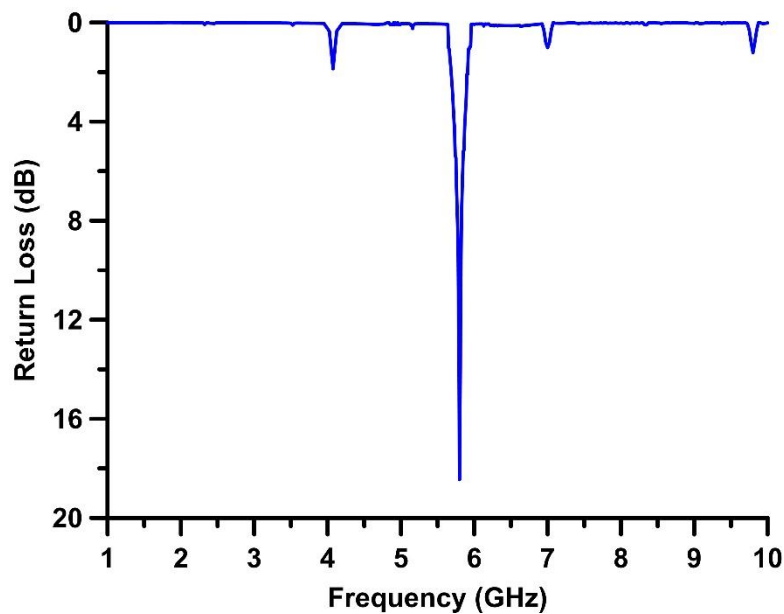


Figure 6.4–7: Return loss of the filtenna.

6.5: Design of an Inkjet-Printed Antenna for 5G Applications

6.5.1: Specifications

This section presents an antenna based on the specifications given in Table 6.5–1. The specifications require a single-element monopole antenna operating at the 5G band of 28 GHz. The antenna is required to have a microstrip-based feeding method; where the characteristic impedance of the feed network and the system should be 50 Ω . Moreover, the specifications require the antenna to be fabricated via inkjet-printing technology. Since there are no unwanted or interfering wireless services present near the 28 GHz frequency band, the antenna does not have to be integrated with any filters.

Table 6.5–1: Required specifications of the antenna.

Parameter	Description of Parameter	Value
Filtenna	Type of filtenna	Single Element
Technology	Fabrication technology	Inkjet-Printed
Feed	Feeding method	Microstrip
Z_0	Characteristic impedance of system	50 Ω
n_{PB}	Number of passbands	Single
f_c	Resonant frequency	28 GHz

6.5.2: Realised Structure and Final Parameters

A) Final Layout

The geometry of the designed antenna which meets the specifications given above is illustrated in Figure 6.5–1; with the values of its dimension parameters provided in Table 6.5–2.

The antenna is based on microstrip technology. It is excited via a port connected to the transmission feed line of the antenna. Since the required characteristic impedance, Z_0 , of the transmission feed line is 50 Ω , the corresponding value of the width, W_F , of the transmission feed line can be calculated using the equations from

section 2.1. The length of the transmission feed line does not significantly affect the response of the antenna. Thus the length, L_F , of the transmission feed line is chosen to be at least 3 mm in order to provide an adequate connection for an SMA connector. The transmission feed line then transitions/tapers over the course of a length, L_1 , of 0.41 mm to a transmission line whose end has an impedance of 11Ω . Thereafter, three other transmission lines carry forward the feeding circuit of the antenna. The end of the transmission feed line is directly connected to the radiating element. As can be seen from the given geometry, inset transmission line feeding technique was adopted. This also reduces the total area occupied by the antenna. The radiating element has a standard shape and is designed using (6.1)–(6.11) to radiate at the frequency of 28 GHz. The area of the overall structure, $W_T \times L_T$, is 3 mm \times 15.5 mm. Whereas, the effective area occupied by the antenna is extremely small; at just 2.62 mm \times 11.545 mm.

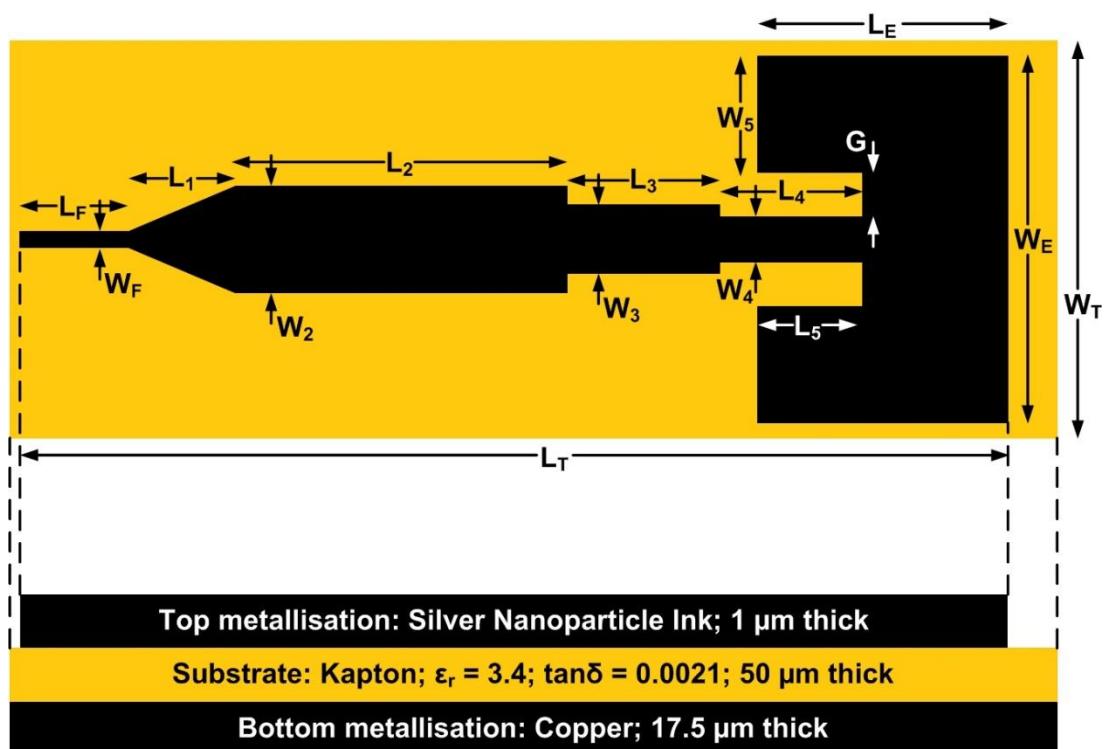


Figure 6.5–1: Geometry of the antenna.

Table 6.5–2: Values of the dimension parameters of the antenna.

Parameter	Value (mm)	Parameter	Value (mm)
W_T	3	L_3	1.34
L_T	15.5	W_4	0.5
W_F	0.1	L_4	0.85
L_F	3	W_5	0.785
L_1	0.41	L_5	0.65
W_2	0.79	W_E	2.62
L_2	6.55	L_E	3.045
W_3	0.51	G	0.275

B) Fabrication of Final Layout

Inkjet-printed antennas for wireless 5G systems should be conformal and robust. Therefore, the antenna is designed on a flexible Kapton substrate of a thickness of 50 μm , having a dielectric permittivity of $\epsilon_r = 3.4$ and a dielectric loss factor of $\tan \delta = 0.0021$. It is modelled and simulated using the commercial full-wave electromagnetic simulation software program CST Microwave Studio. The proposed circuit is printed using the Dimatix Materials Printer DMP-3000. The top-layer metallisation is NovaCentrix JS-B80HV silver nanoparticle ink of a thickness of 1 μm . The bottom-layer metallisation for the ground plane is a sheet of copper of a thickness of 17.5 μm . Each layer of the antenna was modelled with its respective physical and electrical properties.

The fabrication process is the same as the one given in the previous section. The conductivity of the printed top-layer is expected to be at a maximum of 1.5–2.0 $\times 10^7$ S/m. After being cured and taken out of the furnace, the bottom-layer copper sheet is affixed to the printed circuit by means of a conductive silver epoxy metallic adhesive paste.

The depth of the top-layer ink metallisation where the skin effect is valid is calculated using (2.60). At the lower end of the maximum expected conductivity, the skin depth comes to be about 0.78 μm . Hence, the final thickness of the top-layer at 1 μm is passable — but still not fully sufficient; unless it would have been at least 1.5 μm .

6.5.3: Results

A) Return Loss

The return loss of the antenna was simulated between the frequency range of 25 GHz and 31 GHz. The attained result is shown in Figure 6.5–2. The passband of the antenna at a return loss 10 dB is from 27.55 GHz to 27.78 GHz; giving an absolute bandwidth of about 230 MHz. Furthermore, the result shows the resonant frequency of the antenna to be present at 27.66 GHz. The return loss of the inkjet-printed antenna at this point is about 16.28 dB. The downwards shift of the achieved frequency from the desired frequency of 28 GHz indicates that the length of the radiating element needs to be slightly optimised further. In the frequency region outside the aforementioned passband bandwidth, the antenna is shown to have a good stopband selectivity since there are no frequency harmonics and noise present.

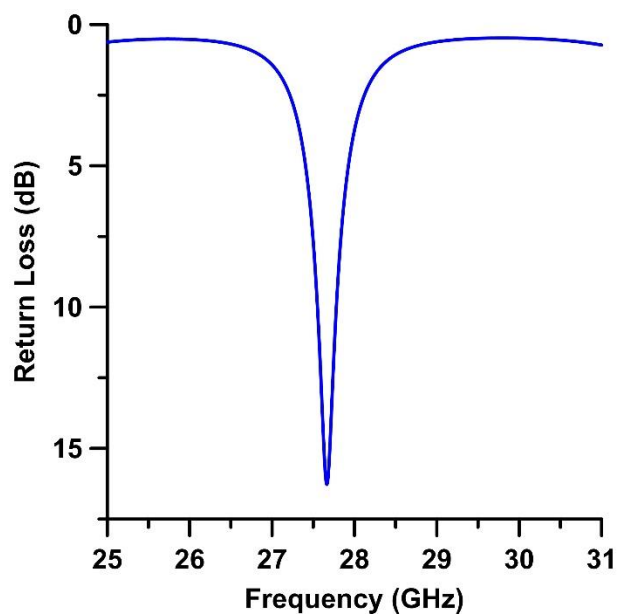


Figure 6.5–2: Return loss of the antenna.

B) Distribution of Surface Currents

The distribution of the surface currents at the resonant frequency of 27.66 GHz was simulated and is shown in Figure 6.5–3. As can be seen from the result, the scattering of the surface currents is spread over the radiating element. A larger quantity of the current is seen flowing along the edges and in the middle of the radiating element. The direction of the arrows signifying the flow of the current is outwards, towards the top-end of the radiating element.

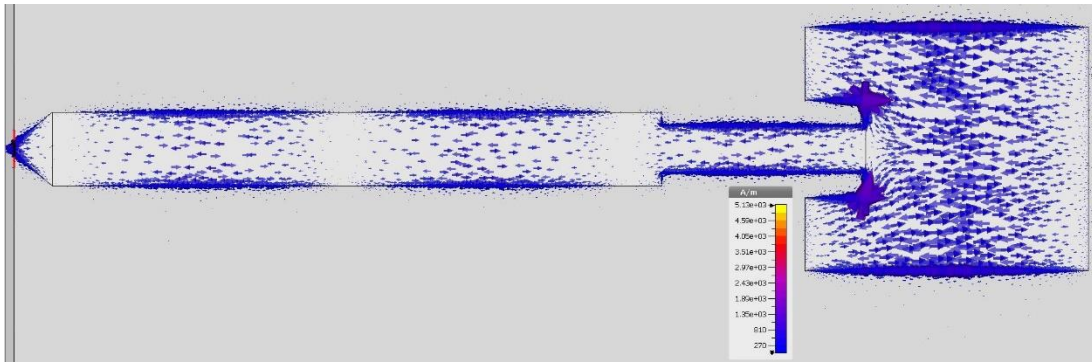


Figure 6.5–3: Distribution of surface currents in the antenna at 27.66 GHz.

C) Radiation Patterns

The radiation patterns of the antenna in the E-plane and the H-plane were obtained at the resonant frequency of 27.66 GHz. The radiation patterns have been calibrated to the gain of the antenna. The acquired results are shown in Figure 6.5–4. At this frequency, maximum radiation is emitted at the top of the antenna as seen by the main radiation lobe in the E-plane. The antenna loses energy as signified by the minor and the side lobes as shown in the bottom part of the E-plane. Stable omnidirectional patterns are present in the H-plane; implying the antenna radiates in all directions.

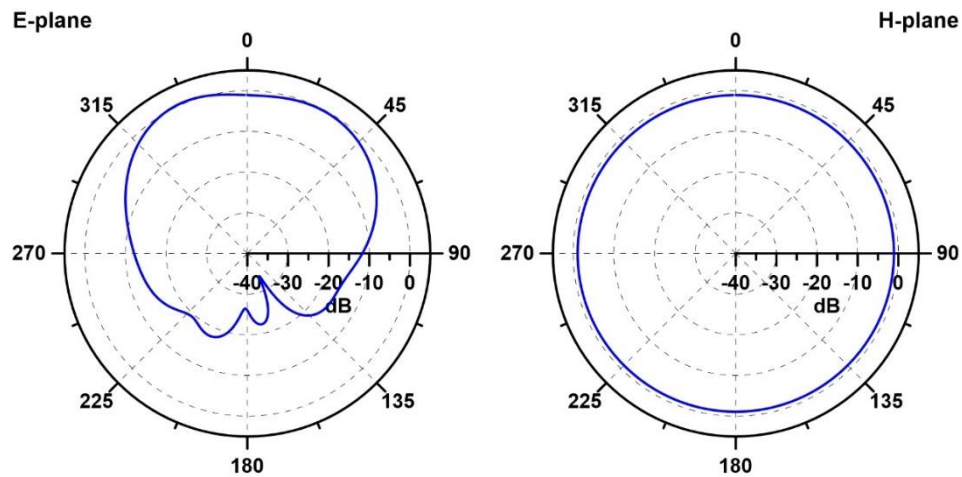


Figure 6.5–4: Radiation patterns of the antenna at 27.66 GHz.

D) Gain

The gain of the antenna was simulated and the acquired result is shown in Figure 6.5–5. Between 25–31 GHz, the gain varies from -5.49–0.43 dBi; with the peak value, i.e. 0.43 dBi, being at the resonant frequency of 27.66 GHz.

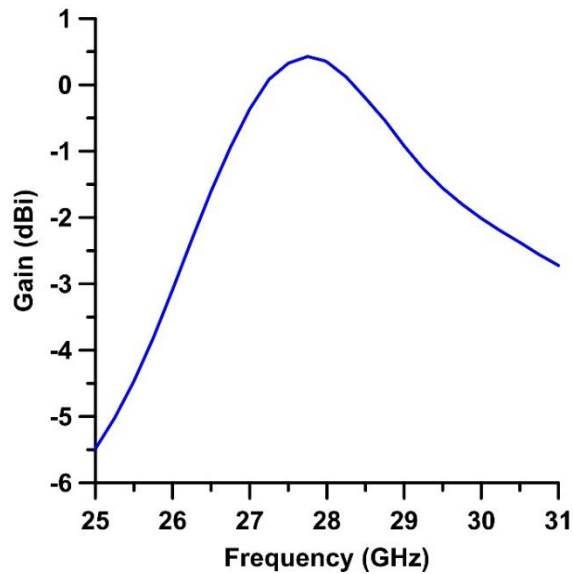


Figure 6.5-5: Gain of the antenna.

E) Efficiency

The simulated efficiency of the antenna was obtained between the range of 25 GHz and 31 GHz. The result is given in Figure 6.5-6. The efficiency plot echoes the gain plot given above. As can be seen, the efficiency result shows a single peak; which corresponds to the resonant frequency of 27.66 GHz. The efficiency of the antenna at this point is about 18.63 %. The antenna exhibits a low efficiency at its resonant frequency, firstly, due to the extremely low conductivity — $1.5\text{--}2.0 \times 10^7$ S/m — of the silver nanoparticle ink used for the top-layer metallisation and, secondly, due to the particularly small thickness — $1 \mu\text{m}$ — of the top-layer metallisation.

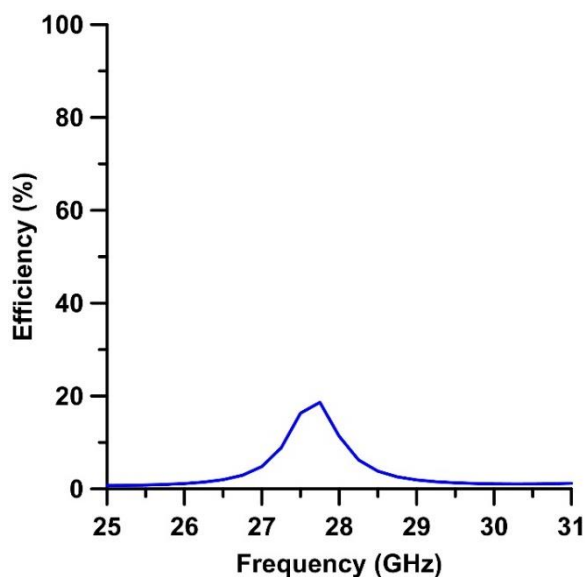


Figure 6.5-6: Efficiency of the antenna.

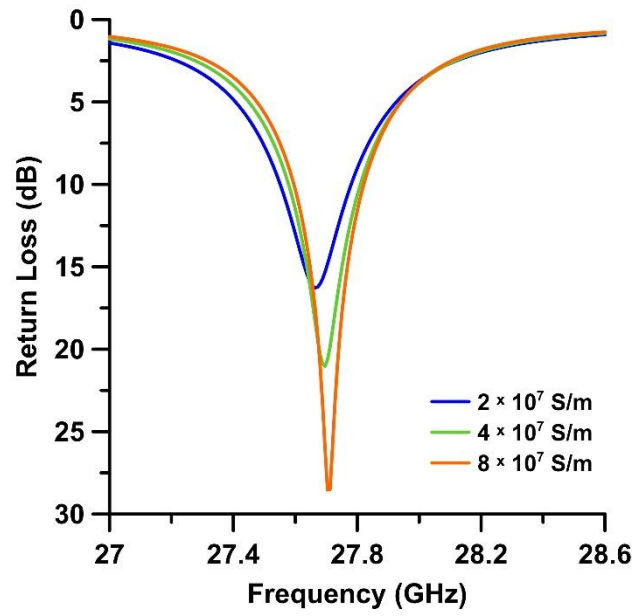
F) Parametric Study of Conductivity and Thickness of Ink

Since the results of the return loss, gain and efficiency presented above indicate that the performance of the antenna is reasonable but not outstanding at its resonant frequency, the particularly low conductivity used for the silver nanoparticle ink was assumed to be the major source of the poor results. Therefore, with the aim of proving this assumption and also to observe how the operational characteristics of the antenna will change, the results of the return loss, gain and efficiency of the antenna were acquired for different values of the conductivity. The values used were 2.0×10^7 S/m, 4.0×10^7 S/m and 8.0×10^7 S/m. At the same time, the thickness of the ink metallisation was kept fixed to the final value of 1 μm . The results are presented in the three graphs in Figure 6.5–7.

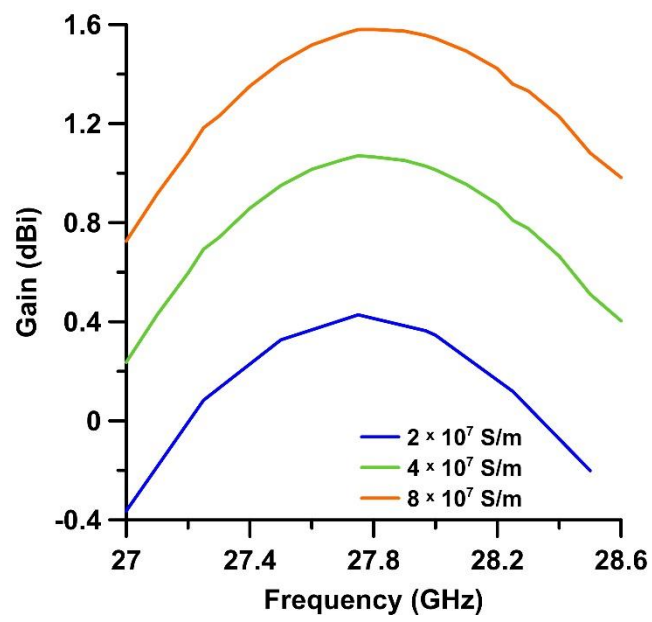
The subsequent return losses of the antenna at the three values of the conductivity are given in Figure 6.5–7 (a) and show a substantial variance between the three plots at the resonant frequency. As can be seen from the plots, doubling the electrical conductivity from the final used value of 2.0×10^7 S/m to 4.0×10^7 S/m increases the return loss by a margin of 4.76 dB; resulting in about 21 dB. When the conductivity is again doubled from 4.0×10^7 S/m to 8.0×10^7 S/m, the third plot shows a further rise by a factor of 7.5 dB; resulting in a return loss of about 28.54 dB at the resonant frequency.

The ensuing gains and efficiencies of the antenna at the three values of the conductivity are given in Figure 6.5–7 (b) and Figure 6.5–7 (c) respectively. Both results are similar with regards to the parametric result of the return loss. At the resonant frequency of 27.66 GHz, the antenna originally has a gain and efficiency of 0.43 dBi and 18.63 % respectively. When the conductivity is doubled to 4.0×10^7 S/m, the gain and the efficiency increase as well. The values become 1.07 dBi and 22.8 % respectively. Another twofold increase of the conductivity to 8.0×10^7 S/m results in the gain and the efficiency of the antenna going up to 1.58 dBi and 25.7 % respectively.

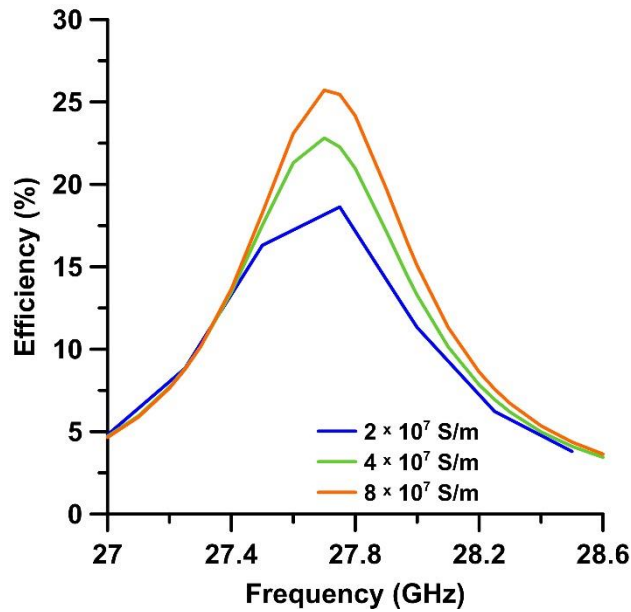
Practically, the conductivity of the ink used can be increased by increasing the percentage of the silver content in the nanoparticle ink solution and/or by increasing the curing temperature and the time.



(a)



(b)



(c)

Figure 6.5–7: Parametric study of the effects on the (a) return loss, (b) gain and (c) efficiency of the antenna by varying the conductivity of the ink.

The second assumption from the results presented previously was that the thickness of the top-layer ink metallisation to be the second biggest cause of the high losses exhibited by the antenna. Thus, with the purpose of verifying this, another parametric investigation was carried out by obtaining the resultant return loss of the antenna for various values of the thickness of the ink metallisation. The final value of the thickness was 1 μm and the values used for the parametric study are in the order of 2x of the final value; i.e. 2 μm , 4 μm , 8 μm and 16 μm . The conductivity of the ink was kept fixed to the final value of 2.0×10^7 S/m. The results of the study are given in Figure 6.5–8.

The results show that when the thickness was increased from 1 μm to 2 μm , the difference in the return loss was only 0.07 dB. Another doubling of the thickness to 4 μm resulted in a bigger difference of 0.58 dB; causing the return loss to become 16.93 dB. However, another two-fold increase of the thickness to 8 μm , resulted in a comparatively bigger difference of 0.95 dB; making the return loss at the resonant frequency to become 17.88 dB. Finally, at the value of 16 μm , the return loss increased by a margin of about 1.59 dB; bring the resulting return loss at the resonant frequency to almost 19.5 dB. Further increases (not shown) of the thickness of the ink metallisation showed no significant increase in the return loss at the resonant frequency.

As can be deduced from these results, although, not as significant as the conductivity of the ink, the thickness of the top-layer ink metallisation to indeed be one of the contributors to the losses incurred by the inkjet-printed antenna. Practically, the thickness of the ink metallisation can be increased either by reducing the drop spacing of the inkjet printer or by increasing the nozzle volume of the ink cartridges.

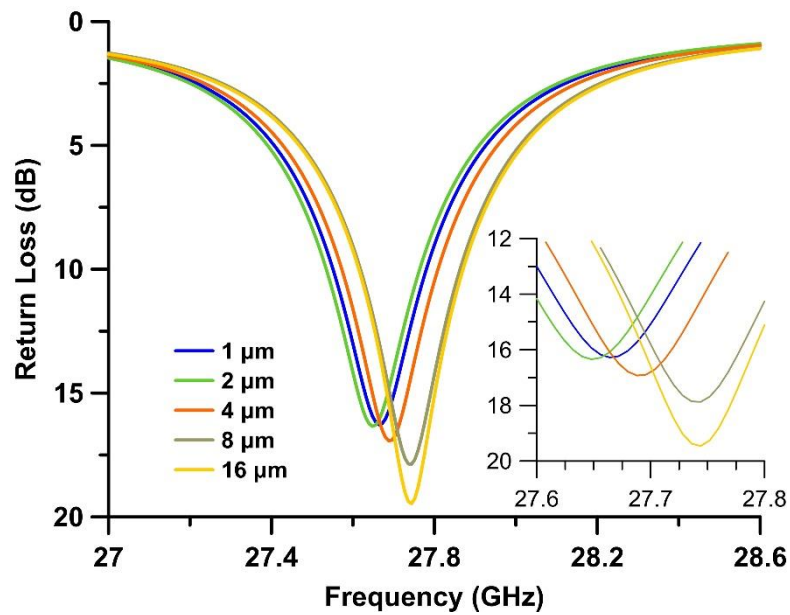


Figure 6.5–8: Parametric study of the effects on the return loss of the antenna by varying the thickness of the ink metallisation.

6.6: References

- [6-1] W. K. Toh, X. Qing, and Z. Chen, "A planar dualband antenna array," *IEEE Transactions on Antennas and Propagation*, vol. 59, no. 3, pp. 833–838, March 2011.
- [6-2] C. Lin and S. Chung, "A filtering microstrip antenna array," *IEEE Transactions on Microwave Theory and Techniques*, vol. 59, no. 11, pp. 2856–2863, November 2011.
- [6-3] M. Rivera, J. Costantine, Y. Tawk, and C. Christodoulou, "Failure detection and correction in switch reconfigurable antenna arrays," *IEEE International Symposium on Antennas and Propagation and North American Radio Science Meeting*, pp. 976–979, 2011.
- [6-4] S. Dasgupta, B. Gupta, and H. Saha, "Development of circular microstrip patch antenna array for rectenna application," *IEEE Annual India Conference INDICON*, pp. 1–6, December 2010.
- [6-5] R. Vyas, V. Lakafosis, H. Lee, G. Shaker, L. Yang, G. Orecchini, A. Traille, M. M. Tentzeris, and L. Roselli, "Inkjet printed, self powered, wireless sensors for environmental, gas, and authentication-based sensing," *IEEE Sensors Journal*, vol. 11, no. 12, pp. 3139–3152, December 2011.
- [6-6] B. S. Cook and A. Shamim, "Inkjet printing of novel wideband and high gain antennas on low-cost paper substrate," *IEEE Transactions on Antennas and Propagation*, vol. 60, no. 9, pp. 4148–4156, September 2012.
- [6-7] L. Yang, A. Rida, R. Vyas, and M. M. Tentzeris, "RFID tag and RF structures on a paper substrate using inkjet-printing technology," *IEEE Transactions on Microwave Theory and Techniques*, vol. 55, no. 12, pp. 2894–2901, December 2007.
- [6-8] J. G. Andrews, S. Buzzi, W. Choi, S. V. Hanly, A. Lozano, A. C. K. Soong, and J. C. Zhang, "What will 5G be?," *IEEE Journal on Selected Areas in Communications*, vol. 32, no. 6, pp. 1065–1082, June 2014.
- [6-9] W. Roh, J.-Y. Seol, J. Park, B. Lee, J. Lee, Y. Kim, J. Cho, K. Cheun, and F. Aryanfar, "Millimeter-Wave beamforming as an enabling technology for 5G cellular communications: theoretical feasibility and prototype results," *IEEE Communications Magazine*, pp. 106–113, February 2014.

- [6-10] P. Pietraski, D. Britz, A. Roy, R. Pragada, and G. Charlton, "Millimeter wave and terahertz communications: feasibility and challenges," *ZTE Communications*, vol. 10, no. 4, pp. 3–12, December 2012.
- [6-11] C. A. Balanis, *Antenna Theory: Analysis and Design*. Hoboken, New Jersey, United States of America: John Wiley & Sons, Inc., 2005.
- [6-12] D. Zayniyev, "Development of planar filters and diplexers for wireless transceiver front ends," PhD thesis, Faculty of Science and Technology, University of Westminster, London, United Kingdom, 2010.

Chapter 7:

Conclusion

7.1: Concluding Statements

Filters and antennas are parts of all wireless communication systems. They are amongst the fundamental components of the wireless transceivers of such wireless communication systems. Within most wireless transceivers, these components are realised separately. This increases the design complexity, the size and the cost of the construction of wireless transceivers. The main goal of the undertaken research was the integration of filters and antennas with each other — forming single components known as “filtennas” — for wireless transceivers. In order to achieve this goal, a number of objectives were set in section 1.3 for the research. The undertaken research adopted a methodical approach so as to achieve the objectives.

Firstly, an in-depth examination of the relevant research published previously was conducted in section 1.2 in order to achieve objective [O-1]. Filtennas, with and without reconfigurable features, and based on conventional PCB technology and inkjet-printing technology, for various wireless communication systems were studied. The main findings of the past work were discussed and the limitations of the research were critically analysed. This helped in identifying gaps in the knowledge where new research could be carried out, evaluated and published.

The theory behind the working of microstrip transmission lines and the theory behind the working of antennas was given in section 2.1 and section 2.2 respectively. The two theories were later expanded to include broadband and narrowband antennas and bandpass filters. The theories formed the basis and the starting point for the development of filtennas. The explanation of the theories fulfilled objective [O-2].

A new reconfigurable element based on Graphene, a popular new material, was developed. This was accomplished by the controlling of the parameters which determine the surface conductivity of Graphene, i.e. the relaxation time and the chemical potential. This, then, led to the control of the resistance of the new switches. The resistance can be increased to a level reaching a switch OFF state or decreased to a level reaching a switch ON state. The formation of a new reconfigurable element satisfied objective [O-3].

Two reconfigurable bandpass filters for UWB applications with notchband for interfering wireless services were developed. One filter had a single notchband for the WLAN band and the other filter had independently controlled dual notchband for

the WiMAX and the satellite communications system bands. The notchband can be switched off or switched on as required. This reconfigurability was introduced by the use of Graphene based switches and PIN diodes. Thus, objectives [O-4], [O-5], [O-6] and [O-10] were fulfilled.

Four broadband planar monopole filtennas were developed by the integration of resonators, which had a filtering effect, with broadband planar monopole antennas. Three filtennas were for UWB applications with dual notchband for WiMAX and WLAN bands. In two of the three filtennas, the notchband were changeable to and fro between switch OFF state and switch ON state. The reconfigurability was achieved by the use of Graphene based switches and PIN diodes. The fourth filtenna was for wireless transceivers of S-band, ISM band and UWB applications, with fixed triple notchband for the interfering WiMAX, WLAN and satellite communications system bands. The development of the four broadband filtennas with their specific properties achieved objectives [O-4], [O-5], [O-7], [O-9] and [O-10].

Three narrowband planar microstrip filtennas for the purpose of suppressing noise and harmonics near the main operating frequency band were developed for WLAN and 5G wireless transceivers. This was accomplished by first designing three narrowband planar microstrip antennas. The first was a 1×2 antenna array for dual WLAN bands, the second was a single-element antenna for WLAN band and the third was a single-element antenna for 5G applications. The first two antennas showed multiple resonances, harmonics and noise near the main operating frequencies. Hence, in these instances, pseudo-interdigital bandpass filters were cascaded with the narrowband antennas. Although the third antenna did not show any noise and harmonics near its operating frequency, filtering resonators could have been integrated within the structure if the need had been present. The integrations led to the formation of the narrowband planar microstrip filtennas which were able to subdue the harmonics and the noise, while allowing the frequency of operation. This formation satisfied objective [O-11] and objective [O-12].

Four of the developed filtennas — of which three were broadband and one was narrowband — were designed and fabricated using conventional PCB technology. The structures of the filtennas were designed in a circuit designer software program and then printed on rigid boards with copper as the metallisation using a PCB prototyping/plotter machine. Objectives [O-13] and [O-14] were thus achieved. The rest of the three filtennas — of which one was broadband and two were narrowband — were fabricated using the newly emerging inkjet-printing technology. The filtennas were printed on flexible Kapton substrate with silver nanoparticle ink as the

metallisation. The development and the fabrication of the filtennas by means of inkjet-printing technology and following the printing process with the aforementioned materials fulfilled objectives [O-15] and [O-16]. From the presented work on inkjet-printing technology, it can be said that the inkjet-printed filtennas were able to achieve almost the same — or, at least, similar — performance as the PCB filtennas. Although inkjet-printed filtennas had more advantages due to the inherent positive aspects of inkjet-printing technology, their performance was hindered by two main factors: the conductivity and the thickness of the ink metallisations. These can be easily improved by making use of inks which have a higher content (percentage) of the conducting metal in their solutions and by printing more layers respectively. The drawback is that both would significantly add to the cost of fabrications.

In addition to the understanding and use of the theoretical knowledge and working mechanism, full-wave electromagnetic solvers were utilised for the development of each and every filtenna. Thus, objective [O-17] was satisfied. The simulated results, such as the S-parameters, radiation patterns, gains and efficiencies, of each development stage were acquired from the full-wave electromagnetic solvers. The measured S-parameters of the fabricated filtennas were obtained using network analysers, satisfying objective [O-18], and the measured radiation patterns of the fabricated filtennas were obtained using anechoic chambers, satisfying objective [O-19]. The attained simulated and measured results were presented for the intermediate components, i.e. filters and antennas before integration, and, as well as, for each and every final filtenna. Furthermore, the results were compared, critically analysed and their worth and limitations discussed. This approach fulfilled objectives [O-20] and [O-21].

7.2: Contributions of the Research

The research presented in this thesis has made the following contributions to knowledge:

- [CR-1] The research has addressed the issue of size and cost of wireless transceivers by proposing that filters and antennas be combined together into single components.
- [CR-2] In addition to reductions in the size and cost by the formation of filtennas, the research has shown that filtennas can use be used to reject specific frequency bands within the passband of broadband antennas and suppress noise and harmonics near the passband of narrowband antennas.
- [CR-3] For the first time, the theoretical working, development and use of novel Graphene based switches so as to realise reconfigurability in circuits has been presented.
- [CR-4] The research has presented several approaches to successfully reject multiple interfering signals of wireless services in UWB bandpass filters.
- [CR-5] A reconfigurable bandpass filter for wireless transceivers of UWB applications with a single notchband for the rejection of the WLAN band has been proposed. The filter has a fractional bandwidth of 125.1–123 % and the notchband can be switched off or switched on without significantly affecting the performance of the filter.
- [CR-6] A highly linear reconfigurable bandpass filter for wireless transceivers of lower UWB applications with dual notchband for the rejection of the WiMAX and the satellite communications system bands has been proposed. The filter has a fractional bandwidth of 53.92–45.84 %. The two notchband can be switched off or switched on independent of each other. Hence, the filter can operate in four different states while maintaining a good performance in its passband. Furthermore, the proposed filter is highly linear even when both notchband are switched on.
- [CR-7] The use of the new inkjet-printing technology in order to design and fabricate flexible broadband and flexible narrowband filtennas using nanoparticle ink has been demonstrated.

- [CR-8] The research has shown various approaches to effectively reject multiple interfering signals of wireless services in broadband planar monopole antennas.
- [CR-9] The research has presented techniques to incorporate frequency reconfigurability in broadband planar monopole filterennas.
- [CR-10] A reconfigurable filterenna for wireless transceivers of UWB applications with dual notchband for the rejection of the two WLAN bands has been proposed. The dual notchband are produced by the capacitive coupling of stepped impedance resonators with the monopole antenna. Reconfigurability in the filterenna has been introduced by the use of two different reconfigurable elements within the stepped impedance resonators. The resulting dual notchband are very close to each other, yet sharp and distinct. The dual notchband can be switched off or switched on as needed.
- [CR-11] A reconfigurable filterenna for wireless transceivers of UWB applications with dual notchband for the rejection of the WiMAX and the WLAN bands has been proposed. The dual notchband are produced by the inductive and capacitive coupling of ring resonators with the monopole antenna. Reconfigurability in the filterenna has been introduced by the use of two different reconfigurable elements within the ring resonators. The dual notchband can be switched off or switched on as necessary.
- [CR-12] For the first time, a novel inkjet-printed flexible filterenna for wireless transceivers of broadband applications with triple notchband for the rejection of the WiMAX, the WLAN and the satellite communications system bands has been proposed. The triple notchband are produced by integrated straight and ring resonators. The filterennas is fabricated using inkjet-printing technology with silver nanoparticle ink as the metallisation and Kapton as the flexible substrate. Furthermore, the flexibility of the filterenna has been characterised experimentally and the performance has been shown to remain mostly consistent at various levels of bending.
- [CR-13] Narrowband filterennas have been proposed for wireless transceivers. The research has proposed procedures to successfully suppress noise and harmonics in narrowband planar microstrip antennas. It has been shown that bandpass filters integrated with narrowband planar microstrip antennas can successfully suppress the noise and the harmonics near the passband of the antennas. This also results in an improved filterenna performance.

- [CR-14] A 1×2 filtenna array for wireless transceivers of dual WLAN applications has been proposed. The standalone array displayed noise and harmonics near the two passbands. Hence, two pseudo-interdigital bandpass filters were merged with the antenna array. The ensuing filtenna array showed a successful suppression of the noise and harmonics.
- [CR-15] An inkjet-printed flexible filtenna for wireless transceivers of WLAN applications using inkjet-printing technology has been proposed. The standalone antenna exhibited noise and harmonics, which deteriorated the main signals. A pseudo-interdigital filter was designed and integrated with the antenna. The subsequent filtenna has been shown to successfully suppress the noise and harmonics. The filtennas is fabricated using inkjet-printing technology with silver nanoparticle ink as the metallisation and Kapton as the flexible substrate.
- [CR-16] An inkjet-printed flexible antenna for wireless transceivers of 5G applications using inkjet-printing technology has been proposed. The antenna was designed and was shown not to exhibit any frequency harmonics and noise near its passband. Hence, filters were not integrated with the antenna. The antenna is fabricated using inkjet-printing technology with silver nanoparticle ink as the metallisation and Kapton as the flexible substrate.

7.3: Suggestions for Future Work

The core theme and the goal of the undertaken research was the development of integrated filter antennas for wireless transceivers. Two different types of filter antennas, i.e. broadband filter antennas and narrowband filter antennas, were developed. Several approaches were taken in order to realise the two types of the filter antennas. These included the inclusion of reconfigurability using novel Graphene based switches and customary PIN diodes switching elements, the use of conventional PCB technology and new inkjet-printing technology. Nonetheless, during the course of attaining the aims and fulfilling the objectives of the research, further questions arose and ideas came to light. These questions and notions clearly indicate that there is still a scope for an expansion of the undertaken research in the future. These possible lines of investigations for the future are as follows:

- [FW-1] Reconfigurable bandpass filters for UWB applications were developed in Chapter 3, but they were not integrated with any antennas. The combination of the reconfigurable UWB filters with UWB antennas could be the formation of a new type of reconfigurable filter antenna for wireless transceivers of UWB applications.
- [FW-2] The development of multi-band bandpass filters and multi-band antennas. The two could be combined together to form filter antennas with improved channel separation.
- [FW-3] Combining the filter antennas developed during the course of the undertaken research with rectifying circuits to form rectifying filter antennas for wireless energy harvesting applications.
- [FW-4] All the designs presented in this research were either single-layered or double-layered. On the other hand, a multi-layer design approach could be adopted for the development of filter antennas; resulting in more compact structures and further reductions in the size.
- [FW-5] The novel Graphene based switches were biased electrically with the purpose of achieving their reconfigurable characteristics. Practically, a large voltage is required for this kind of biasing. Another method for attaining the reconfigurable characteristics could be by magnetically biasing the Graphene based switches.
- [FW-6] All the developed inkjet-printed filter antennas had fixed passbands and stopbands. A possible line of future work would be as to how

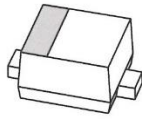
reconfigurability could be incorporated in the inkjet-printed circuits. Although PIN diodes would be highly unsuitable because they are rigid elements, are at least 650 μm thick and would need to be soldered, optical/photoconductive switches might be a better idea. Optical/photoconductive switches have high switching speeds, are resistant to electromagnetic interferences, do not require any external biasing circuitry. Moreover, they are about 300 μm thick. Although the thickness is six times the typical thickness of the developed inkjet-printed filterennas, the switches could still be combined while retaining the flexibility of the filterennas.

- [FW-7] The inkjet-printed filterennas in this research were fabricated using silver nanoparticle ink. It would be interesting to use other types of conductive inks and observe their results.
- [FW-8] Near the end of the research time period, Graphene polymer ink was invented. Novel Graphene-printed flexible filterennas could be developed using this product.
- [FW-9] The potential use of Graphene ink to realise reconfigurability or tunability in both the PCB filterennas and the inkjet-printed filterennas.

Appendices

Appendix A: Datasheets

A.1: NXP™ PIN Diode BAP65-02 SOD523



BAP65-02

Silicon PIN diode

Rev. 5 — 28 September 2010

Product data sheet

1. Product profile

1.1 General description

Planar PIN diode in a SOD523 ultra small SMD plastic package.

1.2 Features and benefits

- High voltage, current controlled
- RF resistor for RF switches
- Low diode capacitance
- Low diode forward resistance (low loss)
- Very low series inductance

1.3 Applications

- RF attenuators and switches
- Bandswitch for TV tuners
- Series diode for mobile communication transmit/receive switch

2. Pinning information

Table 1. Pinning

Pin	Description	Simplified outline	Graphic symbol
1	cathode		 sym006
2	anode		

3. Ordering information

Table 2. Ordering information

Type number	Package		Version
	Name	Description	
BAP65-02	-	plastic surface-mounted package; 2 leads	SOD523

4. Marking

Table 3. Marking codes

Type number	Marking code
BAP65-02	K6



5. Limiting values

Table 4. Limiting values

In accordance with the Absolute Maximum Rating System (IEC 60134).

Symbol	Parameter	Conditions	Min	Max	Unit
V_R	continuous reverse voltage		-	30	V
I_F	continuous forward current		-	100	mA
P_{tot}	total power dissipation	$T_s \leq 90\text{ °C}$	-	715	mW
T_{stg}	storage temperature		-65	+150	°C
T_j	junction temperature		-65	+150	°C
T_{amb}	ambient temperature		-40	+85	°C

6. Thermal characteristics

Table 5. Thermal characteristics

Symbol	Parameter	Conditions	Typ	Unit
$R_{th\ j-s}$	thermal resistance from junction to soldering point		85	K/W

7. Characteristics

Table 6. Characteristics

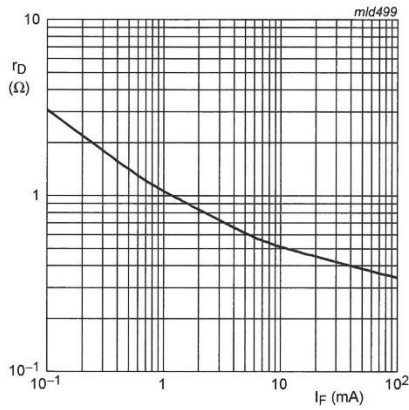
$T_j = 25\text{ °C}$ unless otherwise specified.

Symbol	Parameter	Conditions	Min	Typ	Max	Unit	
V_F	forward voltage	$I_F = 50\text{ mA}$	-	0.9	1.1	V	
I_R	reverse leakage current	$V_R = 20\text{ V}$	-	-	20	nA	
C_d	diode capacitance	$V_R = 0\text{ V}; f = 1\text{ MHz}$	-	0.65	-	pF	
		$V_R = 1\text{ V}; f = 1\text{ MHz}$	-	0.55	0.9	pF	
		$V_R = 3\text{ V}; f = 1\text{ MHz}$	-	0.5	0.8	pF	
		$V_R = 20\text{ V}; f = 1\text{ MHz}$	-	0.375	-	pF	
r_D	diode forward resistance	$I_F = 1\text{ mA}; f = 100\text{ MHz}$	-	1	-	Ω	
		$I_F = 5\text{ mA}; f = 100\text{ MHz}$	[1]	-	0.65	0.95	Ω
		$I_F = 10\text{ mA}; f = 100\text{ MHz}$	[1]	-	0.56	0.9	Ω
		$I_F = 100\text{ mA}; f = 100\text{ MHz}$	-	-	0.35	-	Ω
$ S_{21} ^2$	isolation	$V_R = 0; f = 900\text{ MHz}$	-	10	-	dB	
		$V_R = 0; f = 1800\text{ MHz}$	-	5.8	-	dB	
		$V_R = 0; f = 2450\text{ MHz}$	-	4.4	-	dB	
$ S_{21} ^2$	insertion loss	$I_F = 1\text{ mA}; f = 900\text{ MHz}$	-	0.11	-	dB	
		$I_F = 1\text{ mA}; f = 1800\text{ MHz}$	-	0.13	-	dB	
		$I_F = 1\text{ mA}; f = 2450\text{ MHz}$	-	0.16	-	dB	
$ S_{21} ^2$	insertion loss	$I_F = 5\text{ mA}; f = 900\text{ MHz}$	-	0.08	-	dB	
		$I_F = 5\text{ mA}; f = 1800\text{ MHz}$	-	0.11	-	dB	
		$I_F = 5\text{ mA}; f = 2450\text{ MHz}$	-	0.13	-	dB	

Table 6. Characteristics ...continued
 $T_j = 25\text{ }^\circ\text{C}$ unless otherwise specified.

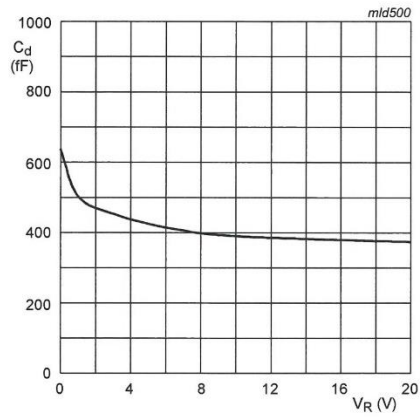
Symbol	Parameter	Conditions	Min	Typ	Max	Unit
$ S_{21} ^2$	insertion loss	$I_F = 10\text{ mA}$; $f = 900\text{ MHz}$	-	0.07	-	dB
		$I_F = 10\text{ mA}$; $f = 1800\text{ MHz}$	-	0.1	-	dB
		$I_F = 10\text{ mA}$; $f = 2450\text{ MHz}$	-	0.13	-	dB
$ S_{21} ^2$	insertion loss	$I_F = 100\text{ mA}$; $f = 900\text{ MHz}$	-	0.07	-	dB
		$I_F = 100\text{ mA}$; $f = 1800\text{ MHz}$	-	0.1	-	dB
		$I_F = 100\text{ mA}$; $f = 2450\text{ MHz}$	-	0.128	-	dB
τ_L	charge carrier life time	when switched from $I_F = 10\text{ mA}$ to $I_R = 6\text{ mA}$; $R_L = 100\text{ }\Omega$; measured at $I_R = 3\text{ mA}$	-	0.17	-	μs
L_S	series inductance	$I_F = 100\text{ mA}$; $f = 100\text{ MHz}$	-	0.6	-	nH

[1] Guaranteed on AQL basis: inspection level S4, AQL 1.0.



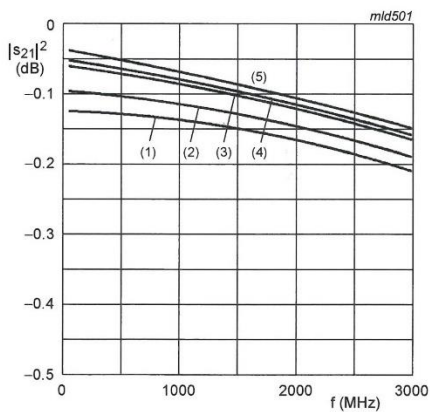
f = 100 MHz; T_j = 25 °C

Fig 1. Forward resistance as a function of forward current; typical values



f = 1 MHz; T_j = 25 °C

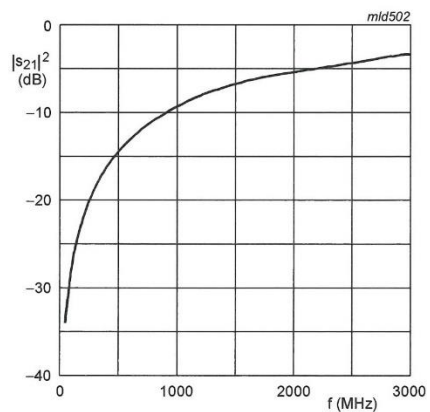
Fig 2. Diode capacitance as a function of reverse voltage; typical values



- (1) I_F = 0.5 mA
- (2) I_F = 1 mA
- (3) I_F = 5 mA
- (4) I_F = 10 mA
- (5) I_F = 100 mA

Diode inserted in series with a 50 Ω stripline circuit and biased via the analyzer Tee network. T_{amb} = 25 °C.

Fig 3. Insertion loss ($|s_{21}|^2$) of the diode as a function of frequency; typical values



Diode zero biased and inserted in series with a 50 Ω stripline circuit. T_{amb} = 25 °C.

Fig 4. Isolation ($|s_{21}|^2$) of the diode as a function of frequency; typical values

8. Package outline

Plastic surface-mounted package; 2 leads

SOD523

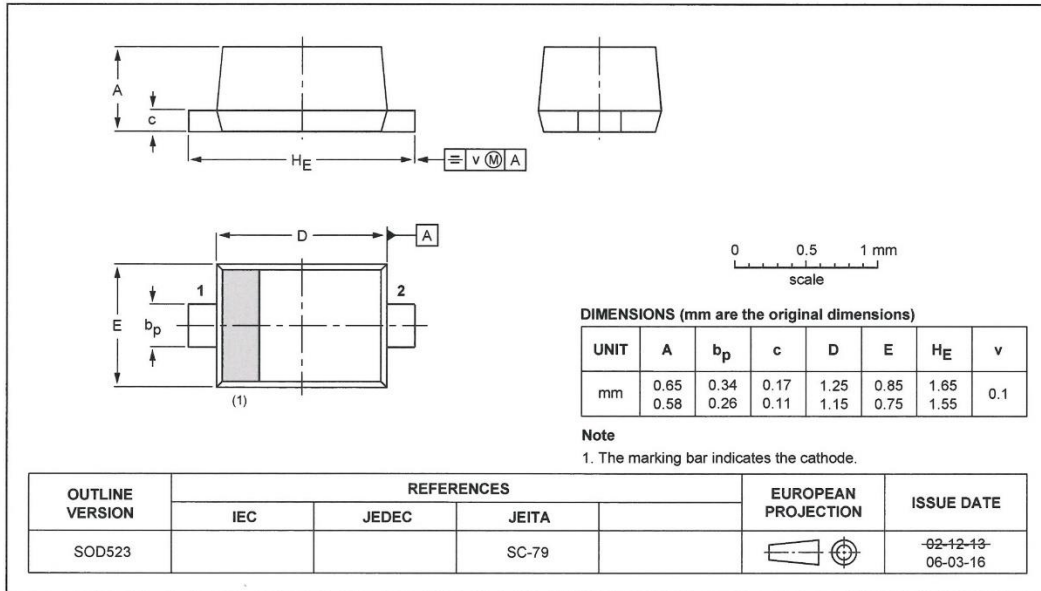


Fig 5. Package outline SOD523

9. Revision history

Table 7. Revision history

Document ID	Release date	Data sheet status	Change notice	Supersedes
BAP65-02 v.5	20100928	Product data sheet	-	BAP65-02_N v.4
Modifications:		<ul style="list-style-type: none"> The format of this data sheet has been redesigned to comply with the new identity guidelines of NXP Semiconductors. Legal texts have been updated. Table 4 "Limiting values": added T_{amb} (ambient temperature). 		
BAP65-02_N v.4	20080108	Product data sheet	-	BAP65-02 v.3
BAP65-02 v.3 (9397 750 08364)	20010511	Product specification	-	BAP65-02 v.2
BAP65-02 v.2 (9397 750 08237)	20010507	Product specification	-	BAP65-02 v.1
BAP65-02 v.1 (9397 750 07724)	20001220	Product specification	-	-

10. Legal information

10.1 Data sheet status

Document status ^{[1][2]}	Product status ^[3]	Definition
Objective [short] data sheet	Development	This document contains data from the objective specification for product development.
Preliminary [short] data sheet	Qualification	This document contains data from the preliminary specification.
Product [short] data sheet	Production	This document contains the product specification.

[1] Please consult the most recently issued document before initiating or completing a design.

[2] The term 'short data sheet' is explained in section "Definitions".

[3] The product status of device(s) described in this document may have changed since this document was published and may differ in case of multiple devices. The latest product status information is available on the Internet at URL <http://www.nxp.com>.

10.2 Definitions

Draft — The document is a draft version only. The content is still under internal review and subject to formal approval, which may result in modifications or additions. NXP Semiconductors does not give any representations or warranties as to the accuracy or completeness of information included herein and shall have no liability for the consequences of use of such information.

Short data sheet — A short data sheet is an extract from a full data sheet with the same product type number(s) and title. A short data sheet is intended for quick reference only and should not be relied upon to contain detailed and full information. For detailed and full information see the relevant full data sheet, which is available on request via the local NXP Semiconductors sales office. In case of any inconsistency or conflict with the short data sheet, the full data sheet shall prevail.

Product specification — The information and data provided in a Product data sheet shall define the specification of the product as agreed between NXP Semiconductors and its customer, unless NXP Semiconductors and customer have explicitly agreed otherwise in writing. In no event however, shall an agreement be valid in which the NXP Semiconductors product is deemed to offer functions and qualities beyond those described in the Product data sheet.

10.3 Disclaimers

Limited warranty and liability — Information in this document is believed to be accurate and reliable. However, NXP Semiconductors does not give any representations or warranties, expressed or implied, as to the accuracy or completeness of such information and shall have no liability for the consequences of use of such information.

In no event shall NXP Semiconductors be liable for any indirect, incidental, punitive, special or consequential damages (including - without limitation - lost profits, lost savings, business interruption, costs related to the removal or replacement of any products or rework charges) whether or not such damages are based on tort (including negligence), warranty, breach of contract or any other legal theory.

Notwithstanding any damages that customer might incur for any reason whatsoever, NXP Semiconductors' aggregate and cumulative liability towards customer for the products described herein shall be limited in accordance with the *Terms and conditions of commercial sale* of NXP Semiconductors.

Right to make changes — NXP Semiconductors reserves the right to make changes to information published in this document, including without limitation specifications and product descriptions, at any time and without notice. This document supersedes and replaces all information supplied prior to the publication hereof.

Suitability for use — NXP Semiconductors products are not designed, authorized or warranted to be suitable for use in life support, life-critical or safety-critical systems or equipment, nor in applications where failure or

malfunction of an NXP Semiconductors product can reasonably be expected to result in personal injury, death or severe property or environmental damage. NXP Semiconductors accepts no liability for inclusion and/or use of NXP Semiconductors products in such equipment or applications and therefore such inclusion and/or use is at the customer's own risk.

Applications — Applications that are described herein for any of these products are for illustrative purposes only. NXP Semiconductors makes no representation or warranty that such applications will be suitable for the specified use without further testing or modification.

Customers are responsible for the design and operation of their applications and products using NXP Semiconductors products, and NXP Semiconductors accepts no liability for any assistance with applications or customer product design. It is customer's sole responsibility to determine whether the NXP Semiconductors product is suitable and fit for the customer's applications and products planned, as well as for the planned application and use of customer's third party customer(s). Customers should provide appropriate design and operating safeguards to minimize the risks associated with their applications and products.

NXP Semiconductors does not accept any liability related to any default, damage, costs or problem which is based on any weakness or default in the customer's applications or products, or the application or use by customer's third party customer(s). Customer is responsible for doing all necessary testing for the customer's applications and products using NXP Semiconductors products in order to avoid a default of the applications and the products or of the application or use by customer's third party customer(s). NXP does not accept any liability in this respect.

Limiting values — Stress above one or more limiting values (as defined in the Absolute Maximum Ratings System of IEC 60134) will cause permanent damage to the device. Limiting values are stress ratings only and (proper) operation of the device at these or any other conditions above those given in the Recommended operating conditions section (if present) or the Characteristics sections of this document is not warranted. Constant or repeated exposure to limiting values will permanently and irreversibly affect the quality and reliability of the device.

Terms and conditions of commercial sale — NXP Semiconductors products are sold subject to the general terms and conditions of commercial sale, as published at <http://www.nxp.com/profile/terms>, unless otherwise agreed in a valid written individual agreement. In case an individual agreement is concluded only the terms and conditions of the respective agreement shall apply. NXP Semiconductors hereby expressly objects to applying the customer's general terms and conditions with regard to the purchase of NXP Semiconductors products by customer.

No offer to sell or license — Nothing in this document may be interpreted or construed as an offer to sell products that is open for acceptance or the grant, conveyance or implication of any license under any copyrights, patents or other industrial or intellectual property rights.

Export control — This document as well as the item(s) described herein may be subject to export control regulations. Export might require a prior authorization from national authorities.

Quick reference data — The Quick reference data is an extract of the product data given in the Limiting values and Characteristics sections of this document, and as such is not complete, exhaustive or legally binding.

Non-automotive qualified products — Unless this data sheet expressly states that this specific NXP Semiconductors product is automotive qualified, the product is not suitable for automotive use. It is neither qualified nor tested in accordance with automotive testing or application requirements. NXP Semiconductors accepts no liability for inclusion and/or use of non-automotive qualified products in automotive equipment or applications.

In the event that customer uses the product for design-in and use in automotive applications to automotive specifications and standards, customer (a) shall use the product without NXP Semiconductors' warranty of the

product for such automotive applications, use and specifications, and (b) whenever customer uses the product for automotive applications beyond NXP Semiconductors' specifications such use shall be solely at customer's own risk, and (c) customer fully indemnifies NXP Semiconductors for any liability, damages or failed product claims resulting from customer design and use of the product for automotive applications beyond NXP Semiconductors' standard warranty and NXP Semiconductors' product specifications.

10.4 Trademarks

Notice: All referenced brands, product names, service names and trademarks are the property of their respective owners.

11. Contact information

For more information, please visit: <http://www.nxp.com>

For sales office addresses, please send an email to: salesaddresses@nxp.com

12. Contents

1	Product profile	1
1.1	General description	1
1.2	Features and benefits	1
1.3	Applications	1
2	Pinning information	1
3	Ordering information	1
4	Marking	1
5	Limiting values	2
6	Thermal characteristics	2
7	Characteristics	2
8	Package outline	5
9	Revision history	6
10	Legal information	7
10.1	Data sheet status	7
10.2	Definitions	7
10.3	Disclaimers	7
10.4	Trademarks	8
11	Contact information	8
12	Contents	9

Please be aware that important notices concerning this document and the product(s) described herein, have been included in section 'Legal information'.

© NXP B.V. 2010.

All rights reserved.

For more information, please visit: <http://www.nxp.com>

For sales office addresses, please send an email to: salesaddresses@nxp.com

Date of release: 28 September 2010

Document identifier: BAP65-02

A.2: Fujifilm™ Dimatix™ Materials Printer DMP-3000 for Inkjet-Printing

FUJIFILM

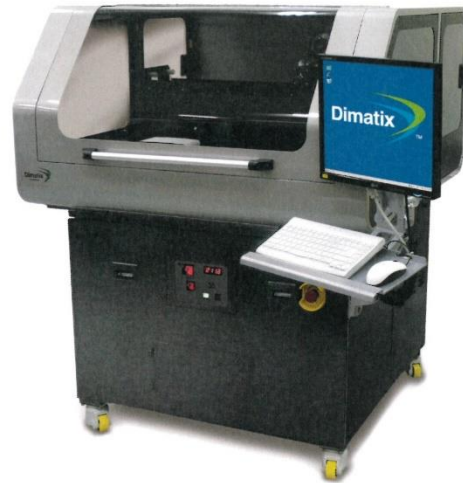
Dimatix Materials Printer DMP-3000

System Description

- XYZ stage, inkjet deposition system
- User-fillable piezoelectric inkjet print cartridges and printheads
- Built-in drop watcher camera system for jetting analysis
- Fiducial camera for substrate alignment and measurement
- Variable printing resolution
- PC-controlled with graphical user interface (GUI) application software
- Wide range of fluid compatibilities
- Heated vacuum platen
- Printhead maintenance and cleaning station
- Includes PC, monitor and software

Mechanical System

- Printable parameters
 - Printable area: 300 x 300 mm
 - Substrate up to 30 mm thickness
 - System positional accuracy: $\pm 5 \mu\text{m}$
 - Repeatability: $\pm 1 \mu\text{m}$
- Substrate holder
 - Vacuum platen
 - Temperature adjustable; ambient to 60°C
- System footprint: 1.2 x 1.4 x 1.6 m
- Weight approximately 1100 kg
- Power 100-120/200-240 VAC 50/60 Hz, 1.5 kW maximum
- Operating range 15-30°C at 5-80% RH non-condensing
- Operates at altitudes up to 2000 m
- Safety and EMC compliant: CE/FCC/UL/RoHS/WEEE



Fiducial Camera

- Allows substrate alignment using reference marks
- Allows print origin or reference point positioning to match substrate placement
- Provides feature location and measurement
- Provides post-print pattern inspection and image capture

Cartridges

- Type: Piezo-driven jetting device with integrated reservoir and heater
- Usable Ink Capacity: 1.5 ml fluid capacity
- Materials Compatibility: Broad materials compatibility
- Number of Nozzles: 16 nozzles, 254 μm spacing, single row
- Drop Volume: 1 (DMC-11601) and 10 (DMC-11610) picoliter nominal



Printheads

- SX3, SE3 and SE-DPN
- D-128/1 DPN and D-128/10 DPN



Control PC and Application Software

- Pre-loaded patterned templates
- Pattern preview
- Editors: Waveform and cleaning cycle
- Bitmap (1 bit) files accepted
- DXF, Gerber, GDSII and OASIS file conversion to Bitmap

Replaceable Items

- Print cartridge with one-time user-fillable reservoir
- SX3, SE3 and SE-DPN
- D-128/1 DPN and D-128/10 DPN
- Nozzle blotting material for cleaning station



POS00086 Rev. 01 10/29/12

www.dimatix.com



**Dimatix Materials Printer
DMP-3000**

DMP-3000 Cartridges & Printheads

Printheads/Operating Parameters	Individual tunable nozzles	Nozzle plate	Nozzle diameter (microns)	Calibrated drop size (picoliters)	Adjustment drop size range (picoliters)	Maximum operating frequency (kHz)
 DMC-11601	✓	Silicon with non-wetting coating	9	1	± 20%	15
 DMC-11610	✓	Silicon with non-wetting coating	21	10	± 20%	60
 D-128/1 DPN	✓	Silicon with non-wetting coating	9	1	± 20%	15
 D-128/10 DPN	✓	Silicon with non-wetting coating	21	10	± 20%	20
 SX3	✓	Silicon with non-wetting coating	19	8	8 - 10	10
 SE3	✓	Silicon with non-wetting coating	42	35	30 - 40	15
 SE-DPN	✓	Electroformed nickel-gold	35	30	25 - 30	40



Corporate Office:
FUJIFILM Dimatix, Inc.
2250 Martin Avenue
Santa Clara, CA 95050
USA
Tel: (408) 565-9150
Fax: (408) 565-9151
Email: info@dimatix.com

New Hampshire Facility:
FUJIFILM Dimatix, Inc.
109 Etnie Road
Lebanon, NH 03766
USA
Tel: (603) 443-5300
Fax: (603) 446-9870
Email: info@dimatix.com

Japan Office:
FUJIFILM Global Graphic Systems Co., Ltd.
2-26-30 Nishiazabu
Minato-ku, Tokyo 106-0031
Japan
Advanced Marking Strategy Division
Phone: +81 3 6419 0530
Fax: +81 3 6419 9840
E-mail: dmp_ffgs@ffgs.fujifilm.co.jp

Europe Office:
Tel: +44 7739 883 505
Fax: +44 870 167 4328
Email: euro@dimatix.com

Korea Office:
Email: mdkorea@dimatix.com

Taiwan Office:
Email: mdtsiwen@dimatix.com

China Office:
FUJIFILM Dimatix China Service Center
Building 30, 1000 Jinhai Road
Pudong New Area, Shanghai
China 201206
Email: china@dimatix.com

Singapore Office:
Email: mdsingapore@dimatix.com

www.dimatix.com

PDS30086 Rev. 01 10/29/12

A.3: DuPont™ Kapton® Flexible Polyimide Substrate for Inkjet-Printing



DuPont™ Kapton® HN
polyimide film

Technical Data Sheet

DuPont™ Kapton® HN general-purpose film has been used successfully in applications at temperatures as low as -269°C (-452°F) and as high as 400°C (752°F). HN film can be laminated, metalized, punched, formed or adhesive coated. Kapton® HN is the recommended choice for applications that require an all-polyimide film with an excellent balance of properties over a wide range of temperatures.

Applications

- Mechanical parts
- Electronic parts
- Electrical Insulation
- Pressure sensitive tape
- Fiber optics cable
- Insulation blankets
- Insulation tubing
- Automotive diaphragms sensors and manifolds
- Etching
- Shims

Product Specifications

Kapton® HN is manufactured, slit and packaged according to the product specifications listed in H-38479, Bulletin GS-96-7.

Certification

Kapton® HN meets ASTM D-5213 (type 1, item A) requirements.



The miracles of science™

Table 1
Physical Properties of DuPont™ Kapton® HN at 23°C (73°F)

Property	Unit	1 mil 25µm	2 mil 50µm	3 mil 75µm	5 mil 125µm	Test Method
Ultimate Tensile Strength at 23°C, (73°F) at 200°C (392°F)	psi (MPa)	33,500(231) 20,000(139)	33,500(231) 20,000(139)	33,500(231) 20,000(139)	33,500(231) 20,000(139)	ASTM D-882-91, Method A*
Ultimate Elongation at 23°C, (73°F) at 200°C (392°F)	%	72 83	82 83	82 83	82 83	ASTM D-882-91, Method A
Tensile Modulus at 23°C, (73°F) at 200°C (392°F)	psi (GPa)	370,000 (2.5) 290,000 (2.0)	370,000 (2.5) 290,000 (2.0)	370,000 (2.5) 290,000 (2.0)	370,000 (2.5) 290,000 (2.0)	ASTM D-882-91, Method A
Density	g/cc	1.42	1.42	1.42	1.42	ASTM D-1505-90
MIT Folding Endurance	cycles	285,000	55,000	6,000	5,000	ASTM D-2176-89
Tear Strength-propagating (Elmendorf), N (lbf)		0.07 (0.02)	0.21 (0.02)	0.38 (0.02)	0.58 (0.02)	ASTM D-1922-89
Tear Strength, Initial (Graves), N (lbf)		7.2 (1.6)	16.3 (1.6)	26.3 (1.6)	46.9 (1.6)	ASTM D-1004-90
Yield Point at 3% at 23°C, (73°F) at 200°C (392°F)	MPa (psi)	69 (10,000) 41 (6,000)	69 (10,000) 41 (6,000)	69 (10,000) 41 (6,000)	69 (10,000) 41 (6,000)	ASTM D-882-91
Stress to produce 5% elong. at 23°C, (73°F) at 200°C (392°F)	MPa (psi)	90 (13,000) 61 (9,000)	90 (13,000) 61 (9,000)	90 (13,000) 61 (9,000)	90 (13,000) 61 (9,000)	ASTM D-882-92
Impact Strength at 23°C, (73°F)	N•cm•(ft lb)	78 (0.58)	78 (0.58)	78 (0.58)	78 (0.58)	DuPont Pneumatic Impact Test
Coefficient of Friction, kinetic (film-to-film)		0.48	0.48	0.48	0.48	ASTM D-1894-90
Coefficient of Friction, static (film-to-film)		0.63	0.63	0.63	0.63	ASTM D-1894-90
Refractive Index (sodium D line)		1.70	1.70	1.70	1.70	ASTM D-542-90
Poisson's Ratio		0.34	0.34	0.34	0.34	Avg. three samples, elongated at 5, 7, 10%
Low temperature flex life		pass	pass	pass	pass	IPC-TM-650, Method 2.6.18

*Specimen size 25 x 150 mm (1.6 in); jaw separation 100 mm (4 in), jaw speed, 50mm/min (2 in/min). Ultimate refers to the tensile strength and elongation measured at break.

Table 2
Thermal Properties of DuPont™ Kapton® HN Film

Thermal Property	Typical Value	Test Condition	Test Method
Melting Point	None	None	ASTM E-794-85 (1989)
Thermal Coefficient of Linear Expansion	20 ppm/°C (11 ppm/°F)	-14 to 38°C (7 to 100°F)	ASTM D-696-91
Coefficient of Thermal Conductivity, W/m•K $\frac{\text{cal}}{\text{cm}\cdot\text{sec}\cdot\text{°C}}$	0.12 2.87 x 10 ⁻¹	296K 23°C	ASTM F-433-77 (1987)
Specific Heat, J/g•K (cal/g•°C)	1.09 (0.261)		Differential calorimetry
Heat Sealability	not heat sealable		
Solder Float	pass		IPC-TM-650 Method 2.4.13A
Smoke Generation	D _{sm} =<1	NBS smoke chamber	NFPA-258
Shrinkage, % 30 min at 150°C 120 min at 400°C	0.17 1.25		IPC-TM-650 Method 2.2.4A; ASTM D-5214-91
Limiting Oxygen Index, %	37-45		ASTM D-2863-87
Glass Transition Temperature (T _g)	A second order transition occurs in Kapton [®] between 360°C (680°F) and 410°C (770°F) and is assumed to be the glass transition temperature. Different measurement techniques produce different results within the above temperature range.		

Table 3
Typical Electrical Properties of DuPont™ Kapton® HN Film at 23°C (73°F), 50% RH

Property Film Gage	Typical Value		Test Condition	Test Method
<u>Dielectric Strength</u> 25 µm (1 mil) 50 µm (2 mil) 75 µm (3 mil) 125 µm (5 mil)	V/m kV/mm 303 240 205 154	(V/mil) (7700) (6100) (5200) (3900)	60 Hz 1/4 in electrodes 500 V/sec rise	ASTM D-149-91
<u>Dielectric Constant</u> 25 µm (1 mil) 50 µm (2 mil) 75 µm (3 mil) 125 µm (5 mil)	3.4 3.4 3.5 3.5		1 kHz	ASTM D-150-92
<u>Dissipation Factor</u> 25 µm (1 mil) 50 µm (2 mil) 75 µm (3 mil) 125 µm (5 mil)	0.0018 0.0020 0.0020 0.0026		1 kHz	ASTM D-150-92
<u>Volume Resistivity</u> 25 µm (1 mil) 50 µm (2 mil) 75 µm (3 mil) 125 µm (5 mil)	•cm 1.5 x 10 ¹⁷ 1.5 x 10 ¹⁷ 1.4 x 10 ¹⁷ 1.0 x 10 ¹⁷			ASTM D-257-91

Dimensional Stability

The dimensional stability of DuPont™ Kapton® polyimide film depends on two factors—the normal coefficient of thermal expansion and the residual stresses placed in the film during manufacture. The latter causes Kapton® to shrink on its first exposure to elevated temperatures as indicated in the bar graph in **Figure 1**. Once the film has been exposed, the normal values of the thermal coefficient of linear expansion as shown in **Table 4** can be expected.

Figure 1. Residual Shrinkage vs. Exposure Temperature and Thickness, DuPont™ Kapton® HN and VN Films

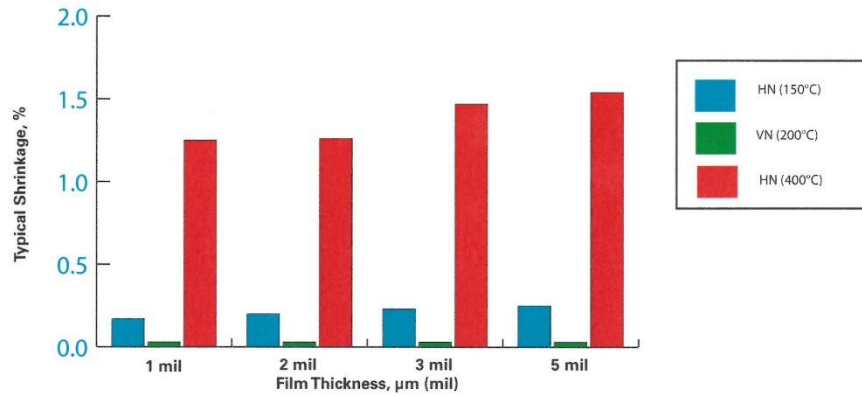


**Table 4
Thermal Coefficient of Expansion,
DuPont™ Kapton® HN Film, 25 µm (1 mil),
Thermally Exposed**

Temperature Range, °C. (°F)	ppm/°C
30–100 (86–212)	17
100–200 (212–392)	32
200–300 (392–572)	40
300–400 (572–752)	44
30–400 (86–752)	34

For more information on DuPont™ Kapton® or other polyimide films, please contact your local representative, or visit our website for additional regional contacts:

Americas

DuPont High Performance Films
U.S. Rt. 23 & DuPont Road
Circleville, OH 43113
Tel: 800-967-5607

Europe

DuPont de Nemours (Luxembourg)
S.A.R.L.
Rue General Patton
L-2984 Luxembourg
Tel: 352-3666-5935

Asia

DuPont Taiwan
No. 45, Hsing-Pont Road
Taoyuan, Taiwan, R.O.C.
Tel: 888 3 377 3688

Japan

DuPont-Toray Co., Ltd.
5-6 Nihonbashi Honcho 1-chome
Chuo-ku, Tokyo 103-0023 Japan
Tel: 81-3-3245-5061

kapton.dupont.com

©2011 DuPont. All rights reserved. The DuPont Oval Logo, DuPont™, The miracles of science™, and Kapton® are registered trademarks or trademarks of E.I. du Pont de Nemours and Company or its affiliates.

This information corresponds to our current knowledge on the subject. It is offered solely to provide possible suggestions for your own experimentations. It is not intended, however, to substitute for any testing you may need to conduct to determine for yourself the suitability of our products for your particular purposes. This information may be subject to revision as new knowledge and experience becomes available. Since we cannot anticipate all variations in actual end-use conditions, DuPont makes no warranties and assumes no liability in connection with any use of this information. Nothing in this publication is to be considered as a license to operate under or a recommendation to infringe any patent right.

Caution: Do not use in medical applications involving permanent implantation in the human body. For other medical applications, see "DuPont Medical Caution Statement", H-51459 or H-50102-2.

K-15345-1 04/11



The miracles of science™

A.4: NovaCentrix® Metalon® Silver Nanoparticle Ink JS-B80HV for Inkjet-Printing



Metalon® Conductive Inks for Printed Electronics

www.novacentrix.com

Metalon® JS-B25HV

Nanosilver Ink – Aqueous dispersion for Dimatix Printheads

JS-B25HV is an electrically conductive ink designed to produce circuits on porous and non-porous substrates including inkjet papers, PET, polyimide, and glass. JS-B25HV ink is specially formulated for compatibility and stability with Dimatix printheads. A printing waveform for Dimatix DMP heads is available.

Performance Properties	<p>Metalon JS-B25HV when printed and cured, produces conductive traces that attain as low as 2× bulk Ag resistivity.</p> <p>Sample Conductivity</p> <table border="1" style="width: 100%; border-collapse: collapse;"> <thead> <tr> <th></th> <th style="text-align: center;">Units</th> <th style="text-align: center;">JS-B25HV</th> </tr> </thead> <tbody> <tr> <td>Thin film resistivity</td> <td style="text-align: center;">Micro ohm-cm</td> <td style="text-align: center;">2.8</td> </tr> <tr> <td>Thin film sheet resistance</td> <td style="text-align: center;">Milliohm/square</td> <td style="text-align: center;">50</td> </tr> <tr> <td>Bulk resistivity comparison</td> <td style="text-align: center;">$\rho(\text{film})/\rho(\text{bulk Ag})$</td> <td style="text-align: center;">1.8</td> </tr> </tbody> </table> <p>Sample Information</p> <p>Substrate¹: Novele™ IJ-220 (a coated PET) Printer: Dimatix Materials Printer (DMP-2800 Series) Post-Process Tool: PulseForge® 3100 in 6" configuration Environment: Atmosphere – no special preparation</p>		Units	JS-B25HV	Thin film resistivity	Micro ohm-cm	2.8	Thin film sheet resistance	Milliohm/square	50	Bulk resistivity comparison	$\rho(\text{film})/\rho(\text{bulk Ag})$	1.8						
	Units	JS-B25HV																	
Thin film resistivity	Micro ohm-cm	2.8																	
Thin film sheet resistance	Milliohm/square	50																	
Bulk resistivity comparison	$\rho(\text{film})/\rho(\text{bulk Ag})$	1.8																	
Physical Properties	<p>General Description Water-based Ag ink Flash Point Non-flammable</p> <table border="1" style="width: 100%; border-collapse: collapse;"> <thead> <tr> <th></th> <th style="text-align: center;">Units</th> <th style="text-align: center;">JS-B25HV</th> </tr> </thead> <tbody> <tr> <td>Ag content</td> <td style="text-align: center;">wt%</td> <td style="text-align: center;">25</td> </tr> <tr> <td>Viscosity</td> <td style="text-align: center;">cP</td> <td style="text-align: center;">8</td> </tr> <tr> <td>Surface tension</td> <td style="text-align: center;">dyne/cm</td> <td style="text-align: center;">30-32</td> </tr> <tr> <td>Z-avg particle size²</td> <td style="text-align: center;">nm</td> <td style="text-align: center;">60</td> </tr> <tr> <td>Specific gravity</td> <td style="text-align: center;">–</td> <td style="text-align: center;">1.3</td> </tr> </tbody> </table> <p>² Malvern dynamic light scattering</p>		Units	JS-B25HV	Ag content	wt%	25	Viscosity	cP	8	Surface tension	dyne/cm	30-32	Z-avg particle size ²	nm	60	Specific gravity	–	1.3
	Units	JS-B25HV																	
Ag content	wt%	25																	
Viscosity	cP	8																	
Surface tension	dyne/cm	30-32																	
Z-avg particle size ²	nm	60																	
Specific gravity	–	1.3																	
Shipping and Packaging	<p>Standard sample order is 50 mL or multiples of 50 mL. Bulk packaging is also available.</p>																		

¹recommended for use on the following substrates: inkjet paper, Novele™ IJ-220, PET, Polyimide, glass

www.novacentrix.com
Contact us today to learn more.
 Stan Farnsworth: 512 491 9500 x210
stan.farnsworth@novacentrix.com



Metalon® Conductive Inks for Printed Electronics

www.novacentrix.com

Metalon® JS-B25HV

Nanosilver Ink – Aqueous dispersion for Dimatix Printheads

JS-B25HV is an electrically conductive ink designed to produce circuits on porous and non-porous substrates including inkjet papers, PET, polyimide, and glass. JS-B25HV ink is specially formulated for compatibility and stability with Dimatix printheads. A printing waveform for Dimatix DMP heads is available.

Performance with Traditional Oven Thermal Processing on Novele™ IJ-220

Time (min)	Resistivity (μohm-cm)			
	25C	60C	100C	125C
0	31	35	38	35
5	25	9.8	6.9	5.8
480 (8 hours)	8.0	7.4	6.5	5.7

www.novacentrix.com

Contact us today to learn more.

Stan Farnsworth: 512 491 9500 x210

stan.farnsworth@novacentrix.com

Appendix B: Programming Codes

B.1: SonnetLab and MATLAB Code for Graphene based Switches

```

%%%%%%%%%%%%%%%%%%%%%%%%%%%%%%%%%%%%%%%%%%%%%%%%%%%%%%%%%%%%%%%%%%%%%%%%
% *****
% ***** MATLAB Code for Simulating Graphene based Switches in Sonnet *****
% ***** by WAQAS AHMAD *****
% *****
%%%%%%%%%%%%%%%%%%%%%%%%%%%%%%%%%%%%%%%%%%%%%%%%%%%%%%%%%%%%%%%%%%%%%%%%

```

```

%%%%%%%%%%%%%%%%%%%%%%%%%%%%%%%%%%%%%%%%%%%%%%%%%%%%%%%%%%%%%%%%%%%%%%%%
% *****
% ***** NOTES BEFORE USING CODE *****
% As per MATLAB colour coding, syntax is in blue colour and comments are in green colour
% Graphene metallisation should be set to "Metal # 1" in Sonnet
% If copper is used anywhere else in the circuit, it should be set to "Metal # 2" in Sonnet
% Copper coding is currently commented. It needs to be uncommented before and if it is to
be used
% If copper is not used anywhere else, Sonnet will automatically use a lossless (PEC) metal
% *****
%%%%%%%%%%%%%%%%%%%%%%%%%%%%%%%%%%%%%%%%%%%%%%%%%%%%%%%%%%%%%%%%%%%%%%%%

```

```

clear all
close all
clc
echo off

```

```

NAME = 'ENTER_NAME_HERE.son'; % enter name of sonnet file to be simulated

```

```

counteruc = 0; % defining uc counter
for ucv = [0]; % enter value of uc (chemical potential)

```

```

counteruc = counteruc + 1; % defining uc iteration counter loop

% defining values of constants
epsilonV = 8.854187817e-12; % value of epsilon in vacuum
qe = -1.60217657e-19; % value of electron charge
eV = 1.60217657e-19; % value of 1 electron volt
hbar = 1.054571726e-34; % value of reduced Plank's constant
kB = 1.3806488e-23; % value of Boltzmann constant

% defining graphene parameters
uc = ucv*eV; % defining chemical potential of graphene
T = 300; % enter temperature in Kelvin
tau = 0e-12; % enter time in picoseconds
g = (2*tau)^-1; % defining scattering rate of graphene (gamma)
t = 0.34e-9; % defining thickness of graphene

% defining frequencies
fpoints = 10; % enter number of frequency points for each simulation of uc
fmin = 1e9; % enter minimum/starting frequency of simulation
fmax = 7e9; % enter maximum/ending frequency of simulation
finc = (fmax-fmin)/(fpoints-1); % defining increments of frequency points
f = fmin:finc:fmax; % defining frequency array
w = 2*pi*f; % defining angular frequency

% graphene calculations
sigmaintra = -(1i*qe^2/(pi*hbar^2)*uc + (1i*qe^2*kB*T)/(pi*hbar^2)*(2*log(exp(-uc/(kB*T))+1)))/(w-1i*2*g); % defining intraband conductivity of graphene
sigmainter = (-1i*qe^2/(4*pi*hbar))*log((2*abs(uc) - (w-1i*2*g)*hbar)/(2*abs(uc) + (w-1i*2*g)*hbar)); % defining interband conductivity of graphene
sigma = sigmaintra + sigmainter; % defining total conductivity of graphene

% sonnet definitions
counterfrequency = 0; % defining frequency counter
for ftemp = f
counterfrequency = counterfrequency + 1; % defining frequency iteration counter loop
clc
disp(' ');

```

```

disp(['Currently running uc ' num2str(counteruc) ' of total' ]);           % displays uc
iteration counter in matlab main window
disp(' ');
disp(['Currently running frequency ' num2str(counterfrequency) ' of ' num2str(fpoints)]); %
displays frequency iteration counter in matlab main window
disp(' ');

project=SonnetProject(NAME);           % loading sonnet project file in MATLAB

% project.saveAs(strcat(NAME,'.son')); % uncomment to enable saving sonnet file with a
new name before simulation starts

% graphene metallisation (metal # 1) definitions and calculations
grapheneRdc = real(1./sigma(counterfrequency));           % defining
surface resistance of graphene
grapheneXdc = imag(1./sigma(counterfrequency));           % defining
surface reactance of graphene
project.GeometryBlock.ArrayOfMetalTypes{1}.Resistance = grapheneRdc; % updating
resistance of graphene for each simulation point
project.GeometryBlock.ArrayOfMetalTypes{1}.SkinCoefficient = 0; % updating skin
coefficient of graphene for each simulation point
project.GeometryBlock.ArrayOfMetalTypes{1}.Reactance = grapheneXdc; % updating
reactance of graphene for each simulation point
project.GeometryBlock.ArrayOfMetalTypes{1}.KineticInductance = 0; % updating
kinetic inductance of graphene for each simulation point

% % copper metallisation (metal # 2) definitions and calculations
% copperConductivity = 5.8*1e7;           % defining conductivity of copper
% copperMr = 1*4*pi*1e-7;           % defining permeability of copper
% copperThickness = 17.5*1e-6;           % defining thickness of copper
% copperRdc = 1/(copperConductivity*copperThickness); % defining resistance of
copper
% copperRrf = sqrt(pi*copperMr/copperConductivity); % defining skin coefficient
of copper
% copperXdc = copperRrf*sqrt(ftemp);           % defining reactance of copper
% project.GeometryBlock.ArrayOfMetalTypes{2}.Resistance = copperRdc; % updating
resistance of copper
% project.GeometryBlock.ArrayOfMetalTypes{2}.SkinCoefficient = copperRrf; %
updating skin coefficient of copper
% project.GeometryBlock.ArrayOfMetalTypes{2}.Reactance = copperXdc; % updating
reactance of copper
% project.GeometryBlock.ArrayOfMetalTypes{2}.KineticInductance = 0; % updating

```

kinetic inductance of copper

```
% sonnet simulation frequencies calculations
```

```
if counterfrequency == 1
```

```
    fl = ftemp;
```

```
    fh = ftemp + finc/2;
```

```
elseif counterfrequency == length(f)
```

```
    fl = ftemp - finc/2;
```

```
    fh = ftemp;
```

```
else
```

```
    fl = ftemp - finc/2;
```

```
    fh = ftemp + finc/2;
```

```
end
```

```
project.addAbsFrequencySweep(fl/1e9,fh/1e9);    % adding adaptive frequency sweep for  
sonnet simulation
```

```
% project.openInSonnet()    % uncomment to open file in sonnet project editor to check  
results between each frequency point simulation
```

```
% running sonnet simulation
```

```
project.simulate('-x');    % before each simulation, "-c" will delete previous results data and  
"-x" will keep saved previous results data
```

```
end
```

```
end
```

```
%project.openInSonnet()    % uncomment to open file automatically in sonnet project  
editor at the end of simulation
```

Appendix C: List of Publications

C.1: Journals

- [WA-1] **W. Ahmad**, C. Zlebic, J. Kelly, and D. Budimir, "Compact inkjet-printed filtennas with triple bandnotch for flexible wireless applications," *IEEE Transactions on Antennas and Propagation*. (under revision)
- [WA-2] **W. Ahmad** and D. Budimir, "Highly linear reconfigurable UWB filters with independently controlled dual bandnotch," *Microwave and Optical Technology Letters*, vol. 58, no. 11, pp. 2639–2643, November 2016.
- [WA-3] **W. Ahmad** and D. Budimir, "Dual-band filtenna array for WLAN applications," *Microwave and Optical Technology Letters*, vol. 58, no. 2, pp. 477–481, February 2016.

C.2: Conferences

- [WA-4] **W. Ahmad**, A. Tarczynski, and D. Budimir, "Design of Monopole Antennas for UWB Applications," *IEEE International Symposium on Antennas and Propagation and North American Radio Science Meeting*, pp. 2323–2324, July 2017.
- [WA-5] **W. Ahmad** and D. Budimir, "Inkjet-printed antennas for 28 GHz 5G applications," *IEEE Asia Pacific Microwave Conference*, December 2016.
- [WA-6] **W. Ahmad**, M. Tasic, and D. Budimir, "Compact UWB MIMO filtennas with dual bandnotch, high isolation and high diversity," *IEEE Asia Pacific Microwave Conference*, December 2016.
- [WA-7] **W. Ahmad**, C. Zlebic and D. Budimir, "Compact inkjet-printed broadband filtennas with triple bandnotch for wireless applications," *IEEE 46th European Microwave Conference*, pp. 80–83, October 2016.
- [WA-8] **W. Ahmad** and D. Budimir, "Switchable filtennas with sharp dual bandnotch using looped resonators," *IEEE 46th European Microwave Conference*, pp. 445–448, October 2016.

- [WA-9] **W. Ahmad**, C. Zlebic and D. Budimir, "Inkjet-printed UWB filtennas with triple bandnotch," *IEEE International Symposium on Antennas and Propagation and North American Radio Science Meeting*, pp. 825–826, June 2016.
- [WA-10] **W. Ahmad** and D. Budimir, "Reconfigurable UWB filtennas with dual bandnotch for unwanted bands using Graphene based switches," *IEEE International Symposium on Antennas and Propagation and North American Radio Science Meeting*, pp. 2123–2124, June 2016.
- [WA-11] **W. Ahmad** and D. Budimir, "Reconfigurable UWB filtennas with sharp WLAN dual bandnotch," *IEEE 45th European Microwave Conference*, pp. 1228–1231, September 2015.
- [WA-12] **W. Ahmad**, A. Maric, N. Ivanisevic, and D. Budimir, "Inkjet printed bandpass filters and filtennas using silver nanoparticle ink on flexible substrate," *IEEE International Symposium on Antennas and Propagation and North American Radio Science Meeting*, pp. 145–146, July 2015.
- [WA-13] **W. Ahmad** and D. Budimir, "Dual-band WLAN antenna array with integrated bandpass filters for harmonic suppression," *IEEE International Symposium on Antennas and Propagation and North American Radio Science Meeting*, pp. 619–620, July 2015.
- [WA-14] **W. Ahmad** and D. Budimir, "Reconfigurable WLAN notch for UWB filters," *IEEE 44th European Microwave Conference*, pp. 1536–1539, October 2014.

C.3: Seminars

- [WA-15] **W. Ahmad** and D. Budimir, "UWB filtennas with dual bandnotch for WiMAX and WLAN bands using circular and square resonators," *IET 3rd Active and Passive RF Devices Seminar*, February 2016.
- [WA-16] **W. Ahmad** and D. Budimir, "Dual-band WLAN antenna array with integrated filters for harmonic suppression," *IET 2nd Active and Passive RF Devices Seminar*, October 2014.
- [WA-17] **W. Ahmad** and D. Budimir, "Integrated WLAN notchband for broadband antennas," *IET Technical Enterprise Workshop*, February 2013.